2011-01-01

Dispersion Geochemistry at Different Scales at the Nopal I Deposit, Peña Blanca Uranium District, Chihuahua, Mexico

Katrina Pekar-Carpenter
University of Texas at El Paso, katspot@yahoo.com

DISPERSION GEOCHEMISTRY AT DIFFERENT SCALES AT THE NOPAL I DEPOSIT, PEÑA BLANCA URANIUM DISTRICT, CHIHUAHUA, MEXICO

KATRINA EILEEN PEKAR-CARPENTER

Department of Geological Sciences

APPROVED:

_____
Philip C. Goodell, Ph.D., Co-chair

_____
John C. Walton, Ph.D., Co-chair

_____
Elizabeth Y. Anthony, Ph.D.

_____
David Borrok, Ph.D.

_____
Richard P. Langford, Ph.D.

_____
Lin Ma, Ph.D.

_____
Benjamin C. Flores, Ph.D.
Acting Dean of the Graduate School

Dedication

I dedicate this dissertation to my family.

DISPERSION GEOCHEMISTRY AT DIFFERENT SCALES AT THE NOPAL I DEPOSIT, PEÑA BLANCA URANIUM DISTRICT, CHIHUAHUA, MEXICO

by

KATRINA EILEEN PEKAR-CARPENTER, M.S.

DISSERTATION

Presented to the Faculty of the Graduate School of

The University of Texas at El Paso

in Partial Fulfillment

of the Requirements

for the Degree of

DOCTOR OF PHILOSOPHY

Department of Geological Sciences

THE UNIVERSITY OF TEXAS AT EL PASO

December 2011

Acknowledgements

First, I would like to thank my advisor, Dr. Phil Goodell, for his guidance and support during my research. He made me a better scientist and motivated me to exceed my expectations. I will always regard his as a mentor and friend.

I would also like to thank my co-advisor, Dr. John Walton, who helped me with the modeling portions of my research. I never would have ventured into or succeeded in the mathematical modeling world without his help.

I would like to express my gratitude towards the remaining members of my dissertation committee, Libby Anthony, David Borrok, Rip Langford, and Lin Ma for their time and helpful comments. They especially helped by suggesting alternative research methods for portions of my research.

There are many others who have helped with my research. Special thanks to Dr. Mostafa Fayek at the University of Manitoba for inviting me to Winnipeg for a summer to use the XRD, EMP, and SIMS, through his NSERC Discovery Grant and CRC, and for his continued guidance. The technicians Panseok and Rong deserve my thanks. I met many people there who made my stay more enjoyable: Charles, Alba, Laura, Sharon, Fawn, and the Gottfried family.

I especially would like to thank my family for their love and support without whom I never would have tried or succeeded in this endeavor. Grandpa and Grandma, you fueled my passion for geology as a child and thank you for memories of trips to Yellowstone, Mt. St. Helens, and numerous other places. Mom and Dad, thank you for your continued encouragement that I was doing the right thing. Kevin, my husband, it has been hard at times, especially traveling from El Paso to Boston before you were able to get a job here, but I would not change things for anything. It has been a wild time in El Paso, and I look forward to further adventures together with you. It was a long road, but the rewards are worthwhile.

I would not be at UTEP if not for the members of the Peña Blanca Natural Analogue project. I am grateful for the research materials and collaborations with members of the project. I would especially like to thank Schön Levy for her guidance and encouragement.

This research was prepared in part by the University of Texas at El Paso for the U.S. Department of Energy Office of Civilian Radioactive Waste Management (OCRWM) under Contract Number DE-AC02-05CH11231 as part of the OSTI Program. The research was also performed under appointment of the OCRWM Graduate Fellowship Program administered by Oak Ridge Institute for Science and Education under a contract between the U.S. Department of Energy and the Oak Ridge Associated Universities. The views expressed in this article are those of the author and do not necessarily reflect the views or policies of the U.S. DOE or OCRWM.

Abstract

The Nopal I mine in the Peña Blanca Uranium District, Chihuahua, Mexico is a natural analog for the geologic storage of nuclear waste. This dissertation presents data from two sites within Nopal I: 1) the PB-1 core, which was drilled along the extent of uranium mineralization in the Nopal I mine; and 2) a high-grade stockpile boulder from the mineralized Nopal tuff.

The PB-1 core allowed an investigation into the mineralogical and geochemical changes that are important to research on a nuclear waste repository. Five zones were determined to control these changes: 1) Zone 1, the primary uranium mineralization (quartz-uraninite-pyrite-kaolinite-ilmenite); 2) Zone 2, the oxidized equivalent to zone 1; 3) Zones 3a and 3b, which are redox-transition zones; 4) Zone 4, or the Pozos Uranium Anomaly, which was a reducing zone for uranium and other redox sensitive elements; and 5) Zone 5, the Cretaceous limestone, which serves as a barrier to a majority of radionuclide transport. SIMS U-series investigation of uranium minerals showed that the Pozos Uranium Anomaly formed 375 ka-1 Ma, and unlike the primary uranium assemblage, the younger uranium minerals were associated with anatase and kaolinite, indicating their adsorptive capabilities in a potential repository setting.

The mineralized boulder was analyzed using qualitative and quantitative methods to determine the mode of radionuclide release from the boulder to the soil, the weathering rate, and the transport of radionuclides within the soil from the boulder. The weathering rate of uranium from the boulder (12-34 mg $U/m^2/day$) is ~150 times higher than in laboratory experiments using UO_2 fuel pellets, which may be more representative of the effect uncontrolled, intermittent environmental changes have on weathering. Radionuclide transport from the boulder and within the soil occurs by diffusion, dispersion and filtration, but the amount each contributes is still undetermined.

Table of Contents

List of Tables

List of Figures

1. Introduction

Spent nuclear fuel and the byproduct of its reprocessing are high-level radioactive wastes. They present a problem for disposal, because of their high radioactivity and long lifetime. High-level radioactive waste must be contained and isolated from people and the environment for tens of thousands of years. Storage in engineered geologic repositories is investigated worldwide as an answer to their high-level radioactive waste problem.

In the United States, the Nuclear Waste Policy Act of 1982 (NWPA) supports the use of deep engineered geologic repositories for storage and/or disposal of high-level radioactive wastes (42 U.S. Code §10101 et seq. 1982). The NWPA assigned the Department of Energy (DOE) responsibilities to select an appropriate site using extensive research and then build and operate it. The Environmental Protection Agency (EPA) was directed to develop standards for protection of the environment from offsite releases of radioactive wastes and the Nuclear Regulatory Commission (NRC) has the authority to license the DOE to operate the selected repository if the EPA standards and other requirements are met.

The NWPA was amended in 1987 by Congress and selected Yucca Mountain as the only site to be characterized as the repository for the nation's waste. In 2002, the Secretary of Energy recommended Yucca Mountain as the repository site to President Bush and it was approved. Nevada challenged the ruling, but only succeeded in extending a license compliance period of 10,000 years to one million years, as recommended by the National Academy of Sciences (NAS, 1995). In 2008, the Secretary of Energy submitted the license application to the NRC for review (DOE, 2008). Later in 2010, a new Secretary of Energy withdrew the license application under recommendation of President Obama, but the legality of this decision is under review, because Congress mandated the NWPA and only the federal court system can determine if the President, Secretary of Energy or the Nuclear Regulatory Commission are failing to uphold the law. Therefore, the status of the Yucca Mountain repository is uncertain.

1.1 NATURAL ANALOGUES

The biggest problem scientists must deal with is how spent nuclear fuel, and its storage container, will corrode over geologic scales. Natural analogues, such as uranium deposits, can be used as a proxy for long-term geologic storage of nuclear waste (Bruno et al., 2002). They provide supplemental data that go along with lab experiments designed to understand waste form performance under varied conditions. Fortunately, uranium in spent nuclear fuel, UO_2, has virtually the same composition and an identical structure to natural uraninite, UO_{2+x}, (Janeczek et al., 1996) and their alteration products have a similar mineralogical paragenesis under oxidizing conditions (Finch and Ewing, 1992; Janeczek and Ewing, 1992; Pearcy et al., 1994; Wronkiewicz and Buck, 1999). Unfortunately, natural analogues are long-term natural experiments whose conditions cab be observed, but are not controlled by scientists, which can make interpreting "what happened" more difficult (IAEA, 1999).

There are many types of natural analogues. The "natural reactors" at Oklo, Gabon are 2.2 Ga and are especially important and a brief summary is provided (e.g., Kuroda, 1956; Curtis et al., 1981; Meshik, 2005). Uranium was reduced in a sedimentary basin, and formed sandstone-hosted uranium deposits, but this is not what makes them unique. Two billion years ago, the natural $^{235}U/^{238}U$ ratio was much higher, so that when the uranium was concentrated, the amount of ^{235}U reached a critical amount and periods of sustained nuclear chain reactions moderated by water occurred. The Oklo natural reactors provided an opportunity to understand the conditions that could preserve spent nuclear fuel for billions of years and also the fate and transport of fission products and actinides (Bruno and Ewing, 2006).

Other natural analogs allow observations of uranium mineral behavior under oxidizing and reducing conditions in different host rocks. Some examples are Alligator River, Australia (e.g. ANSTO, 1992), Shinkolobwe, Zaire (e.g., Finch and Ewing, 1991), and Cigar Lake, Canada (e.g. Cramer, 1986). An additional natural analog located in the Peña Blanca uranium district is the focus of this study.

The uranium at Peña Blanca was mined by the Mexican government until 1981, and since then has been the subject of numerous natural analog studies. The Peña Blanca Natural Analog, in particular the Nopal I deposit, was selected for its geologic, tectonic, hydrologic, and geochemical similarities to Yucca Mountain (e.g., Levy et al., 2011). The uranium deposit at Nopal is hosted in rhyolitic ash flow tuffs, which are similar to the rhyolitic ash flow tuffs at Yucca Mountain that would host the spent nuclear fuel (Day et al., 1999; Peterman and Cloke, 2002; Stuckless and O'Leary, 2007). These tuffs are also about 100 m and 300 m above the current water table, respectively (Wong, 1994; Stuckless and Dudley, 2002; Dobson et al., 2008). Both sites contain high-angle normal faults and steeply dipping fractures and are underlain by limestone basement rocks (Day et al., 1999; Stuckless and Dudley, 2002; Stuckless and O'Leary, 2007; Dobson et al., 2008). Annual rainfall is about 300 mm/y at Los Pozos, Chihuahua (Servicio Meterologico Nacional, Mexico), which is near Nopal I, and is higher than Yucca Mountain's 177 mm/y (Sharpe, 2007). The following section provides a more detailed description of Nopal I geology.

2. Geology of Nopal I

The Nopal I deposit is part of the Peña Blanca uranium district located approximately 50 km north of Chihuahua City, Chihuahua, Mexico (Figure 1). The Sierra de Peña Blanca, a horst block located in the Chihuahua tectonic belt, a basin and range province, formed part of the western edge of the Chihuahua trough during the Cretaceous (Goodell, 1981). Dobson et al. (2008) updated the stratigraphic section of Alba and Chavez (1974) specifically for the Nopal I deposit using the PB-1 well drilled in 2003 (Figure 2). Unless otherwise noted, information is summarized from Dobson et al. (2008) in the descriptions below.

The PB-1 well was drilled along the margin of the Nopal I uranium deposit on the +10 level, with UTM coordinates of 3220793 N, 399275 E (NAD83 datum) and a surface elevation of 1463 a.s.l. The well is 250 m deep, and NQ core (4.76 cm diameter) was obtained throughout the drilled section with an over all recovery of 86.2%. Due to drilling problems, three separate sections of core were obtained in adjacent wells. Four main stratigraphic units were intercepted by the well: the Nopal Formation, the Coloradas Formation, the Pozos Formation with several layers of interbedded pumiceous tuff, and an underlying Cretaceous limestone basement. The formations in the vicinity of the Nopal I deposit dip slightly (9-20 degrees, average 13 degrees) (Reyes-Cortes, 1997), which result in apparent thicknesses that are slightly greater than actual thickness of unit. The thickness of the Coloradas Formation in the PB-1 core (114 m in core, 111 m dip corrected) is slightly greater than average thickness (90 m) reported by Reyes-Cortes (1997). The thickness of the Pozos Formation (108 m in core, 105 m dip corrected) is very similar (111.8 m) to the Nopal questa outcrop section, located about 1 km NW of the PB-1 well, measured by Reyes-Cortes (1997). The formations are described in greater detail below.

2.1 NOPAL FORMATION

The Nopal and Coloradas Formations were once described as one unit, but later subdivided into two different units: a series of rhyolitic ash flow tuffs (Nopal Formation) and a basal series of lithic tuffs (Coloradas Formation), with a basal vitrophyre forming the contact

between the two units (Reyes-Cortes, 1997; 2002). K-Ar dates from sanidine in the Nopal Formation were reported by Alba and Chavez (1974) and recalculated by Dobson et al. (2008) to 44.8±0.9 Ma using the decay constants of Steiger and Jäger (1977).

The Nopal Formation was sampled over 0-22.30 m of the core. It is a densely welded, crystal-rich, rhyolitic ash-flow tuff that is highly altered, with devitrification of the glassy matrix and kaolinitization of feldspars and groundmass. Also observed were relict flattened pumice and volcanic lithic fragments. Quartz, chlorite, and montmorillonite are common alteration minerals.

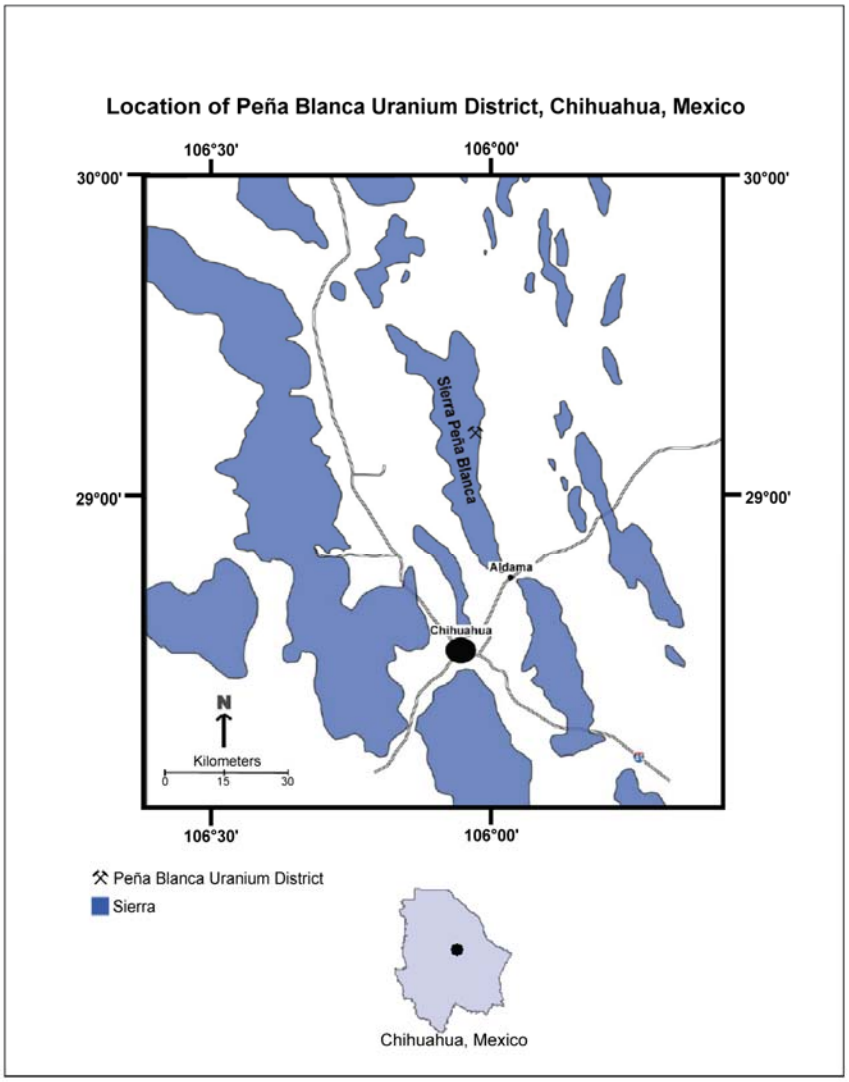

Figure 1. Location map for the Peña Blanca Uranium District, Chihuahua, Mexico. The Nopal I mine is one of several mines in the district.

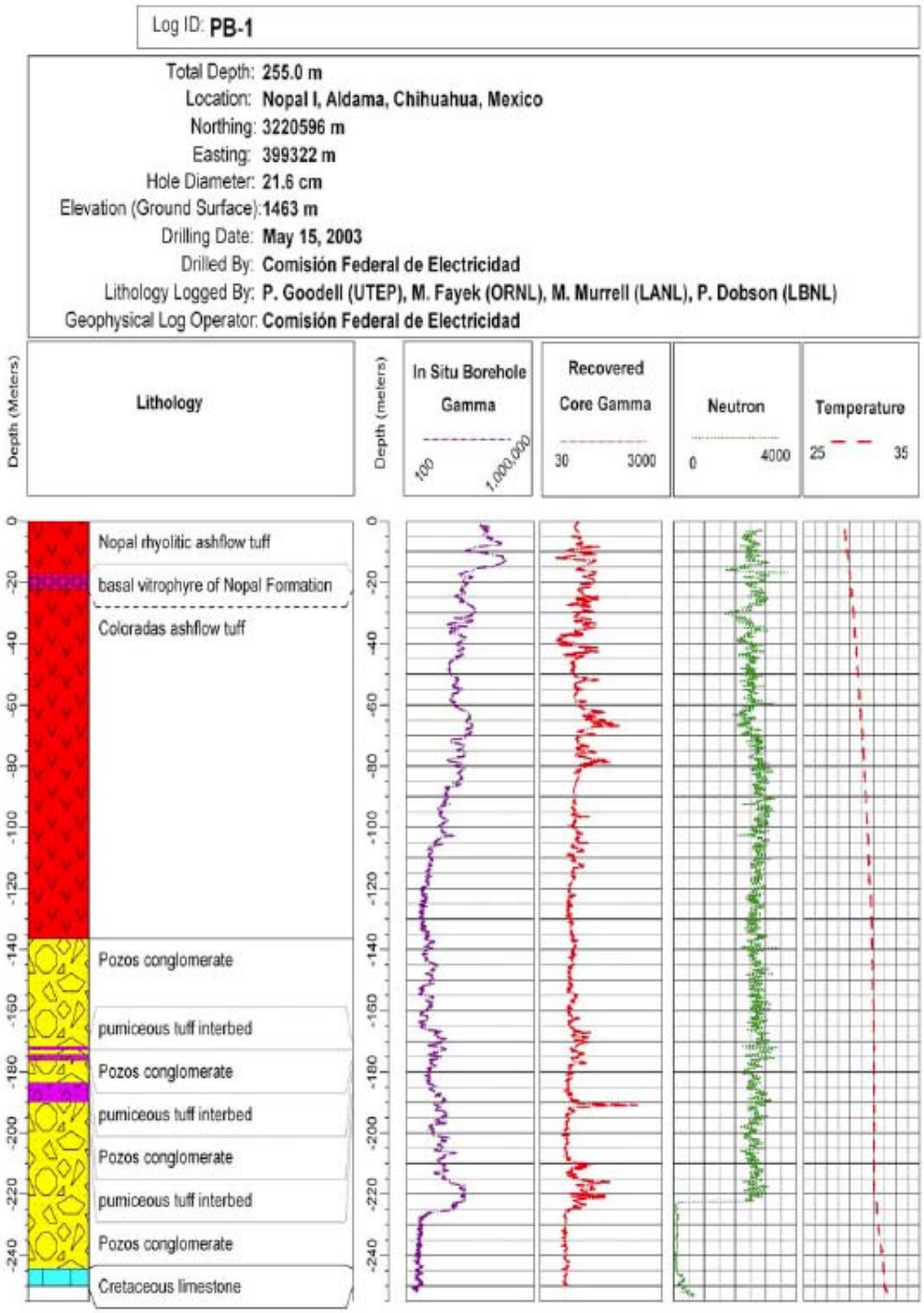

Figure 2. PB-1 Well log from Dobson et al. (2008). Borehole and core gamma is measured in counts per second (log scale), neutron measurements are in API units, and temperatures are in degrees Celsius.

Previous work has reported zeolites (Reyes-Cortes, 2002), but they were not identified in the core. Highly brecciated portions of the core, immediately adjacent to the ore body, contain fracture fillings of hematite, limonite, and goethite. The basal vitrophyre of the Nopal Formation (17.45-22.30 m) is intensely, argillically-altered to kaolinite and montmorillonite.

2.2 COLORADAS FORMATION

The Coloradas Formation (22.30-136.38 m) portion of the core is a fractured and brecciated, welded, lithic-rich, rhyolitic ash-flow tuff. About 10-20% of the altered tuff contains volcanic lithic fragments with some pumice-rich intervals (up to 30%). Similar to the Nopal Formation, the cored section of the Coloradas formation is highly-altered, showing devitrification, oxidation (e.g., hematite, limonite, and goethite) and argillic alteration of primary minerals and matrix. Secondary quartz occurs as both a low temperature phase in veins and pores and a devitrification product. A sharp contact with the underlying Pozos Formation in the PB-1 core is at a depth of 136.38 m.

2.3 POZOS FORMATION

The Pozos Formation (136.38-244.40 m) in the core is a poorly-sorted conglomerate with minor sandstone interbeds. Clasts of subangular to subrounded fragments of volcanic rocks, limestone, and chert range in size from 1 mm to over 10 cm in diameter. Three thin (2-6 m) intervals of intercalated, pumiceous tuffs were observed within this unit in the PB-1 core, and may be correlative to the Corrales Formation tuffs. Bleached and oxidized zones observed within the formation are interpreted as changes in oxidation state. For example, iron oxyhydroxides occur above ~180 m, whereas pyrite exists below that depth, indicating a change in redox environment. Many fractured and brecciated zones are associated with secondary mineralization—limonite, hematite, silica, calcite, kaolinite, and clays. The contact in the PB-1 core between the Pozos Formation and the underlying Cretaceous limestone was observed at a depth of 244.40 m.

2.4 CRETACEOUS LIMESTONE

At the base of the PB-1 core, a massive, micritic limestone was encountered from 244.40-250.00 m. It is considered Cretaceous in age (Reyes-Cortes 2002), corresponding with either the uppermost Tamaulipas Formation or Cuesta del Cura Formation. The limestone contains microfossils of foraminifera, ostrocods, bryozoans, and gastropods (Dobson et al., 2008). Minor thin veins of calcite crosscut cut the limestone, especially in brecciated zones (Dobson et al., 2008).

3. Implications for Radionuclide Transport Based on Uranium Mobility from Analysis of the PB-1 Core

3.1 INTRODUCTION

The PB-1 core from the Nopal I mine, Peña Blanca Uranium District, Chihuahua, Mexico provides a unique opportunity to study radionuclide transport in the vertical direction. Fractures are important, because they could serve as fast pathways for radionuclide migration from a nuclear waste repository to the groundwater table. Studies on Yucca Mountain provide evidence for fractures acting as fast pathways (Fabryka-Martin et al., 1993; Nicholl et al., 1994, Paces et al., 1996; Su et al., 1999; Salve et al., 2003). Questions need to be answered about the behavior of radionuclides in fractures. Are the radionuclides passing through or are they retarded or even reduced by minerals within and around the fractures? What minerals act as radionuclide getters or reducing agents? Is radionuclide migration still occurring, and on what timescales? What implications do these answers have on Yucca Mountain repository science? This study of the PB-1 core will provide answers to some of these questions, but others are beyond the scope of this investigation. The purpose for drilling and collecting the core is helpful to understanding this section.

Vertical fractures are present at Nopal I (Figure 3). Research wells— PB-1, PB-2, and PB-3—were drilled by the DOE, Office of Civilian Radioactive Waste Management in 2003 and initial studies of Nopal I by the Peña Blanca Natural Analog project began in 2004 (Levy et al., 2011). The goals were to understand the processes at work between the Nopal I uranium deposit and the groundwater table and develop a three-dimensional model of radionuclide transport at Nopal I (Levy et al., 2011). The gamma log of the wells (Figure 4) indicated multiple radioactive zones, the Nopal I ore body, an associated and possibly connected sub-anomaly, and an anomaly near the bottom of the PB-1 well, which will be referred to as the Pozos uranium anomaly.

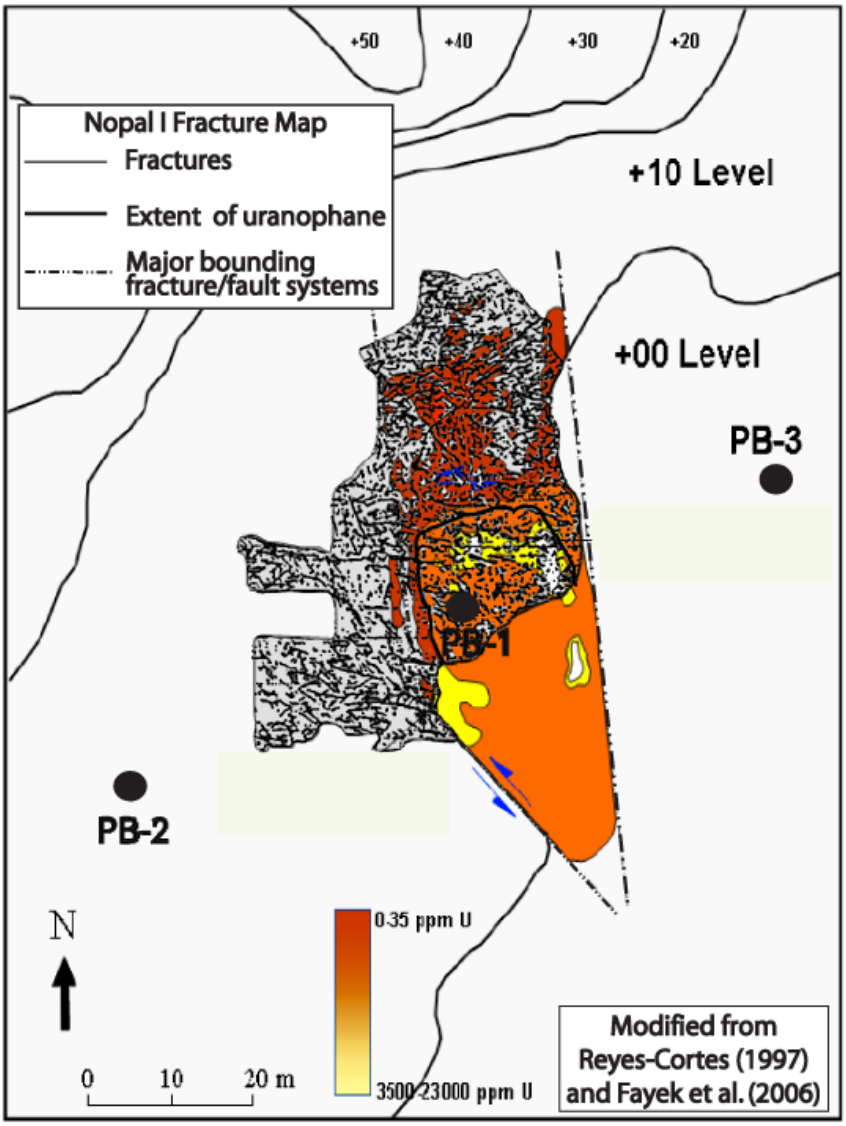

Figure 3. Map of fractures on the +00 level of Nopal I (modified from Reyes-Cortes, 1997; Fayek et al., 2006). The gray area shows the visible fractures (black lines) and uranium concentration (red to yellow area) bounded by faults/fractures on the cleared surface of the +00 level. These fractures will be investigated in the PB-1 core to determine how they influence radionuclide migration.

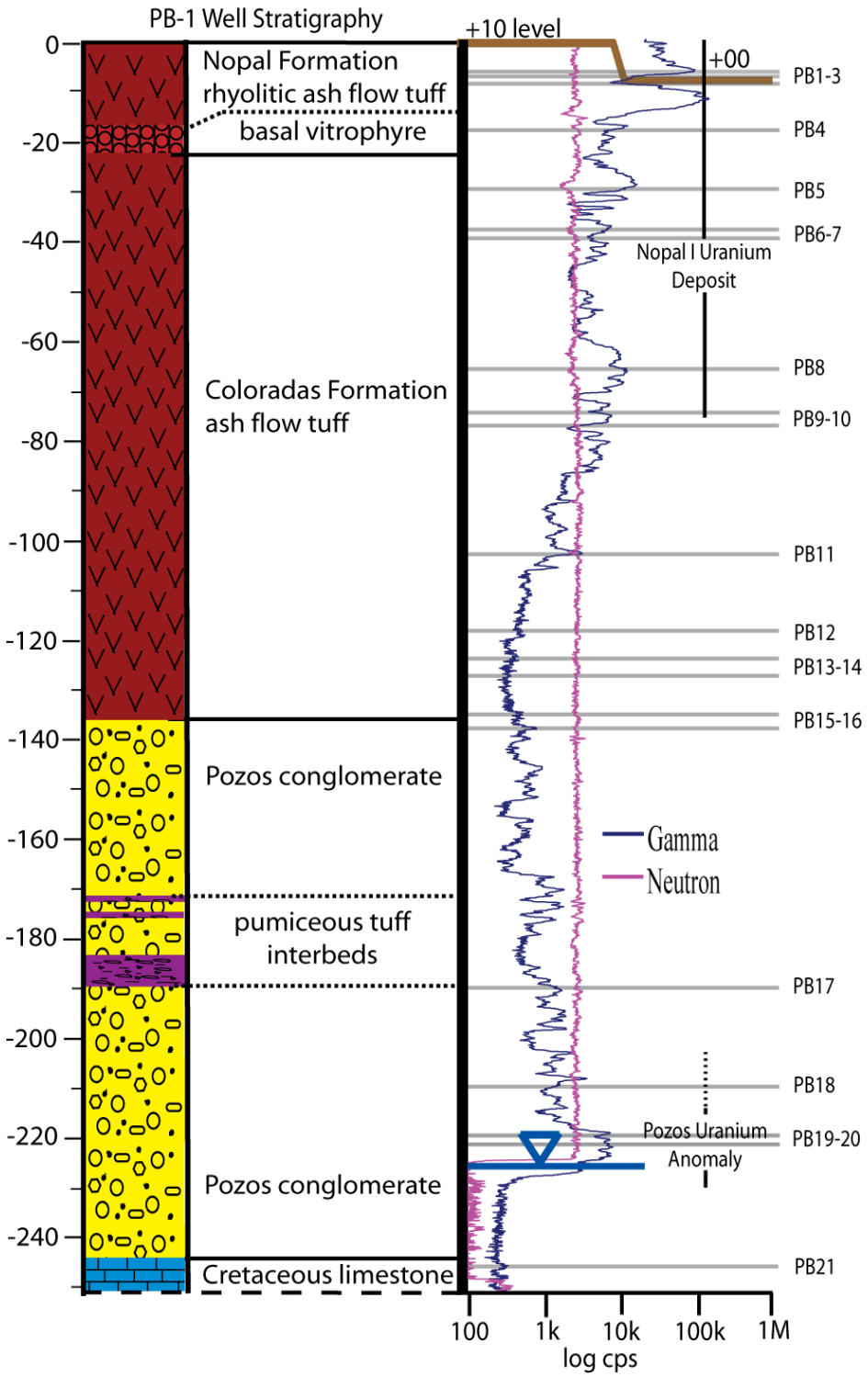

Figure 4. Modified from Dobson et al. (2008). Drill-hole template with gamma (blue) and neutron (purple) logs on a logarithmic scale. The extent of the Nopal I uranium deposit and the Pozos uranium anomaly are estimated from the gamma ray activities and the uranium deposit model (Figure 5). Gray lines show ordered sample numbers.

A model of the uranium mineralization from Oliver et al. (2005) (Figure 5) is the basis for the depth of the uranium deposit in Figure 4. The model used assay records from mine adits to model the Nopal I uranium deposit. The base of the uranium deposit is approximately 75 m depth based on this model and the decrease in the gamma log intensity from 75 to about 120 m depth is probably due to a second uranium anomaly at the base of the Nopal I deposit (centered ~90 m). Then using only the gamma log data, the model was further extrapolated through to the base of the core. The Pozos uranium anomaly was first identified this way. It is estimated between 190 and 230 m depth, based on this model.

The following sections present and summarize results individually for x-ray diffraction (XRD), electron microprobe (EMPA), multi-element chemistry, and secondary ion mass spectrometry (SIMS), and then a larger discussion synthesizes all the data together at the end of the section. Drill-hole templates are used in each section to explain the data, understand the breadth of sampling, and for data comparison (ex. Figure 4). Tic marks are placed along the core to show sample locations for each data type. A sample catalog with sample numbers from this study along with the type of analysis performed on each sample is provided (Table 1) and a catalog showing equivalent sample designations from previous studies is provided in Appendix A. Both analysis numbers (e.g., PB774 [PB2], PB4009 [PB17]) and ordered samples numbers (e.g., PB2, PB17) are used throughout the section to identify the sample analyzed and its relative depth, repsectively (see Table 1). Five zones will be used to in the following sections to help the reader keep characteristic geologic groups together, but will not be fully described until the overall discussion.

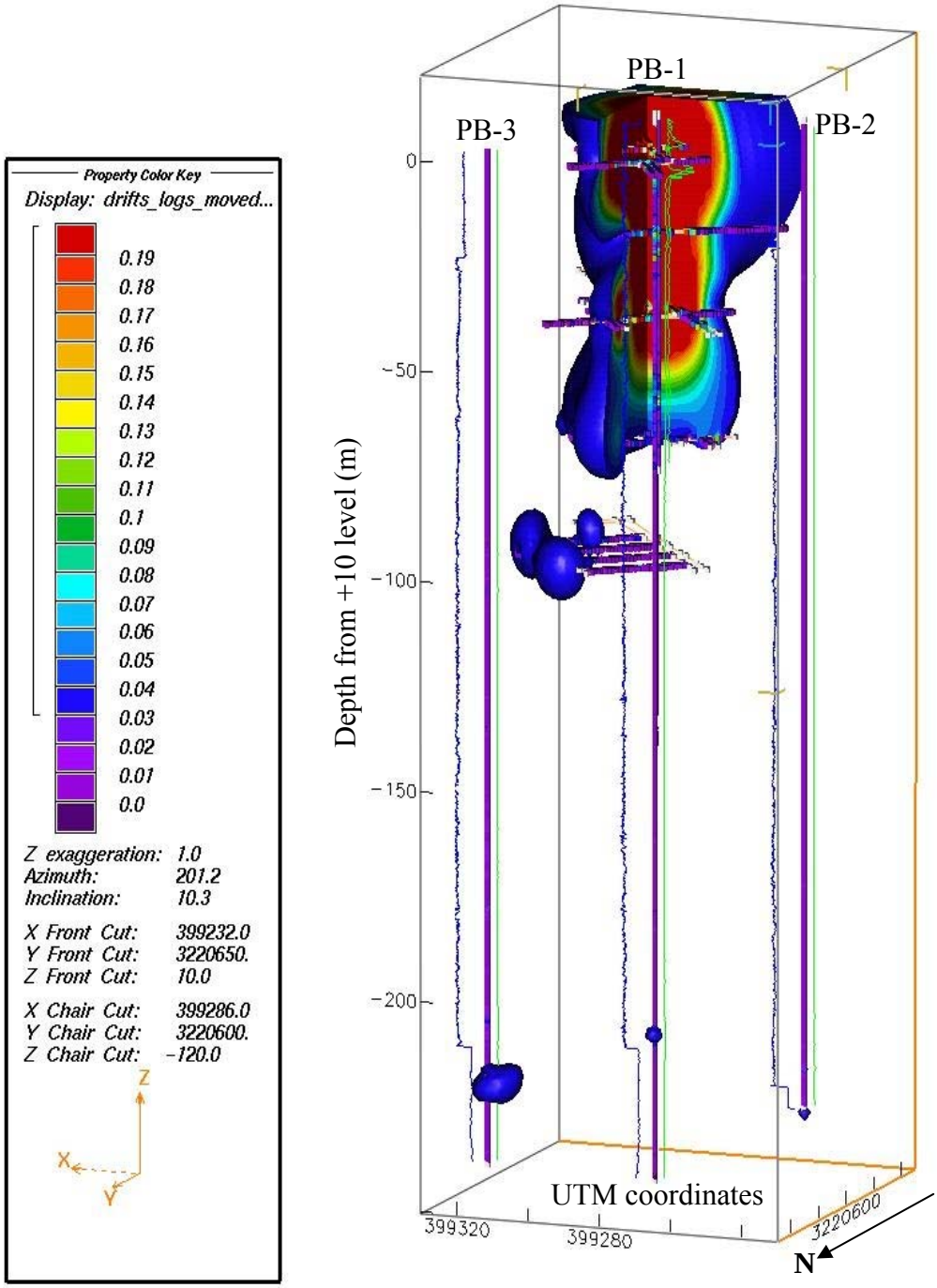

Figure 5. Model of the Nopal I uranium deposit from mine assay records and geophysical log (Oliver et al., 2005). The contours are in %U, and red represents the highest %U, whereas purple represents the lowest %U. Note the Pozos uranium anomaly at about -220 m depth.

Table 1. Sample catalog

Location			Sample numbers		Data types			
Zone	Formation	Depth (m)	Ordered sample numbers	Analysis sample numbers	XRD	EMPA	SIMS	Bulk chemistry
1	Nopal-Mineralized	+00 level	PB-A	PB-A	x			
			PB-B	PB-B	x			
			PB-C	PB-C	x			
			PB-D	PB-D	x			
2	Nopal	-7.5	PB1	PB772				x
		-8.6	PB2	PB 774	x	x		x
		-9.1	PB3	PB 775	x	x		x
		-17.8	PB4	PB 782	x			x
	Coloradas	-29.8	PB5	PB 798	x	x		x
		-37.8	PB6	PB 812	x	x		x
		-40.0	PB7	PB 814	x	x		x
		-66.5	PB8	PB 849	x	x		x
3a		-76.6	PB9	PB 860				x
		-78.2	PB10	PB 862	x	x		x
		-103.7	PB11	PB 891	x			x
		-119.0	PB12	PB 912	x	x		x
		-123.2	PB13	PB 917	x			x
		-127.0	PB14	PB 922				x
		-136.0	PB15	PB 935	x	x		x
3b	Pozos conglomerate	-138.4	PB16	PB 938	x	x		x
4		-190.8	PB17	PB 4009	x	x	x	x
		-210.3	PB18	PB 4035				x
		-219.5	PB19	PB 4049	x			x
		-220.8	PB20	PB 4052	x	x	x	x
5	Cretaceous limestone	-245.6	PB21	PB 4085				x

3.2 X-RAY DIFFRACTION

Prior powder XRD work on Nopal I samples reported an ilmenite-like phase and uraninite (Aniel and Leroy, 1985), clays (Ildefonse et al., 1990a, b), and primary and secondary uranium minerals (Pearcy et al., 1994) from samples accessible on the surface and from the mine adit. This section describes the XRD mineral identification of samples from within the mine adit and fracture and alteration material from down the PB-1 drill core (Figure 6); results from this study and previous work are included.

3.2.1 Methodology

Four mineralized samples from the mine adit and 21 core samples (see Appendix A for all core sample numbers and descriptions) were prepared for powder XRD analysis. Each fracture and/or altered area of the sample was micro-drilled with a Dremel tool to obtain enough sample material for analysis. The drilled material was further powdered with a mortar and pestle, in order to obtain a uniform powder. Finally, each powdered sample was mixed with acetone and dried onto a glass slide.

Samples were analyzed on a Siemens D5000 powder diffractometer at the University of Manitoba, Department of Geological Sciences. Data was collected over the range 3°-66° 2θ for about 20 minutes per sample. Diffraction patterns were analyzed using MDI Jade data processing software and XRD mineral identification catalogs.

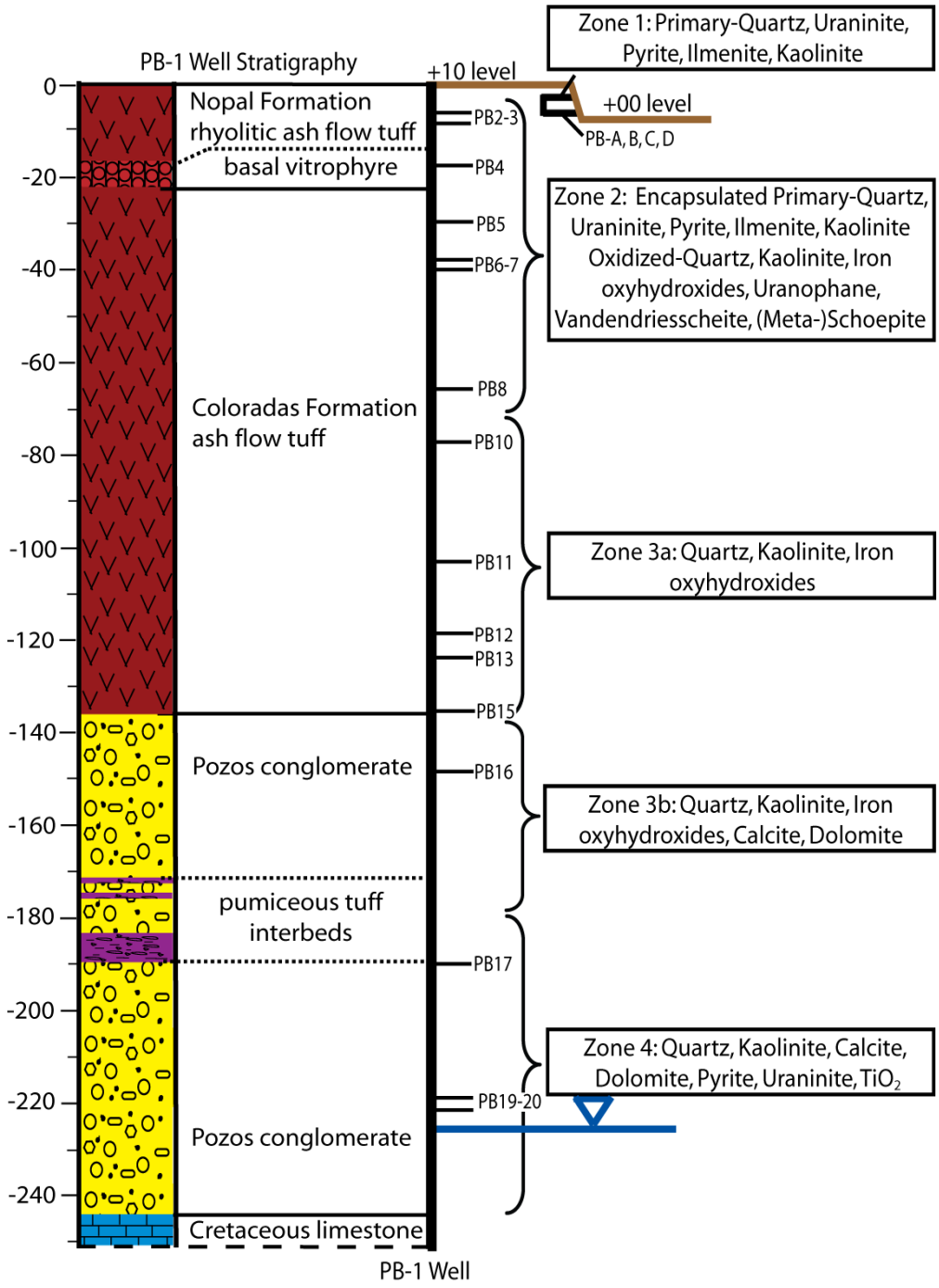

Figure 6. Drill-hole template showing XRD sample locations (black dashes) and mineralogical zones in the core. The primary uranium mineralization (Zone 1) is based on work by Aniel and Leroy (1985) and Pearcy et al. (1994), because some minerals were too low in concentration to be identified by the XRD analysis. Silicification preserved some of the primary mineralization, but is uncommon in the PB-1 core compared to the main Nopal I mineralization. The uraninite and TiO_2 in Zone 4 is reported by Fayek et al. (2006). Sulfides are common below ~180 m within the Pozos conglomerate and Cretaceous limestone and correspond to a downward transition to lower permeability rocks (Dobson et al., 2008; Levy et al., 2011).

3.2.3 Results

Powder XRD results from this study are summarized in Table 2. Twenty-two samples from the Nopal I mine adit, Nopal, Coloradas, and Pozos Formations are represented, but the bedrock Cretaceous limestone was not analyzed. Representative XRD patterns are presented in this section, and the remaining patterns are located in Appendix B.

Table 2. Summary of XRD fracture/alteration mineral identification by formation

Formation	# of samples	Quartz	Kaolinite	Calcite	Dolomite	Pyrite	Goethite	Hematite	U^{+4}	U^{+6}
Zone 1 (mine adit	4	x	x						x	x
Zone 2	7	x	x							
Zone 3a	4	x	x				x	x		
Zone 3b	1	x	x	x	x		x	x		
Zone 4	3	x	x	x	x	x				
Zone 5	N/A									

-U^{+4} represents reduced uranium minerals: uraninite
-U^{+6} represents hexavalent or oxidized uranium minerals: uranophane, vandendriesscheite, and (meta-)schoepite
-Iron minerals: Pyrite is a reduced iron mineral (Fe^{+2}), whereas goethite and hematite are oxidized iron minerals (Fe^{+3}).

In order to fully describe the zones shown in Figure 6, Table 2 results were supplemented with mineralogical data from previous work. For the four mine adit samples, or zone 1, there are both tetravalent (U^{+4}; reduced)—uraninite—and hexavalent (U^{+6}; oxidized)—uranophane, vandendriesscheite, and (meta-)schoepite—uranium minerals (Figure 7). The presence of hexavalent uranium minerals supports an oxidizing environment where uranium mobility can occur. The primary mineralogy of the mineralized zone is quartz-uraninite-pyrite-ilmenite-kaolinite, but may be more than one stage (Aniel and Leroy, 1985; Pearcy et al., 1994). Table 2 XRD data only identifies uraninite, quartz, and kaolinite from this assemblage, because pyrite and ilmenite are minor phases and their abundances are probably too low to identify by XRD. Although the zone 1 primary assemblage is uncommon in the PB-1 core compared to the Nopal I mineralization, silicification has preserved evidence of its existence in zone 2. As for secondary mineralogy, or zone 2, oxidized uranium minerals, kaolinite, and iron oxyhydroxides are evidence of an alteration event(s) throughout Nopal I.

The Nopal (Figure 8) and Coloradas Formations (Figure 9) have similar characteristic fractures and alteration (zone 3a), which is dominated by quartz and kaolinite. They are both variably-welded ash flow tuffs, so the weathering and alteration processes should have similar affects on both of them. The Coloradas Formation does have more iron oxyhydroxides than the Nopal Formation based on these XRD results, because they make up a larger percentage in some samples; however, this does not mean that the Nopal Formation is absent of these minerals, but rather the Nopal Formation has a higher composition of quartz and kaolinite.

The Pozos conglomerate consists of ash flow tuff and limestone rock fragments. The limestone fragments are probably from the underlying Cretaceous limestone and the tuff fragments are probably derived from the 52-53 Ma Cuervo Group (P. Goodell, pers. comm.). Zone 3b (Figure 10) and zone 4 (Figure 11) are from the Pozos conglomerate, it was separated into two zones due to mineralogical and hydrologic characteristics. Both zones have calcite and dolomite, in addition to quartz and kaolinite, but the transition at ~180 m from iron oxyhydroxides in zone 3b to pyrite in zone 4 defines the boundary (Levy et al., 2011). Dobson et al. (2008) reported a downward transition to lower permeability rocks at this depth.

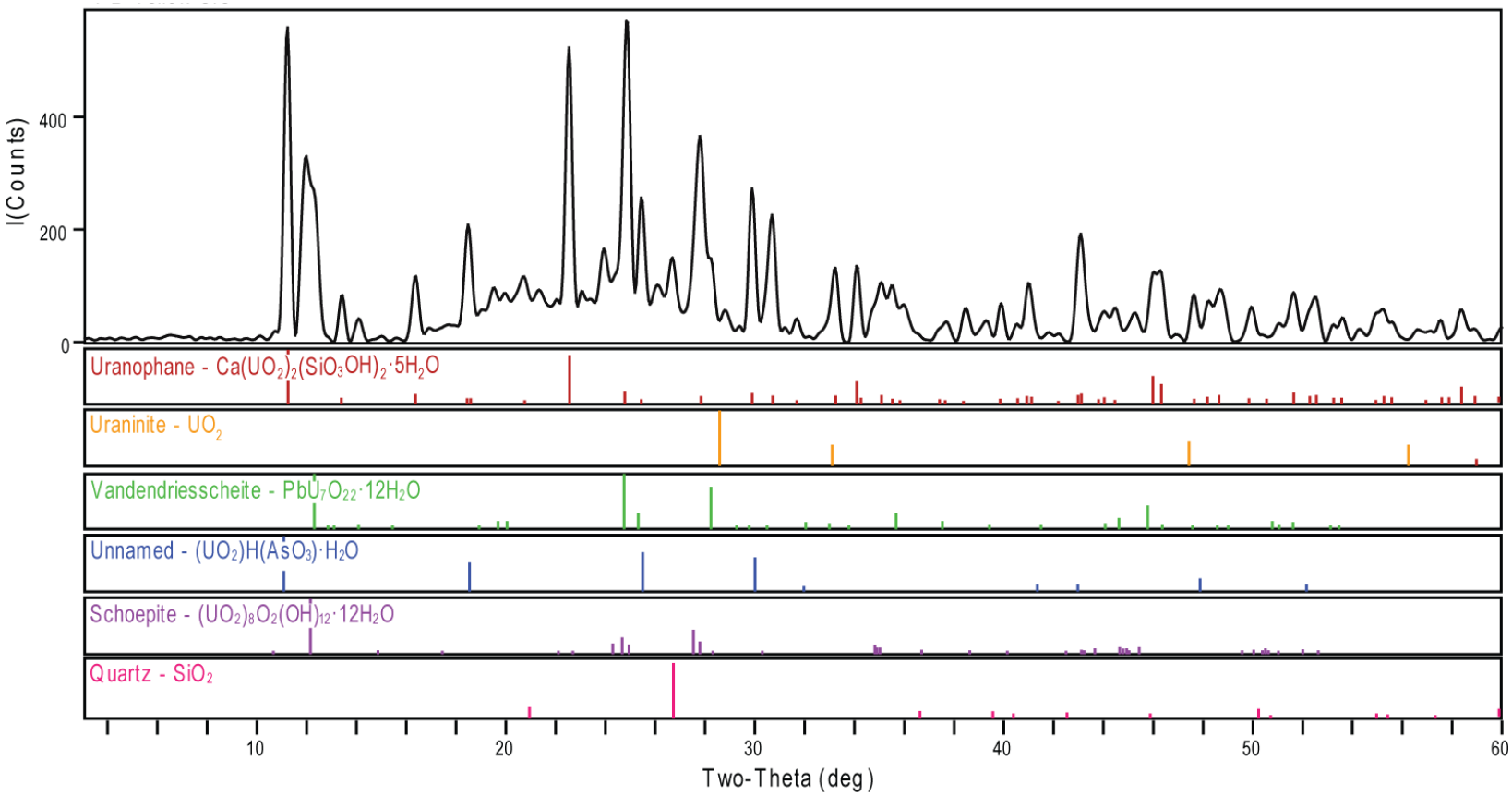

Figure 7. Combined diffraction pattern (peak intensity vs. degrees two-theta) for Nopal I mineralization collected in the +00 level mine adit (ex. zones 1 and 2). The diffraction patterns below (e.g., quartz) are for individual minerals and correspond to peaks in the sample pattern. Note that there are both reduced and oxidized uranium minerals present.

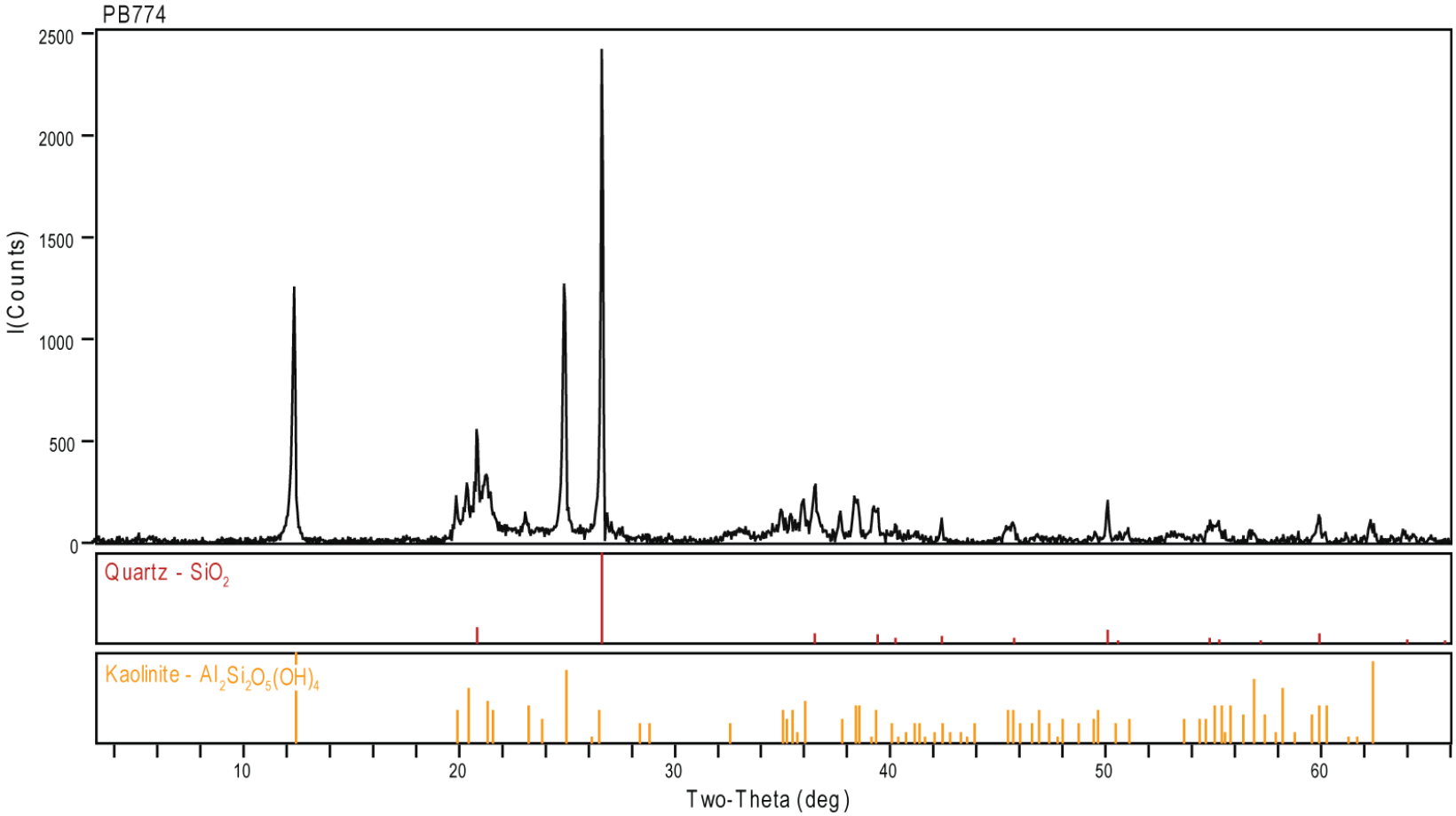

Figure 8. Diffraction pattern (peak intensity vs. degrees two-theta) from PB774, a Nopal Formation sample (ex. zone 3a). The diffraction patterns below (e.g., quartz) are for individual minerals and correspond to peaks in the sample pattern. The alteration mineralogy is almost all kaolinite.

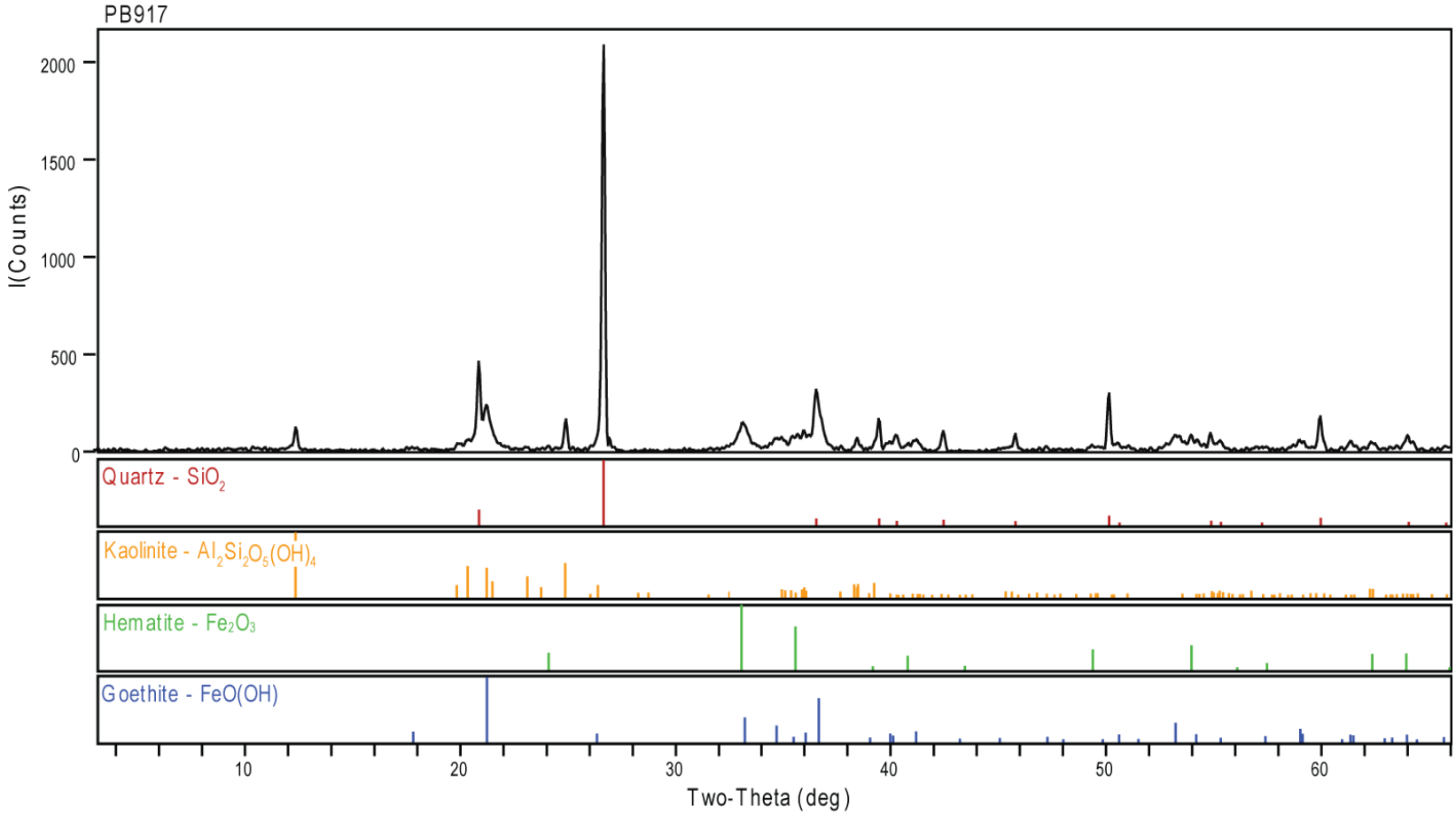

Figure 9. Diffraction pattern (peak intensity vs. degrees two-theta) for PB917, a Coloradas Formation sample (ex. zone 3a). The diffraction patterns below (e.g., quartz) are for individual minerals and correspond to peaks in the sample pattern. It is also dominated by quartz, but has minor amounts of kaolinite, hematite, and goethite.

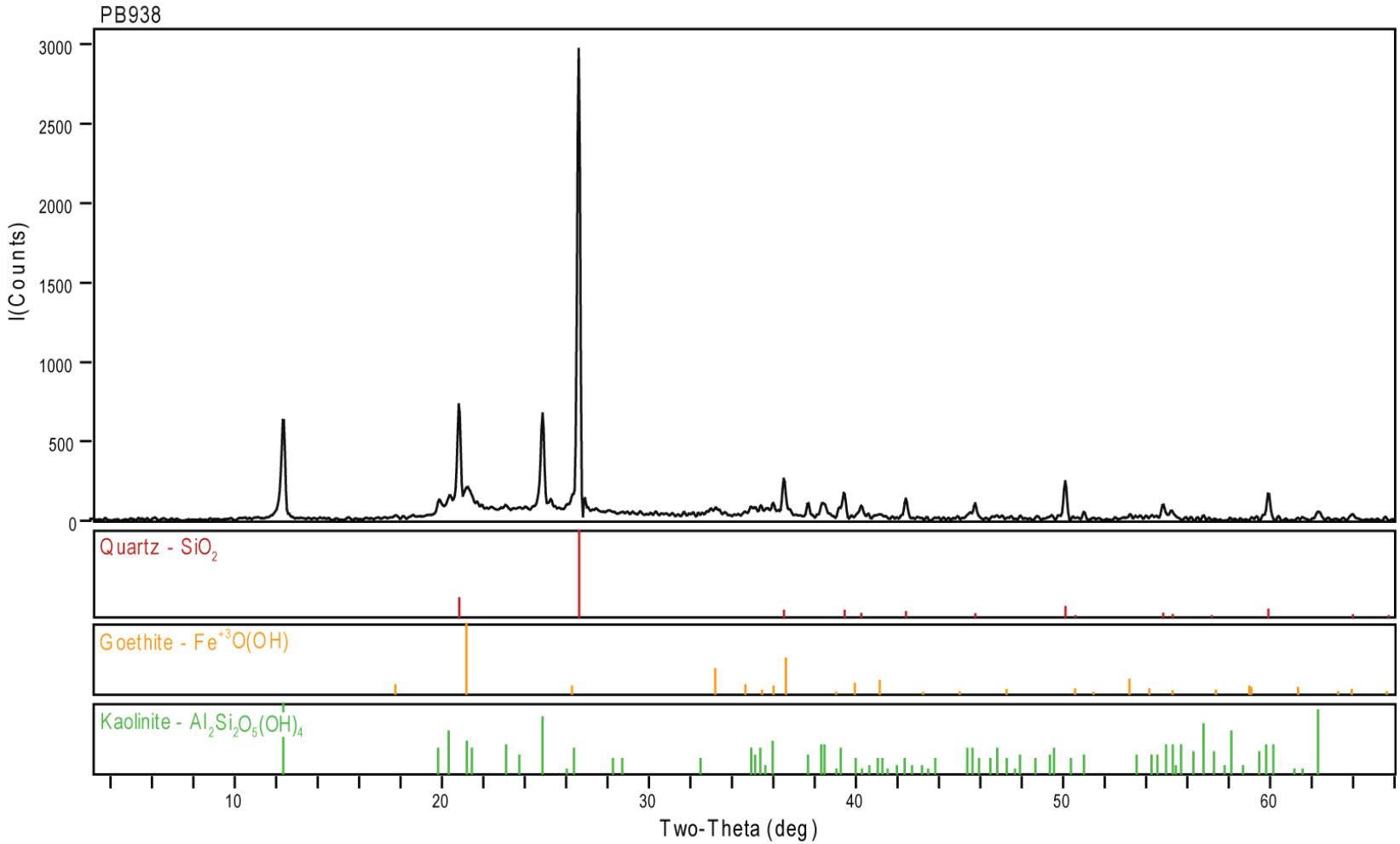

Figure 10. Diffraction pattern (peak intensity vs. degrees two-theta) for PB938, a Pozos conglomerate sample (ex. zone 3b). The diffraction patterns below (e.g., quartz) are for individual minerals and correspond to peaks in the sample pattern. It is also dominated by quartz, but has minor amounts of kaolinite and goethite.

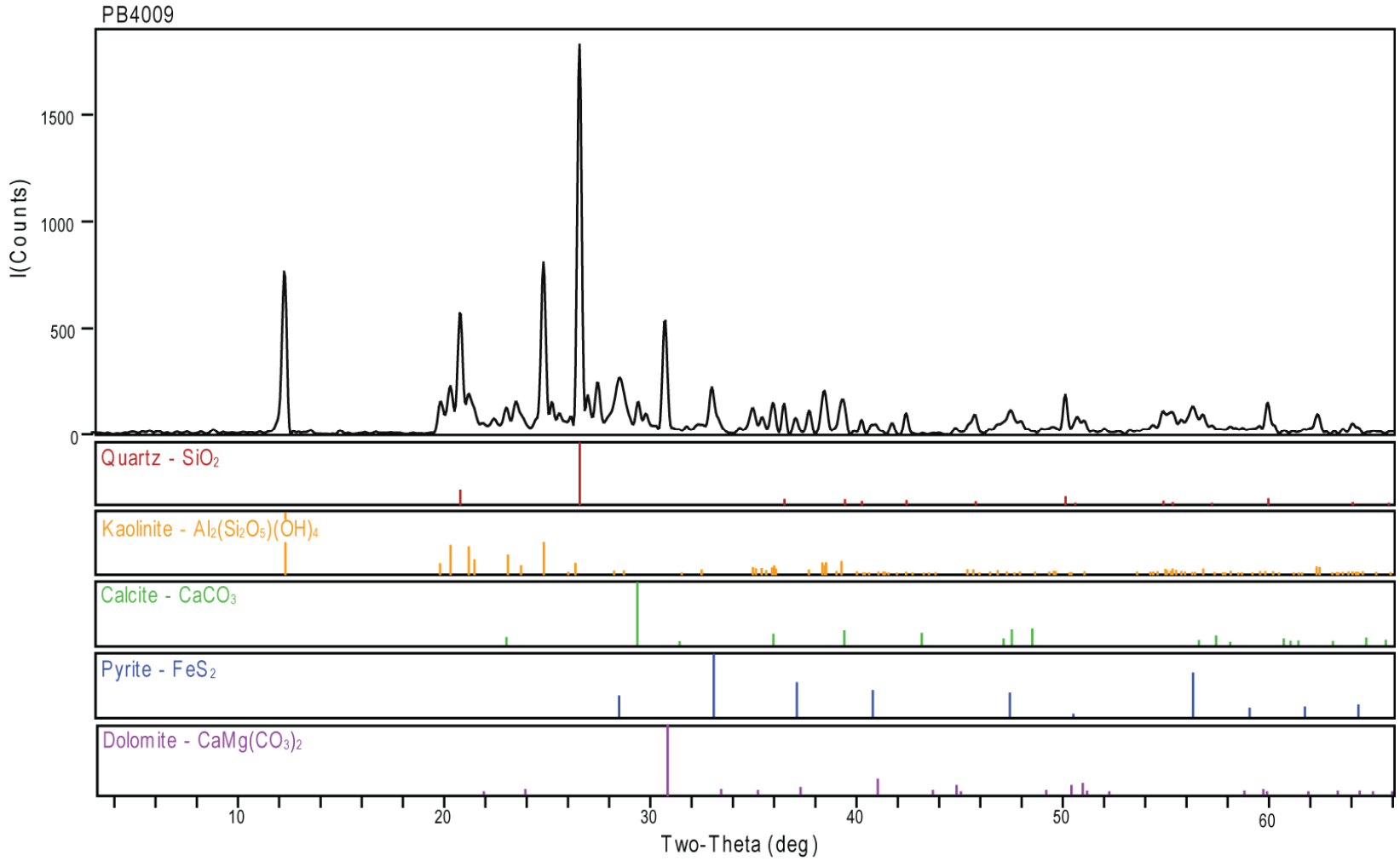

Figure 11. Diffraction pattern (peak intensity vs. degrees two-theta) for sample PB4009, a Pozos conglomerate sample. The diffraction patterns below (e.g., quartz) are for individual minerals and correspond to peaks in the sample pattern. It is still dominated by quartz and kaolinite, but also some carbonates and a smaller amount of pyrite.

3.3 ELECTRON MICROPROBE ANALYSIS

Electron microprobe analysis (EMPA) is used to analyze mineral compositions in situ. EMPA of Peña Blanca samples have been done on uraninite (Pearcy et al., 1994), iron oxyhydroxides (Prikryl et al., 1997), and kaolinite (Ildefonse et al., 1990a, b). However, this study analyzes PB-1 drill core samples below the deposit (Figure 12), whereas previous work has focused on surface material at the Nopal I mine. Multiple analysis points for each sample were taken and averaged in the results tables to follow; for the complete set of analyses see Appendix C. Statistical analysis for this section is located in Appendix D.

3.3.1 Methodology

Twelve samples (see Appendix A for core sample numbers and descriptions) were selected for EMPA and prepared as 1-inch round thin sections. Samples were carbon-coated and placed into a sample tray. Analysis was done on a CAMECA SX100 electron microprobe with PGT energy dispersive spectrometers (EDS) and wavelength dispersive spectrometers (WDS) at the University of Manitoba, Department of Geological Sciences.

Three sample categories—clays, iron oxyhydroxides, and uranium minerals—were used to differentiate data acquisition types. These were simply designations for a type of analysis to be done. Analysis points were focused on any fractures or altered areas visible on the sample slide. Operating conditions for clay analyses were 15 keV and 10 nA with a 10 μm beam size and analyzed for weight percent (wt%) SiO_2, Al_2O_3, Na_2O, MgO, K_2O, CaO, TiO_2, FeO, UO_2, and H_2O (calculated from missing total, not measured). Operating conditions for iron oxyhydroxide analyses were 15 keV and 10 nA with a 5 μm beam size and analyzed for wt% Mn_2O_3, Fe_2O_3, SiO_2, Al_2O_3, and H_2O (calculated from missing total, not measured). Operating conditions for uranium mineral analyses were 15 keV and 10 nA with a 1 μm beam size and analyzed for wt% SiO_2, UO_2, TiO_2, Fe_2O_3, PbO, CaO, Al_2O_3, ThO_2, and SO_2. A smaller beam size was used due to the small size of the uranium minerals and to minimize contamination with surrounding minerals.

The EDS and WDS were used to find suitable target minerals for analysis. They were important for finding uranium mineral candidates for age dating, because the small size of these minerals (majority <5 μm) prevented their identification otherwise. The EDS and WDS were also used to identify trace minerals, like sphalerite, by using the relative peak heights for elements picked up by the spectrometers.

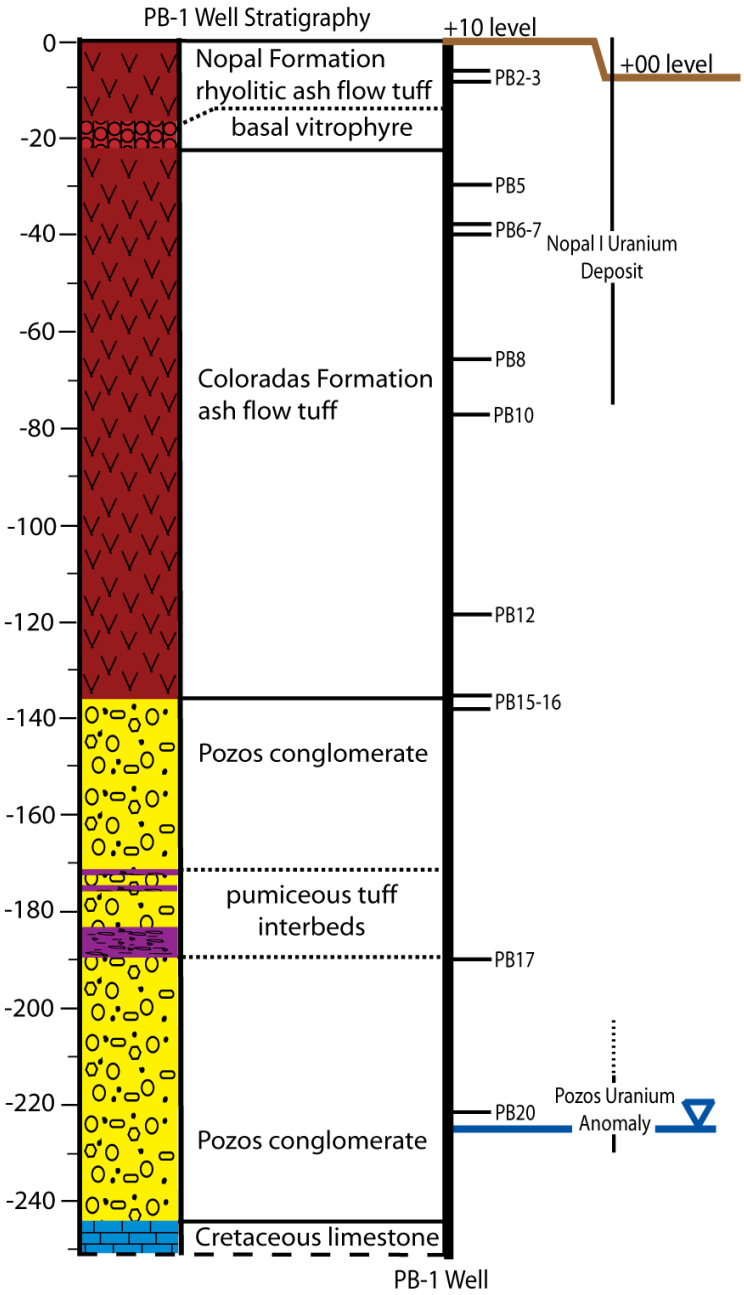

Figure 12. Drill-hole template showing EMPA sample locations (black dashes).

3.3.2 Results

EMPA results for clay (Table 3) and uranium minerals (Table 4) are summarized in this section and the geochemical changes observed in each group are briefly described. First, general observations of clay uranium mineral analyses are described. Then, the titanium in clay and uranium mineral analyses is presented along with a statistics to determine its relationship with uranium. The uranium mineral petrology from BSE images will be presented after the EMPA chemistry. Iron oxyhydroxide data was partially corrupted, so observations related to this data would be limited in scope, so it will not be discussed in detail and is located in Appendix C.

Individual analysis points totaled 55 points from 12 samples for clay minerals, 25 points from six samples for iron oxyhydroxides, and 62 points from 12 samples for uranium minerals. The EMPA results of the iron oxyhydroxide analysis are located in, because the analyses are not indicative of a trend and some data was corrupted.

Clay mineral analysis

In this section, the results of the clay mineral analyses are presented. The characteristics of Table 3 will be discussed. Items of greater importance will be noted and comparisons with other data types will be made.

Table 3. EMPA of kaolinite in the PB-1 core

Kaolinite mineral analyses														
Zone	Sample		Points	%SiO2	%Al2O3	%Na2O	%MgO	%K2O	%CaO	%TiO2	%FeO	%UO2	%H2O	Total
2	PB2	PB774	4	49.09	19.03	0.10	0.61	1.54	0.20	0.03	13.96	0.09	15.30	99.97
		PB774F	2	42.64	29.02	0.15	1.19	2.80	0.18	0.04	4.83	0.00	19.09	99.94
	PB3	PB775	4	42.58	32.85	0.13	0.08	0.05	0.09	0.02	1.29	0.00	22.80	99.90
	PB5	PB798	4	43.15	36.77	0.10	0.18	0.04	0.14	0.01	0.30	0.00	19.19	99.87
	PB6	PB812	5	44.23	34.99	0.10	1.09	0.22	0.17	0.01	1.42	0.06	17.69	99.98
	PB7	PB814	3	39.16	27.70	0.15	0.07	0.16	0.15	0.18	15.04	0.00	17.25	99.90
		PB814F	1	55.05	32.09	0.09	0.09	0.03	0.07	0.00	0.35	0.00	12.17	99.94
	PB8	PB849	3	43.88	38.86	0.04	0.06	0.03	0.11	0.01	3.39	0.00	13.44	99.82
3a	PB10	PB862	5	45.95	35.26	0.16	0.07	0.05	0.07	0.02	2.01	0.00	16.31	99.90
	PB12	PB912	4	46.92	10.48	0.27	0.33	0.31	0.34	0.09	14.27	0.00	26.92	99.95
		PB912F	1	67.98	24.64	0.12	0.09	0.13	0.17	0.09	5.98	0.00	0.67	99.89
	PB15	PB935	5	50.69	29.51	0.03	0.09	0.04	0.17	0.01	2.77	0.00	16.53	99.83
		PB935F	4	52.43	29.48	0.03	0.08	0.03	0.13	0.01	0.87	0.00	16.81	99.86
3b	PB16	PB938	3	61.83	23.30	0.12	1.89	0.12	0.31	0.07	1.24	0.00	10.96	99.84
4	PB17	PB4009	4	42.63	35.19	0.08	0.61	0.32	0.29	3.46	0.66	1.64	15.12	100.00
	PB20	PB4052b	6	42.52	34.29	0.14	0.54	0.86	0.18	0.55	0.85	1.01	19.00	99.94
Kaolinite $Al_2Si_2O_5(OH)_4$				46.55	39.50								13.95	100.00

-"F" denotes sample averages that only include sample analysis points with <10% FeO.

Table 3 gives the averaged values of multiple analysis points within each sample. Based on the XRD analysis presented in the previous section (ex. Figure 8), the EMPA clay mineral is kaolinite. For some samples it is necessary to have a subset of samples, because high iron content is indicative of kaolinite intermixing with iron minerals. The subset of averages only include analysis points with <10% FeO (denoted by an "F" following the sample number). For example, in PB774 [PB2] and PB774F [PB2], Al_2O_3 goes from 19% to 30%, when the high iron samples are removed from the total average. An example of intermixing can be seen in Figure 13, where iron oxyhydroxides are intermixing with quartz and kaolinite. Intermixing is the best explanation for variable iron content in the kaolinite analyses.

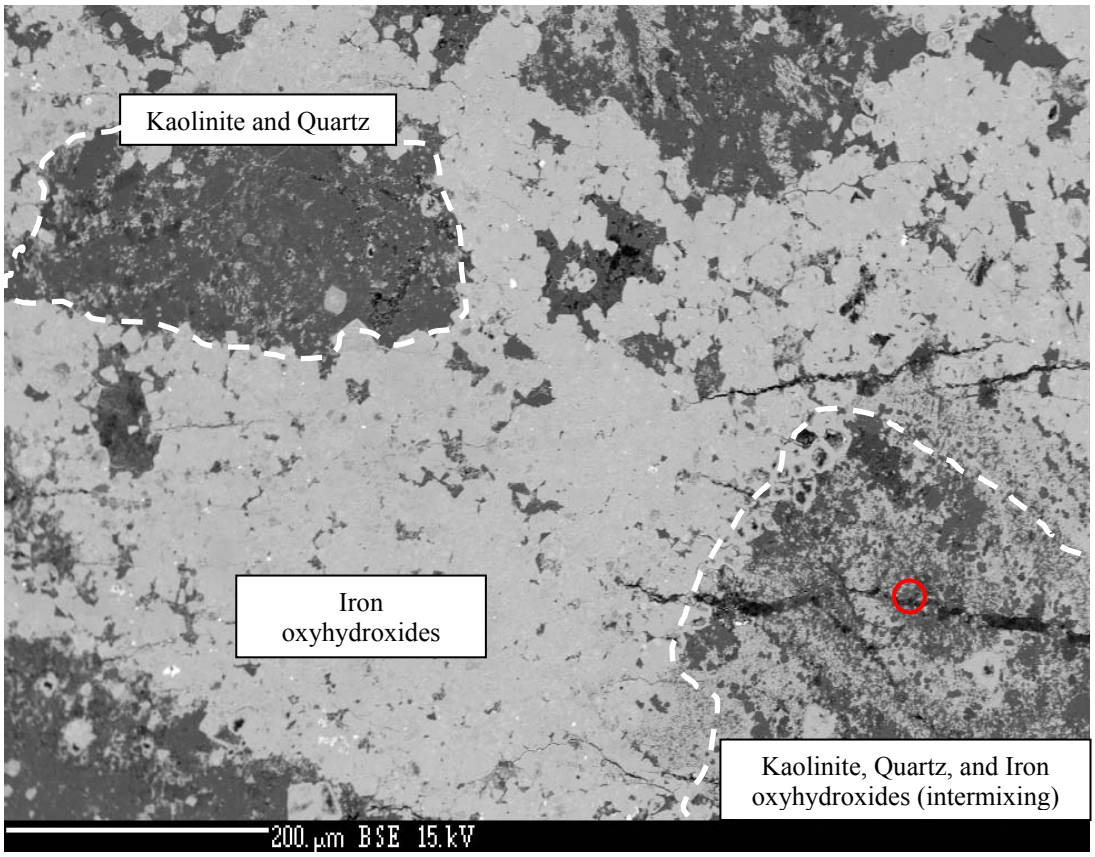

Figure 13. BSE image of PB774 spot 1 [PB2-1]. This image shows the difficulty in analyzing areas of kaolinite without also sampling intermixed iron oxyhydroxides (see lower right corner). Quartz is dark gray, Iron oxyhydroxides are whitish and kaolinite is a medium gray. Kaolinite also has a stippled appearance because of differential polishing. The red circle is the approximate location of analysis.

Kaolinite in the PB-1 core (Table 3) is consistent in its minor constituents, e.g. Na, K, and Ca oxides content. Na_2O averages range from 0.03 to 0.27, K_2O averages range from 0.03 to 2.80, and CaO averages range from 0.07 to 0.34. Only K_2O varies significantly, but no spatially-patterned variation is evident. The increase in CaO and MgO can be explained by the presence of limestone and dolomite in the Pozos conglomerate (zones 3b and 4).

Kaolinite and Titanium

Uranium present in kaolinite is not detected in zones 2-3b, except for two samples, PB774 [PB2] and PB812 [PB6], which average less than 0.1 wt%. Only in zone 4 is UO_2, do the averages of PB4009 [PB17] and PB4052b [PB20] increase to 1.64 and 1.01%, respectively. These two samples are located in the Pozos uranium anomaly (zone 4) as indicated by the gamma log readings (Figure 4). These two samples also have the highest amounts of titanium at 0.55 and 3.46 wt % compared to other kaolinite minerals, which are less than 0.2 wt% in zones 2-3b. Titanium can be a trace constituent in kaolinite, but based on other studies of uranium sorption in kaolinite, it is more likely a separate phase, microcrystalline TiO_2 (Dolcater et al., 1970; Fayek et al., 2006; Bachmaf and Merkel, 2011; Levy et al., 2011).

Uranium mineral analysis

In this section, the results of the uranium mineral analyses are presented. The characteristics of Table 4 will be discussed. Items of greater importance will be noted and comparisons with other data types will be made.

Ideally, if the electron microprobe beam could be focused only onto the uranium mineral under analysis, the results of uranium mineral analyses (Table 4) could be used to calculate mineral formulas based on the relative abundances of the analyzed elements. Many samples are mixed with surrounding material, e.g. quartz, kaolinite, TiO_2, so their chemical formulas are masked. For example, calcium is present in several of the uranium mineral analyses, but not in the correct abundance to calculate the calcium uranyl silicate, uranophane $[Ca(UO_2)_2(SiO_3)_2(OH)_2{\cdot}5H_2O]$. Based on the XRD analyses of the Nopal I mineralization, both

tetravalent (e.g., uraninite) and hexavalent (e.g., uranophane) uranium minerals are present. In the following sections, "uranium minerals" is used instead of a specific mineral name, because of the uncertainty surrounding specific mineral identification.

Table 4. EMPA of uranium minerals in the PB-1 core

Uranium mineral analyses													
Zone	Sample		Points	%SiO2	%UO2	%TiO2	%Fe2O3	%PbO	%CaO	%Al2O3	%ThO2	%SO2	Total
2	PB2	PB774	2	16.38	21.72	3.52	27.90	0.44	1.21	2.21	0.22	0.02	73.63
		PB774F	1	8.01	7.57	0.11	46.54	0.33	0.96	1.37	0.11	0.01	65.00
	PB3	PB775	4	14.10	53.14	1.22	2.21	0.25	0.79	0.30	0.07	0.05	72.13
	PB5	PB798	5	53.80	26.36	5.48	1.36	0.42	0.69	6.88	0.04	1.82	96.86
	PB6	PB812	7	18.38	55.32	4.02	2.99	0.87	2.04	0.95	0.46	4.53	89.56
		PB812F	1	2.49	40.42	10.69	15.00	0.72	1.11	0.11	0.71	27.53	98.78
	PB7	PB814	7	57.99	27.28	2.74	1.04	1.32	0.86	0.89	0.01	0.23	92.36
	PB8	PB849	N/A										
3a	PB10	PB862	6	60.29	28.59	3.20	0.69	0.48	0.92	0.52	0.04	0.64	95.37
	PB12	PB912	5	15.44	60.25	0.00	1.71	0.13	5.74	0.23	0.01	0.02	83.53
	PB15	PB935	N/A										
3b	PB16	PB938	3	18.04	52.68	0.14	2.65	0.14	1.87	0.70	0.01	0.05	76.29
4	PB17	PB4009	7	4.20	56.95	23.73	0.60	0.08	3.28	1.50	0.01	0.06	90.41
	PB20	PB4052b	8	2.75	40.23	44.37	1.05	0.24	2.15	1.40	0.08	0.06	92.32
Uraninite UO_2					100								100

-"F" denotes sample averages that only include sample analysis points with >10% FeO. A subset of samples is needed, because of intermixing with iron minerals.

Uranium and Titanium

A relationship exists between wt% UO_2 and TiO_2 from EMPA (Table 4). Titanium is associated with uraninite in samples from the Nopal I primary mineralization (Aniel and Leroy, 1985; Pearcy et al., 1994). Samples in zones 2-4 average a few wt% TiO_2, and up to 10 wt %. The PB812F [PB6] uranium mineral subgroup, from zone 2, has high the highest titanium (10.7 wt% TiO_2), in addition to iron (15 wt% Fe_2O_3) and sulfur (27.5 wt% SO_2). It is probably a mixed sample of ilmenite or TiO_2, pyrite and uraninite (Figure 14), and may be evidence of the primary mineralization (zone 1): quartz-pyrite-uraninite-ilmenite-kaolinite. In order to determine whether there are separate phases, further analysis with transmission electron microscopy is needed.

Titanium is also associated with uranium minerals in the Pozos uranium anomaly (Table 4). The two samples from zone 4, PB4009 [PB17] and PB4052 [PB20], average 24 and 44 wt %

TiO_2, respectively, which is more than double the averages of zones 2-3. Looking at the relationship between UO_2 and TiO_2 (Figure 15), there appear to be two trends: 1) one with increasing UO_2 and TiO_2 (zones 2-3); and 2) another that is decreasing (zone 4). The negative trend when only zone 4 analyses are plotted (Figure 16) is opposite of what would be expected if there as a relationship between U and Ti; however, it is simply that very little of anything else occurs in association with U at depth, so wt% UO_2 and TiO_2 sum to nearly 100% of the total in varying proportions. A statistical test is the next step in investigating a possible relationship.

The microprobe sampled uranium minerals throughout the core for U, Si Ti, Fe, Pb, Ca, Al, Th, and S. These uranium minerals were generally smaller than the beam size, so the beam also sampled the surrounding minerals. Uranium minerals are defined by their large U concentrations, so high concentrations of another element in the sample could indicate the presence of another mineral, especially when textural evidence exists as to what minerals do occur in the sample. For example, Si could indicate quartz, but Si with a lot of Al could mean kaolinite. Similarly, anatase would be indicated by high Ti concentrations. If this relationship is explored within zone 4, Ti is the next highest concentration to U. In order to test the uranium-titanium association in zone 4, a binomial sign test was performed. The sign test tells the likelihood of all 15 samples having Ti as high as any other metal, through the following equation:

$$\frac{1}{2^{15}} = 3x10^{-5}$$

A small number indicates that this result happening by chance is highly unlikely. Fayek et al. (2006) also analyzed zone 4 samples using TEM, and found that the UO_2 and TiO_2 were not one phase, but rather uraninite and anatase, respectively. Based on the statistics and the textural evidence from the microprobe analyses and Fayek et al. (2006), this result is interpreted as a uranium mineral affinity for microcrystalline TiO_2 within kaolinite (Dolcater et al., 1970; Reynolds et al., 1977; Payne et al., 1990; Bachmaf and Merkel, 2011; Levy et al., 2011).

Uranium minerals are also associated with quartz (Figure 17) in the upper section of the core and with kaolinite in the Pozos uranium anomaly (Figure 18). If the association was due solely to kaolinite, a relationship between silicon and aluminum with uranium should be seen; however, they are negatively correlated. Therefore, an explanation is that the kaolinite has microcrystalline TiO_2 which causes the adsorption. The Pozos uranium anomaly samples (PB4009 [PB17] and PB4052b [PB20]) also have higher values of calcium, which supports the presence of calcite (Figure 19) in the Pozos conglomerate, rather than uranophane.

Uranium mineral petrology

The following results consist of BSE images taken during EMPA analysis. Uranium mineral assemblages are determined semi-quantitatively by using BSE images to identify textural relationships between minerals and the uranium mineral analyses (Table 4) in the previous subsection (3.3.2) to interpret the mineralogy. Table 5 lists the sample numbers and their observed assemblages.

Both primary (encapsulated), zone 1, and oxidized primary assemblages from zones 2-3 are designated P#, because they are considered examples of the primary assemblage preserved by encapsulation and oxidized remnants of the primary assemblage are presented. Then assemblages found in the Pozos uranium anomaly, zone 4, designated PUA# are presented, because they are spatially and temporally separated from P# samples. Four generic uranium assemblages were identified based on textural relationships and EMPA: 1) uranium-quartz-pyrite-ilmenite-kaolinite (P1, PUA1); 2) uranium-quartz (P2, PUA2); 3) uranium-kaolinite (P3, PUA3); and 4) uranium-iron oxyhydroxides (P4, PUA4). Assemblages 2-4 may be considered subsets of assemblage 1. Samples with an asterisk denote a high titanium content, which is found in both primary and secondary assemblages. Samples that fit into more than one assemblage are highlighted in yellow.

The PB-core was drilled along the boundary of the main Nopal I mineralization, but a few samples of the primary assemblage, quartz-pyrite-uraninite-ilmenite-kaolinite (Aniel and

Leroy, 1985; Pearcy et al., 1994), are grouped as P1. Specifically, samples PB774-1 [PB2-1], PB774-4 [PB2-4], PB812-3 [PB6-3], PB812-6 [PB6-3], from zone 2 may be examples of this group (see Figure 14 for examples). These samples texturally are uranium-quartz or uranium-FeOOH, but chemically have evidence of higher iron±sulfur (pyrite) and/or titanium (ilmenite) (for details see Appendix D, uranium mineral analyses), which could be evidence of partially or completely oxidized pyrite or ilmenite.

Three PUA1 assemblages were found in zone 4. These assemblages are temporally different from the P1 equivalent. Examples are shown in Figure 18A, B, and D. One major difference from the P1 assemblage is that pyrite has not been completely oxidized to iron oxyhydroxides.

The majority of samples, based on Table 5, from zone 2-3 are in the P2 (uranium-quartz) assemblage, which was described by Pearcy et al. (1994) as the primary uranium mineralization (uraninite) and contemporaneous silicification (see Figure 17 for examples). Encapsulation could have preserved some of the primary assemblage from oxidation.

The PUA2 assemblage is not very common in zone 4. Two examples are shown in Figure 20. This may be evidence that 1) the primary assemblage did not mineralize in zone 4; 2) that silicification did not greatly affect zone 4; or 3) uranium mineralization occurred in zone 4 after silicification.

P3, the uranium-kaolinite assemblage, is rare in zone 2, but increases in abundance in zone 3a and 3b. Kaolinite is evidence of alteration, but also of the primary mineralization. Two examples are shown in Figure 21.

Based on Table 5, PUA3 is the most common assemblage in zone 4. Uranium minerals surround kaolinite grains, and are found within them, showing the importance of kaolinite as a uranium adsorber, especially when TiO_2 is present (Table 4). Examples of this assemblage are shown in Figure 18 and Figure 19.

Uranium and iron oxyhydroxides, P4, are evidence of the primary mineralization assemblages of pyrite and/or ilmenite that were subsequently oxidized into iron oxyhydroxides in

zones 2-3 (see Figure 22 for examples). Pyrite and iron oxyhydroxides have a related history at Nopal I. Based on the shapes of the iron oxyhydroxides (e.g. cubic and/or pyritohedron) and textural relationships observed previously (Aniel and Leroy, 1985; Ildefonse et al., 1990b; Pearcy et al., 1994; Fayek et al., 2006; Levy et al., 2011), the iron oxyhydroxides in this work are replacing altered pyrite (Figure 22). Ildefonse et al. (1990b) reported that the earliest generation of iron oxyhydroxides, i.e., those closest to the weathering front, adsorbed uranium (ex. Figure 22D); however, later formation of iron oxyhydroxides, after iron and uranium leaching occurred, are devoid of uranium.

This pyrite oxidation is evident downward until reaching zone 4, the Pozos uranium anomaly. In this zone partially oxidized (Figure 18B) and euhedral pyrite (Figure 18D) are common, but not iron oxyhydroxides, so PUA4 is an unlikely assemblage. No examples of this assemblage could be found.

Table 5. Uranium mineral assemblages determined from BSE images throughout the PB-1 core

Zone	Sample	P1	P2	P3	P4
		U+Qtz+Py+Il+Kaol	U+Qtz	U+Kaol	U+FeOOH
2	PB2		PB774-1* PB774-2 PB774-4*		PB774-1* PB774-4*
	PB3		PB775-4	PB775-1 PB775-2	PB775-5*
	PB5		PB798-1 PB798-3* PB798-4* PB798-6 PB798-7*		
	PB6	PB812-3* PB812-6*	PB812-1* PB812-2* PB812-3* PB812-4 PB812-5 PB812-6* PB812-7*		
	PB7		PB814-1 PB814-2* PB814-3 PB814-4 PB814-5 PB814-6 PB814-7		
	PB8				PB849-1 PB849-2 PB849-3
3a	PB10	PB862-2* PB862-3*	PB862-1 PB862-2* PB862-3* PB862-4 PB862-5* PB862-6		
	PB12			PB912-1 PB912-2 PB912-3 PB912-4 PB912-5	
3b	PB16			PB938-1 PB938-2 PB938-3	

Zone	Sample	PUA1	PUA2	PUA3	PUA4
		U+Qtz+Py+Il+Kaol	U+Qtz	U+Kaol	U+FeOOH
4	PB17	PB4009-2*	PB4009-3* PB4009-4*	PB4009-1* PB4009-2* PB4009-5*	
	PB20	PB4052b-3* PB4052b-7*		PB4052b-1* PB4052b-2* PB4052b-3* PB4052b-4* PB4052b-5* PB4052b-6* PB4052b-7*	

Primary uranium assemblages from zones 2-3 are designated P#. Uranium assemblages from zone 4 are designated PUA#. Different analysis spots are listed after the sample number, e.g. PB774-1 [PB2] is spot 1.

U-Uranium minerals; Qtz-Quartz; FeOOH-Iron oxyhydroxides; Kaol-Kaolinite; *-Titanium-rich

Yellow highlighting indicates assemblages that fit more than one category, based on textural and chemical data.

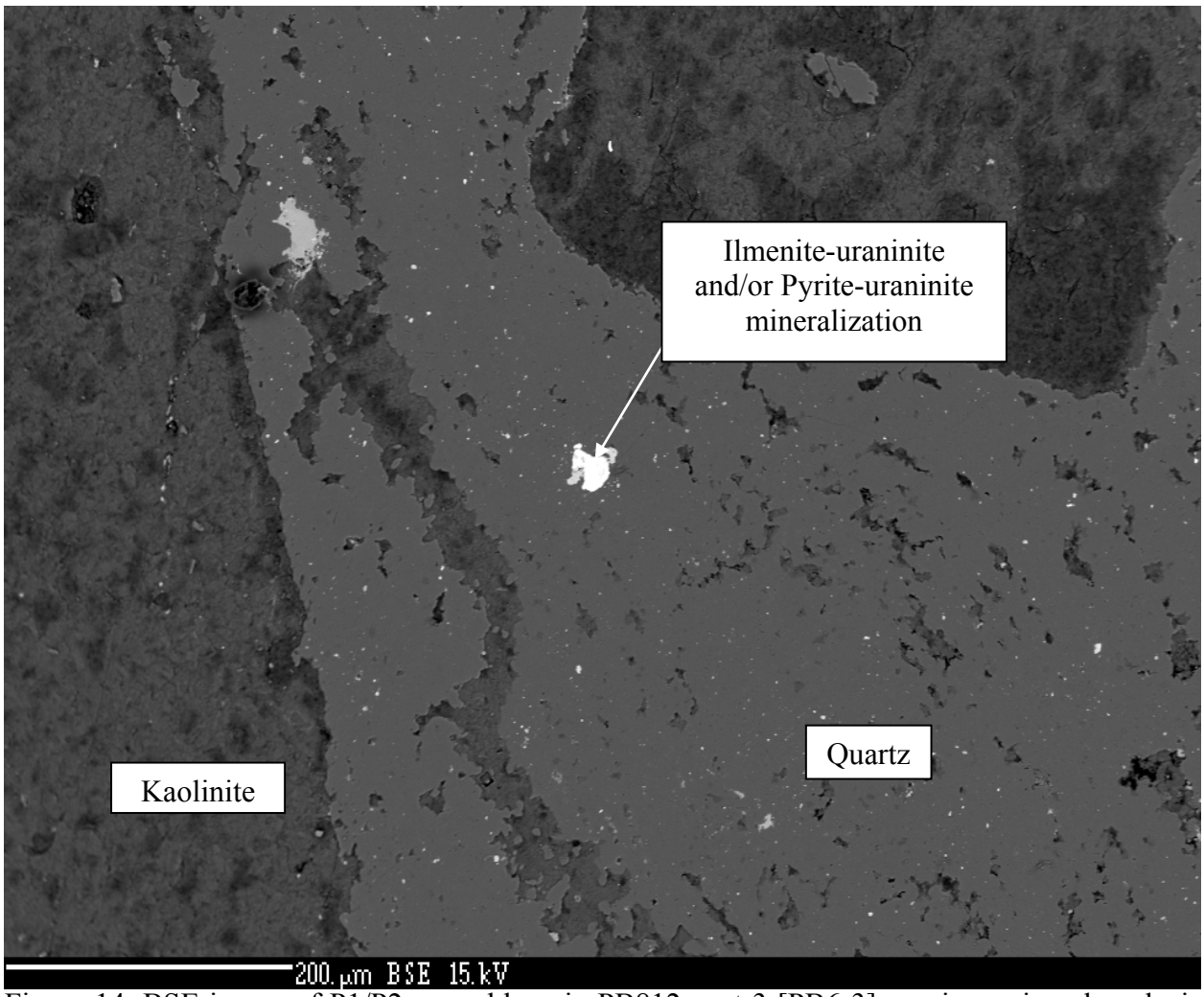

Figure 14. BSE image of P1/P2 assemblage in PB812 spot 3 [PB6-3] uranium mineral analysis (zone 2). It is a mixture of ilmenite, pyrite, and uraninite (bright white), which were described as two separate mineralization events, and earlier ilmenite-uraninite stage and a later pyrite-uraninite stage by Aniel and Leroy (1985). This sample also may show evidence of crustification, which is where successive minerals form crusts on one another. In this case quartz and kaolinite precipitate in what appears to be a fracture.

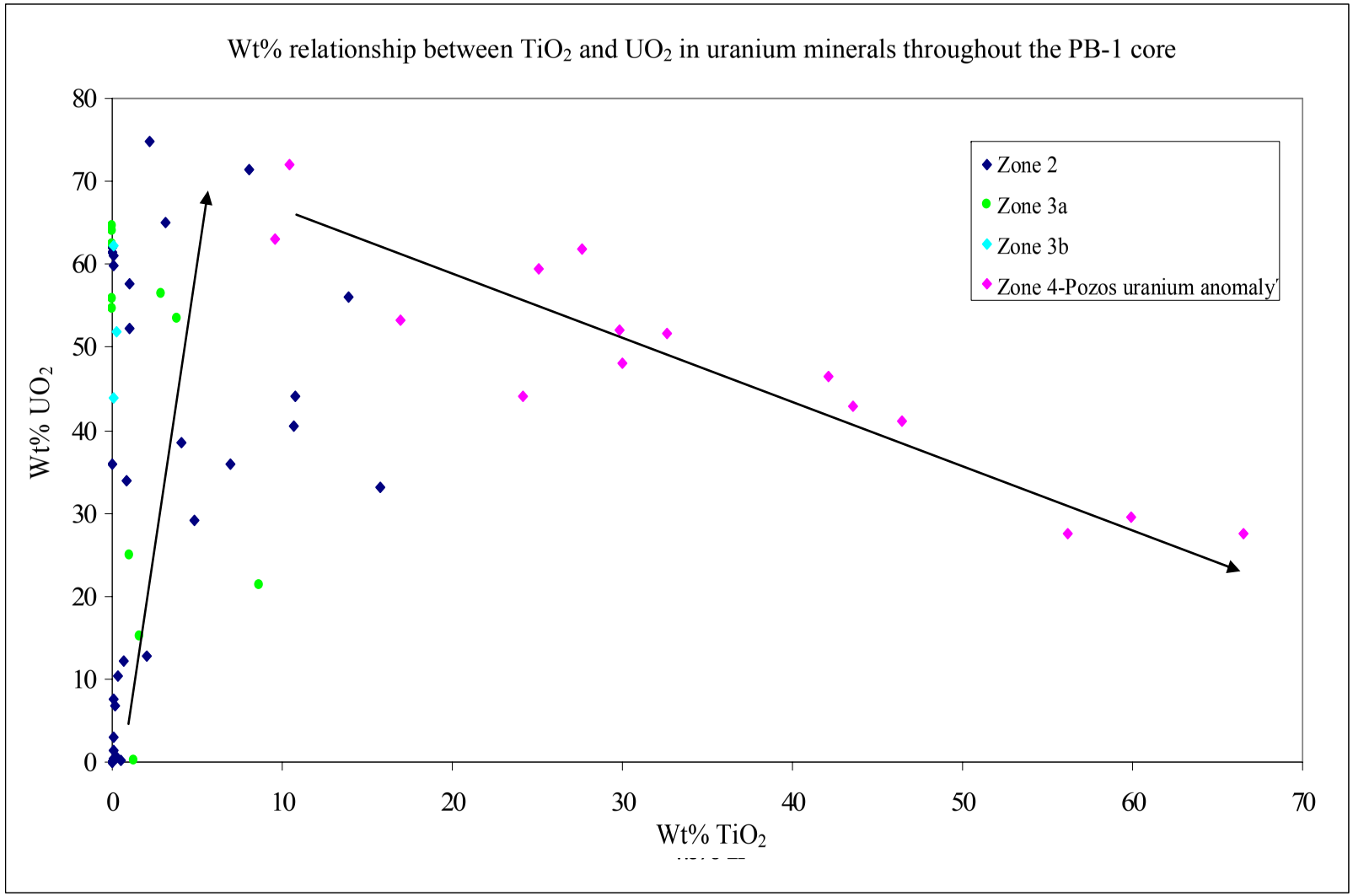

Figure 15. Relationship between wt% TiO_2 and UO_2 in EMPA uranium mineral analyses (see Appendix D for individual analyses). These samples are from throughout the core from the Nopal to the Pozos Formations and zones 2-4. The arrows show two trends: 1) zones 2, 3a, and 3b; and 2) zone 4-Pozos uranium anomaly. Trend 2 is shown in more detail in Figure 16.

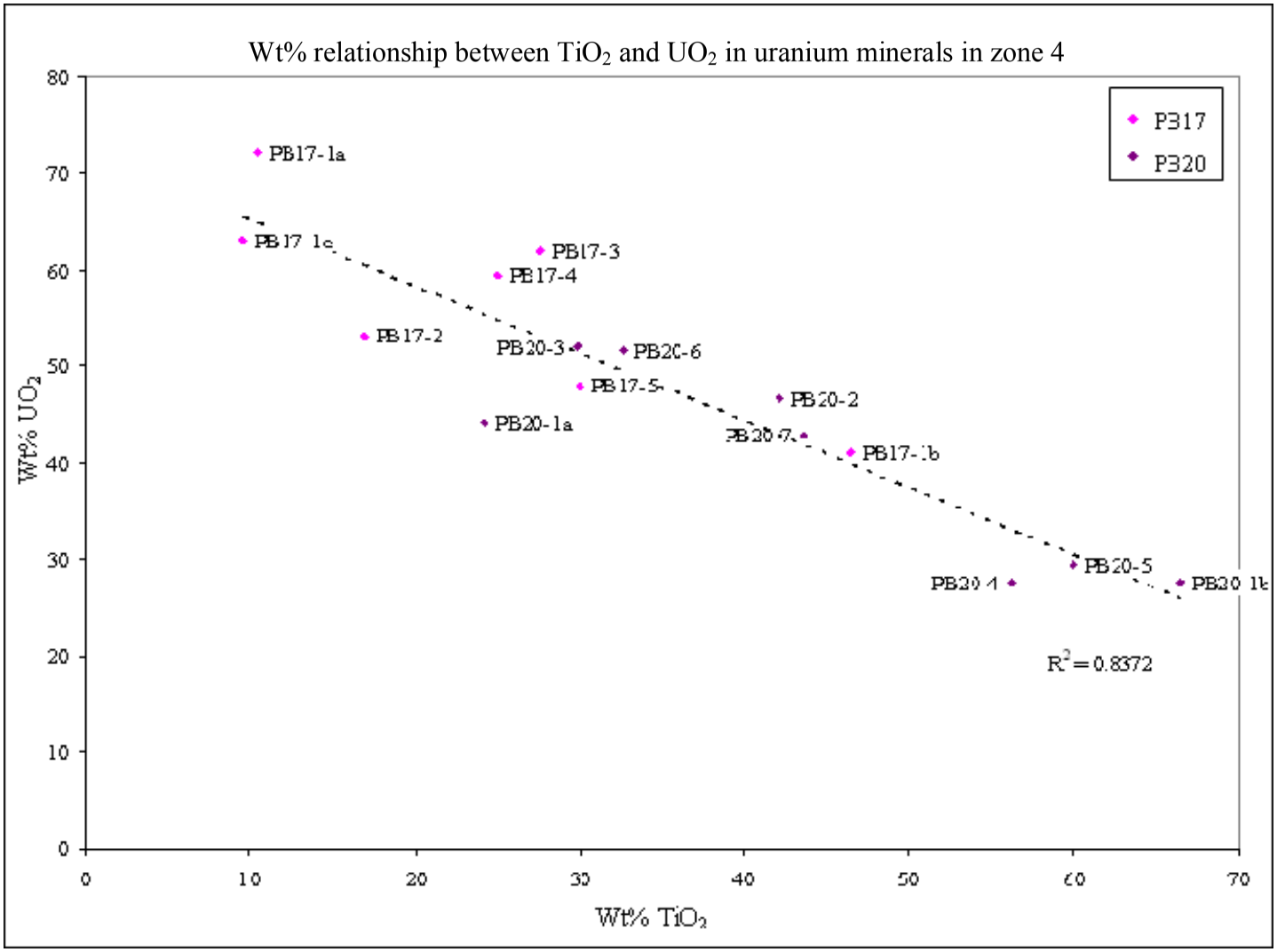

Figure 16. Relationship between wt% TiO_2 and UO_2 in EMPA uranium mineral analyses in zone 4, the Pozos uranium anomaly (see Appendix D for individual analyses). PB17 [PB4009] is from -190 m depth and PB20 [PB4052b] is from -220 m depth. Sample analysis points are given after the sample number, e.g., PB17-1a. There is more titanium and less uranium with increasing depth in uranium minerals based on these two samples.

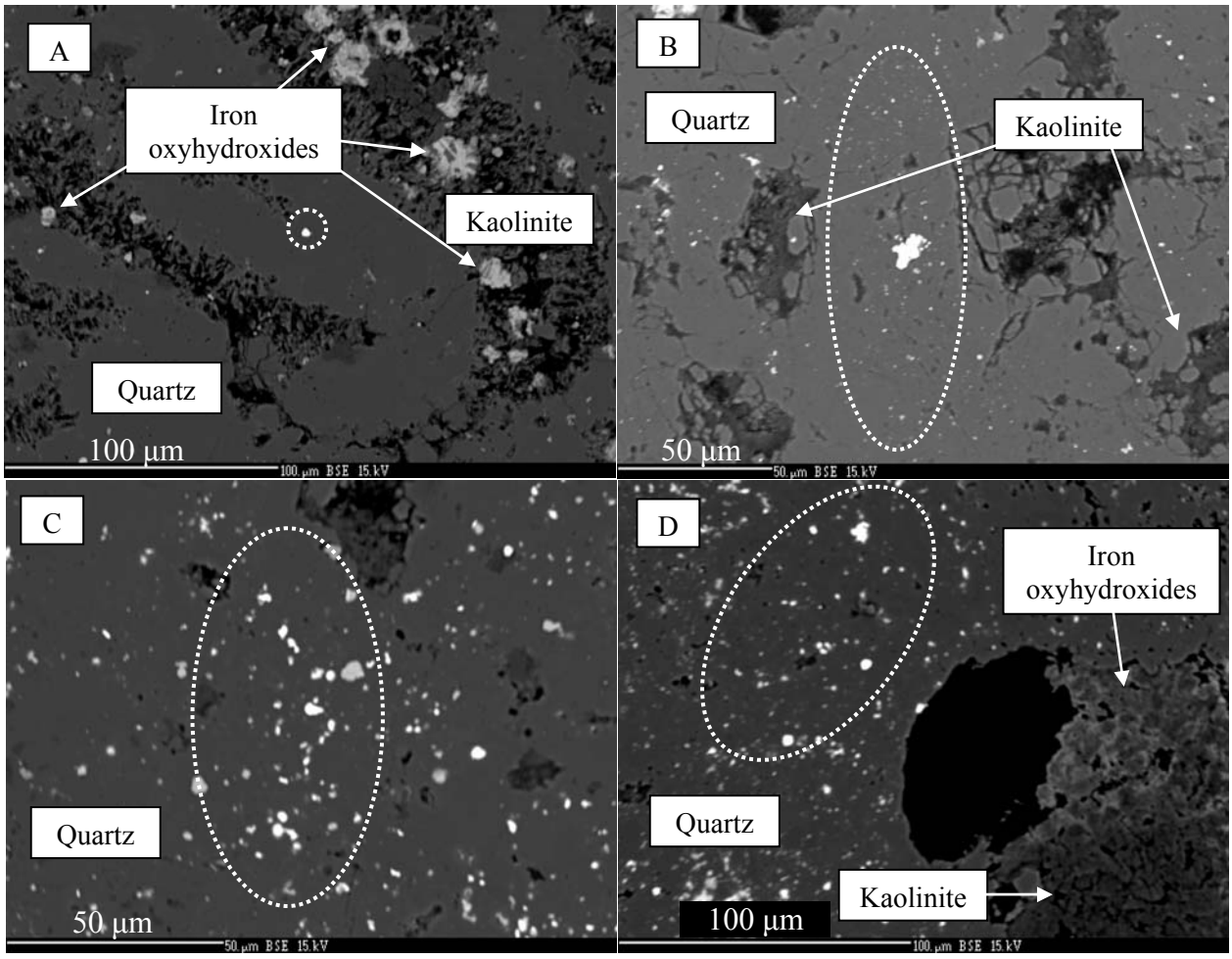

Figure 17. BSE images of P2 assemblages. These images show uranium minerals (bright white, within dashed ovals) in the Nopal and Coloradas Formations (zone 2). With the exception of A, most of the uranium minerals are found as groups of very small (a few microns in size) blebs. A) PB774 spot 2 [PB2-2] has one uranium mineral centered in quartz. This spot may also show crustification with alternating bands of quartz and kaolinite. The light gray minerals spots are iron oxyhydroxides after pyrite based on their shapes. B) PB798 spot 6 [PB5-6] has a group of small uranium minerals and one larger uranium mineral. Smaller zones of kaolinite are present, but are barren of uranium minerals. C) PB812 spot 6 [PB6-6] is similar to the previous description for B. D) PB814 spot 3 [PB7-3] is similar to B and C, but has a large area of iron oxyhydroxides and kaolinite to the right side past the hole.

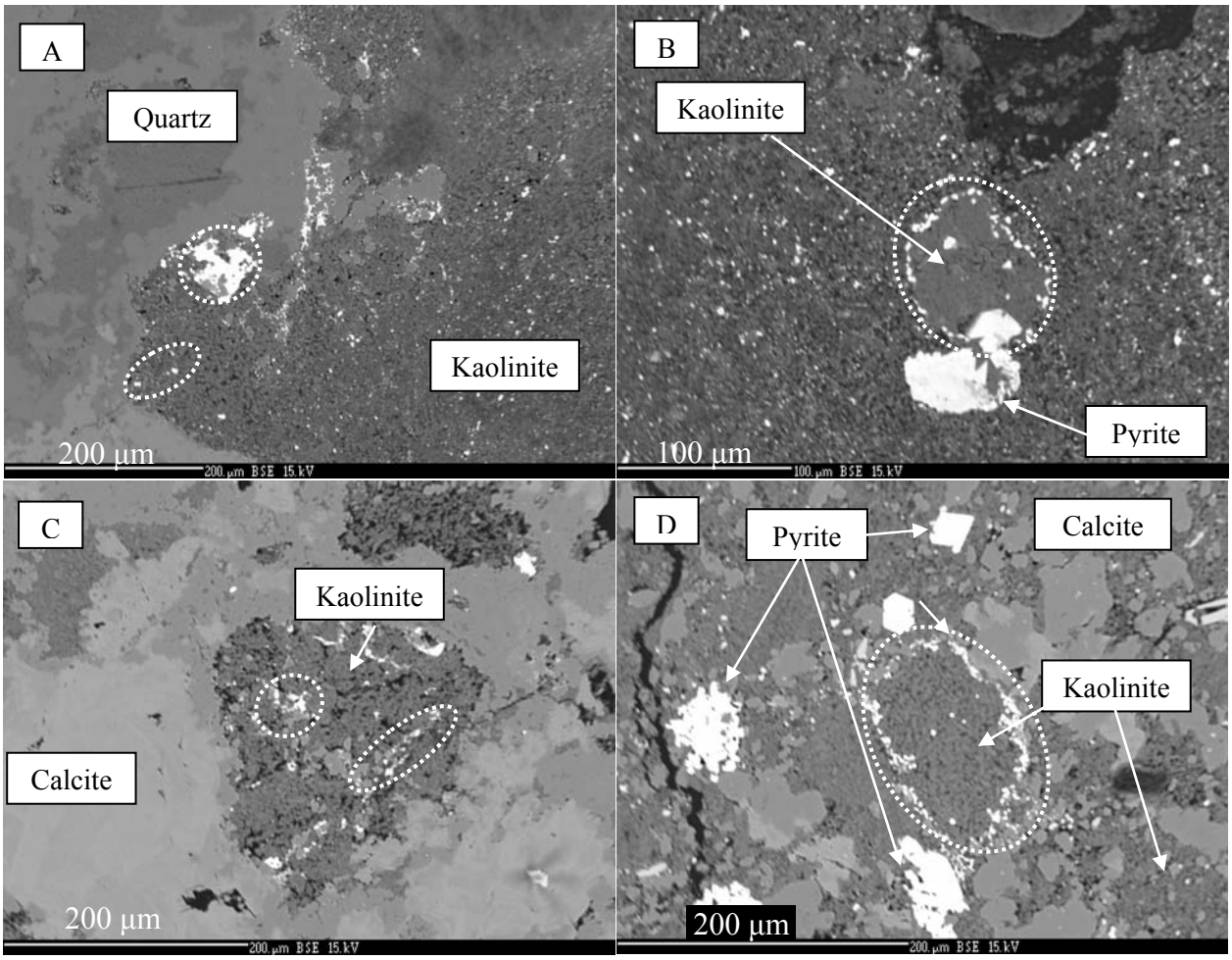

Figure 18. BSE images of uranium minerals (bright white, dashed ovals) in the Pozos uranium anomaly (zone 4). A) PB4009 spot 1 [PB17-1], PUA1/PUA3, has one large uranium mineral that is replacing pyrite based on its cubic shape. Smaller uranium minerals are also in the kaolinite. B) PB4009 spot 2 [PB17-2], PUA1/PUA3, is a kaolinite grain surrounded by uranium minerals and a partially leached pyrite. C) PB4052b spot 4 [PB20-4], PUA3, is a kaolinite grain with uranium minerals surrounded by calcite. D) PB4052 spot 7 [PB20-7], PUA1/PUA3, has uranium minerals surrounding kaolinite, but has calcite and euhedral pyrite. These examples show uranium mineral affinity for kaolinite through textural relationships.

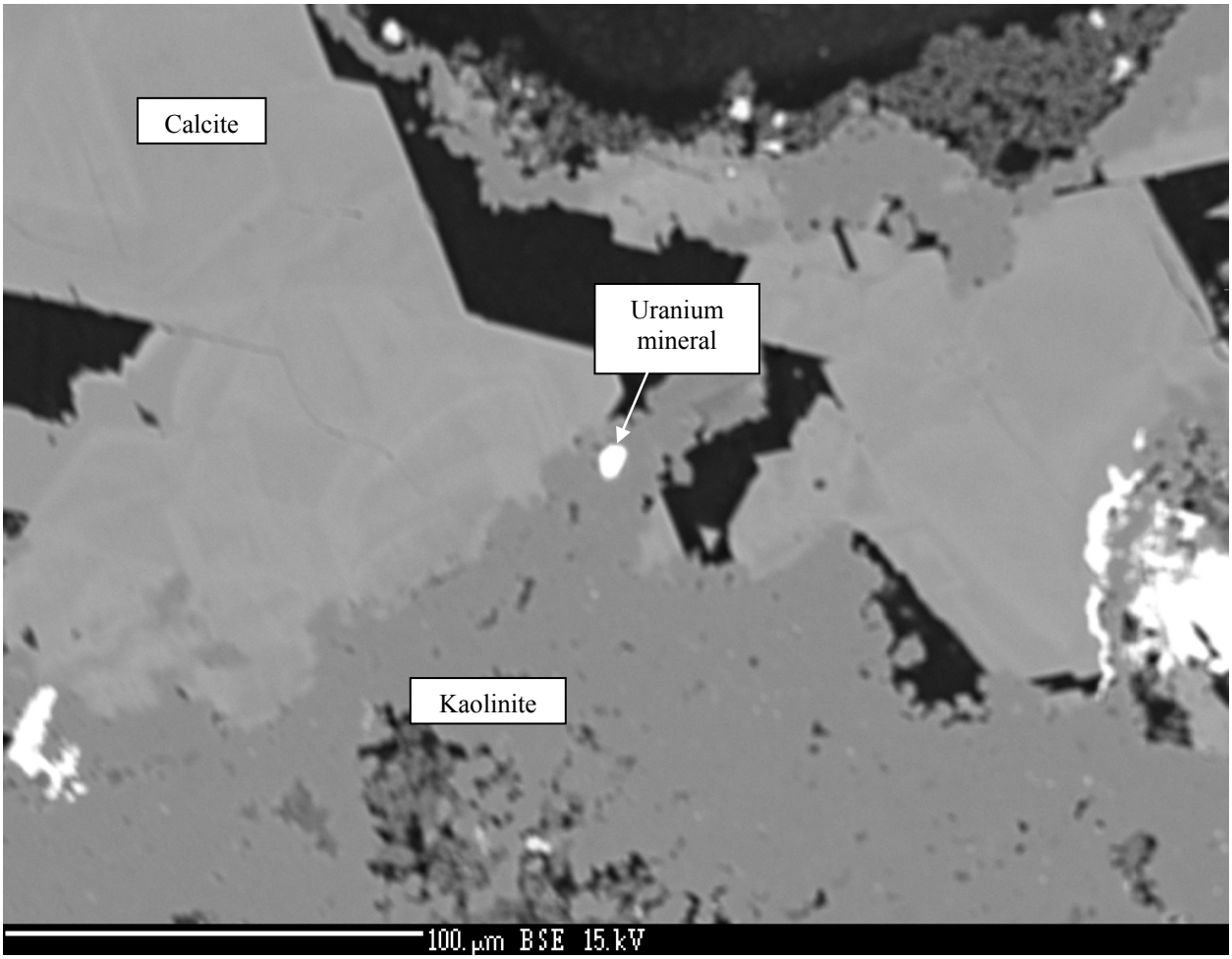

Figure 19. BSE image of PB4052b spot 2 (PUA3). This is an example of a uranium mineral (bright white) surrounded by kaolinite (med. gray) from the Pozos uranium anomaly (zone 4). Calcite (light gray) is a later stage mineral to kaolinite based on textural relationships and has overgrowths indicating multistage growth.

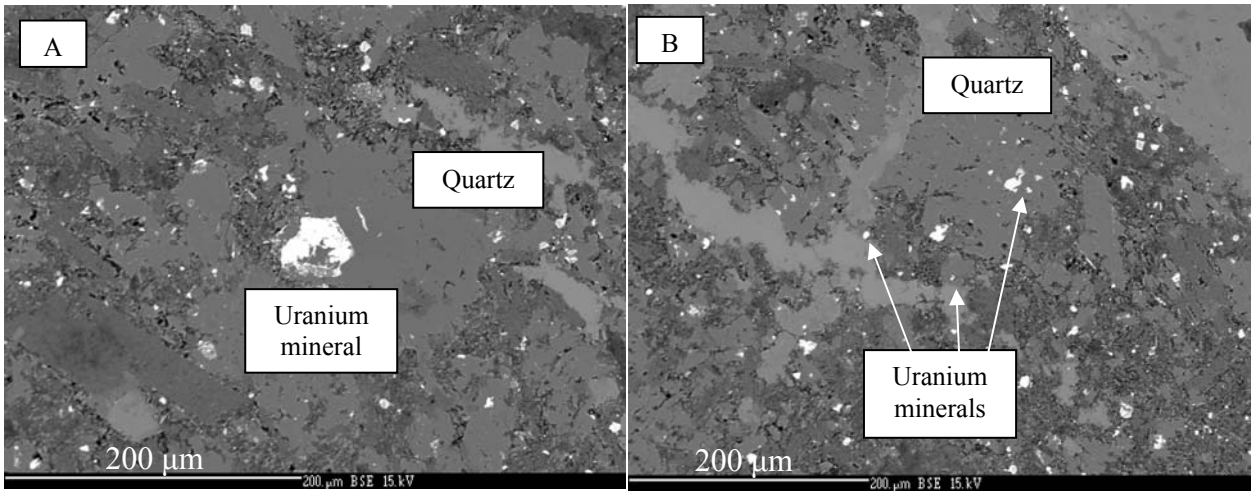

Figure 20. BSE images showing PUA2 assemblage. These images show uranium minerals (bright white) in zone 4, Pozos uranium anomaly. A) PB4009 spot 3 [PB17-3] has a large uranium mineral (bright white) surrounded by quartz (smooth gray). The stippled areas are mostly kaolinite. The uranium mineral looks like it may be replacing pyrite, but almost no iron (0.17 wt %) was detected during the analysis. B) PB4009 spot 4 [PB16-1] has small uranium minerals (bright white) surrounded by quartz (smooth gray). Some of the bright white minerals in these images are pyrite, but are usually cubic or pyritohedron in shape.

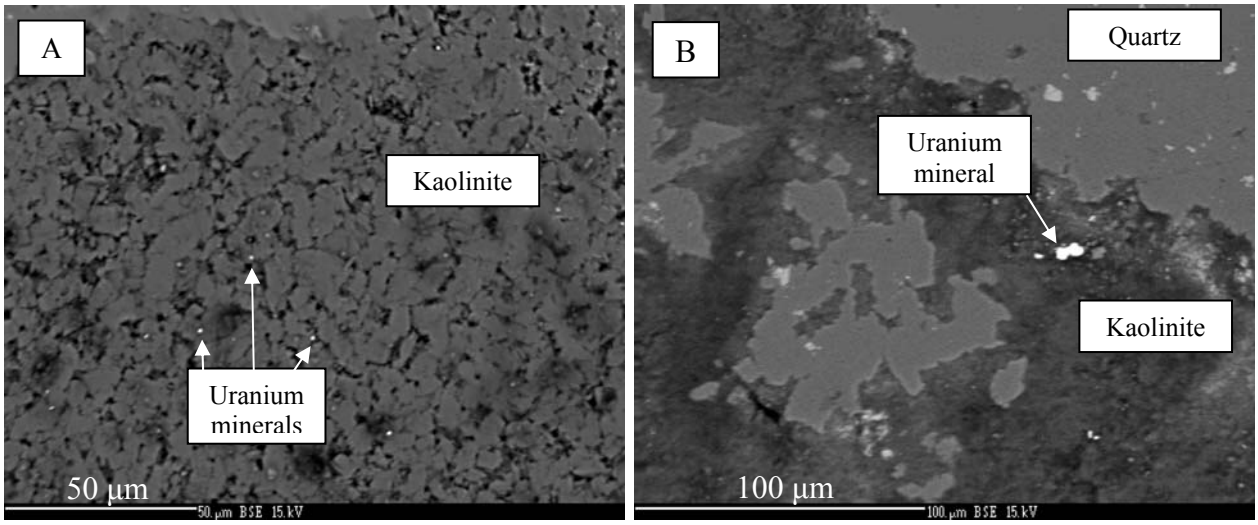

Figure 21. BSE images showing P3 assemblage. These images show uranium minerals (bright white) in zones 2 and 3b. A) PB775 spot 1 [PB3-1] has small uranium minerals surrounded by kaolinite (gray). B) PB938 spot 1 [PB16-1] has a large uranium mineral surrounded by kaolinite (dark gray) in between quartz grains (smooth med. gray).

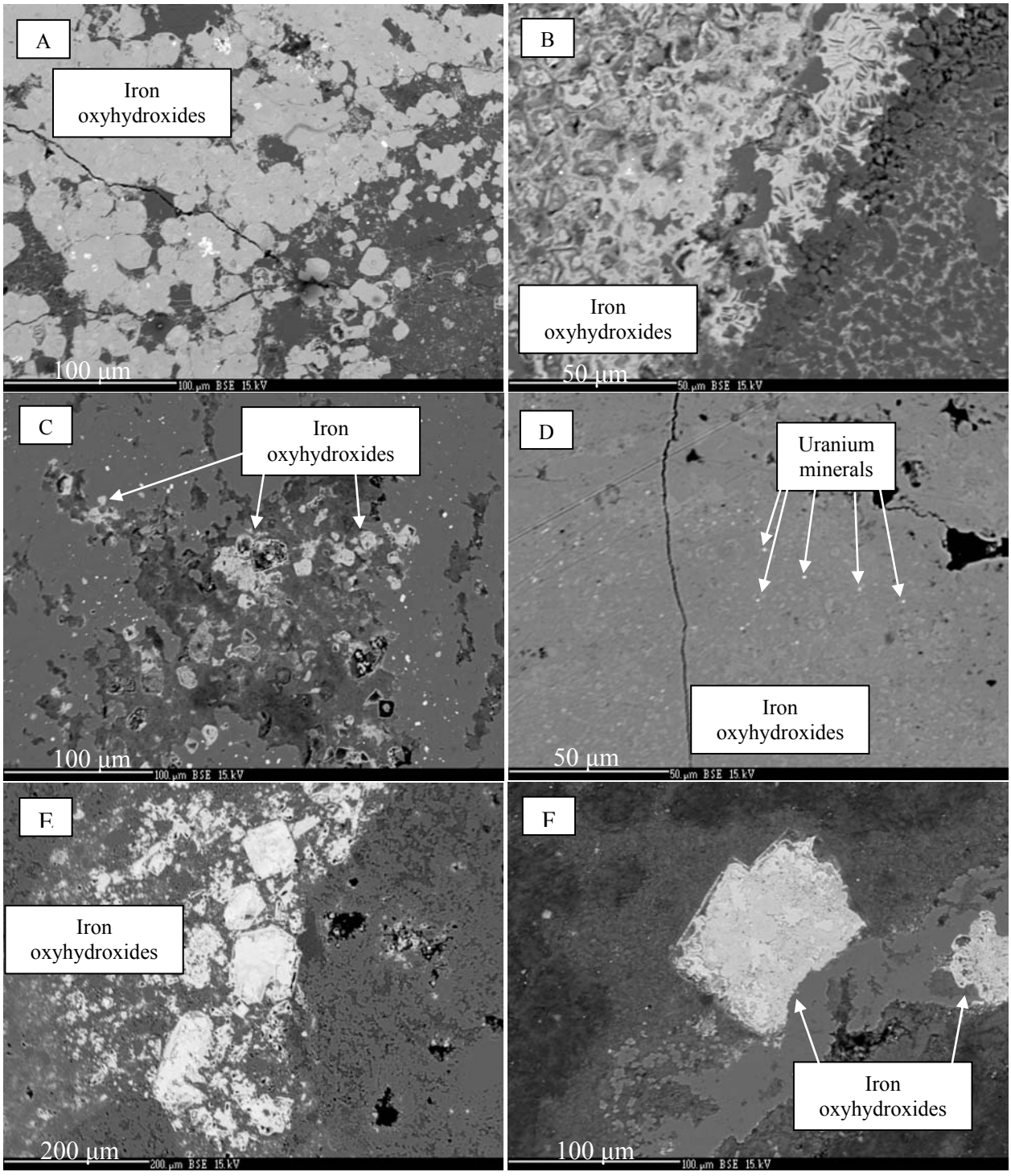
A
Iron oxyhydroxides
100 µm
B
Iron oxyhydroxides
50 µm
C
Iron oxyhydroxides
100 µm
D
Uranium minerals
Iron oxyhydroxides
50 µm
E
Iron oxyhydroxides
200 µm
F
Iron oxyhydroxides
100 µm

Figure 22. BSE images of P4 assemblage. A) PB774 [PB2] spot 2, B) PB775 [PB3] spot 5, C) PB812 spot 4 [PB6-4], E) PB935 spots 1a,b [PB15-1a,b], and F) PB938 spots 3a,b [PB16-3a,b] all show iron oxyhydroxides (whitish color) replacing pyrite based on the cubic and pyritohedron shapes. These may have been a P1 assemblage originally, but during oxidation would have lost iron, sulfur, and uranium. In most of these examples, iron oxyhydroxides are in quartz (dark gray), but close to areas of kaolinite (stippled gray color), which is also evidence of alteration. Only D) PB849 spot 3 [PB8-3] has uranium minerals, and is rare association with iron oxyhydroxides, because uranium is usually associated with quartz and/or kaolinite in samples analyzed by this study.

3.4 MULTI-ELEMENT CHEMISTRY

In this section, the sample selection, method and data analysis are described. Results for PB-1 core analyses are compared to existing datasets in order to see changes in the vertical direction compared to fresh rock.

Twenty-nine samples from the PB-1 core were selected for multi-element chemical analysis (major and trace elements) (Figure 23). These samples were selected for the presence of alteration and/or fractures along the length of the core. One sample from the Cretaceous limestone was also selected, but did not have visible alteration or fractures. The data are compared to previously collected data by Magonthier (1984) on unaltered Nopal tuff and rhyolite, Goodell (1985) from Nopal tuff and vitrophyre, and Calas et al. (2008) on unaltered rock from Nopal and Coloradas Formations. These datasets are not equivalent, because analytical methods are different and elements selected by the authors are not the same, so symbols will be used to designate each sample suite from the authors above. Previously published data for the Pozos Formation could not be found for comparison.

Not all elements analyzed show distinct patterns or relationships with other elements or with depth. Elements presented in this section are representative of a group, such U, Fe_2O_3, and S for redox sensitive elements. These selected elements are more thoroughly described in the overall discussion section and the remaining species are provided in Appendix E.

3.4.1 Methodology

PB-1 core samples (see Table 1) selected for their alteration were broken to separate the altered areas from less-altered rock. These were bagged and sent to Actlabs (www.actlabs.com; Options: 4E-Research and organic carbon) for analysis, which included major element oxides (e.g., SiO_2) and trace elements (e.g. U, S, REEs).

The concentration of each chemical concentration was plotted versus depth. Outliers were identified by their low SiO_2 and high Fe_2O_3 concentrations compared to the Nopal and Coloradas sample averages. The following outliers were identified and removed: PB798-white

[PB5-white], PB798-yellow [PB5-yellow], and PB-849 [PB8]. The small sample sizes of PB-798-yellow [PB5-yellow] and PB798-white [PB5-white] also prevented the full chemical analysis to be completed by Actlabs.

Statistical analysis of the data was performed using SPSS. After outliers were removed, univariate, bivariate, and multivariate analyses were completed. Then the correlations between elements, factor analysis (FA) with a varimax rotation in R-mode of the multi-element chemistry, and discriminatory and multivariate linear regressions were performed. See Appendix F for the results of statistical analyses.

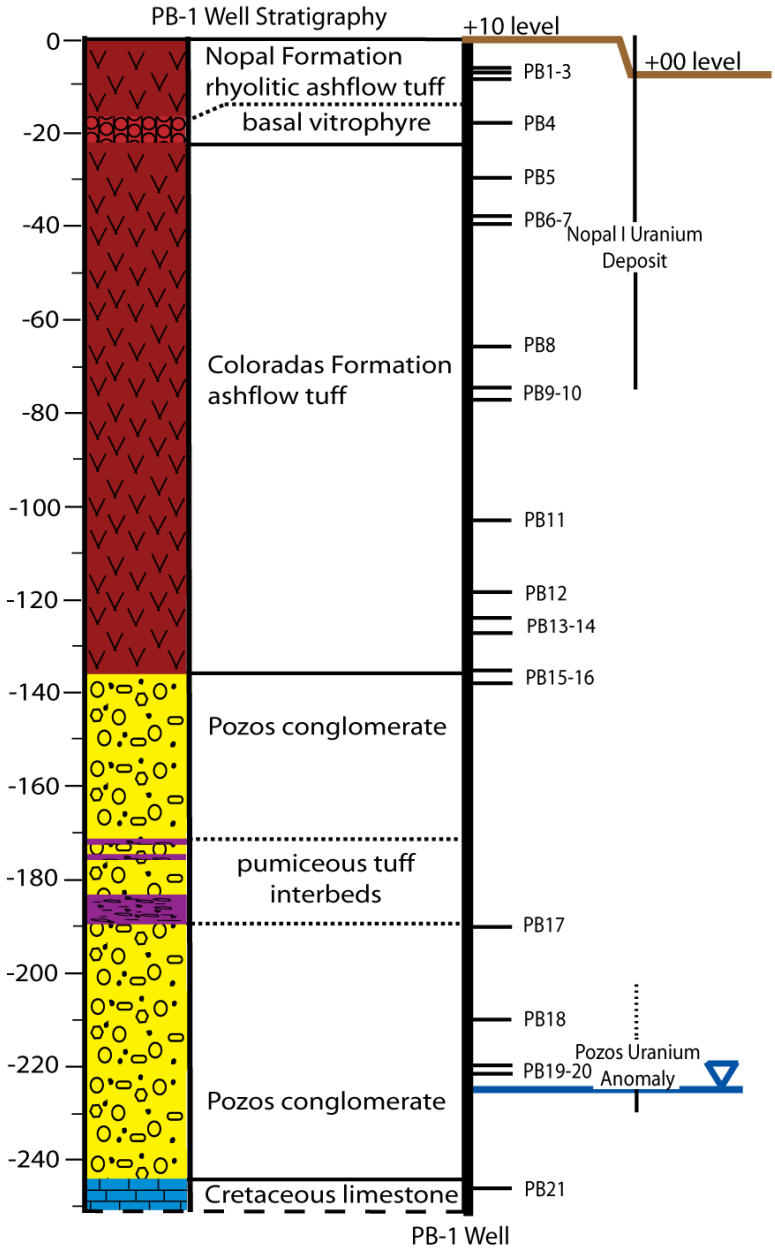

Figure 23. Drill-hole template showing samples with multi-element chemical analyses. Samples were selected for the presence of alteration or fracture material.

3.4.2 Results

In this section, the geochemical results are presented and briefly discussed in terms of variable change with depth and chemical associations. Statistical analysis using univariate (Table 6) and multivariate (correlation coefficients) results are presented as necessary in this section (see Appendix F for full analyses). Finally, factor analysis results are presented and discussed.

Table 6 shows the geochemical results of in four zones and standard statistics are given (average, minimum, maximum, and standard deviation). These zones are based on geochemical and mineralogical similarities and will be discussed further in the overall discussion section.

Individual elements are plotted using their concentration (or log concentration) versus depth. Elements that are unique or represent groups of elements were selected to provide the best examples of geochemical change along the PB-1 core. The symbols present at the top of the graph represent previously published results for comparison.

Table 6. Sample zones and standard statistics

Group	**Zone 2 (11)**				**Zone 3a (6)**				**Zone 3b (1)**	**Zone 4 (7)**				**Zone 5 (1)**
Depth (m)	**+10 to -78**				**-103 to -136**				**-136 to -180**	**-180 to -242**				**> -242**
wt%	*avg*	*max*	*min*	*s.d.*	*avg*	*max*	*min*	*s.d.*		*avg*	*max*	*min*	*s.d.*	
SiO2	74.69	82.96	66.70	4.43	74.79	79.55	68.13	4.80	78.39	64.89	69.37	55.98	4.51	7.78
Al2O3	11.58	21.75	6.90	4.07	11.06	13.22	9.50	1.23	11.25	13.46	20.59	7.59	3.93	0.53
Fe2O3(T)	5.20	14.67	0.76	4.30	5.14	10.33	3.22	2.66	4.29	3.22	4.03	2.13	0.72	0.21
MnO	0.033	0.230	0.005	0.066	0.150	0.345	0.007	0.154	0.013	0.097	0.166	0.049	0.046	0.050
MgO	0.03	0.05	0.02	0.01	0.10	0.16	0.02	0.05	0.12	1.73	3.25	0.55	1.00	0.33
CaO	0.11	0.17	0.09	0.02	1.24	6.77	0.10	2.71	0.23	4.98	8.98	2.54	2.69	50.91
Na2O	0.14	0.34	0.06	0.09	0.09	0.20	0.04	0.06	0.10	0.15	0.31	0.06	0.11	0.03
K2O	1.68	6.07	0.08	2.01	0.20	0.25	0.09	0.06	0.33	0.49	1.37	0.22	0.40	0.08
TiO2	0.245	0.359	0.158	0.063	0.221	0.244	0.176	0.024	0.406	0.614	0.756	0.338	0.152	0.016
P2O5	0.04	0.09	0.02	0.02	0.05	0.10	0.02	0.03	0.08	0.14	0.23	0.04	0.06	0.04
S	0.059	0.238	0.003	0.077	0.005	0.007	0.003	0.002	0.009	0.844	1.530	0.449	0.431	0.092

Table 6. Sample groups and standard statistics (continued)

Group	Zone 2 (11)				Zone 3a (6)				Zone 3b (1)	Zone 4 (7)				Zone 5 (1)
Depth (m)	+10 to -78				-103 to -136				-136 to -180	-180 to -242				> -242
ppm	*avg*	*max*	*min*	*s.d.*	*avg*	*max*	*min*	*s.d.*		*avg*	*max*	*min*	*s.d.*	
Ag	1.85	7.90	0.25	2.09	0.41	1.20	0.25	0.39	0.25	0.80	1.20	0.25	0.43	0.25
As	606	2130	41	595	219	435	34	163	358	47	122	19	38	5
Ba	205	572	14	155	119	422	27	157	89	1270	2894	28	1420	5
Be	2.9	5.0	2.0	0.9	1.8	2.0	1.0	0.4	1.0	1.1	2.0	0.5	0.6	0.5
Cd	14.60	70.70	0.60	20.85	1.28	3.50	0.25	1.35	0.70	0.25	0.25	0.25	0.00	0.25
Co	30.6	158.0	2.1	54.2	11.0	30.5	4.2	9.8	14.8	14.1	22.6	7.9	5.5	0.6
Cr	27.37	59.30	8.60	16.17	12.24	18.40	0.25	6.62	11.60	10.41	15.50	0.25	5.29	4.40
Cs	4.4	8.7	2.0	2.1	5.2	6.4	2.7	1.3	4.4	7.0	9.9	4.5	2.0	0.4
Cu	15	77	3	21	22	82	2	34	16	19	25	10	6	1
Hf	9.9	15.1	5.9	3.0	8.7	22.7	0.1	7.5	7.0	9.5	20.7	4.4	6.0	0.1
Mo	110	488	1	152	17	44	7	15	13	3	7	1	2	1
Ni	10	35	3	10	11	14	9	2	23	19	25	14	4	2
Pb	530	2300	15	676	53	139	3	53	22	13	21	6	6	3
Rb	66	250	5	81	12	20	5	7	10	17	40	5	13	5
Sb	24.9	92.6	1.2	26.6	4.6	16.5	0.1	6.4	1.8	1.0	2.4	0.4	0.8	0.2
Sc	6.98	11.60	2.72	3.03	6.54	11.40	2.93	2.89	3.83	9.54	19.20	4.98	5.08	2.09
Se	0.69	5.10	0.25	1.46	2.83	12.40	0.25	4.87	4.20	36.38	217.00	0.25	88.49	0.25
Sr	137	299	41	73	147	274	53	75	127	267	573	150	168	514
Ta	2.2	3.4	1.6	0.5	1.3	1.9	0.2	0.6	0.2	1.7	7.1	0.2	2.7	0.2
Th	26.9	39.0	18.7	6.0	17.4	27.6	13.1	5.2	7.6	15.8	34.5	5.5	10.4	0.3
U	581	1670	24	458	62	146	16	55	30	1445	3090	362	919	7
V	225	475	44	153	141	286	67	83	149	98	177	71	36	17
W	40	173	8	47	8	13	1	5	8	8	19	1	8	1
Y	49	104	24	25	57	158	20	50	21	29	97	8	30	2
Zn	2062	7600	156	2123	417	1330	1	490	107	36	59	1	19	6
Zr	415	767	227	204	265	570	161	156	187	256	783	96	237	7
La	73.1	112.0	31.3	23.0	39.0	56.5	26.0	10.6	20.1	71.0	128.0	21.3	39.0	1.3
Ce	142	404	73	91	86	114	60	22	41	98	397	1	165	3
Nd	78	171	35	41	32	49	1	17	17	83	344	1	142	1
Sm	16.99	33.60	7.03	8.85	9.59	15.40	4.91	3.79	3.31	30.90	65.60	0.01	28.04	0.62
Eu	0.716	2.150	0.003	0.882	0.901	2.260	0.003	0.893	0.950	1.747	3.040	0.670	0.907	0.150
Tb	1.59	4.30	0.05	1.29	1.59	4.00	0.05	1.30	0.30	0.05	0.05	0.05	0.00	0.05
Yb	4.76	12.90	2.61	2.93	6.38	17.80	2.95	5.70	2.62	3.23	10.40	0.78	3.57	0.16
Lu	0.269	1.410	0.005	0.490	0.945	2.590	0.460	0.818	0.630	0.005	0.005	0.005	0.000	0.005

The symbols used with the corresponding authors' datasets are listed in Table 7. Data from the Cretaceous limestone is not included on the graphs, because it is distinct geochemically compared to other samples.

The results presented in this section are accompanied by brief discussions. Further discussion of the multi-element chemistry is found in the overall discussion section (3.6) as it applies to geochemical zones within the PB-1 core.

Table 7. Data from previous studies used for comparison

Symbol	Source	Rock type	Elements analyzed
	Magonthier (1984)	unaltered Nopal tuff	SiO_2, Al_2O_3, TiO_2, Fe_2O_3, *FeO*, MnO, MgO, CaO, Na_2O, K_2O, P_2O_5, Ba, Co, Cr, Cs, *F*, Hf, Ni, Pb, Rb, Sb, Sc, Sr, Ta, Th, U, Zr, La, Ce, Eu, Tb, Yb
	Magonthier (1984)	unaltered Nopal rhyolite	SiO_2, Al_2O_3, TiO_2, Fe_2O_3, *FeO*, MnO, MgO, CaO, Na_2O, K_2O, P_2O_5, Ba, Co, Cr, Cs, *F*, Hf, Ni, Pb, Rb, Sb, Sc, Sr, Ta, Th, U, Zr, La, Ce, Eu, Tb, Yb
	Goodell (1985)	Nopal tuff	SiO_2, Al_2O_3, TiO_2, Fe_2O_3, *FeO*, MnO, MgO, CaO, Na_2O, K_2O, P_2O_5, As, Ba, Be, Co, Cr, Cs, Cu, *F*, *Hg*, *Li*, Mo, Ni, Pb, S, Sb, Se, *Sn*, U, V, W, Zn, Zr, org. C
	Goodell (1985)	Nopal vitrophyre	SiO_2, Al_2O_3, TiO_2, Fe_2O_3, *FeO*, MnO, MgO, CaO, Na_2O, K_2O, P_2O_5, As, Ba, Be, Co, Cr, Cs, Cu, *F*, *Hg*, *Li*, Mo, Ni, Pb, S, Sb, Se, *Sn*, U, V, W, Zn, Zr, org. C
	Calas et al. (2008)	unaltered Nopal Formation	SiO_2, Al_2O_3, TiO_2, Fe_2O_3, MnO, MgO, CaO, Na_2O, K_2O, P_2O_5, U, Th
	Calas et al. (2008)	unaltered Coloradas Formation	SiO_2, Al_2O_3, TiO_2, Fe_2O_3, MnO, MgO, CaO, Na_2O, K_2O, P_2O_5, U, Th

Based on statistics in Table 6, there are some basic observations that can be made. Highly mineralized samples exist in zone 2, which are mostly chalcophile elements (e.g., As, Pb, Zn), and other redox sensitive elements, such as Co, Mo, U, and V, and are highly correlated (Figure 24). These elements decrease in concentration from zone 2 to 5.

Uranium averages 581 ppm in zone 2, and decreases in zones 3a and 3b to 62 and 30 ppm, respectively. However, uranium drastically increases again in zone 4 to an average of 1445, and the highest concentration in the PB-1 core, 3090 ppm in one sample. A few other species, specifically, TiO_2, P_2O_5, and S are highly correlated with uranium (Figure 25).

The overall decreasing concentration with depth trend for most elements indicated by the average concentrations is deceiving. The high variability of many of these elements, especially

within the oxidized and reduced groups is more obvious when plotted individually. This will be further clarified in the following graphs and descriptions.

Zone 5, the Cretaceous limestone sample is very similar in composition to the average values of Peña Blanca limestones reported by Goodell (1985) for the species listed in Table 7. It acts as an impermeable barrier to uranium migration except through faults and fractures (Stege et al., 1981). Fractures or alteration were not visible on the sample analyzed, so other mobile species probably were unable to alter the limestone.

Silicification (SiO_2>75%) is evident in the wt% SiO_2 graph (Figure 26). It shows a negative correlation with depth, i.e., decreases with depth. Ash flow tuffs, like Nopal and Coloradas (zones 2 and 3a), should have high SiO_2 content; however, percentages greater than 75% show that this is not typical silica content. The Pozos conglomerate (zones 3b and 4) has tuff fragments and clays, so its silica content can be explained by these constituents. The Cretaceous limestone is low in SiO_2 at 7.8%.

A monotonically decreasing curve from zone 2 to 3b was identified. The following species follow this pattern: Fe_2O_3 total (Figure 27), K_2O (Figure 28), Na_2O, P_2O_5, As, Cd, Cr, Cu, Mo, Pb, Rb, S (Figure 29), Sb, Ta, Th, U (Figure 30), V, W, Zn, and the light REEs. Al_2O_3, Cd, and MnO (Figure 31) may also follow this pattern, but they are not as clear. Zone 2 contains the oxidized primary assemblage, which is the mineralized source for these elements, in addition to the tuffs.

In zone 3a, MnO (avg. 0.15 ppm) increases in concentration compared to zones 2, 3b, and 4 (avg. <0.10). Fe_2O_3 average concentrations decrease in each zone with depth, but it should be similar geochemically to MnO. Looking at the individual data points within zone 3a for iron (Figure 27), they are all higher than the results reported by previous authors (Table 7), so it has a relatively higher concentration than first observed. A similar observation can be made on the MnO graph (Figure 31), even though there is only one previously reported value.

In zone 4, similar species have increased concentrations compared to zones 3a and 3b; they are Na_2O, MnO, P_2O_5, Co, Cu, Ni, S, Ta, Th, U, V, W, and light REEs (±Cr, Sb). These

species are redox sensitive, which indicates changes in redox conditions have a major influence on the movement of elements vertically along the PB-1 core.

Two constituents, TiO_2 and P_2O_5, are especially high in zone 4 (0.61 and 0.14 wt%, respectively), which 3x greater than zones 2-3a and 1.5x zone 3b. They both increase in concentration with depth (Figure 32) and their correlation is 0.75, which means there is greater than 99.9% probability that TiO_2 and P_2O_5 are related (Figure 25). As described previously, TiO_2 is associated with uranium minerals throughout the deposit, but especially in the Pozos uranium anomaly. The Pozos uranium anomaly is also where the highest phosphorous concentrations are located. It is unlikely that uranium-bearing phosphate minerals, like monazite or apatite, could account for such a high correlation when few or none were identified during EMPA or XRD analysis.

Uranium is a redox sensitive element and important for radionuclide transport studies (Figure 30). Uranium decreases with depth within the Nopal I uranium deposit to near background levels, and then increases in concentration within the Pozos uranium anomaly. Uranium is highly variable, as indicated by the large standard deviations in each group.

CaO, MgO, Sr, and Ba are evidence for the presence of carbonates in the Pozos conglomerate and Cretaceous limestone. This group was identified through its low concentrations in the oxidized and redox transition groups and high concentration in the Pozos conglomerate and Cretaceous limestone, and also through multivariate (Figure 25) and factor analysis (next subsection). The relationship between these elements is related to carbonate minerals, calcite and dolomite, and trace elements, like Sr, which is 2+ and can substitute for Ca^{+2}. XRD and EMPA analysis of the Pozos conglomerate showed calcite, dolomite, and minor barite, which would account for these elements.

Only one sample from the Pozos uranium anomaly, PB4035 [PB18] 0.19% organic carbon, yielded a sample with organic carbon content greater than the detection limit of 0.05% (see Appendix E). This might be from organic material within the Pozos conglomerate or later

reduced in the Pozos conglomerate from groundwater. Organic carbon could play a role in reducing other elements in the Pozos uranium anomaly.

Factor analysis

Twenty-six samples and 46 variables (chemical species) was used to run a FA. Two general recommendations, for sample size and sample to variable ratio, are made when determining the applicability of FA, but they vary greatly among researchers. Sample size minimum suggestions are 100 to over 1000 and ratios from 3 to 20 times the number of variables (Preacher and MacCallum, 2002; Mundfrom et al., 2005). However, there have been few studies to support these recommendations, and those studies suggest smaller sample sizes where communality is high and when the number of variables to factors ratio increases (Preacher and MacCallum, 2002; Mundfrom et al., 2005). Based on this information, the number of samples may be too low for a factor to stand on its own, but is interpreted with results from other sections.

The FA resulted in eight factors, which accounted for >99% of the variables. The factor analysis finds families within the multi-element chemistry correlations, and can be used to identify processes, units, or minerals. Not every factor can be easily explained, especially with respect to individual species that may not fit a previous interpretation. For example, in the factors described below, Fe_2O_3 is not always positively loaded with redox sensitive elements. This is probably because iron at Nopal I is left behind in iron oxyhydroxides, even when the original pyrite has been completely oxidized (Aniel and Leroy, 1985; Pearcy et al., 1994). Only factors that could be reasonably interpreted are presented in this section. The factor loading needs to have an "R" or correlation coefficient greater than ~0.38 in order to have a 95% or greater probability of significance, based on the total number of samples. Therefore, interpretations are drawn from species that are greater than 0.38.

Factor 1 (Figure 33) and 2 (Figure 34) are both REE factors. LREEs are positively loaded in factor 1 and negatively loaded with a fresh rock signature. This factor also is

positively loaded with several redox sensitive elements (e.g., Co, V, As). Factor 2 is the opposite of factor 1, because HREEs are positively loaded in addition to resistate elements (e.g., Sc, Zr). It is negatively loaded with the Pozos conglomerate signature.

Factor 3 (Figure 35) has P_2O_5 and TiO_2 strongly loaded (>0.8), along with Ba, S, and U; this is interpreted as the Pozos uranium anomaly factor. MgO and Sr are enriched in carbonates, which also supports this interpretation, because the Pozos conglomerate has calcite and dolomite (Table 2). Barite is also found in the Pozos conglomerate, so barium and sulfur can be explained by this factor. Pyrite is also found in the Pozos, but Fe_2O_3 is negatively loaded with sulfur and the other elements. This could be explained by the high concentration of iron in oxyhydroxides in the Nopal and Coloradas Formations, which would have a negative association with sulfur.

Factor 4 (Figure 36) shows positive loading in the mobile alkali and alkaline earth elements. K_2O was leached during silicification (Goodell, 1985), so this may be evidence of other elements that were mobilized in addition to potassium.

In factor 5 (Figure 37), only MnO is significantly loaded. Manganese is the only element that is enriched in the rock between the Nopal I uranium deposit and the Pozos uranium anomaly. It indicates a redox change where it precipitates.

Factor 7 (Figure 38) has positively loaded CaO and Sr, and it is interpreted as the Cretaceous limestone factor. Calcium and strontium are both +2 elements in the alkali earths, and their geochemical behavior is similar. The negative loading with SiO_2, Al_2O_3, and other elements more closely associated with silicic rock supports this interpretation as well.

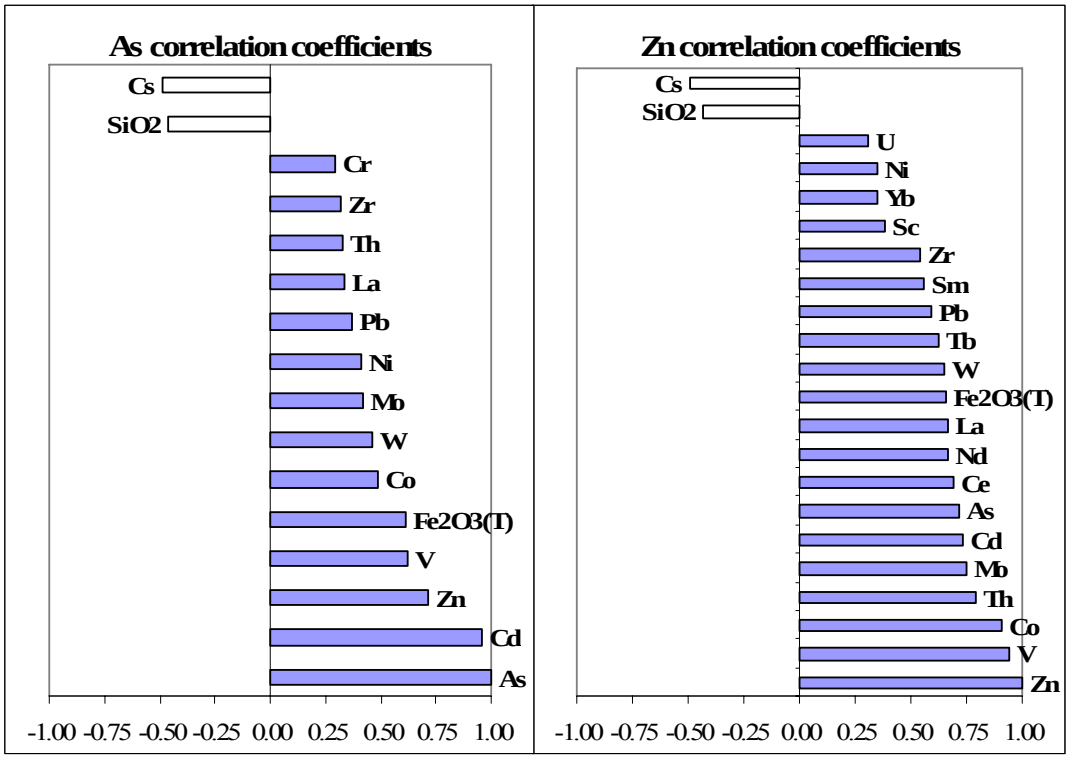

Figure 24. Correlation coefficients for As and Cu (excluding values -0.3 to 0.3). The positive correlations are almost all (excluding Th, etc.) redox sensitive elements. These elements have a high probability of significance (90%). There is a negative correlation with SiO_2 and Cs.

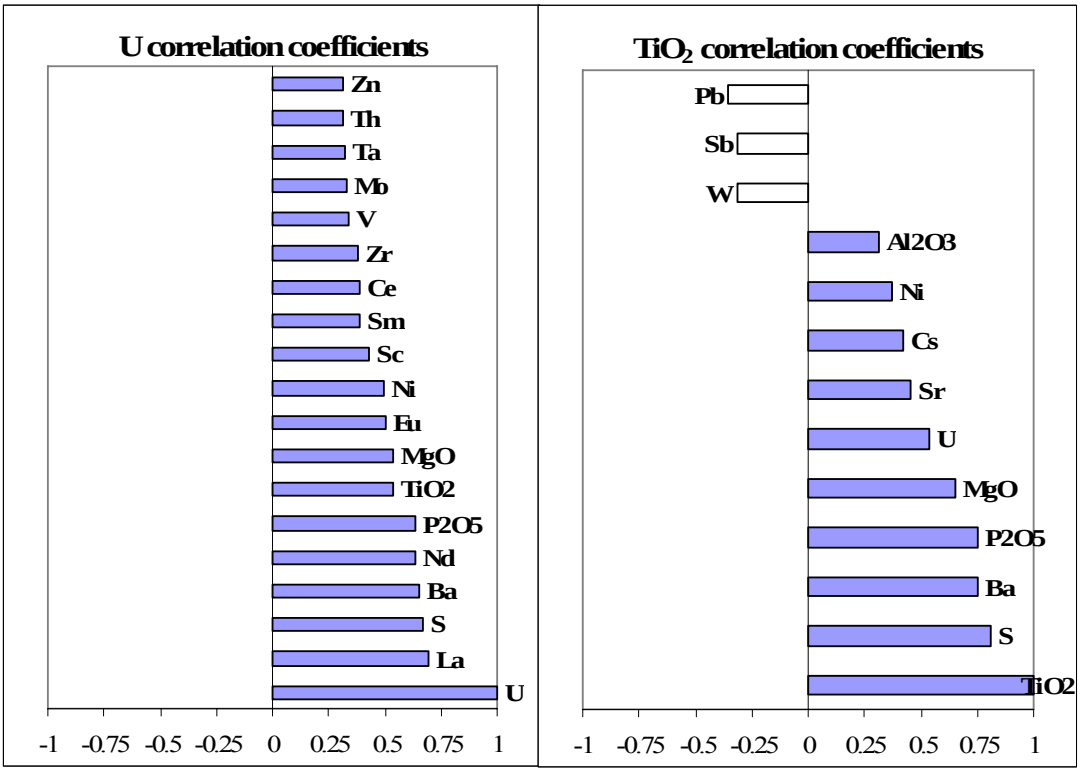

Figure 25. Correlation coefficients for U and TiO_2 (excluding values -0.3 to 0.3). Uranium is positively correlated with the LREEs, other redox sensitive elements (e.g. Mo, V, S), and Ba, MgO, TiO_2, and P_2O_5. Ba and MgO are associated with the Pozos conglomerate and TiO_2 and P_2O_5 are uranium adsorbers. TiO_2 and P_2O_5 are also positively correlated with each other. See text for details.

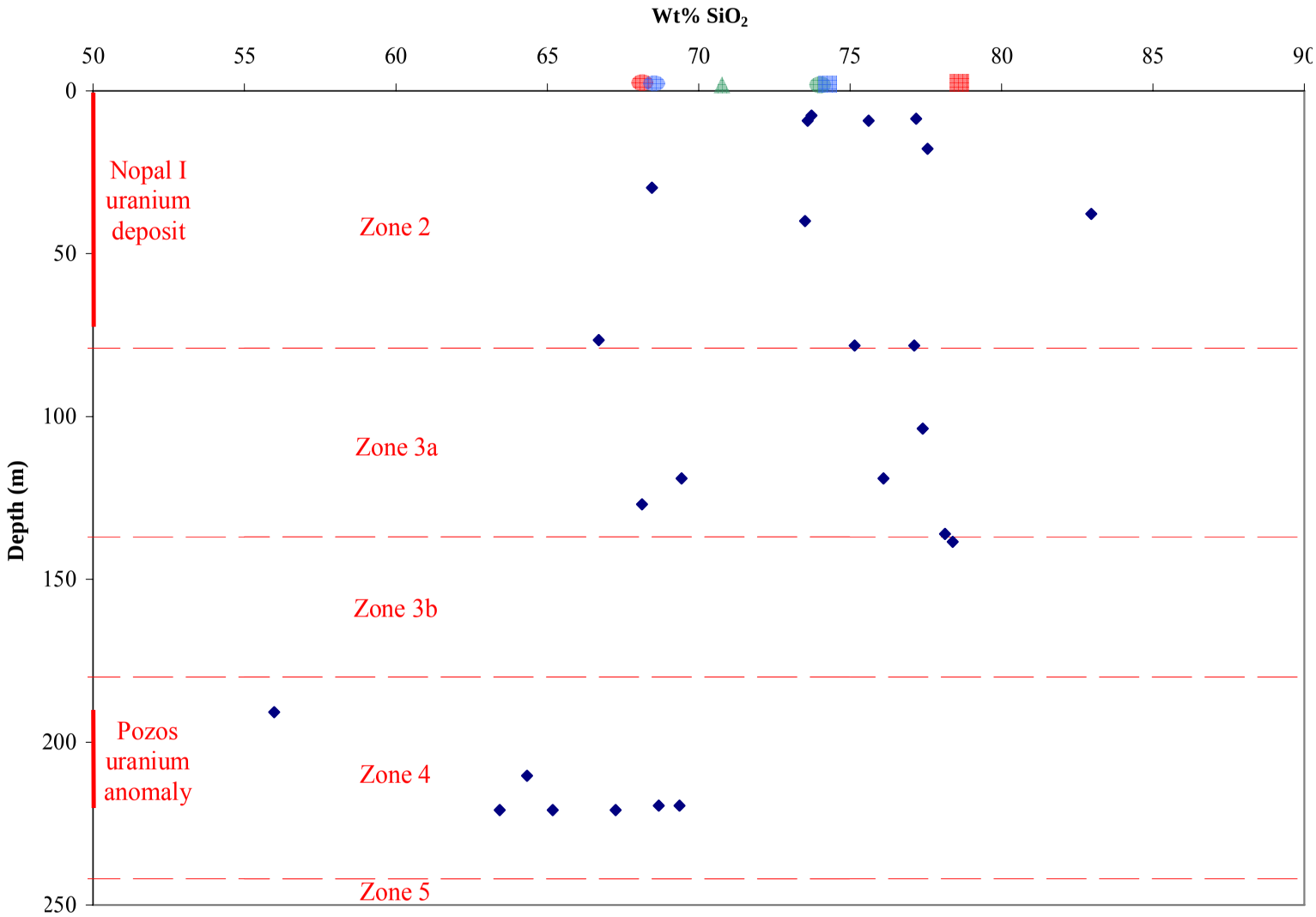

Figure 26. Change in wt% SiO_2 concentration with depth down the PB-1 core. Symbols at the top of the graph are as noted in Table 7. The solid red lines show the extent of the Nopal I uranium deposit and the Pozos uranium anomaly as noted. The red dashed lines separate the zones as noted.

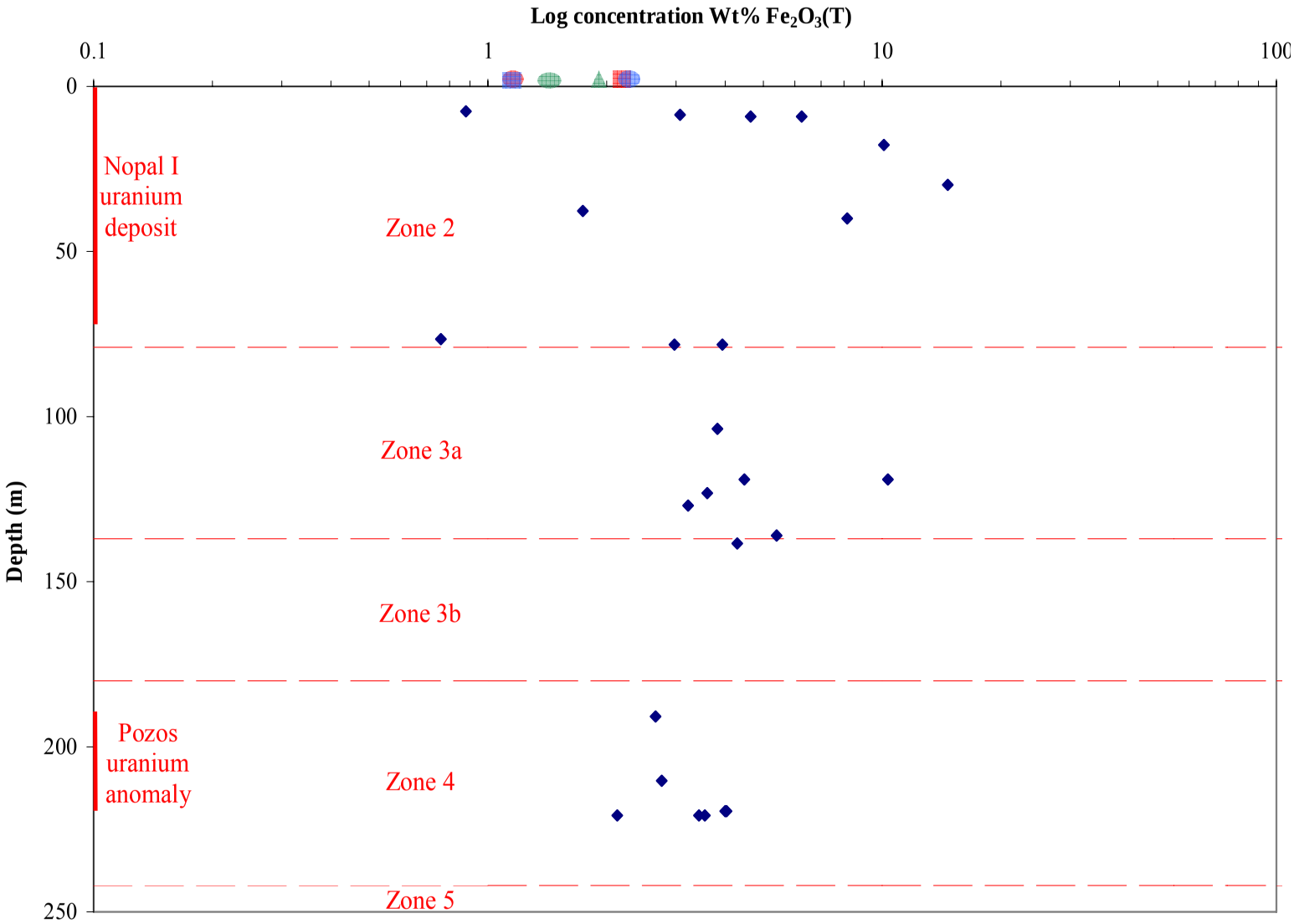

Figure 27. Change in log wt% Fe_2O_3 total concentration with depth down the PB-1 core. Symbols at the top of the graph are as noted in Table 7. The solid red lines show the extent of the Nopal I uranium deposit and the Pozos uranium anomaly as noted. The red dashed lines separate the zones as noted.

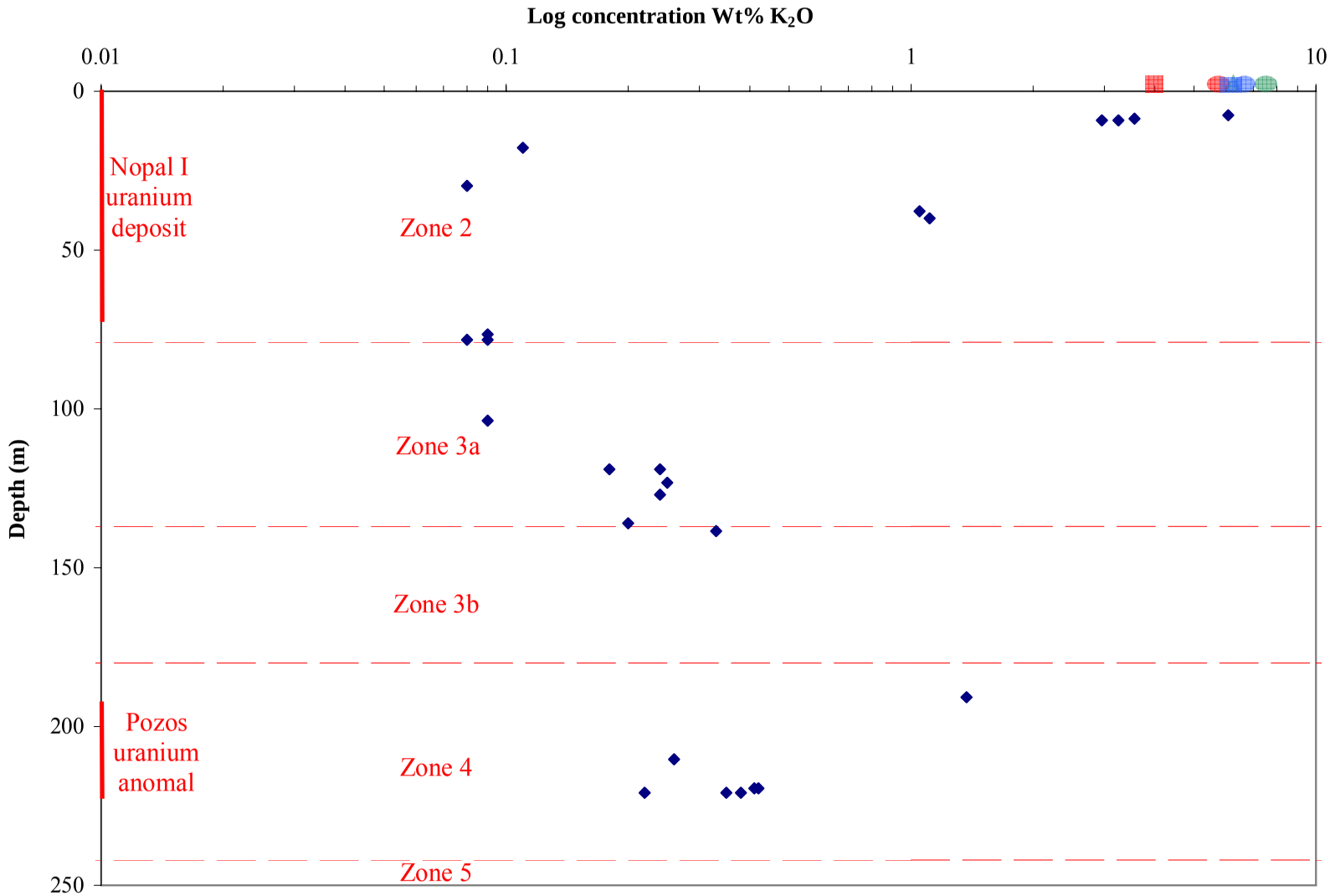

Figure 28. Change in log wt% K_2O concentration with depth down the PB-1 core. Symbols at the top of the graph are as noted in Table 7. The solid red lines show the extent of the Nopal I uranium deposit and the Pozos uranium anomaly as noted. The red dashed lines separate the zones as noted.

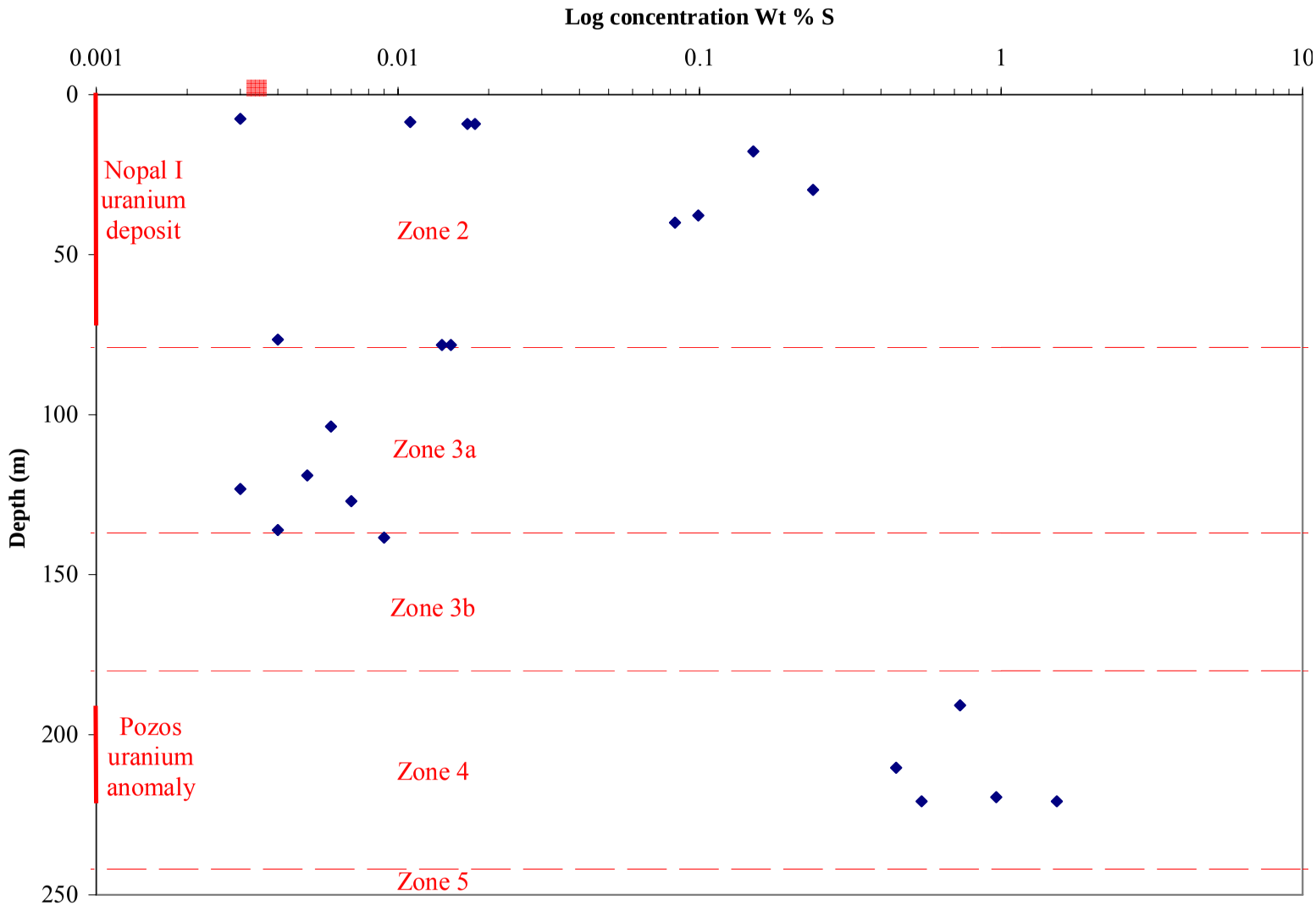

Figure 29. Change in log wt% S concentration with depth down the PB-1 core. Symbols at the top of the graph are as noted in Table 7. The solid red lines show the extent of the Nopal I uranium deposit and the Pozos uranium anomaly as noted. The red dashed lines separate the zones as noted.

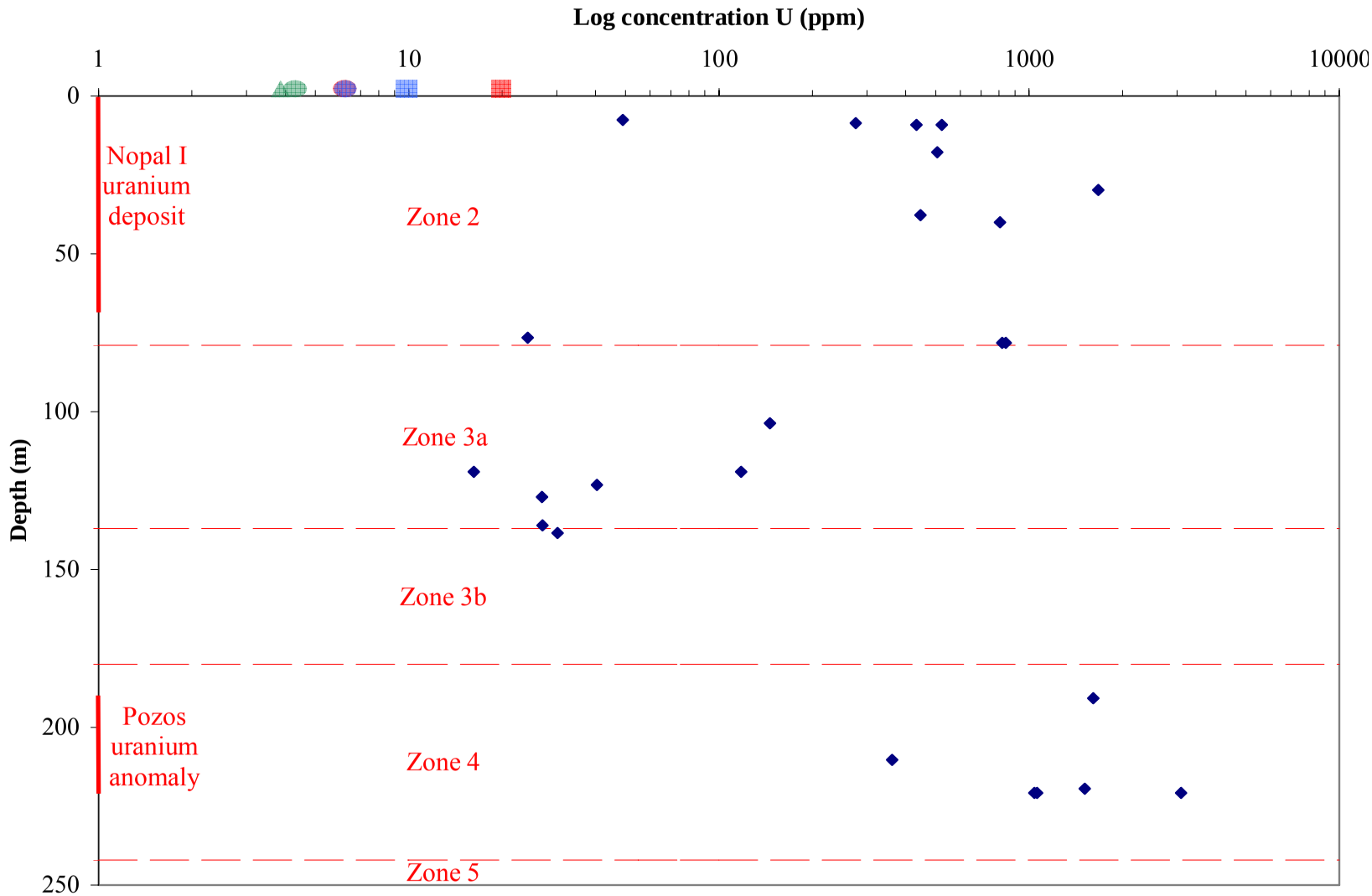

Figure 30. Change in U (ppm) concentration with depth down the PB-1 core. Symbols at the top of the graph are as noted in Table 7. The solid red lines show the extent of the Nopal I uranium deposit and the Pozos uranium anomaly as noted. The red dashed lines separate the zones as noted.

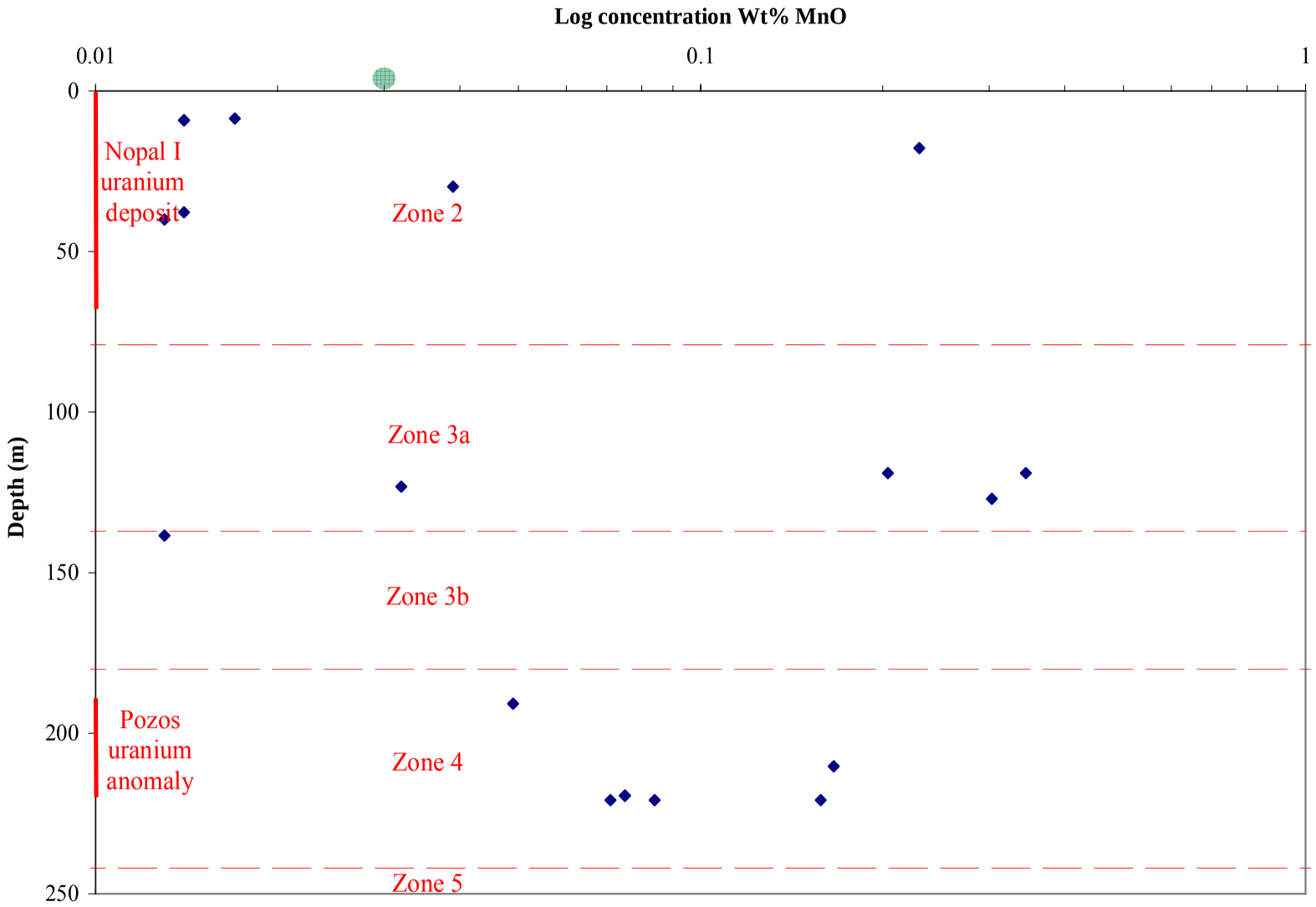

Figure 31. Change in log wt% MnO concentration with depth down the PB-1 core. Symbols at the top of the graph are as noted in Table 7. The solid red lines show the extent of the Nopal I uranium deposit and the Pozos uranium anomaly as noted. The red dashed lines separate the zones as noted.

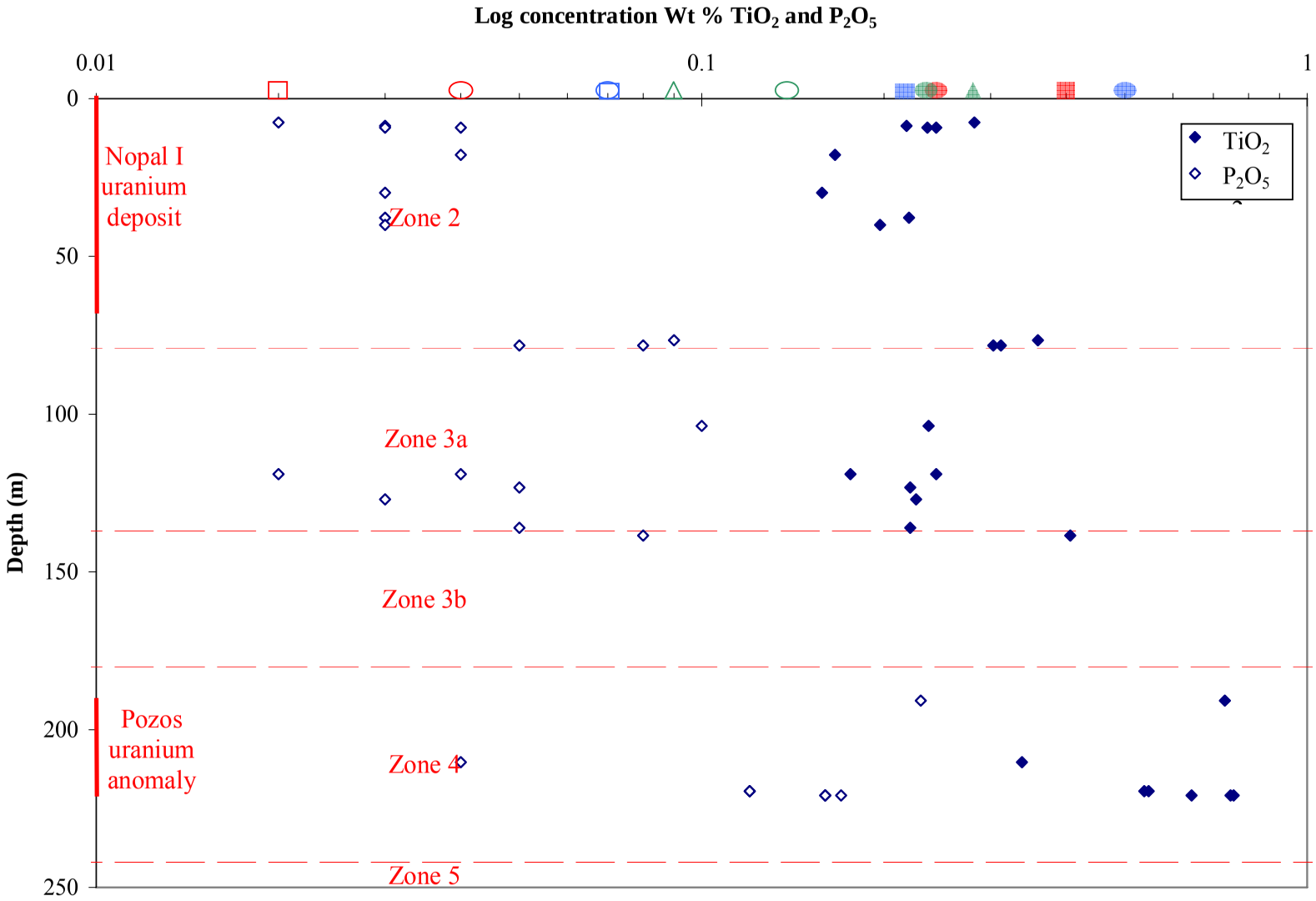

Figure 32. Change in log wt% TiO_2 (closed) and P_2O_5 (open) concentrations with depth down the PB-1 core. Symbols at the top of the graph are as noted in Table 7. The solid red lines show the extent of the Nopal I uranium deposit and the Pozos uranium anomaly as noted. The red dashed lines separate the zones as noted.

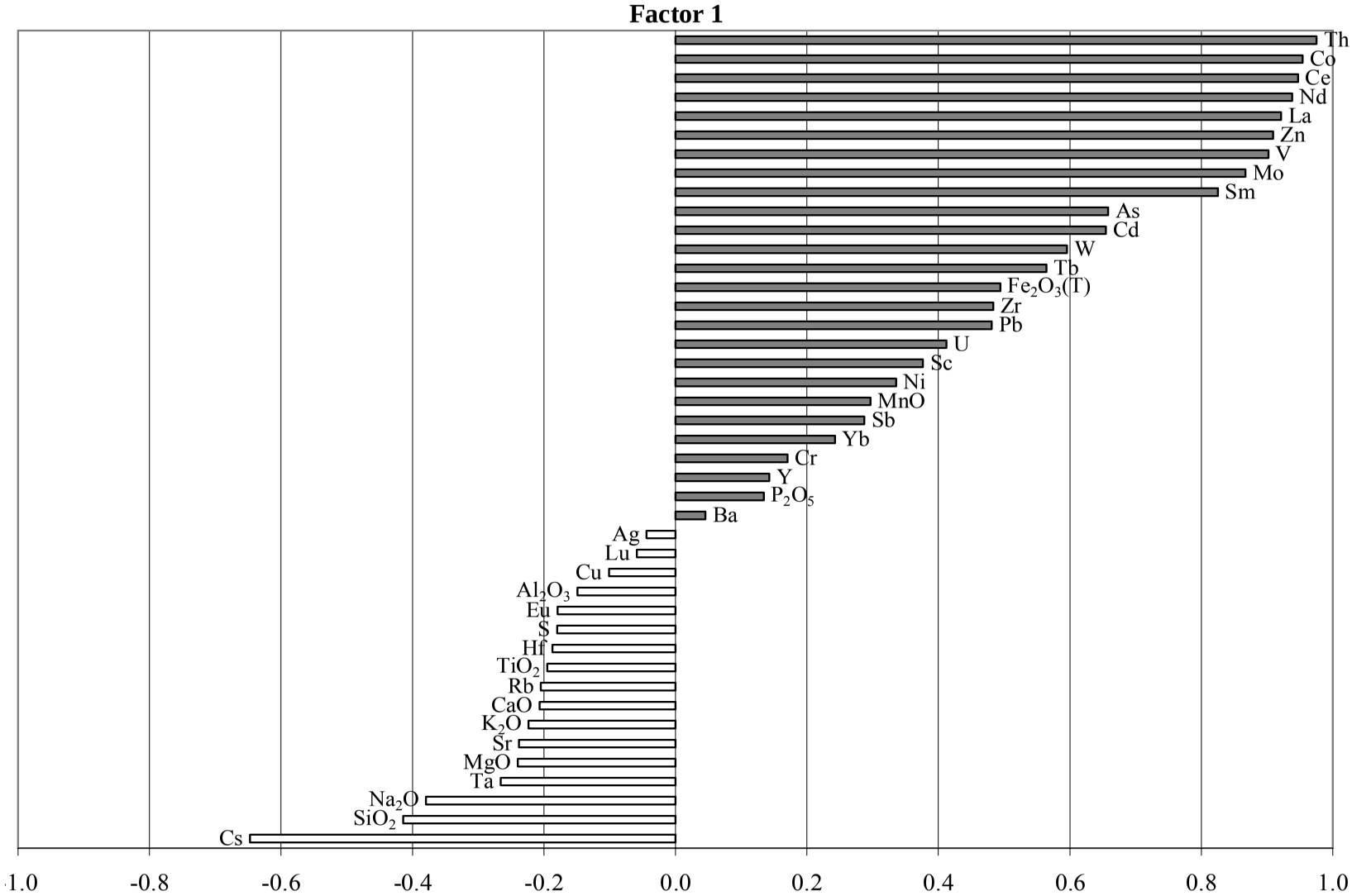

Figure 33. Factor analysis of multivariate correlation coefficients for the multi-element chemistry. Each species has a corresponding factor loading shown on the x-axis. Positive loading is in black filled bars and negative loading is in white bars. Factor loading is 95% significant above 0.38 with 25 samples. Factor 1 shows positive loading in the LREEs and many redox sensitive elements and negative loading with elements representing fresh volcanic rock.

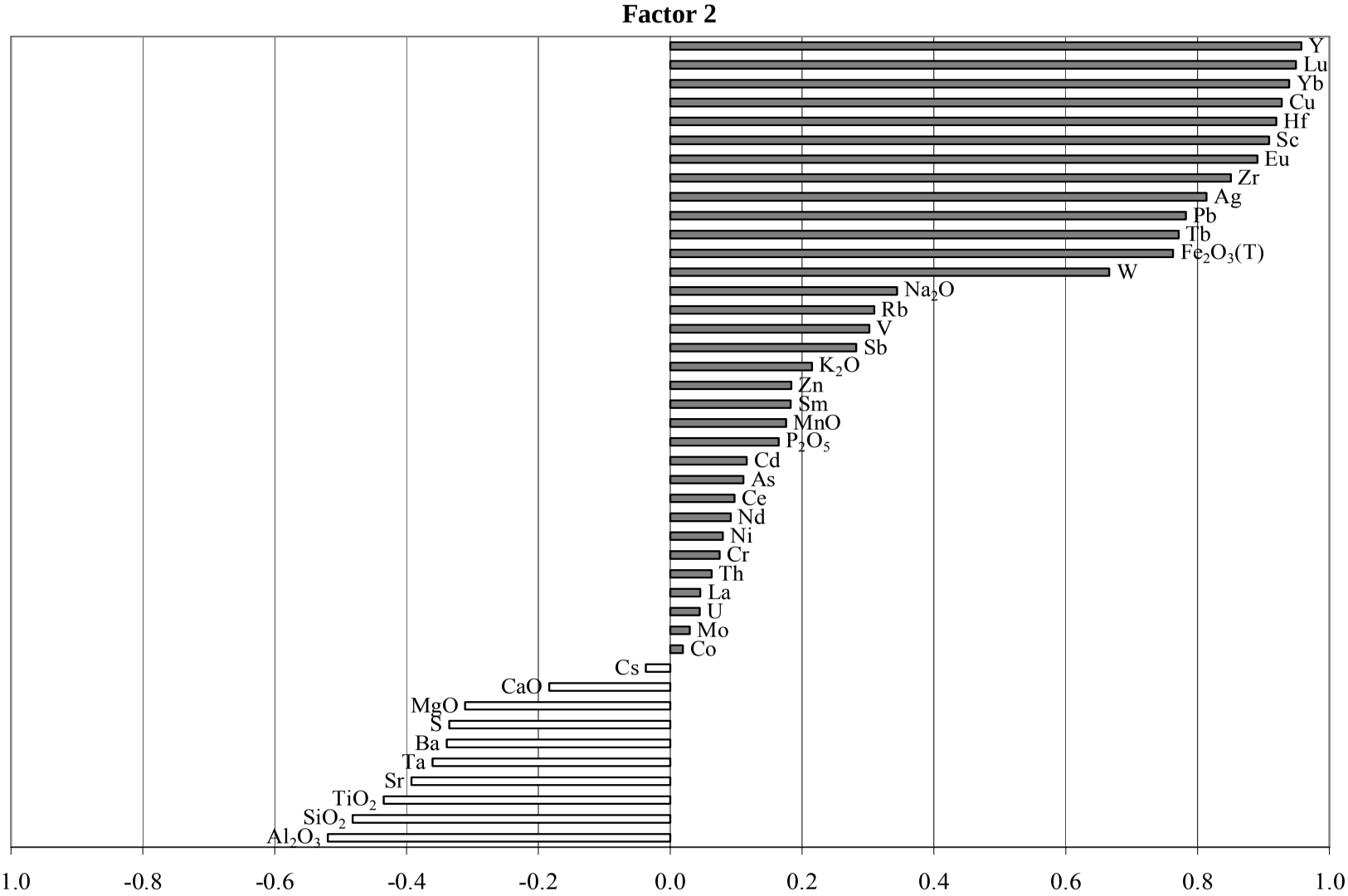

Figure 34. Factor analysis of multivariate correlation coefficients for the multi-element chemistry. Each species has a corresponding factor loading shown on the x-axis. Positive loading is in black filled bars and negative loading is in white bars. Factor loading is 95% significant above 0.38 with 25 samples. Factor 2 shows positive loading among HREEs and resistate elements and negative loading with elements representing species in the Pozos conglomerate.

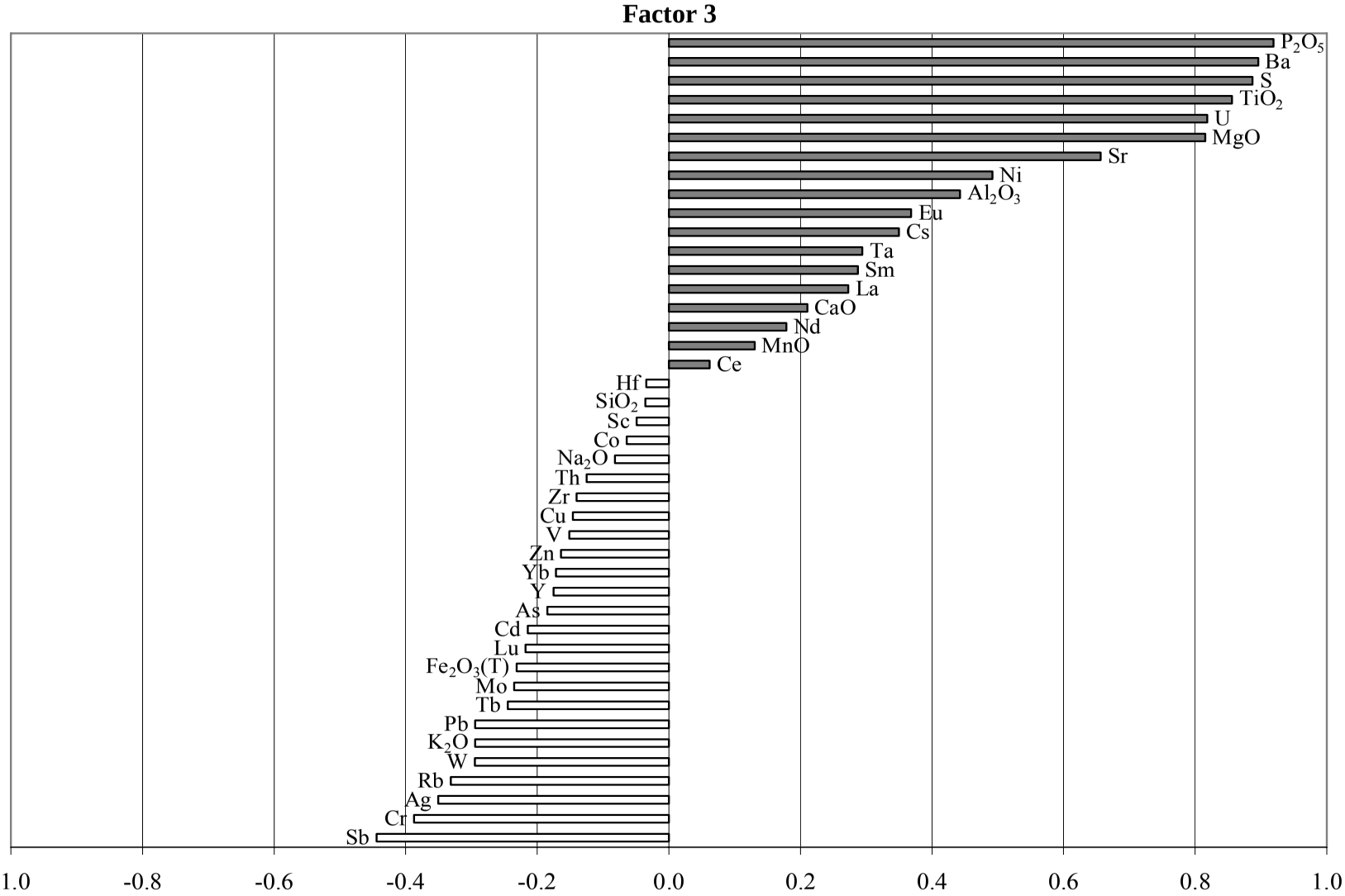

Figure 35. Factor analysis of multivariate correlation coefficients for the multi-element chemistry. Each species has a corresponding factor loading shown on the x-axis. Positive loading is in black filled bars and negative loading is in white bars. Factor loading is 95% significant above 0.38 with 25 samples. Factor 3 is interpreted as the Pozos uranium anomaly mineralization factor.

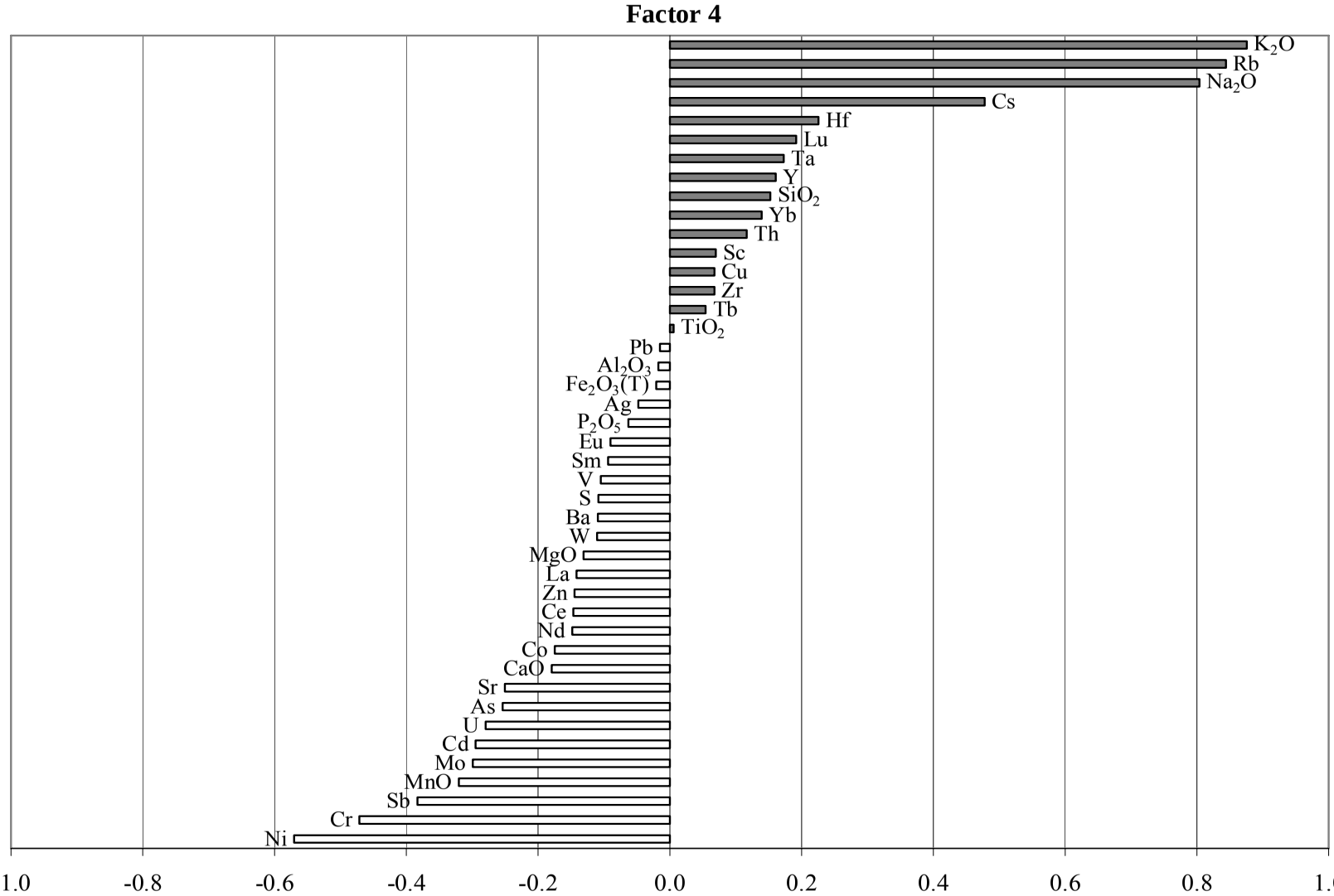

Figure 36. Factor analysis of multivariate correlation coefficients for the multi-element chemistry. Each species has a corresponding factor loading shown on the x-axis. Positive loading is in black filled bars and negative loading is in white bars. Factor loading is 95% significant above 0.38 with 25 samples. Factor 4 shows positive loading in the mobile alkali and alkaline earth elements.

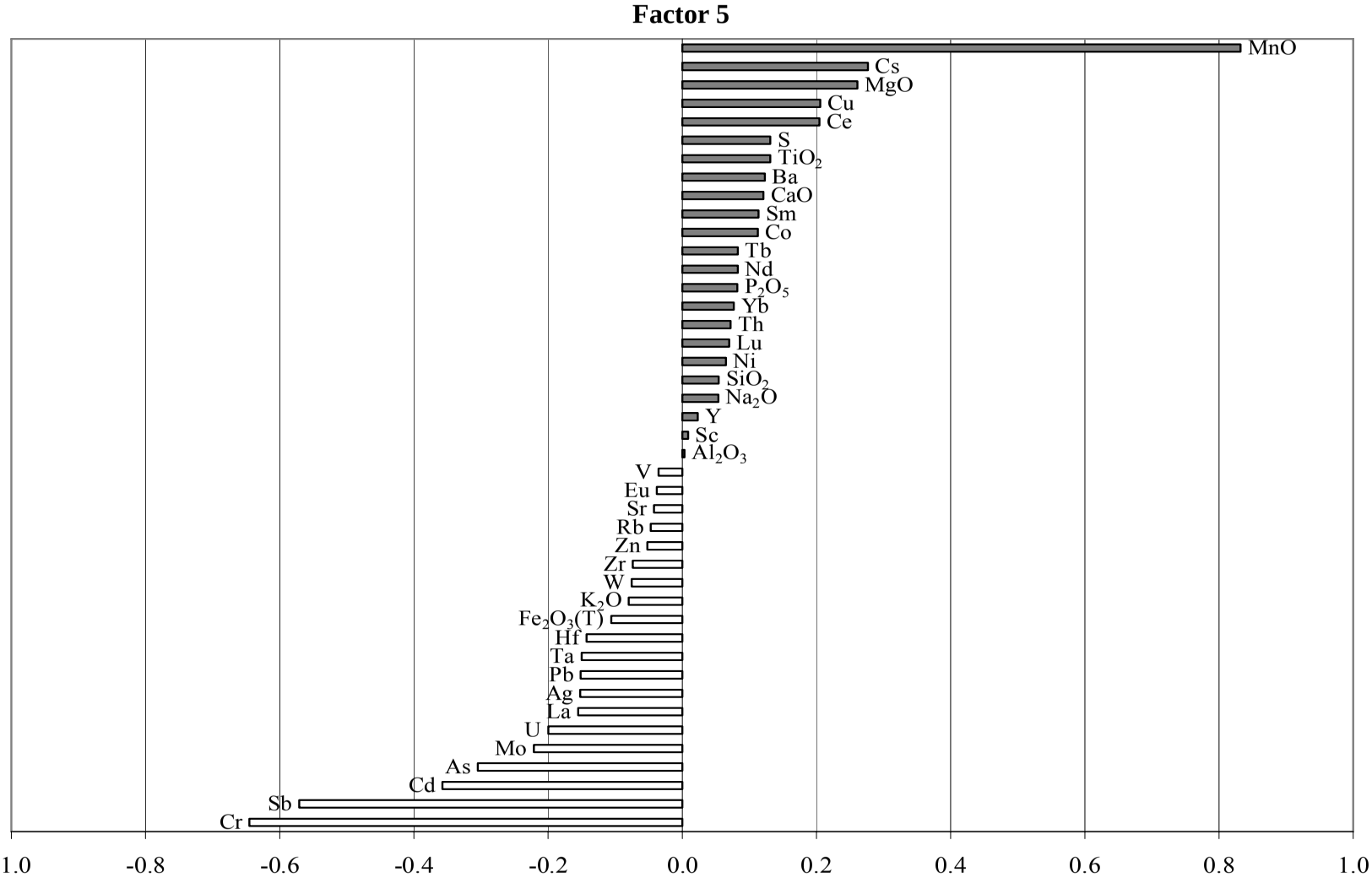

Figure 37. Factor analysis of multivariate correlation coefficients for the multi-element chemistry. Each species has a corresponding factor loading shown on the x-axis. Positive loading is in black filled bars and negative loading is in white bars. Factor loading is 95% significant above 0.38 with 25 samples. Factor 5 is the Mn precipitation factor, because MnO is identified as significant loading. Manganese is the only element that is enriched in the rock between the Nopal I uranium deposit and the Pozos uranium anomaly. It may indicate a redox change where it precipitates.

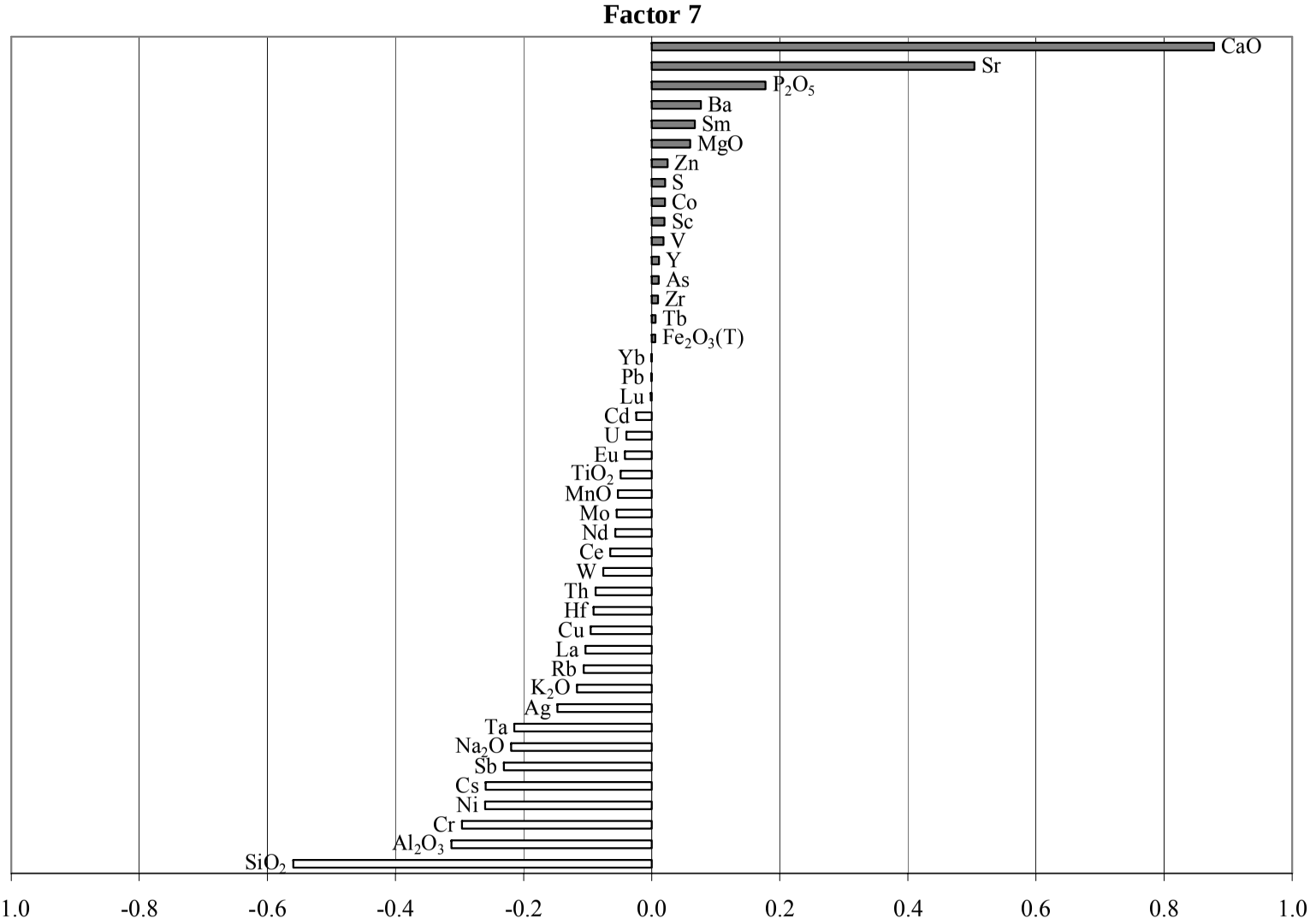

Figure 38. Factor analysis of multivariate correlation coefficients for the multi-element chemistry. Each species has a corresponding factor loading shown on the x-axis. Positive loading is in black filled bars and negative loading is in white bars. Factor loading is 95% significant above 0.38 with 25 samples. Factor 7 has positively loaded CaO and Sr, so it interpreted as the Cretaceous limestone factor.

3.5 U-SERIES DATING OF NOPAL I URANIUM MINERALS

In this section, the ^{238}U-decay series parent-daughter ratios are presented. The relevant isotopes are highlighted in Figure 39. The principles of disequilibrium dating are described and then the SIMS method and results.

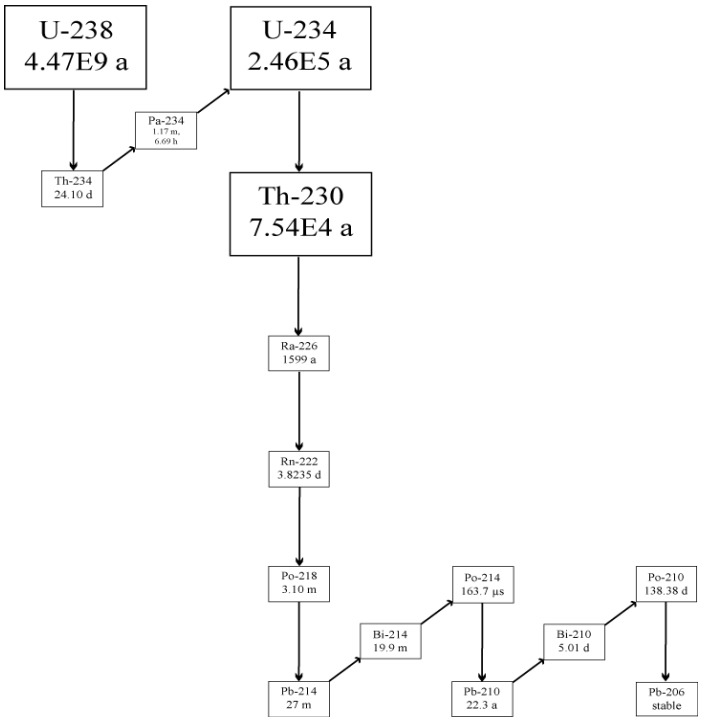

Figure 39. The ^{238}U decay chain. Only the isotopes relevant to this section are highlighted: ^{238}U, ^{234}U, and ^{230}Th.

Radionuclides decay into daughter products over time. These daughters can also decay with a different half-life than the parent. If this decay chain is uninterrupted, then the radionuclides would be in secular equilibrium. Secular equilibrium means that when a parent-daughter or daughter-parent ratio is measured, it will be equal to one or unity. However, in many geologic systems, this series of parents and daughters in secular equilibrium with each other can be altered through physical or chemical means (e.g. solid to gas phase, solubility differences). When that happens, the parents and daughters are considered to be in disequilibrium.

Disequilibrium in the activity ratio must be more or less than one, because if it is at one or unity, it is in secular equilibrium. This is important, because a disequilibrium dating method is only useful in giving ages up to unity, which would be the maximum age possible. Of the

many disequilibrium dating techniques available, only some are in an appropriate dating range for Yucca Mountain timescales of 1 Ma. The one selected for this study is the $^{230}Th/^{234}U$ ratio.

$^{230}Th/^{234}U$ ratio can give a range of ages from recent to approximately 375 ka. The half-life of ^{230}Th is 75 ka, so it has a maximum calculable ingrowth time of 375 ka, because over 5-6 half-lives it will achieve secular equilibrium with its parent, ^{234}U, if no additional disequilibrium event occurs. ^{234}U has half-life of about 250 ka, so the $^{234}U/^{238}U$ ratio has a maximum clock of about 1.25 Ma. By using these ratios, it is possible to bracket the age of the uranium minerals, if no further disequilibrium events occur.

Disequilibrium can be achieved in several ways. First, a chemical difference in solubility exists between uranium and thorium. Uranium has two stable oxidation states, U(IV), which is insoluble, and U(VI), which is soluble. This is in contrast to thorium, which has one stable oxidation state, Th^{+4}, which has a very low solubility. In addition, radioactive disequilibrium usually exists between ^{234}U and ^{238}U, because α-decay of ^{238}U causes radiation damage in the crystal lattice, enhancing the solubility of U-bearing minerals and can cause preferential dissolution of ^{234}U (e.g. Gascoyne et al., 2002). Either or both of these mechanisms could be the cause of radioactive disequilibrium in Peña Blanca uranium minerals.

3.5.1 Secondary Ion Mass Spectrometry

A secondary ion mass spectrometer, shown in Figure 40, bombards the surface of a sample with a focused beam of ions a few microns in diameter and allows in situ analysis of a polished surface. Some atoms are ionized during this bombardment, or sputtering, and are focused and accelerated as a "secondary" beam of ions through a slit and into the mass spectrometer (Reed, 1989; Fayek et al., 2006; Valley and Kita, 2009). For uranium and thorium analysis, an O^- primary beam is used, because it enhances the yield of secondary ions (e.g. U^+, UO^+, Th^+).

SIMS analysis was chosen for $^{230}Th/^{234}U$ disequilibrium dating, because the beam size is smaller than that of laser-ablation ICP-MS. This is particularly important for Peña Blanca

uranium minerals, because crystals and aggregates are so small in size, which makes them difficult to analyze (Fayek et al., 2006). From the EMPA, two samples (three separate uranium mineral sites) were chosen for their larger and identifiable uranium minerals. The SIMS sample locations in the PB-1 core are shown in (Figure 41), which are located in zone 4, the Pozos uranium anomaly.

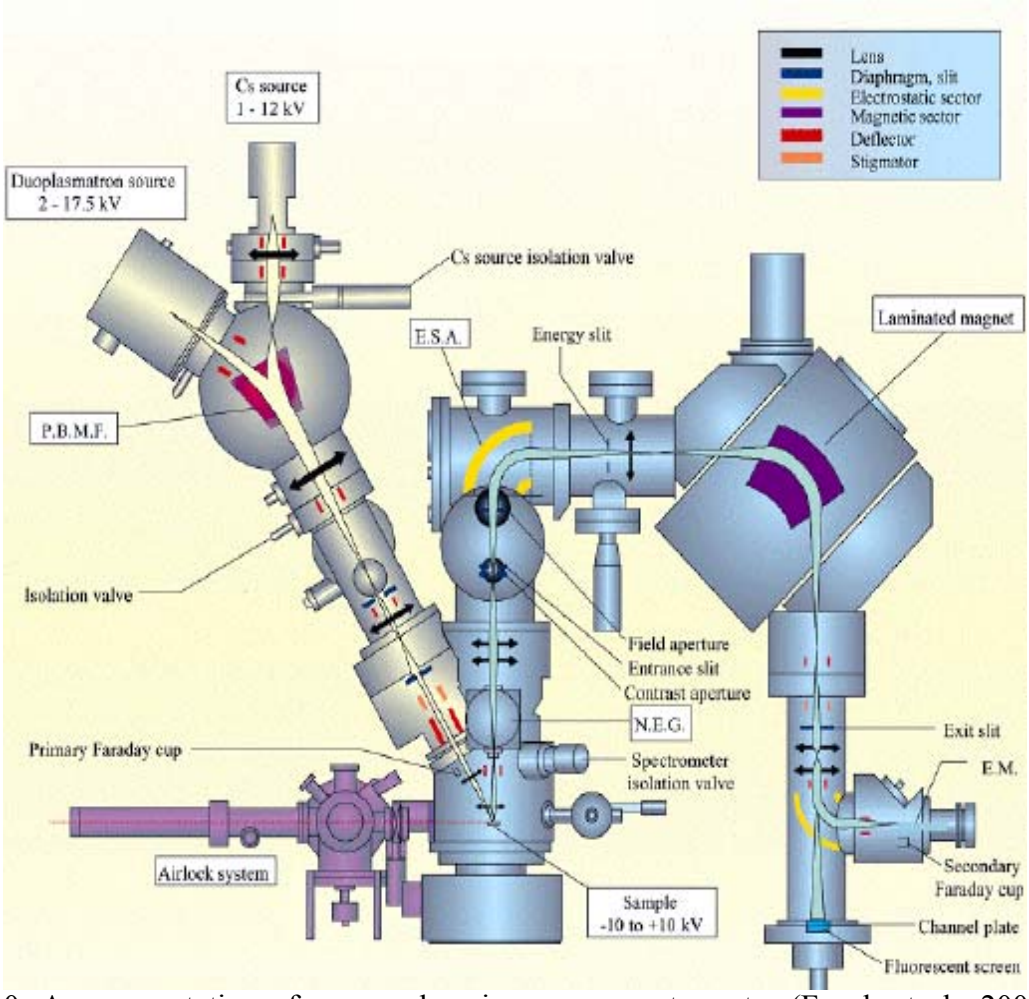

Figure 40. A representation of a secondary ion mass spectrometer (Fayek et al., 2005). The samples were placed in the airlock (purple) for at least four hours to reduce oxygen on the surface of the samples. The duoplasmatron source sends a beam of oxygen atoms, negative in this case, at the sample surface.

3.5.2 Methodology

Uranium minerals in the Pozos uranium anomaly were identified using EMPA. To prepare the samples for SIMS analysis, the carbon coat from the EMPA analysis was polished off and the samples were recoated with gold. Samples were placed in the vacuum chamber at least four hours before analysis to reduce oxygen buildup on the sample surface. The operating conditions for analysis for the Cameca IMS 7f SIMS (University of Manitoba) were a 5 nA diameter O^- beam with a current of 8000 volts, a mass resolution of 1400, and 100 cycles per analysis (modified from Fayek et al., 2002). The isotopes analyzed for were ^{230}Th, ^{234}U, ^{235}U, and ^{238}U.

The samples were analyzed in addition to the Topsham mine, Maine (TS-A) uraninite standard. The TS-A standard was chosen because it is a singular cube of uraninite, and is dated to 314±10 Ma (Fayek et al., 2006), which is old enough to be in secular equilibrium with respect to the $^{230}Th/^{234}U$ ratio. It also had the lowest amount of Pb of the three available standards, 3.1 wt% (Fayek et al., 2002). Reducing the amount of Pb was very important, because of a molecular interference with ^{230}Th. For example, $^{208}Pb+^{22}Na$ and $^{207}Pb+^{23}Na$ also make mass 230. These interferences are important when analyzing for ^{230}Th in young rocks, because decay of ^{238}U and its daughters will not have produced very much in a geologically short period of time, so its signal can be wiped out by interferences, leading to a $^{230}Th/^{234}U$ ratio at, or even above, unity. This makes the resulting age unreliable.

After analysis, the isotope pairs ($^{235}U/^{238}U$, $^{234}U/^{238}U$, and $^{230}Th/^{234}U$) were corrected using the TS-A standard. The uranium isotopes do not ionize equally, due to instrumental mass fractionation, so a correction needs to be made using the $^{235}U/^{238}U$ ratio. It is equal to 1/137.88 or 0.00725, and the difference between the true ratio and the $^{235}U/^{238}U$ ratio in the TS-A standard allowed a percent IMF per atomic mass unit (amu) to be calculated. %IMF/amu is calculated by:

$$\frac{\%IMF}{amu} = \frac{\frac{\left(^{235}U/^{238}U\right)_{obs} - \left(^{235}U/^{238}U\right)_{true}}{\left(^{235}U/^{238}U\right)_{true}} x100}{3amu}$$

where $(^{235}U/^{238}U)_{obs}$ is the measured ratio, $(^{235}U/^{238}U)_{true}$ is 0.00725, and amu is the difference between the isotope masses, in this case there are 3 amu, because there are 3 atomic mass units between ^{235}U and ^{238}U. The %IMF correction is applied to correct ^{234}U, but uses a 4 amu difference. The corrected ratios are presented in the following section.

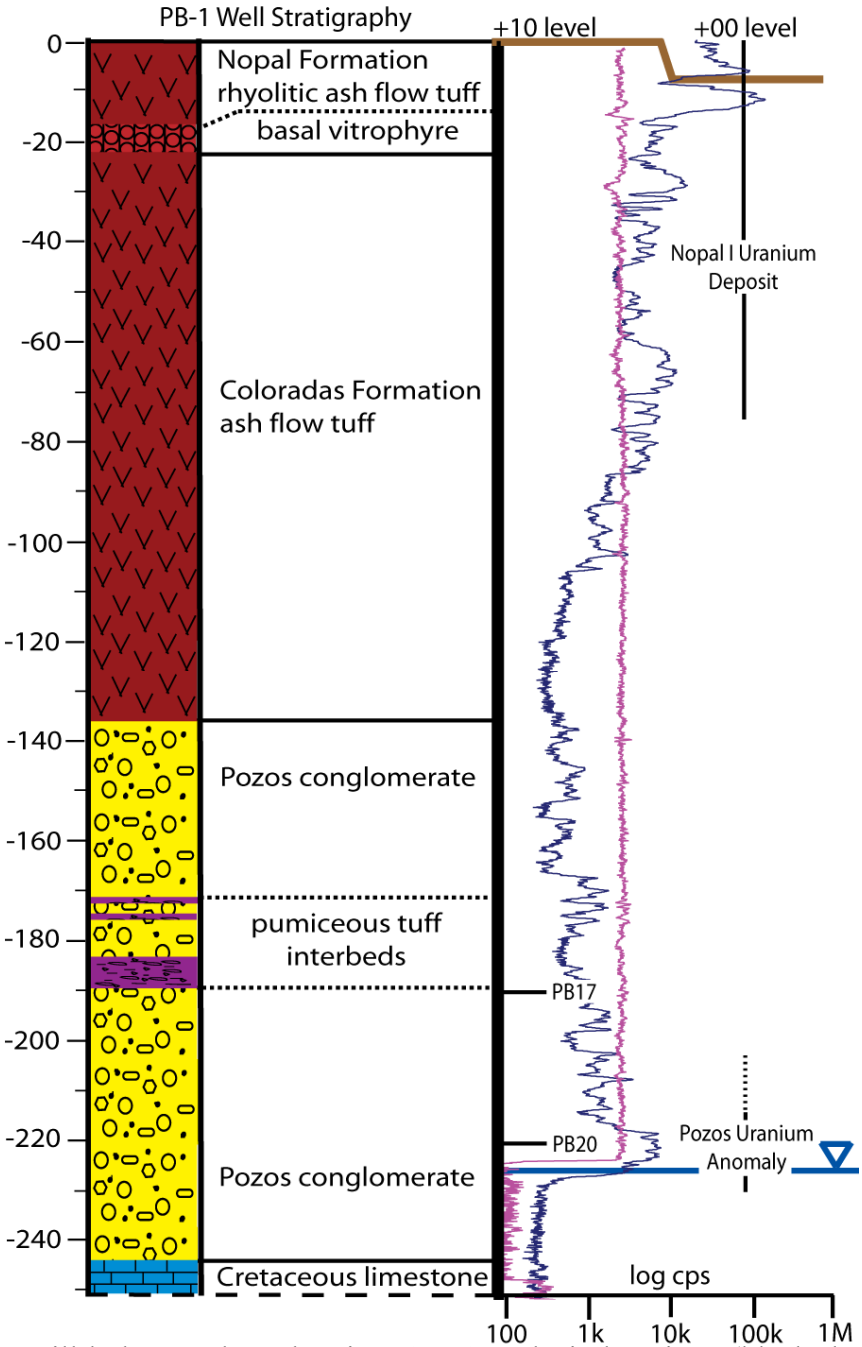

Figure 41. Drill-hole template showing SIMS analysis locations (black dashes) for age dating uranium minerals.

3.5.3 Results

Examples of SIMS analysis sites and their corresponding BSE images are given in Figure 42. The $^{230}Th/^{234}U$, $^{230}Th/^{238}U$, and $^{234}U/^{238}U$ disequilibrium ratios are listed in Table 8, and plotted in Figure 43. $^{230}Th/^{238}U$, which was not initially measured, but necessary for comparing to additional datasets, was calculated by multiplying the $^{230}Th/^{234}U$ and $^{234}U/^{238}U$ with each other. The $^{234}U/^{238}U$ ratio is commonly used in uranium-series disequilibrium plots, because it can indicate the presence of ^{234}U enrichment. This enrichment is usually caused by the preferential dissolution of ^{234}U over ^{238}U, due to the recoil effect when ^{238}U decays to ^{234}Th and breaks the crystal lattice and subsequent decay to ^{234}U, which is then "free" to mobilize when an aqueous fluid comes into contact with it.

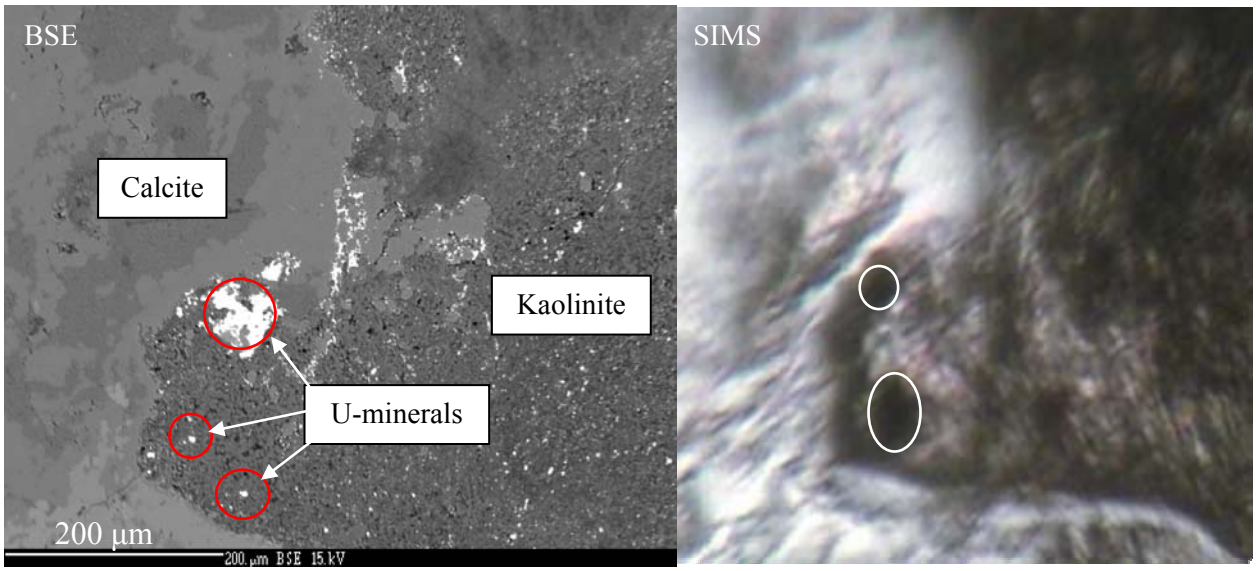

Figure 42. BSE (left) and SIMS (right) images from sample PB4009. The uranium minerals (red circles) were identified using the BSE image, because the SIMS camera resolution is much lower, as seen in comparing the images. The dark areas circled in white on the SIMS image are analysis points for the uranium minerals.

All $^{230}Th/^{234}U$ and $^{230}Th/^{238}U$ ratios are at or close to 1 (Table 8; Figure 43), which means the uranium minerals are in secular equilibrium and are older than 375 ka. This age is based on two separate locations from two different depths within the Pozos uranium anomy, and U-Pb

dating of uraninite in the Pozos uranium anomaly indicated that they were <1 Ma (Fayek et al., 2006; Levy et al., 2011). This supports the age of the uranium minerals to less than 1 Ma.

The U-series systematics of the Pozos uranium anomaly samples can be more robust in terms of defining open vs. closed system behavior over time by comparing $^{230}Th/^{234}U$, $^{230}Th/^{238}U$, and $^{234}U/^{238}U$ with each other.

The $^{234}U/^{238}U$ ratios are slightly deficient (less than unity), and are usually caused by preferential leaching of ^{234}U relative to ^{238}U, due to the alpha recoil process (Osmond and Ivanovich, 1992). An existing disequilibrium could add support to the 375 ka to 1 Ma age range for the uranium minerals, because ^{234}U will in grow to secular equilibrium with ^{238}U within 1.25 Ma in a closed system. Based on the <1 Ma U-Pb age from uraninite in the Pozos uranium anomaly (Fayek et al., 2006; Levy et al., 2011), this is a reasonable explanation. However, it is not most likely scenario as explained below.

Table 8. Results of SIMS U-series dating

Sample numbers		$^{230}Th/^{234}U$ ± % error	$^{230}Th/^{238}U$ ± % error	$^{234}U/^{238}U$ ± % error
PB17	PB4009-1a	0.996 ± 4.3	1.006 ± 4.3	1.010 ± 1.7
	PB4009-1b	1.072 ± 4.5	0.992 ± 4.5	0.925 ± 2.1
PB20	PB4052A-1	1.244 ± 23.6	1.013 ± 23.6	0.815 ± 6.3
	PB4052A-2	1.046 ± 15.6	0.905 ± 15.6	0.865 ± 4.1

The results from seepage water in the mine adit and groundwater measurements (Table 9) from Goldstein et al. (2010) and S. Goldstein (pers. comm.) and causes of disequilibrium are added to Figure 43 to illustrate the processes that may be active at Nopal I. The $^{234}U/^{238}U$ ratios from the seepage and adit waters (Table 9) are enriched in ^{234}U, so if these represent the source water for the Pozos uranium anomaly, uranium minerals formed within it should preserve the ^{234}U excesses. However, $^{234}U/^{238}U$ ratios in uranium minerals have a ^{234}U deficiency. A possible cause of this deficiency in Pozos uranium anomaly minerals would be a period of closed system behavior from 375 ka to 1 Ma, which would allow an ingrowth of ^{230}Th to secular equilibrium with ^{234}U. Then, a more recent period of open system behavior would allow

uranium remobilization and would cause a deficiency in $^{234}U/^{238}U$, but allow the $^{230}Th/^{234}U$ and $^{230}Th/^{238}U$ ratios to ingrow quickly back to secular equilibrium. Two possible ways ^{234}U is more easily leached than ^{238}U are: 1) alpha recoil, which makes ^{234}U more susceptible to leaching due to its radiation damaged site (e.g. Osmond and Ivanovich, 1992; Gascoyne et al., 2002); and 2) under reducing conditions, ^{234}U is more easily oxidized than ^{238}U, which increases the solubility of ^{234}U (e.g. Suksi and Rasilainen, 2000).

Table 9. Summary of data from adit and saturated zone samples (Goldstein et al., 2010; S. Goldstein, pers. comm.)

Sample location	Collection date	$^{234}U/^{238}U$	$^{230}Th/^{238}U$
Front of adit	7-Mar-01	1.023 ± 0.002	0.357 ± 0.002
	25-Feb-00	1.06 ± 0.001	0.078 ± 0.0005
	25-Feb-00	0.939 ± 0.002	0.009 ± 0.00006
	7-Mar-01	0.92 ± 0.004	0.158 ± 0.001
Middle of adit	25-Feb-00	1.177 ± 0.002	0.009 ± 0.0003
	7-Mar-01	1.173 ± 0.001	0.005 ± 0.00003
Back of adit	25-Feb-00	2.207 ± 0.006	0.033 ± 0.0001
	7-Mar-01	2.588 ± 0.005	0.958 ± 0.003
PB-1 and PB-2	2003-2006	1.005-1.090	0.000412-0.029
PB-3	2003-2006	1.36-1.97	0.00457

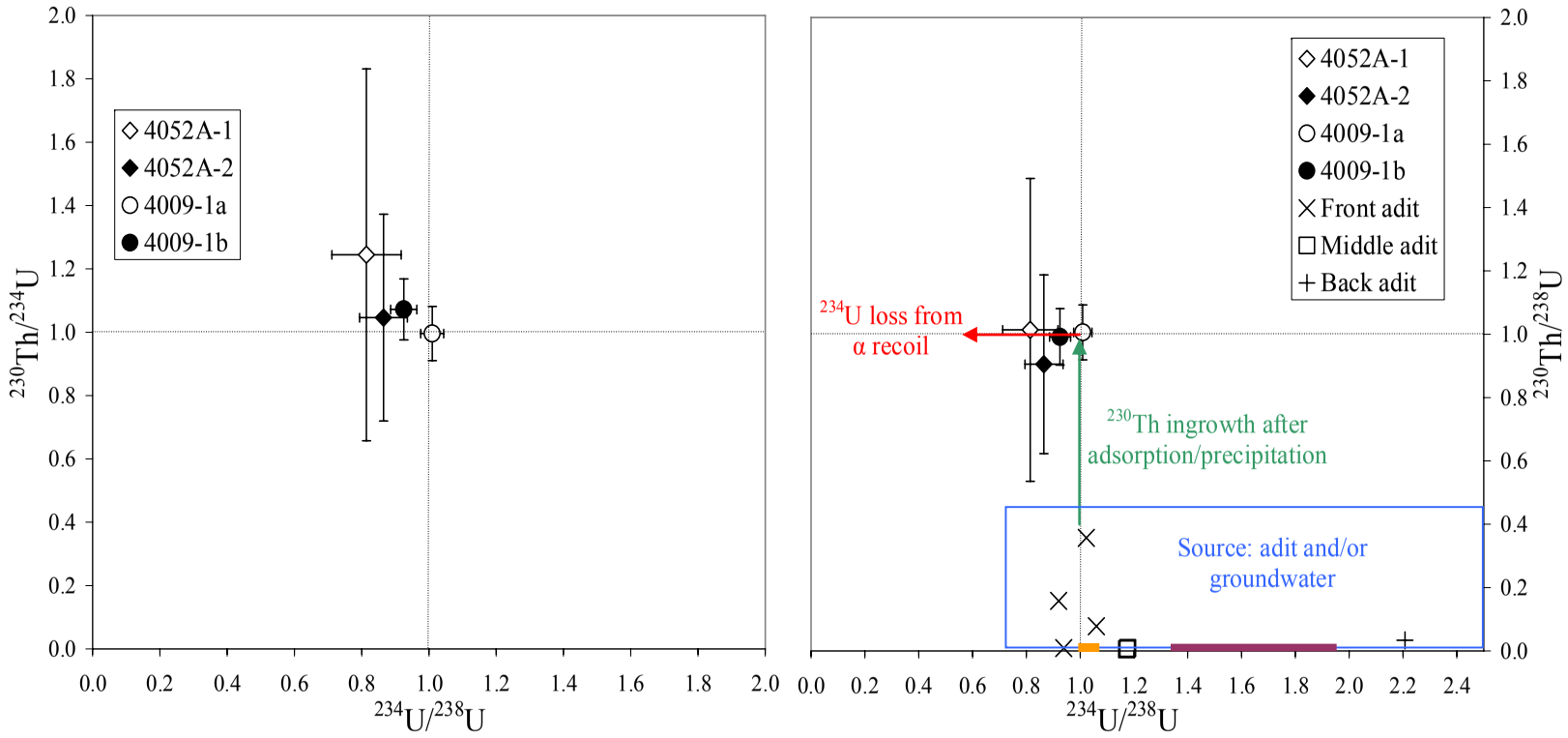

Figure 43. U-series ratios of PB4009 [PB17] (circles) and PB4052a [PB20] (diamonds) from the Pozos uranium anomaly. The $^{230}Th/^{234}U$ and $^{230}Th/^{238}U$ ratios are within error of unity, which means secular equilibrium for about 375 ka. The $^{234}U/^{238}U$ ratio shows a ^{234}U deficiency, which means that within the last 1.25 Ma, some remobilization of ^{234}U has occurred. These ratios indicate that a period of closed system behavior existed over 375 ka and was followed by a period of open system behavior for ^{234}U. The alpha recoil process allows ^{234}U to be remobilized at a higher rate than ^{238}U and thorium is generally insoluble, so ^{234}Th would not be affected.

The graph to the right includes data from Goldstein et al. (2010) and S. Goldstein (pers. comm.) from water collected in the Nopal I mine adit (symbols in key) and groundwater analyses (PB1-2, purple; PB3, orange). The blue area assumes adit water as a possible source or U-series water for the Pozos uranium anomaly. The green arrow represents the ingrowth of ^{230}Th relative to ^{234}U once uraninite is precipitated in the Pozos uranium anomaly reducing environment. The red arrow represents loss of ^{234}U relative to ^{238}U due to the alpha recoil process and could be from source water or later oxidation of the uraninite.

3.6 DISCUSSION

3.6.1 Paragenesis and zoning of the Nopal I uranium deposit

Analysis of the XRD, EMPA, multi-element geochemistry, and SIMS data allows for interpretation of the paragenesis of Nopal I uranium deposit as a source term for radionuclide migration. A flow chart of the paragenesis at Nopal I is provided to illustrate a complex history (Figure 44). Another conceptual model shows how the Pozos uranium anomaly formed, to help visualize the processes discusses in the following subsections (Figure 45). The Pozos uranium anomaly will serve as an example of a working geologic barrier to waste migration. The conditions that caused uranium to adsorb and precipitate will be discussed, because those conditions are an important question for future geologic storage sites. The data presented in the previous sections, in addition to prior studies, will be used to justify the paragenesis.

This study also proposes a model for the present configuration of the deposit. The chemical distribution of elements and mineralogy down the PB-1 core forms the basis for the zone boundaries (Figure 46). Five zones within the PB-1 core were proposed in the introduction and used to present the results of the XRD, EMPA, geochemistry, and SIMS. Zone 1 consists of the primary assemblage: quartz-pyrite-uraninite-ilmenite-kaolinite, and serves as the source term for radionuclides and other mobilized constituents in the PB-1 core. This zone exists in limited amounts preserved by silicification, and is otherwise oxidized. Zone 2 is oxidized area from the top of the core to approximately 75 m depth. Zone 3a is a redox transition zone from the base zone 2 to the top of the Pozos conglomerate (about 75 to 135 m). Zone 3b (about 135 to 180 m) is similar in characteristics to zone 3a, but the lithology change from tuff to conglomerate changes the mineralogy. Zone 4 is a reduced zone, also referred to as the Pozos uranium anomaly, which is within the Pozos down to the limestone basement contact (about 180 to 242 m). Finally, the Cretaceous limestone, which is the last unit in the PB-1 core serves as a boundary for this study. Each of these zones is discussed in greater detail in this section, especially in terms of radionuclide transport.

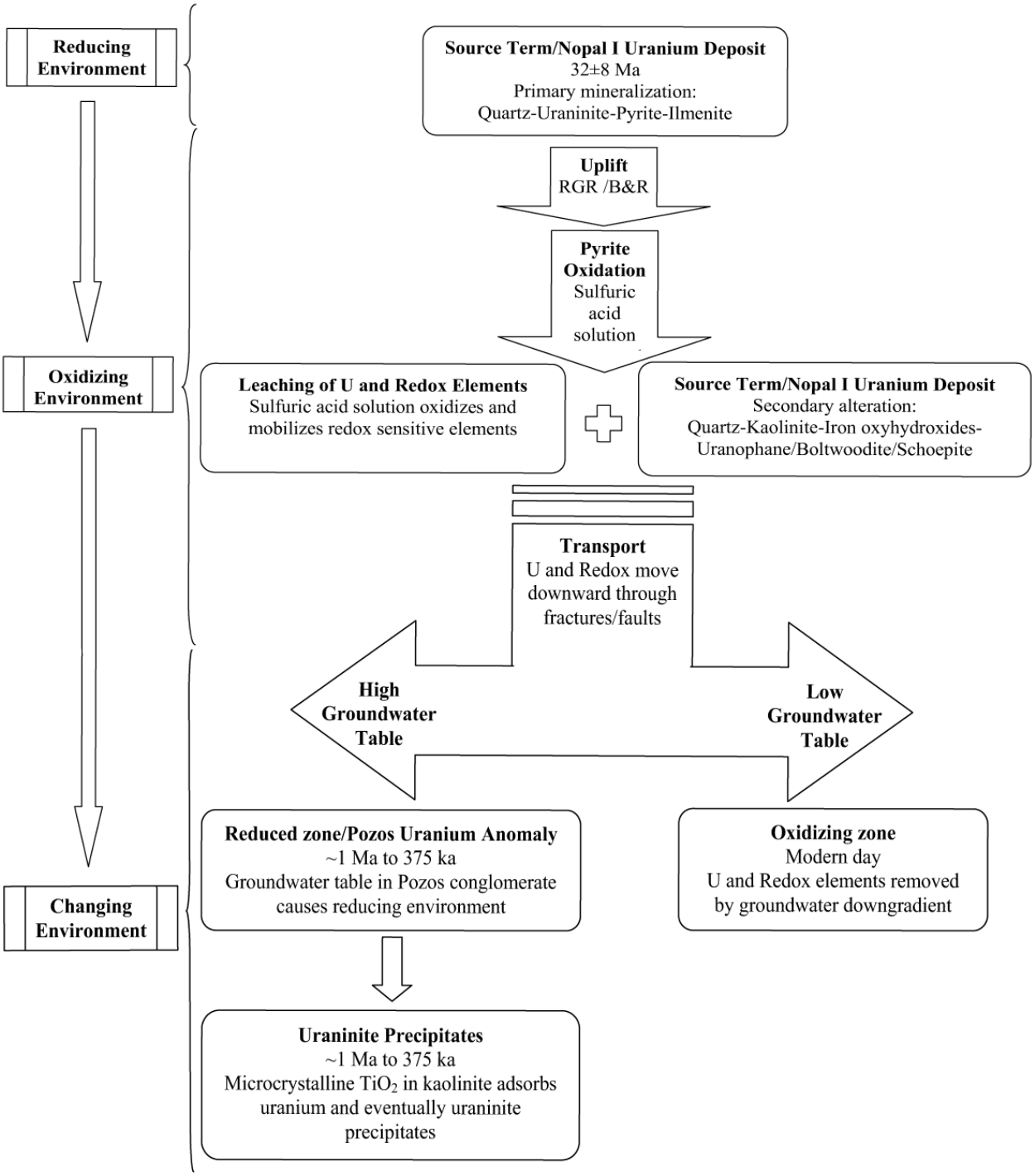

Figure 44. This flow chart illustrates the paragenesis of Nopal I from post-deposition of the Nopal I uranium deposit to the modern day. The generalized redox environment is described in the boxes on the left. The flowchart ends with two different redox condition end members, which are groundwater controlled. During periods of high groundwater, a reducing zone forms within the Pozos conglomerate, and the Pozos Uranium Anomaly is an example. Low groundwater table periods, like currently exist, act as an oxidizing environment. They do not preferentially adsorb or precipitate redox sensitive elements, like in the Pozos Uranium Anomaly example, so redox elements are removed from Nopal I through the groundwater down gradient.

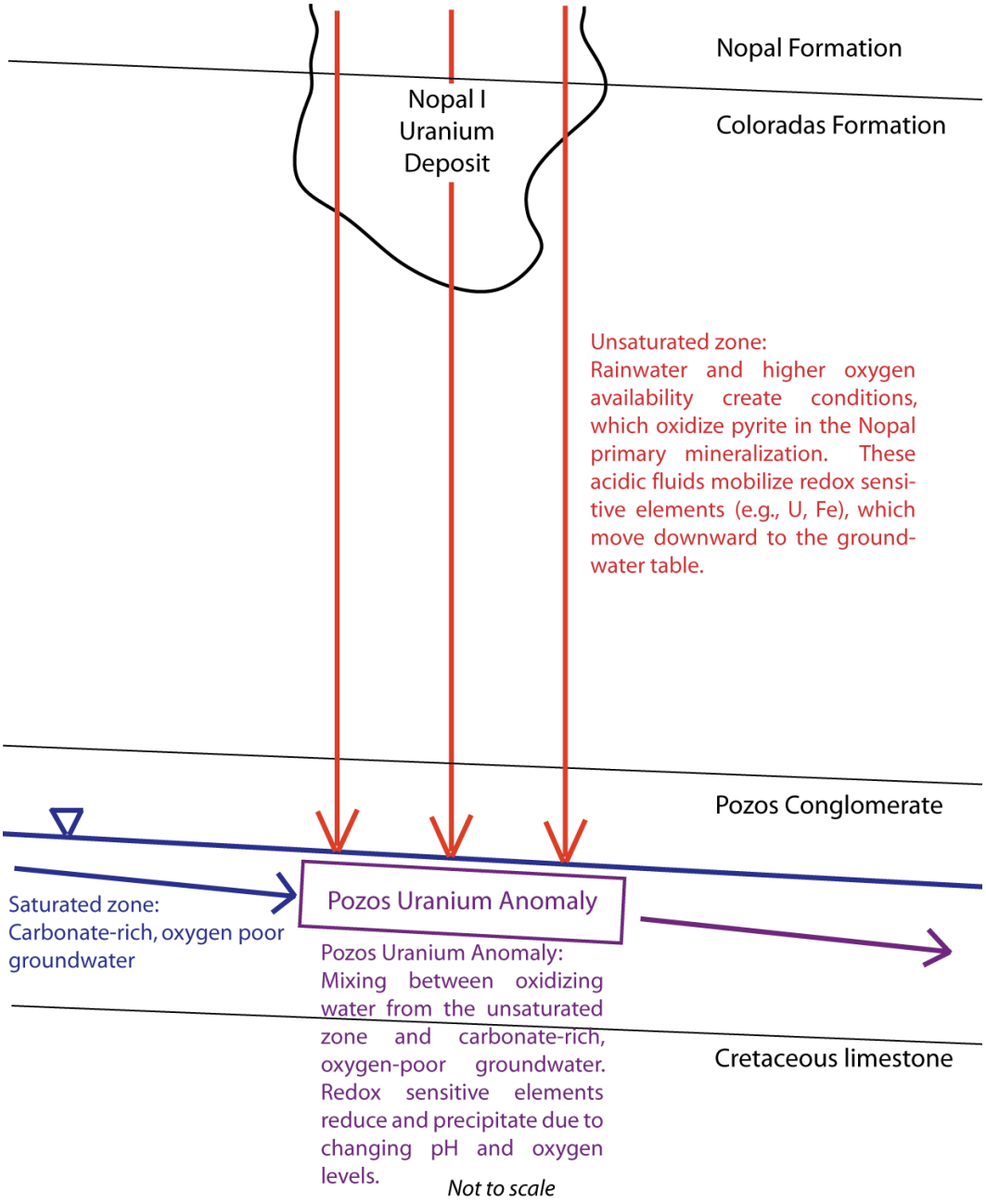

Figure 45. Conceptual model of the Pozos uranium anomaly. Rainwater percolating through the unsaturated zone has dissolved oxygen levels at near saturation. The pH decreases through pyrite oxidation and mobilizes redox sensitive elements. This solution travels downward to the water table, where it mixes with carbonate-rich, oxygen-poor groundwater. The increase in pH and decrease in oxygen saturation cause redox sensitive elements to reduce and adsorb onto clays and TiO_2 or directly precipitate in the Pozos uranium anomaly. This configuration lasted from 375 ka-1 Ma, based on uranium mineral ages. Currently, the water table is lower, close to the contact between the Pozos Conglomerate and the Cretaceous limestone. U-series disequilibria indicate that leaching of uranium from the Pozos uranium anomaly has occurred within the last 375 ka.

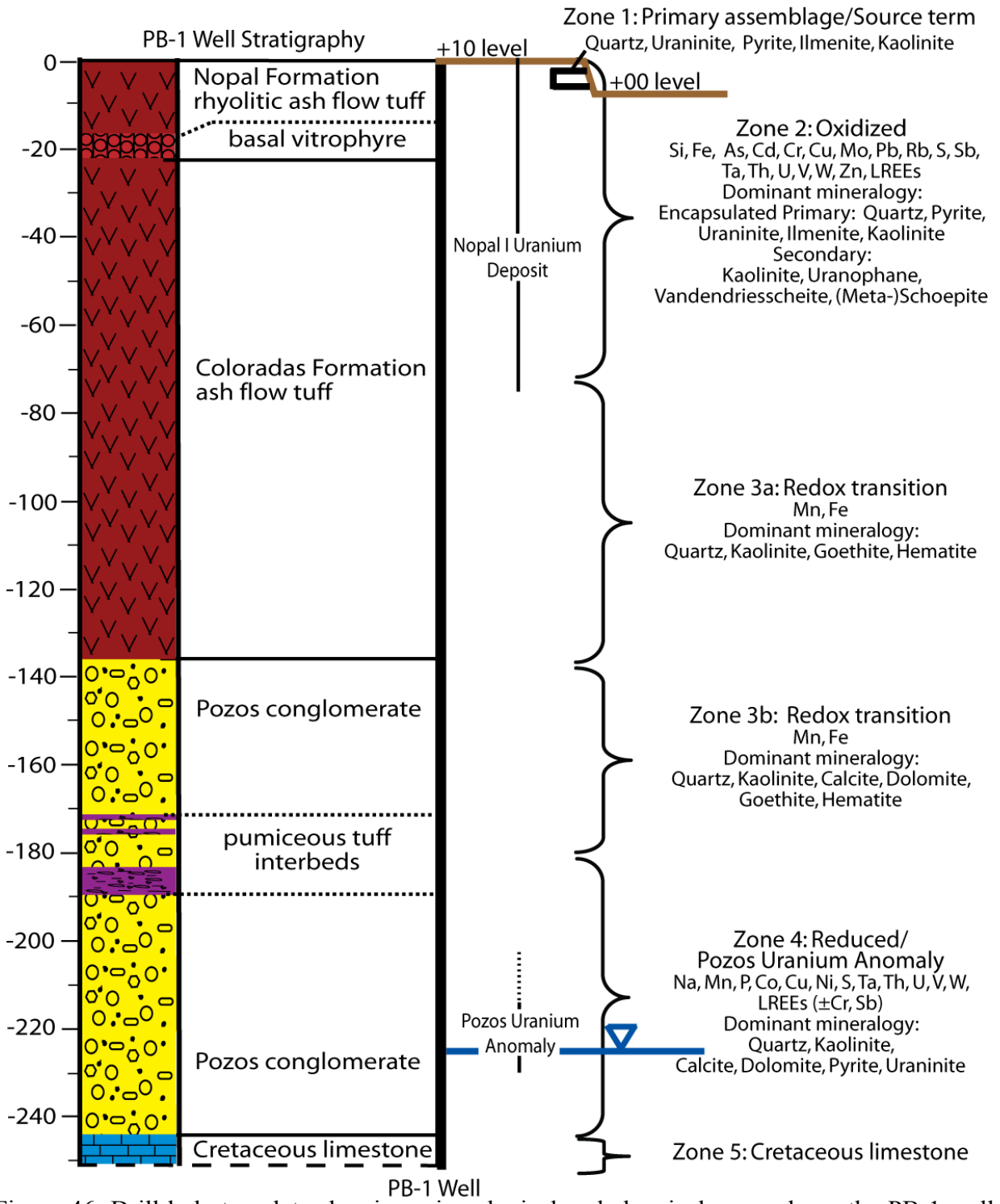

Figure 46. Drill-hole template showing mineralogical and chemical zones down the PB-1 well. Elements enriched in each zone are shown. Note that the redox transition zones are deficient in most of the elements relative to the oxidized and reduced zones.

Zone 1: Primary Nopal I uranium mineralization/Source term

In this section, the characteristics of zone 1 are presented in terms of formation temperature, geochemical, and mineralogical relationships. Then potential mechanisms for the uranium mineralization are discussed.

The primary mineralization, quartz-pyrite-uraninite-ilmenite-kaolinite, of the Nopal I uranium deposit has been described previously and is considered the source term for nuclear waste transport by this study. Primary uraninite from the mineralized zone at Nopal I is dated to 32±8 Ma (Fayek et al., 2006). Aniel and Leroy (1985) described two stages of primary mineralization: an earlier ilmenite-uraninite stage and a later pitchblende-pyrite stage. Pearcy et al. (1994) reported euhedral and granular uraninite (or pitchblende), typically intergrown with kaolinite and pyrite, with later stage colloform uraninite, which is free of discernable, primary intergrowths. Based on textural relationships, euhedral uraninite is reported to replace syngenetic pyrite and fills intergranular pores within silicified breccia fragments. Pearcy et al. (1994) appears to have grouped the primary mineralization into what would be equivalent to the uraninite-pyrite stage of Aniel and Leroy (1985). This study uses a modified primary assemblage of quartz-uraninite-pyrite-ilmenite-kaolinite based on Aniel and Leroy (1985) and Pearcy et al. (1994).

Fayek et al. (2006) studied $\delta^{18}O$ values in uraninite from Nopal I and estimated meteoric equilibration temperatures of 45-55°C based on uraninite equilibration with local meteoric water ($\delta^{18}O$=-9‰) in zones 2 and 4. Calas et al. (2008) described $\delta^{18}O$ and δD values of kaolinite that indicated a high water/rock interaction and low temperature (50-75°C) epithermal mineralization from meteoric fluids being recycled at depth. Unaltered Cretaceous limestone supports these low temperature results.

The primary uranium mineralization is associated with a silicification event (Pearcy et al., 1994). Silicification is evident in samples analyzed by this study, both chemically and texturally. As shown previously in the multi-element chemistry section, samples from the Nopal and Coloradas Formations can have >75 wt% SiO_2 (Figure 26), which is indicative of silicification.

Goodell (1985) described a mineralization associated with intense silicification at Nopal I and described an associated leaching of K_2O (Figure 28). Leaching of K_2O is also true of samples from this study, which only has one sample concentration (PB772 [PB1], 6.07 wt %) equivalent to that of the fresh rock, whereas the remaining samples are only a few weight percent.

Evidence of silicification is important to this study, because uraninite at Nopal I has only been observed in strongly silicified breccia (Pearcy et al., 1994). Based on the relationships between uraninite, euhedral quartz and silicified host tuff, Pearcy et al. (1994) suggested that silicification of the tuff occurred during the primary mineralization event. The silicification encapsulated the quartz-uraninite-pyrite-ilmenite-kaolinite assemblage, which preserved the assemblage during oxidation of the Nopal I uranium deposit. BSE images of uranium minerals from this study in the Nopal and Coloradas Formations are almost always surrounded by quartz (see Figure 14, Figure 17, Table 5). This indicates encapsulated uraninite is more resistant than unencapsulated uraninite to oxidation and mobilization that occurred later at Nopal I.

The presence of syngenetic pyrite is an interesting observation by Pearcy et al. (1994). This means that the pyrite was precipitated during uranium mineralization and is evidence of a reducing environment. Groundwater becomes increasingly stagnant with depth (e.g., Suksi, 2001; Tullborg et al., 2003), which acts as a reducing environment. Sulfur and uranium are both redox sensitive elements, and whether or not the groundwater or devitrification or a mixture of both were the source of the elements, a reducing zone in the groundwater would be a favorable environment for their precipitation. Goodell (1981) suggested mineral deposition was caused by reducing groundwaters derived from organic or pyrite-rich basin sediments. The age of the primary mineralization at 32±8 Ma would indicate that the deposit formed prior to subsequent down dropping of the water table through Basin and Range and/or Rio Grande Rift tectonism.

Ilmenite and/or pyrite could provide a surface for adsorbing uranium and subsequent precipitation of uraninite. Iron-titanium oxides are observed to be replaced by FeS_2 (e.g., pyrite) in roll-type uranium deposits from south Texas (Reynolds et al., 1977). The expelled titanium is

reprecipitated as TiO_2 after replacement in and around the relict iron-titanium oxides and adsorbs uranium. At Nopal I, this textural relationship is observed (Levy et al., 2011), and the association of uranium and titanium could be explained by this alteration scenario.

Ilmenite-uraninite phases have been described previously in other areas. Zielinski (1978) observed a relationship between Fe-Ti-Mn oxides in rhyolites of the western United States. Lindroos and Smellie (1979) and Smellie (1982) reported that uranium released from devitrification of ignimbrites in Duoblon, Sweden precipitated along ilmenite and titanomagnetite contacts as fine-grained uraninite, or pitchblende and destabilization of these phases led to urano-titanate complexes. Caruso et al. (1982) also observed deposition of pitchblende in ilmenite and hematized feldspar microfractures in the Geevor Tin Mine, Cornwall. A low temperature coffinite-TiO_2-quartz assemblage in the Lower Old Red Sandstone sediments, Scotland, was attributed to adsorption of uranium by altered titanium minerals (e.g., ilmenite) prior to precipitation of the uranium minerals (Pointer et al., 1989). The Dalmatov uranium ores of western Siberia resulted from iron leaching of ilmenite, which were able to adsorb uranium from groundwater and precipitate pitchblende (Vinokurov and Nesterova, 2010). At the Ambassador deposit, Gunbarrel Basin, in western Australia, Douglas et al. (2011) reports uranium is associated with U- and Ti-silicate/oxide minerals, in addition suggesting adsorption of uranium by pyrite and other sulfide species.

A relationship between pyrite and uraninite has also been reported. Stewart et al. (2000) examined microscopically pre- and post-leach roll-front uranium deposits and found that uranium is widely associated with pyrite and pyrite partially dissolved by a mine leaching solution. At Fernald, a DOE contaminated site in Ohio, uranium is sometimes concentrated in overgrowths on earlier pyrite grains suggesting precipitation of uranium through reduction (Bryan et al., 2004). Pyrite is known to reduce U(VI) to U(IV), which decreases solubility and increases adsorption (Scism, 2006; Scott et al., 2007; Qafoku et al., 2009).

Zone 2: Oxidized primary uranium assemblage/Source term (+10 to -75 m)

In this section, zone 2, the mechanism for oxidation of the deposit is discussed geochemically. It uses zone 1 as the source and target of oxidation and explains what happened under this assumption. Additional results from the XRD and multi-element chemistry sections are used to support and characterize zone 2.

Following the primary mineralization (zone 1) in a reducing environment, an oxidizing environment is necessary to mobilize uranium and other redox elements. XRD analysis of adit samples (zone 1) showed both quadrivalent and hexavalent uranium minerals (see Figure 7), which supports previous analyses (e.g., Ildefonse et al., 1990b; Pearcy et al., 1994) and the presence of oxidizing conditions favorable for uranium migration. One major oxidation event, which mobilized uranium and reprecipitated it as uranophane, occurred about 3-3.1 Ma (Pickett and Murphy, 1997; Fayek et al., 2006). Previous work has identified numerous episodes of uranium oxidation less than 1 Ma old using fracture minerals, caliche and opal from the E-W fracture zone (Wong, 1994; Pearcy et al., 1995; Wong et al., 1996, 1999; Murrell et al., 2002; Pickett and Murphy, 2002). In zone 1, another uraninite mineralization event occurred at ~1.6 Ma, and mineral ages from the margins of the deposit suggested subsequent oxidizing events that precipitated schoepite (~85 ka) and boltwoodite (~41 ka) (Fayek et al., 2006; Levy et al., 2011).

One way to create the oxidizing environment is to uplift the deposit above the groundwater table (Murphy and Codell, 1999). Nopal I is exposed to the surface along the eastern face of a horst block (Goodell, 1981). Once the Nopal I uranium deposit is in an oxidizing environment, the pyrite in the primary quartz-uraninite-pyrite-ilmenite-kaolinite assemblage would oxidize, producing a sulfuric acid solution (Pearcy et al., 1994).

Assuming sulfuric acid is the mechanism for oxidation, it is possible to use Eh-pH diagrams to construct the environment. Eh-pH diagrams (Brookins, 1988) were used to determine the potential oxidation system with species selected because of they include significant and variable mineralogy and geochemical assemblages described in prior sections (Figure 47). Uranium Eh-pH diagrams (Figure 47A and D) were selected, because U is the focus

of this study, but also because it is sensitive to changing redox conditions. Based on the XRD results, both quad- and hexavalent uranium minerals are present in the Nopal I uranium deposit and uranium concentration decreases with depth, then increases in the Pozos uranium anomaly. The U-C-O-H Eh-pH diagram shows an example of a stability field where uranium ore, in this case, the primary assemblage—quartz-uraninite-pyrite-ilmenite-kaolinite—is found. Iron and sulfur, represented by the Fe-S-O-H Eh-pH diagram (Figure 47B), were selected, because pyrite oxidation would be the source of both iron and sulfur geochemical changes throughout the PB-1 core. The iron oxyhydroxides identified in the XRD and BSE sections show that not all iron was mobilized. Finally, the generic Eh-pH diagram for water (Figure 47C) is used to show the type of environments that are possible in natural waters, e.g., the mine water region-number 1.

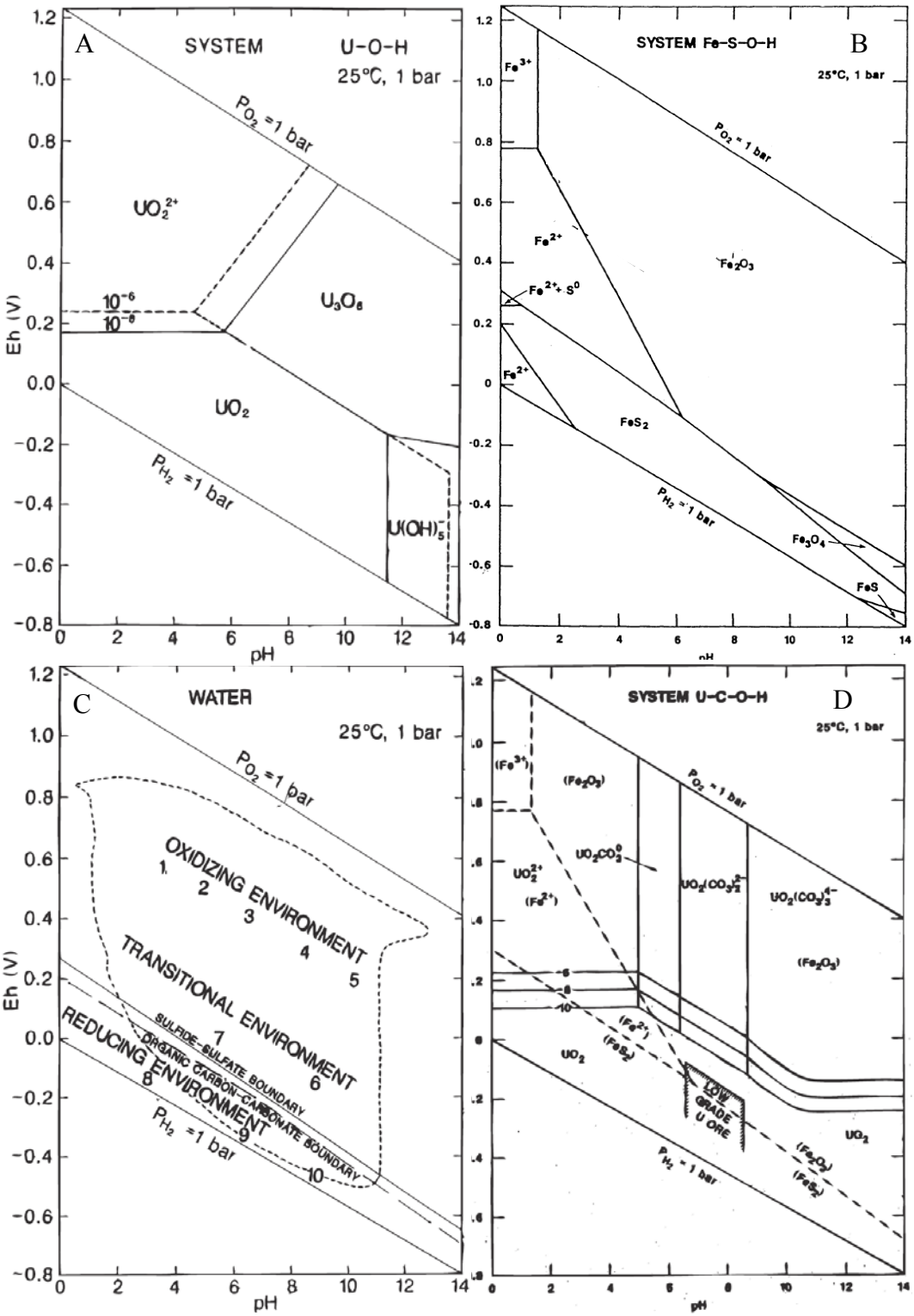

Figure 47. Eh-pH diagrams at 25°C and 1 bar (Brookins, 1988). A) U-O-H; B) Fe-S-O-H; C) Natural waters with a dashed line representing the range of natural Eh-pH water measurements reported by Bass Becking et al. (1960). The number 1 represents mine waters. D) U-C-O-H showing the stability field for low grade uranium ore.

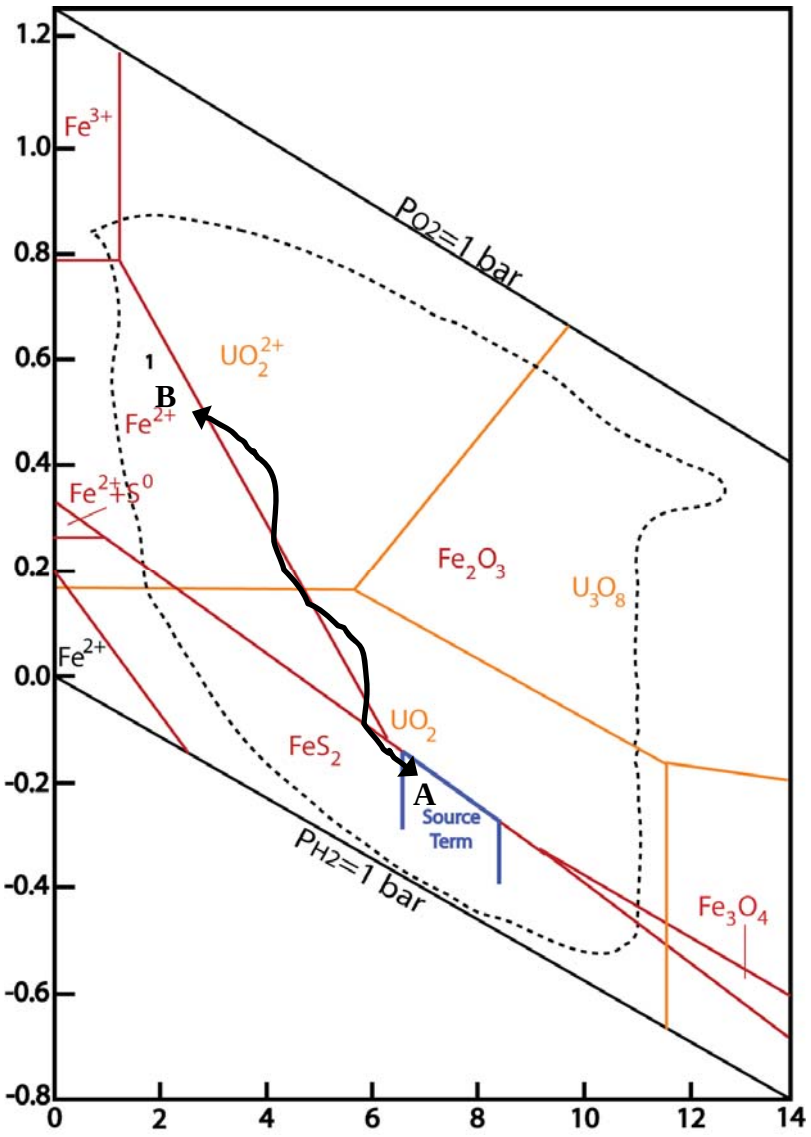

Figure 48. This Eh-pH diagram was constructed using Eh-pH diagrams in Figure 47 (modified from Brookins, 1988; Bass Becking et al., 1960). Species expected to have a significant influence of the chemistry at Nopal I were superimposed on each other; the U-O-H system is in yellow, and the Fe-S-O-H system is in red. **A** is the chemical stability region for the source term, the primary quartz-uraninite-pyrite-ilmenite-kaolinite assemblage, zone 1. The arrow from **A** to **B** is a path for the oxidized species (zone 2), and at location **B**, U, Fe, and S should be in solution (zone 3). The number **1** and dashed line are taken from Figure 47C and represent mine water and the Eh-pH range of natural waters, respectively. Finally, the arrow from **B** to **A** represents a path for eventual reduction and precipitation of species that forms the Pozos uranium anomaly at **A** (zone 4).The source term (blue) is taken from Figure 47D and represents the Nopal I uranium deposit and Pozos uranium anomaly field.

These Eh-pH diagrams were also used to construct a paragenesis on the Eh-pH diagram (Figure 48). The location **A** is located in the stability field for the primary assemblage, quartz-uraninite-pyrite-ilmenite-kaolinite, which is the starting point for mobilizing the important species: U, Fe, and S. An arrow from **A** to **B** is the path where those species are oxidized due to sulfuric acid produced by oxidizing pyrite, and eventually end up at **B,** where they are all expected to be in solution with each other. The majority of the species expected to be in solution are within the Eh-pH range of natural waters (Bass Becking et al., 1960) and the mine water region denoted by the number **1**.

Zone 2 has higher concentrations of Fe_2O_3 (Figure 27), K_2O (Figure 28), Na_2O, P_2O_5, As, Cd, Cr, Cu, Mo, Pb, Rb, S (Figure 29), Sb, Ta, Th, U (Figure 30), V, W, Zn, and the light REEs compared to the zones 3a and 3b. They monotonically decrease through zone 2, meaning they decrease in concentration with increasing depth down the PB-1 core. Several of these species, i.e. Fe, S, U, and chalcophile elements, are redox sensitive. These would be oxidized and mobilized by the sulfuric acid discussed above. Adit infiltration water and groundwater from PB-1 contains these elements in solution, which suggests an oxidizing environment still exists (Goldstein et al., 2010; Rearick et al., unpublished).

The presence of iron oxyhydroxides after pyrite is also indicative of an oxidizing environment (ex. Figure 22). Based on this mineralogical change and iron and sulfur concentrations (Figure 27and Figure 29, respectively) described in previous sections, iron and sulfur are soluble, because pyrite has been leached and formed iron oxyhydroxides as relict pyrite and is also found as massive fracture fillings. Previous work (Aniel and Leroy, 1985; Ildefonse et al., 1990b; Pearcy et al., 1994) has also described this pyrite leaching. While the pyrite was leached, the iron may have remained in the oxidized zone while the sulfur was preferentially removed. The presence of iron oxyhydroxides in relict pyrite shapes supports this hypothesis. Ilmenite is also altered, because many of the uranium mineral analyses from the

oxidized zone have titanium (see Table 4), and the concentration of titanium at Nopal I increases with depth (Figure 32).

Sulfur (Figure 29) follows the same patterns as the other redox sensitive elements (see figures in section 3.3), and is evidence for changing redox conditions. It exhibits the strongest evidence of zones within the PB-1 core. Previously reported values by Goodell (1985) for sulfur in fresh rock from the base of the Nopal Formation, also known as the vitrophyre, are 363±226 ppm (~0.01 to 0.06 wt % S), which is consistent with the range of values in zone 3. The maximum value from the multi-element chemistry in zone 2 is 0.24 wt % sulfur (PB798 [PB5]), which is much higher than the fresh rock. This is still a significant amount of sulfur, even after leaching.

Zone 3: Redox transition zone (-75 to -180 m)

The geochemical and mineralogical attributes of zone 3 are discussed. The reasoning for splitting zone 3 into two parts: 3a and 3b, is integrated into the discussion.

The transition zone is so named, because some, but not all redox sensitive elements begin to accumulate in this zone compared to zones 2 above and 4 below. The main mineralization at Nopal I (Figure 5) extends down to about 75 m depth, with the highest concentration of uranium only down to about 50 m. This corresponds well to the decrease in redox zone elements and the start of the transition zone.

Only two elements, iron (Figure 27) and manganese, are enriched in this zone. In zone 2 above, these elements decrease in concentration with depth, but then increase again in zone 3, unlike the other redox elements described in the previous section. The reason for this increase is unknown, but changes in the redox environment or saturation could cause those elements to adsorb or precipitate.

Zone 3 was split into two subzones to account for the lithologic change from Coloradas tuff (zone 3a) to Pozos conglomerate (zone 3b). The Pozos conglomerate contains fragments of both tuff and carbonates, and the carbonates make the geochemistry of this unit radically

different, especially in terms of calcium and magnesium concentration. It is also different from zone 4 samples (also in the Pozos conglomerate), and closer to zone 3a in characteristics, even though there is only one sample to make this determination. Levy et al. (2011) reports a downward transition of rare to common sulfide preservation at 180 m (zone 4), whereas iron oxyhydroxides are more common above this depth (zone 3b), which supports a separate zone 3b.

Zone 4: Reduced zone/Pozos uranium anomaly (-180 to -242 m)

In this section, the characterization of the Pozos uranium anomaly is described. Geochemical, mineralogical, and U-series age dating provide evidence for uranium mineral precipitation much later than the Nopal I primary mineralization.

Zone 4 makes up at least the bottom 50 m of the Pozos conglomerate, which is termed the Pozos uranium anomaly. It was initially investigated because a radioactive hotspot was identified from the PB-1 gamma log (Figure 4). There were three possible reasons for its presence: 1) another primary uranium mineralization; 2) a secondary deposition from remobilized uranium; and 3) efflorescence or a capillary fringe of uranium from the groundwater. By age dating the uranium minerals from this zone to less than 1 Ma (Fayek et al., 2006; Levy et al., 2011) and greater than >375 ka (U-series dating) and the evidence presented in the rest of this section, uranium remobilization and subsequent precipitation in a reducing environment is the best explanation.

The difference in oxygen concentration between the unsaturated zone (zones 1-3b) and the saturated zones (zones 4-5) is one possible mechanism for reduction in the Pozos uranium anomaly. Generally dissolved oxygen in water moving through the unsaturated zone is considered at near air saturation, but decreases below the water table, where it is no longer exchangeable with air. The mobility of redox sensitive elements, including radionuclides, in groundwater is a critical parameter in controlling their solubility (e.g., Robertson, 1975; Holloway et al., 1982; White et al., 1990). Decreased concentrations of several elements in the

unsaturated zone [Na, Mn, P, Co, Cu, Ni, S, Ta, Th, U, V, W, and light REEs (±Cr, Sb)] are higher in the reduced zone of the Pozos uranium anomaly.

Many of these elements are commonly associated with one another in other types of uranium deposits. Roll-front and tabular sandstone deposits contain significant concentrations of U, V, Cu, Ag, Se, and Mo, along with varied amounts of Cr, Pb, Zn, As, Co, and Ni (Granger and Warren, 1974; Rackley, 1976; Spirakis, 1996; Min et al., 2005; Guilbert and Park, 2007; Davis and Curtis, 2007). In a study of unconformity-type deposits in the Athabasca Basin, Canada, these deposits exhibit the same mineralogical and geochemical features as traditional sedimentary roll-front deposits (Mercadier et al., 2011). U, Fe, Ca, Pb, S, REEs, V, Y, W, Mo, and Se were affected by changing redox conditions related to cold (<50°C) and late meteoric fluid infiltration (Mercadier et al., 2011). Kotzer and Kyser (1995) reported U associated with K, Mg, Ca, B, Ni, Co, As, Cu, and Fe in the Athabasca Basin. Trace elements observed in Athabasca sandstone-hosted mineralization are Ag, As, Au, Co, Cu, Mo, Ni, Pb, platinum-group elements, Se, and Zn (Thomas et al., 1998; Jefferson et al. 2007; Kyser and Cuney, 2008).

The source of uranium in the Pozos uranium anomaly is most likely the Nopal I mineralization (zone 1), which is supported by the lack of redox sensitive elements in zone 3 of the core between the Nopal I uranium mineralization and the higher concentration of redox sensitive elements leached from the Nopal I uranium mineralization in the Pozos uranium anomaly (Figure 30). Mixing this oxidizing water with a low oxygenated groundwater could cause reduction of some elements. A higher groundwater table that rises into the Pozos conglomerate, would create the necessary environment for precipitation. Another possibility is that higher groundwater levels in the past caused uranium to precipitate directly from the groundwater into the Pozos conglomerate. High levels of TiO_2 and kaolinite, sulfur, and/or organic material (Fayek, pers. comm.; Levy et al., 2011) could act as adsorbers.

Fayek et al. (2006) reported $\delta^{18}O$ values in uraninite from Nopal I and estimated meteoric equilibration temperatures of 10-20°C for uraninite in the Pozos conglomerate; whereas, the

reported values in the primary uraninite mineralization are 45-55°C. The lower mineralization temperature supports a different mineralization for the Pozos uranium anomaly. The "cold" fluids (10-20°C) still allow mobilization of uranium and other elements as described in the Athabasca basin (Mercadier et al., 2011). A reducing environment, which is geochemically similar to processes that occur in roll-front or unconformity-type uranium deposits, that allows adsorption and/or precipitation of uranium and other redox sensitive elements (e.g., Co, Cu, Ni, LREEs) could create the Pozos uranium anomaly.

The presence of pyrite from XRD and EMPA analyses further supports a reducing zone in the Pozos uranium anomaly, because pyrite primary to the zone would have easily weathered during the fluvial deposition of the Pozos conglomerate. Instead, later precipitation from iron and sulfur rich fluids is a better explanation. Secondary precipitation of pyrite is possible at low-temperature (<100°C) through abiotic (Schoonen and Barnes, 1991a,b) and biotic means (Donald and Southam, 1999). The uraninite-pyrite association has been described previously for the Nopal I mineralization (Aniel and Leroy, 1985; Ildefonse et al., 1990b; Pearcy et al., 1994); however, pyrite may have a role in the Pozos uranium anomaly as an uranium adsorber (Stewart et al., 2000; Scism, 2006; Scott et al., 2007; Qafoku et al., 2009).

The Pozos uranium anomaly has the most applicability to geologic storage of nuclear waste. The quartz-uraninite-pyrite-ilmenite-kaolinite primary assemblage would act as the source term, which releases radionuclides, such as uranium, in an oxidizing environment. The lack of redox sensitive elements, like uranium, in the area between the oxidizing zone or source term and the reduced zone, means that unique conditions existed to adsorb and precipitate uranium to form the Pozos uranium anomaly. These factors are further described in section 3.6.7.

The Pozos uranium anomaly is best described in terms of a changing redox environment (see Figure 48). Zone 1, the primary mineral assemblage, has been leaching for several million years, as evidenced by the deposit formation age (32±8 Ma) and younger secondary uranium

mineral ages (e.g., Pearcy et al., 1994; Pickett and Murphy, 1998; Fayek et al., 2006). Groundwater and seepage analyses from the Nopal I adit, PB wells (Appendix G), and nearby storage tanks show leaching of U and other redox sensitive elements (e.g., Fe, Mn, S) continues to the present day. The pH of the seepage and groundwater may not be the same as presently measured, because most of the pyrite present in the Nopal I mineralization that would serve as a source of acid has been leached away.

The pH of the water moving through the Nopal I mineralization could vary significantly over time. Caliche is present at Nopal I at the surface, so rainwater at the surface would initially be neutral to basic. Water percolating through the unsaturated zone would be at near-saturation with respect to dissolved oxygen, which would create an oxidizing fluid. This water would oxidize pyrite and become acidic. The caliche and/or slow rate of pyrite oxidation (over millions of years) would mean a less acidic pH. However, the presence of jarosite, which forms in highly acid and oxidizing conditions (Stoffregen, 1993; Rye and Alpers, 1997; Lueth et al., 2005), supports an oxidizing and acidic environment existed in the past. In either scenario, redox sensitive elements (e.g., U, Fe, Mn, S) would have increased solubility.

The oxic, acidic water then moves downward to the water table, where it mixes with relatively reducing groundwater. It could also be buffered by carbonates in the Pozos conglomerate. The saturated zone, from at least 375 ka-1 Ma, may have been higher (~180 m depth) compared to the present (~220 m depth) in the Pozos conglomerate. Liesegang bands of iron observed in fractures between 173-175 m within the Pozos conglomerate formed when coprecipitating ions interdiffused in a porous rock and the alternating bands, usually iron oxide and iron oxyhydroxide, result from the reaction of oxygenated groundwater with soluble iron (Levy et al., 2011), which could be evidence of this mixing. The changing redox conditions would cause decreased solubilities in many elements and cause precipitation in zone 4. Uranium is one example (Figure 30) of higher concentration in the Pozos uranium anomaly.

There are decreased concentrations of Fe (Figure 27) and Mn (Figure 31) in zone 4 compared to zones 1-3, even though it would be precipitating due to the changing redox conditions. The concentration of S (Figure 29) is higher in zone 4, but S may be a rate limiting concentration with respect to Fe and Mn precipitation. If S concentration was higher, Fe and Mn would be completely reduced, but they are present in the groundwater. The presence of euhedral pyrite (see zone 4, Figure 18) in zone 4 supports this hypothesis, but without knowing the age of the pyrite, it is hard to make definitive statements about how it formed: 1) in association with the Nopal I primary mineralization or 2) precipitation in the reducing Pozos uranium anomaly 375 ka-1 Ma. The presence of iron oxyhydroxides above ~180 m depth, and pyrite below it, indicates that a higher groundwater table may have preserved the pyrite at that time (Levy et al., 2011).

These redox elements are also found in groundwater samples, which indicate that complete reduction has not occurred, but the lower groundwater table present today may not represent past conditions affecting the Pozos uranium anomaly. The $^{234}U/^{238}U$ ratios from SIMS data (Figure 43) show renewed leaching of uranium minerals from the Pozos uranium anomaly, which shows conditions have changed over the last 1 Ma.

Zone 5: Cretaceous limestone (below -242 m)

The Cretaceous limestone sample is very similar in composition to the average values for Peña Blanca limestones reported by Goodell (1985) for the species listed in Table 7. Stege et al. (1981) suggested that the lime mud-rich limestone at Peña Blanca is impermeable, except through faults and fractures. The hydrologic barrier prevented downward and lateral migration of uranium-bearing solutions (Stege et al., 1981), so other mobile species are also unable to penetrate the limestone. The sample analyzed from the PB-1 core did not have visible fractures or alteration, but other unsampled areas could have fractures and be altered.

3.6.7 Implications for geologic storage of nuclear waste

The natural analog aspect of PB-1 core will be discussed in this section. Natural analogs are useful for researching the spatial and temporal dimensions of nuclear waste repository processes that cannot be tested by field or laboratory-scale experiments (Simmons and Stuckless, 2010). Analogs can add insight into waste performance by investigating uraninite oxidation, formation of secondary minerals, and by tracking the movement of species, such as U, in rock and groundwater (Simmons and Stuckless, 2010).

The data provided by the PB-1 core allows interpretation about uranium redox processes and uraninite stability. In this case, the Nopal I uranium deposit (zone 1) serves as the source term and the Pozos uranium anomaly (zone 4) may be an example of how geologic media serves as a barrier to uranium transport in the natural world. The sorption and precipitation of uranium by different minerals and species in the Pozos uranium anomaly is discussed first, and then the age and stability of uranium minerals in the Nopal I primary mineralization and the Pozos uranium anomaly will follow.

Sorption/Precipitation of Uranium in the Pozos Uranium Anomaly

In this section, the sorption of uranium and subsequent precipitation of uranium minerals in the Pozos uranium anomaly is discussed. The following relationships are presented: 1) uranium, kaolinite, and TiO_2, 2) uranium and P_2O_5, 3) uranium and pyrite. Finally, a statistical test of these potential relationships is given to determine their order of importance.

BSE images of uranium minerals in the PB-1 core are associated with three phases: iron oxyhydroxides (Figure 22) and kaolinite (e.g., Figure 18) and/or quartz (Figure 17). Through chemical and textural relationships observed in this study, uranium minerals are more often associated with kaolinite and/or quartz. This is an important relationship, because several studies have looked at both iron oxyhydroxides (Hsi, 1981; Hsi and Langmuir, 1985; Triay et al., 1991; Gabriel et al., 1998; Giammar and Hering, 2001; Wazne et al., 2003; Scism, 2006) and clays (Triay et al., 1991; Stammose et al., 1992; Syed, 1999; Catalano and Brown, 2005; Scism, 2006)

that can adsorb or precipitate uranium and other radionuclides in a contamination or waste disposal setting. Further work would investigate the relationship between uranium and other minerals using TIMS, to identify the minerals present, and XANES to determine the chemical state(s) that uranium and other trace elements applicable to nuclear waste.

Using only the BSE images (see section 3.3.3) from the Pozos uranium anomaly, it was clear that kaolinite was "host" for uranium minerals. However, these images in conjunction with the uranium mineral EMPA data (Table 4) indicated an additional association: titanium. There are higher amounts of titanium in the uranium minerals of the Pozos uranium anomaly (avg. 35 wt %) compared to zones 2-3 (avg. 2.3%). Initially the titanium was thought to indicate the presence of the uraniferous Ti-oxide, brannerite [$(U,Ca,Y,Ce)(Ti,Fe)_2O_6$]. However, a previous investigation of this relationship by Fayek et al. (2006) identified two separate phases using high-resolution transmission electron microscopy and BSE images found separate phases: uraninite and anatase (TiO_2), which was both disseminated TiO_2 and TiO_2 replacing highly altered sphere. The data suggest that TiO_2 was actively sequestering mobile uranium from fluids in the Pozos uranium anomaly.

TiO_2 is commonly found in kaolinite. Dolcater et al. (1970) analyzed 10 kaolinite samples from six different sources and found that 86% of titanium was actually TiO_2 rather than Ti substituted into kaolinite. Payne et al. (2004) reported in a study of Georgia kaolinite that the uranyl phase preferentially adsorbed to TiO_2 impurities in kaolinite, and cautioned a reexamination of the significance of kaolinite as a uranium adsorber. They modeled this observation by using a simple non-electrostatic surface complexation model and found that at low uranium concentrations, uranyl has a strong preference for the titanol (>TiOH) over the aluminol (>AlOH) sites. Bachmaf and Merkel (2011) reported that the presence of anatase impurities in kaolinite increased the binding of uranyl-carbonate complexes with surface sites. These additional studies support uranium sequestration by TiO_2 in the Pozos uranium anomaly.

TiO_2 and P_2O_5 appear to be intimately related through all zones (Figure 32). They both increase with depth and their correlation coefficient is 0.75, which means there is a 99.9% or greater probability that TiO_2 and P_2O_5 are related. In factor 3 (Figure 35), which was interpreted as Pozos uranium anomaly, these two elements are strongly correlated (>0.8). As described previously, TiO_2 is associated with uranium minerals throughout the deposit, but especially in the Pozos uranium anomaly. The highest P_2O_5 concentrations are found there (0.04 to 0.23, avg. 0.14), whereas zones 1-3 and 5 are about half as much (0.02 to 0.1, avg. 0.07). It is unlikely that uranium-bearing phosphate minerals, like monazite or apatite, or uranium phosphate minerals could account for such a high correlation when few to none of these minerals were identified during EMPA or XRD analysis. Further analysis, beyond the scope of this work, is needed to determine what specific role phosphate plays in sequestering uranium in this system. However, one explanation is the ability of phosphate to increase sorption of uranyl ions by iron through complexation at low pH with decreasing sorption at higher pH (Cheng et al., 2004). In this scenario, phosphate could increase sorption of uranium by pyrite (or other iron minerals) present in the Pozos uranium anomaly.

Pyrite is already associated with uranium in the zone 1 primary mineralization (Aniel and Leroy, 1985; Ildefonse et al., 1990b; Pearcy et al., 1994). Uranium is strongly correlated with sulfur (0.67, >99% probability of significance) in analysis of the whole core. Based on BSE images, areas where pyrite is absent, or leached, as is evidenced by iron oxyhydroxides, the presence of uranium minerals is reduced (Figure 22). However, the role pyrite may have in sorption, by phosphate or otherwise, in the Pozos uranium anomaly is unknown.

Several studies have looked at uranium and pyrite, which show how pyrite could adsorb and/or precipitate uranium. At Fernald, a DOE contaminated site in Ohio, uranium is sometimes concentrated in overgrowths on earlier pyrite grains suggesting precipitation of uranium through reduction (Bryan et al., 2004). Stewart et al. (2000) examined microscopically pre- and post-leach roll-front uranium deposits and found that uranium is widely associated with pyrite and

pyrite partially dissolved by a mine leaching solution. Pyrite is known to reduce U(VI) to U(IV), which decreases solubility and increases adsorption (Scism, 2006; Scott et al., 2007; Qafoku et al., 2009), but the adsorbed uranium is in a mixed oxidation state UO_{2+x} (Descostes et al., 2010). Pyrite sorption of uranium is stronger at pH greater than ~5.5 (Wersin et al., 1994; Descostes et al., 2010) and the presence of dissolved organic material can reduce the effect (Bruggeman and Maes, 2010).

In observing other possible elements adsorbed by pyrite, LREEs are also positively correlated, with Eu^{+3} exhibiting the strongest correlation of the LREEs. Descostes et al. (2010) reported that pyrite also adsorbed Eu^{+3} and Co^{+3}, which may be further evidence of the role pyrite plays as an adsorber in the Pozos uranium anomaly.

In order to test the different uranium relationships, a backward linear regression using U as a dependent variable from the zone 4 multi-element chemistry data was done using SPSS (Figure 49). The species, or predictors, tested were Fe_2O_3 and S (proxy for pyrite), Al_2O_3 and SiO_2 (for kaolinite), TiO_2, and P_2O_5. The initial test using all of these predictors failed, because the fit was too perfect for the model. In order to actually perform the backwards regression, one predictor was removed from the regression each time. For example, SiO_2 would be removed and the backwards regression was run with Fe_2O_3, S, Al_2O_3, TiO_2, and P_2O_5. Next, SiO_2 would be added back in as a predictor and one of the other five species was removed. After running each option, the model with the best R^2 value was the one that removed SiO_2. Based on the model, the best predictor of uranium was Al_2O_3 (adjusted R^2=0.636; >90% probability of significance), which served as a proxy for kaolinite, followed in order of increased prediction by P_2O_5, TiO_2, S, and Fe_2O_3.

Kaolinite and TiO_2 have been established as uranium adsorbers in the Pozos uranium anomaly (Fayek et al., 2006; Levy et al., 2011), in addition to BSE images, EMPA, and additionally with a multivariate linear regression. However, the other species cannot be ruled out by the model from having some kind of relationship, because they do add to the overall regression. However, based on the model, pyrite is the least influential of the selected predictors.

Model	R	R Square	Adjusted R Square	Std. Error of the Estimate
1	.989[a]	.979	.872	334.41019
2	.962[b]	.925	.775	442.48375
3	.911[c]	.830	.660	544.68690
4	.839[d]	.703	.555	622.96281
5	.835[e]	.697	.636	563.31227

a. Predictors: (Constant), Al2O3, Fe2O3, S, P2O5, TiO2

b. Predictors: (Constant), Al2O3, S, P2O5, TiO2

c. Predictors: (Constant), Al2O3, P2O5, TiO2

d. Predictors: (Constant), Al2O3, P2O5

e. Predictors: (Constant), Al2O3

Figure 49. Results of SPSS backward linear regression using U as the dependent variable from the zone 4 multi-element chemistry data. Predictors (independent variables) are SiO_2 (removed from this run), Fe_2O_3, S, Al_2O_3, TiO_2, and P_2O_5. R is the correlation between the observed and predicted values of dependent variable. R Square (R^2) is the proportion of variance in the dependent variable that can be explained by the independent variables. Adjusted R^2 adjusts the true R^2 by penalizing the addition of extraneous predictors to the model. Adjusted R^2=1 - ((1 – R^2)((N- 1) /(N - k - 1)), where k is the number of predictors.

Age and Stability of Uranium Minerals at Nopal I

In this section, the results of the uranium mineral age dating from the Pozos uranium anomaly are discussed in comparison to other uranium mineral ages at Nopal I and the implications for nuclear waste stability.

The age dating of uranium minerals from Peña Blanca is limited to a few prior studies (Pearcy et al., 1994; Pickett and Murphy, 1997; Murrell et al., 2002; Fayek et al., 2006). Further age dating by the current study are similar to those of Murrell et al. (2002) and Fayek et al.

(2006), who found secondary uranium minerals in fractures to be near secular equilibrium and Pozos conglomerate uraninite to be ~1.6 Ma, respectively.

Pozos uranium anomaly uranium minerals have $^{230}Th/^{234}U$ ratio at or near unity, which means a period of uranium migration occurred prior to 375 ka. Based on the ages and the reducing conditions in the Pozos uranium anomaly described in the previous discussion, uranium minerals precipitated due to adsorption by trace Ti or TiO_2 in kaolinite, phosphate, and/or pyrite. Later, local remobilization of ^{234}U occurred, which accounts for the ^{234}U deficiency in the $^{234}U/^{238}U$ ratio. The ^{234}U deficiency is relatively small (close to unity), but this may be explained by the reducing environment in the Pozos. Stagnant conditions increase with depth, and the degree of disequilibrium tends to decrease (e.g. Suksi, 2001; Tullborg et al., 2003). In addition, fluctuations in groundwater conditions due to short (e.g., annual changes in groundwater chemistry) and long (e.g., tectonic uplift) term variations causes the redox zone to migrate (Drake et al., 2009). Therefore, the reduced zone that caused the precipitation of the uranium minerals may have lowered with the groundwater table and/or uplift of the Peña Blanca block, causing re-oxidation of the uranium minerals in the Pozos (see Figure 44 for paragenesis).

If the uranium minerals in the Pozos uranium anomaly are truly a secondary deposition of radionuclides from the Nopal I uranium deposit above, then uranium mineral stability has implications for a nuclear waste repository. As described in the Introduction, Yucca Mountain has a 1 Ma regulatory period. If uranium minerals range in age from 375 ka to 1 Ma, it means they are stable for a relatively long period of time. If the ages of the uranium minerals at Peña Blanca are indicative of stability in a reducing environment, then based on the similarities between Yucca Mountain and the Nopal I environment, uranium, the dominant component of spent nuclear fuel, could be expected to act in the same way. In other words, uranium that would escape in a failure of the engineered barrier of the repository would probably be retarded and/or reduced into a mineral phase that would be stable on the several hundred thousand to million year time scale as long as oxidizing conditions can be prevented. Reducing conditions at Nopal

I have changed multiple times, assuming that each phase of uranium mineral formation indicates a change. Previous work at Nopal I has reported uranophane at 3 Ma (Pickett and Murphy, 1997) to 3.1 Ma (Fayek et al., 2006), which is one of the earliest remobilization events. Studies using U-series disequilibrium dating of fracture minerals and tuff have reported multiple events from fracture minerals and tuffs range from the tens to a few hundred thousand years (Pearcy et al., 1994; 1995; Pickett et al., 1999; Wong et al., 1999; Murrell et al., 2002). More recently, Fayek et al. (2006) reported the formation of uranophane at 3.1 Ma, a later uraninite mineralization at ~1.6 Ma, and multiple oxidation events which precipitated schoepite (~85 ka) and boltwoodite (41 ka). Caliche and opal ages (53.6±0.8 ka) suggest yet another oxidation event (Pearcy et al., 1994). Taken together, these multiple oxidation events show that it is difficult to predict and assume that reducing conditions will be maintained over a 1 Ma regulatory period. Nuclear waste would be encapsulated in engineered systems, but should failure occur, relying on a changing natural environment to completely stop radionuclide migration is an inexact science.

3.7 CONCLUSIONS

The PB-1 core presented a unique opportunity to investigate the paragenesis of the Nopal I uranium deposit and its implications for geologic storage of nuclear waste. The vertical transport direction was a mostly unexplored aspect of the site until now.

The Nopal I uranium deposit has a multistage uranium migration history. The primary mineralization, quartz-uraninite-pyrite-ilmenite-kaolinite, was formed through devitrification of a nearby source of volcanic glass. The uranium and other redox mobilized elements were precipitated at Nopal I through an existing fracture system in a reducing groundwater. The deposit was later uplifted into an oxidizing environment characterized by remobilization of redox sensitive elements by pyrite oxidation and sulfuric acid formation.

The redox environment of the PB-1 core has changed over time, but five zones can describe the paragenesis: 1) primary mineral assemblage/source term, 2) oxidized primary assemblage/source term, 3) redox transition zone, 4) reducing zone/Pozos uranium anomaly, and 5) Cretaceous limestone. The oxidizing environment in the Nopal and Coloradas Formations allows meteoric water and sulfuric acid to form a solution that transports redox sensitive elements to the groundwater table and reducing environments, such as the Pozos uranium anomaly. The reduced zone was larger in the past, when groundwater levels were higher. The Cretaceous limestone provides a boundary layer for reaction zones.

As for the geologic storage of nuclear waste, the PB-1 core allowed an investigation into the Pozos uranium anomaly. This is a relatively young uranium anomaly formed between 375 ka and 1 Ma. The uranium source is the Nopal I uranium deposit, which has experienced multiple mobilization events. The uranium was precipitated in the Pozos uranium anomaly, which was a reducing environment in the recent past, probably caused by higher groundwater levels.

There is strong evidence supporting the importance of titanium, especially as TiO_2, in adsorbing uranium at Nopal I. While kaolinite is usually a "host" for Ti and TiO_2, the role kaolinite plays in adsorption is inferred to be minor based on the evidence presented in this

study. This study agrees with Payne et al. (2004) and recommends a reexamination of the role that kaolinite may have as a uranium adsorber in nuclear waste research. Phosphate and pyrite may also have a role in adsorbing and precipitating radionuclides.

4. Characteristics of Source Term Weathering and Implications for Radionuclide Transport in Soil Using an Uranium Ore Boulder

4.1 INTRODUCTION

Nuclear waste oxidation studies often consider uraninite or species expected in waste repositories (e.g., Np, Pu, Am) in a controlled setting, but natural analogs exist to understand natural processes (e.g., Johnson and Shoesmith, 1988; Wronkiewicz et al., 1992, 1996; Leslie et al., 1993; Oversby, 1994, 1999; Pearcy et al., 1994; Janeczek, 1999; Shoesmith, 2000; Buck et al., 2004; Johnson et al., 2005; Poinssot et al., 2005a, b). Predictive radionuclide transport models of contaminant release into the unsaturated zone from waste sites and repositories require key input parameters such as retardation factors and diffusion coefficients (Pigford and Chambre, 1988). The transport parameters calculated from lab experiments are not able to simulate many aspects of the natural environment especially with respect to the timescale and changing environmental conditions (e.g., temperature, rainfall). The same is true for characterizing oxidation of spent nuclear fuel (e.g., Stout and Leider, 1998), whose equivalent natural analog is quantifying the paragenesis of uranium ore and its weathering rate. It has been suggested that field measurements may provide accurate estimations of transport parameters (e.g., Rutgers van der Loeff and Waijers, 1986; Ivanovich, 1991; Laul, 1992) and weathering rates (e.g., Gordon and Dorn, 2005; Navarre-Sitchler and Brantley, 2007). It is impossible to account for every component of the natural environment, but using an analysis of radionuclide transport in the field can provide a natural comparison for lab and model generated data.

Natural analog studies complement controlled laboratory studies by introducing the natural environment. The greatest benefit of these studies, the natural environment, is also their greatest weakness in terms of quantifiable inputs; however, the long-term behavior of spent nuclear fuel can only be simulated in laboratory settings that readily occur in nature. Natural analog studies can be used in two ways (Simmons and Stuckless, 2010): 1) in a qualitative mode, which allows complex or abstract processes to be understood; and 2) in a quantitative mode to

test models. Several natural analogs have been used to investigate Yucca Mountain (e.g., Oklo, Gabon, Poços de Caldas, Brazil, Palmottu, Finland), in addition to the focus of this study, the Peña Blanca Uranium District, Chihuahua, Mexico (e.g., Levy et al., 2011). The future of Yucca Mountain is uncertain (Shaffer, 2011), but the U.S. Geological Survey believes that the science, analyses, and interpretations from natural analogs can be applied to any future nuclear waste disposal sites or scientific investigations unrelated to waste disposal (Simmons and Stuckless, 2010).

Major goals of this were to determine: 1) semi-quantitatively the rate of radionuclide weathering from the boulder; and 2) whether diffusion or particulate transport best describes the movement of radionuclides from the boulder to the soil and within the soil. The Peña Blanca Natural Analog in Chihuahua, Mexico is one location for answering these questions.

4.1.1 Geologic Setting

The Peña Blanca Uranium District is located approximately 50 km north of Chihuahua City, Chihuahua, Mexico. The Nopal I uranium deposit, part of the district, is mineralized in the Nopal and Coloradas ash flow tuffs. It was explored by a Mexican government agency from 1969 to 1983 (Reyes-Cortes, 1997). During this activity, a stockpile of ore from the Nopal I mine was created on a gentle hill slope about 250 m west of the mine, and it is now referred to as the Prior High Grade Stockpile (PHGS) (Figure 50). The stockpile was removed from the PHGS in 1993 to another location in the district (Reyes-Cortes, 1997), but several mineralized boulders had rolled further downhill during stockpiling and were left behind during cleanup.

One of these mineralized boulders, PST#110, hereafter referred to as "the boulder" or "source term," was identified during a field trip in 2005 (Figure 50). A detailed description of the collection methods is given in French et al. (2006). The unintended consequence of this forgotten boulder is a great opportunity to study a short, well-constrained period of localized contamination from a point source term. This study builds on previous work from the boulder and soil samples collected in 2005 (French et al., 2006).

4.1.2 Previous Studies

In 2006, soils were collected from under and around the boulder. These were analyzed for their radionuclide activities by gamma-ray spectroscopy (French et al., 2006). The reported $^{230}Th/^{234}U$ and $^{226}Ra/^{230}Th$ ratios in most of the samples were greater than 1. The relative abundances of radionuclides in the soil indicated a fast mobilization history of less than ~25 years, i.e., the residence time of the boulder. Over that time period, radionuclide transport penetrated only several centimeters as inferred from decreasing activity with depth. French et al. (2006) hypothesized that mechanical weathering alone could not have accounted for the amount of radionuclides observed at several centimeters depth, so chemical weathering must have played a part. This was supported by the differences in the $^{226}Ra/^{230}Th$ ratios between the boulder and the soil layers. Ratios in the boulder were near unity, whereas ratios in the soil beneath it showed much greater disequilibrium.

A study of radionuclides in dust from the high-grade ore storage sites at Peña Blanca by Velarde (2011) suggested that contamination was localized to less than 100 m in 2.4 years. Electron microprobe analysis of dust samples showed euhedral uranophane crystals (20-300 μm long), which implies that uranophane is stable over short timescales <25 years.

4.1.3 Field sampling

A brief description of field sampling is necessary, because it applies to all of the following sections. Details are taken from French (2006), French et al. (2006), field notes for the Peña Blanca Natural Analog project, and communications with P. Goodell and J. Walton, who were present during sampling.

Although several boulders were initially selected for this study, the PST#110 boulder was determined to be the best candidate, because of its high radioactivity (e.g., estimated U content) and its location away from other mineralized boulders that could contribute additional radionuclides to the investigation site. The drip line of the boulder was marked, and then the boulder was moved a short distance away, so that a gamma survey and soil sampling could be

completed (Figure 51). A scintillometer was used to take 50 gamma surface readings to determine suitable soil sample locations. These gamma readings were corrected for the background contribution of the boulder using the inverse square law before making the gamma map (Figure 51)

Then seven 30 cm x 30 cm blocks were marked on the ground surface where soil samples were to be taken. Eight samples were collected vertically from B1 and B3, and three vertical samples each from B4, B5, B6, B7, and B8 in approximately 30 cm x 30 cm x 2 cm boxes (Figure 51). Each sample was placed in a 700 ml plastic container and weighed approximately 1 kg each.

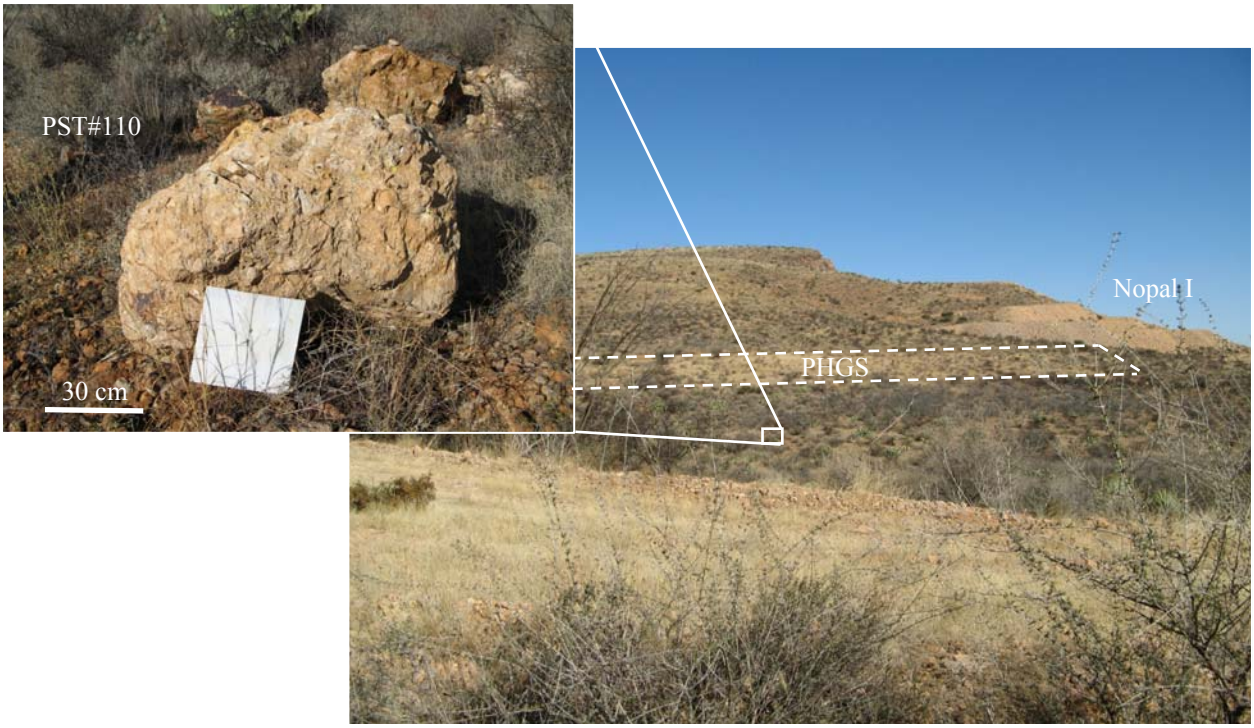

Figure 50. Images taken during a field trip in December 2006 of the boulder (PST#110) and its approximate location relative to the Prior High Grade Site (PHGS) and the Nopal I mine, its probable source. The boulder and soil samples from below and around it are the subjects of this research.

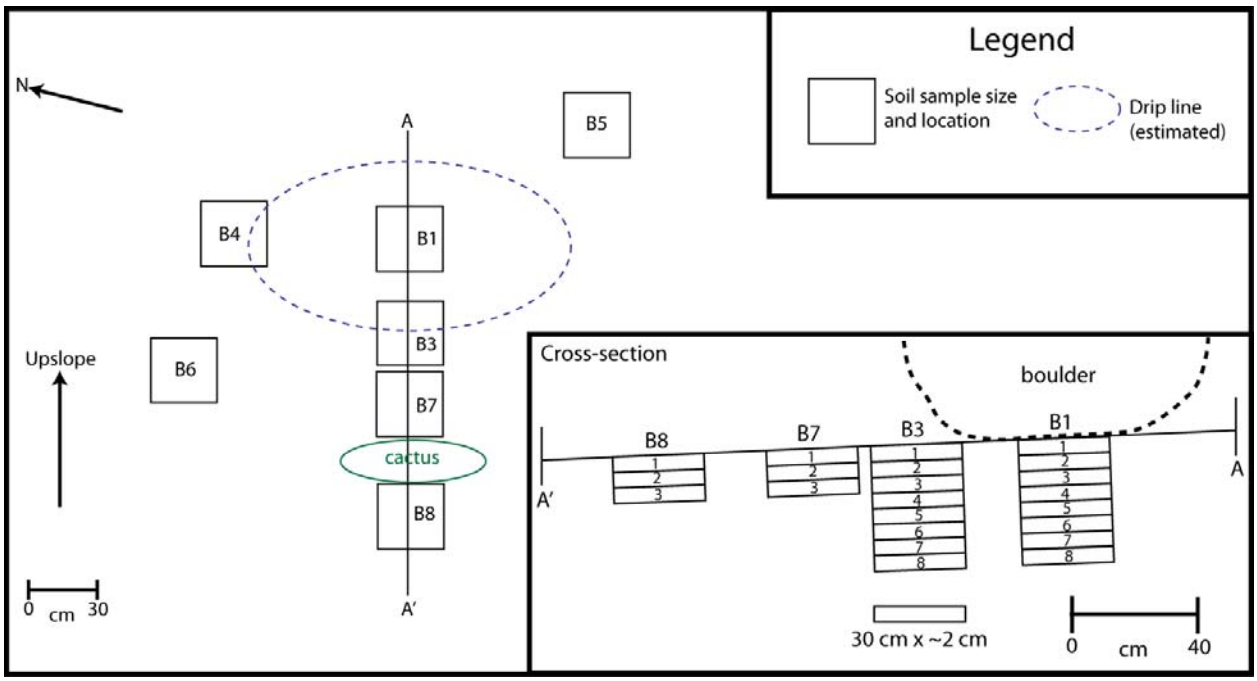

Figure 51. Sample collection map (modified from French et al., 2006). The blue line represents the drip line of the boulder. Samples were taken vertically from eight blocks, B#. B1, B3, B7, and B8 are shown in cross-section and were taken parallel to the hill slope. B1 and B3 had eight samples each, whereas the remaining blocks have three samples each. Sample B2 does not exist.

4.2 METHODS

4.2.1 Rate of Radionuclide Weathering from the Boulder

In this section, the release of radionuclides from the boulder is semi-quantitatively calculated from concentrations within the soil and the surface area of the boulder. The gamma survey results reported by French et al. (2006) are also used to estimate the amount of radionuclides released from the boulder.

Two methods were used to determine the radionuclides released from the boulder: 1) surface area of the boulder; and 2) concentrations in the soil compared with the gamma survey results to determine the relationship between gamma activity and concentration. The methodologies are described separately below.

Surface area of the boulder

The surface area of the boulder was calculated in the following manner. Measurements and pictures of the boulder were taken during a field trip in December 2006. The boulder is neither completely rectangular, nor spherical, so an ellipsoid was used to estimate the surface of the boulder. The surface area of an ellipsoid is estimated using the Knud Thomsen approximation as follows (Xu et al., 2009):

$$SA \approx 4\pi\left(\frac{a^p b^p + a^p c^p + b^p c^p}{3}\right)^{\frac{1}{p}}$$

where a, b, and c are the radii along the x-, y-, and z-axes, respectively, and p is a constant (the approximation has the least relative error (±1.061% in the worse case), when p≈1.6075. The measurement diameter lengths of the boulder are 1.1 m x 0.9 m x 0.9 m, so the radii used are 0.55 m, 0.45 m and 0.45 m. The resulting surface area is 2.9 m^2. The volume is 3.7 m^3.

The increased surface area due to roughness of the boulder was calculated using six boulder pieces and extrapolated up to the full size of the boulder using a modified wetted surface layer area estimation (Harrod and Hall, 1962) and the smooth stone shape area estimation

(Graham et al., 1988) described by Bergey (2006). Dividing the wetted layer surface area by the smooth stone shape area yields a boulder roughness index of 4.1±2.3 (2σ). The area of the smooth boulder (Graham et al., 1988) is 3.2 m^2 and the ellipsoid is 2.9 m^2, which results in total rough surface area estimates of 13.3±3.7 m^2 and 12.1±3.4 m^2, respectively.

Four samples of the boulder were collected by P. Goodell and sent to Actlabs www.actlabs.com; Options: 4EResearch, H_2O, and FeO titration) for geochemical analysis. The average concentration of U was ~31,000 ppm.

Radionuclide concentration in soil

Soil samples from soil groups B1, B3, B7, and B8 (21 separate samples in total) were selected for chemical analysis, because they are in a direct line down slope from the boulder (Figure 51). These soil samples were sent to Actlabs (www.actlabs.com; Options: 4EResearch, Chlorine, and FeO titration) for multi-element chemistry determinations.

The 30 cm x 30 cm radiometric survey contour map from French et al. (2006) was used as the maximum distribution of radionuclides from the boulder (Figure 52.). The area of each contour interval (CI) was calculated and divided by the total area of the gamma map to determine the percentage area of each CI over the total area.

Three surficial soil samples, B1-1, B3-2, and B7-1, highest concentrations of U in the 21 samples sent for analysis. The highest U concentrations were assumed to equal the CI activity from the survey, in addition to an activity of 0 cps for 0 ppm. This allowed for the construction of a linear regression between U concentration and gamma activity (Figure 53). The regression equation was used to estimate U concentration for each CI.

The U concentration was reported in parts per million, which is assumed to be 1 gram of U per kg of soil. An assumption of 1 kg of soil per 30 cm x 30 cm (900 cm^2) area was made, because this was the sampling volume of the soil blocks (~2 cm thick intervals) and their approximate mass. One kg of soil per 900 cm^2 was assumed over the entire radiometric survey area (300 cm x 400 cm=120000 cm^2) for a total of 133 kg soil. This total amount of soil was

multiplied by the percentage of a given CI activity to determine the total amount of soil in each contour. Finally, the grams of U per kg of soil in each CI activity were divided by kg of soil in each CI and to determine the grams of U in each CI.

$$\frac{gU\ \ in\ \ Each\ \ CI}{kgSoil\ \ Each\ \ CI} = \%Total\ \ Area \times 133kg\ \ Soil \times \frac{gU}{1kg\ \ Soil}$$

The amount of U in the surface samples was used as a starting point to integrate the amount of U in the soil samples below. The concentrations in B1, B3, and B7 were used to determine the decrease in concentration with depth, because they are in a line directly down slope from the boulder. B1 and B3 have eight samples each descending to approximately 16 cm depth. Background radioactivity was measured from 7-12 cm depth (B7<B1<B3) and at the surface of B8, so those are the boundaries for the integrated area. The exponential decay slopes calculated from gamma spectroscopy activities for B1, B3, and B7 were very similar (R^2=0.87, N=13) and averaged to:

$$\frac{Cx}{Ci} = 1.43e^{-0.23(x)}$$

where C_x is the concentration at depth (x), and C_i is the concentration in the surface soil. This equation was used to calculate for samples that were not collected, e.g., B7-4.

In order to integrate over the area, a circular area (Figure 54) based on the extent of U concentration above background (distance from center of boulder to B7=7,950 cm^2) was used and a 2 cm depth was applied, so the total cylindrical area of radionuclide dispersal was calculated to 15,900 cm^3. Then the volume of B3 and B1 were subtracted, which estimated the soil packet volumes for each group: B1=2,500 cm^3, B3=5,700 cm^3, and B7=8,700 cm^3. The U concentration in each soil volume at depth yielded a total cylindrical volume of 9 g U.

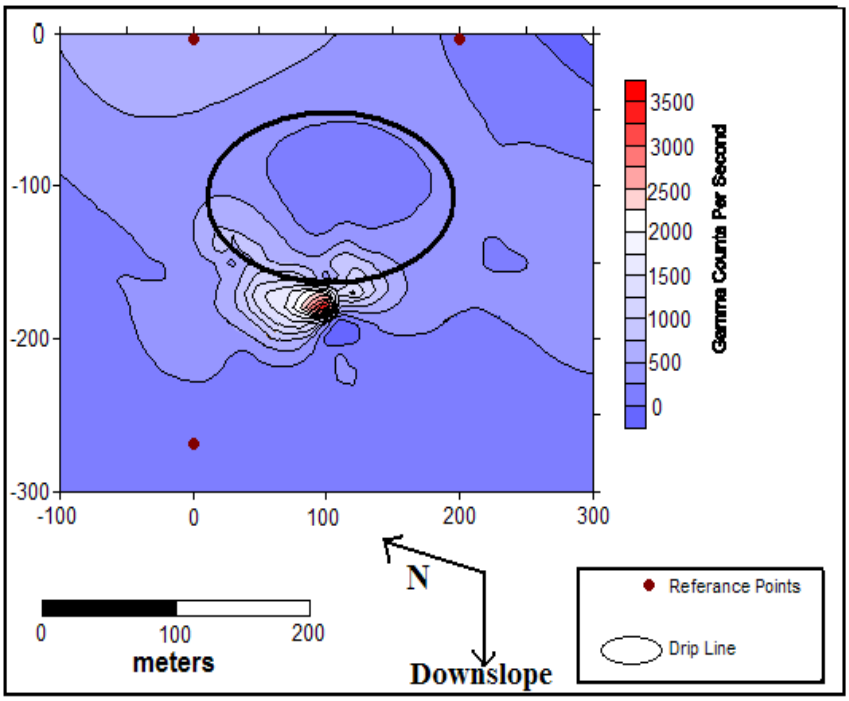

Figure 52. Surface radiometric survey from gamma ray scintillometer (from French et al., 2006) used to estimate radionuclides in the soil.

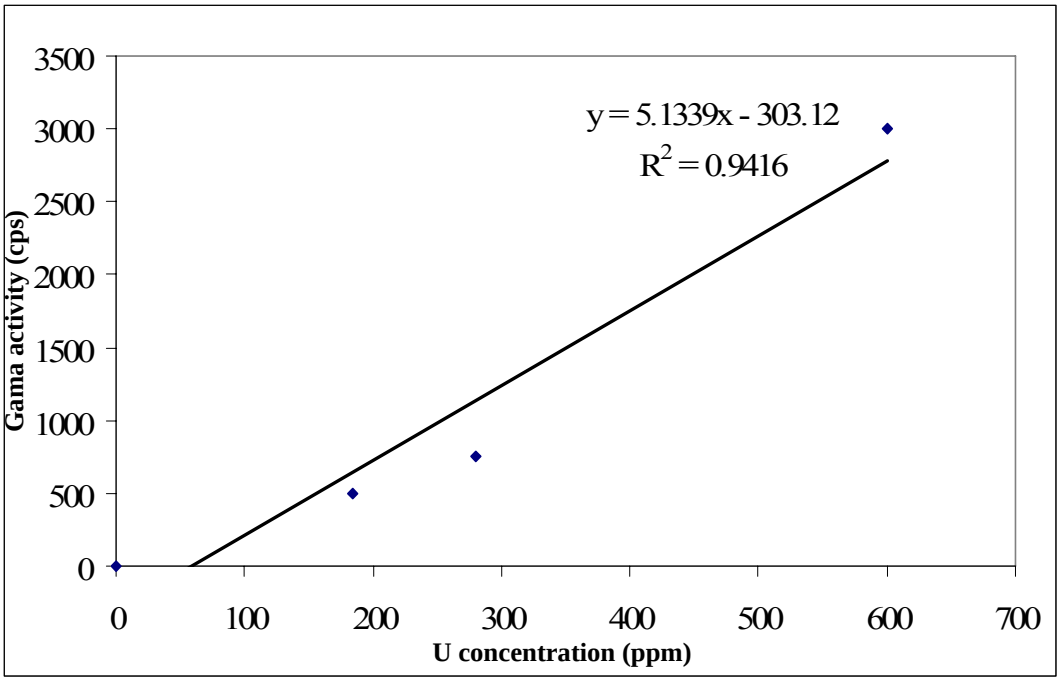

Figure 53. The relationship between U concentration (ppm) and gamma activity (cps) was constructed using known U concentrations at a known location of the radiometric survey (Figure 52.). The linear regression was used to interpolate concentration for each contour interval.

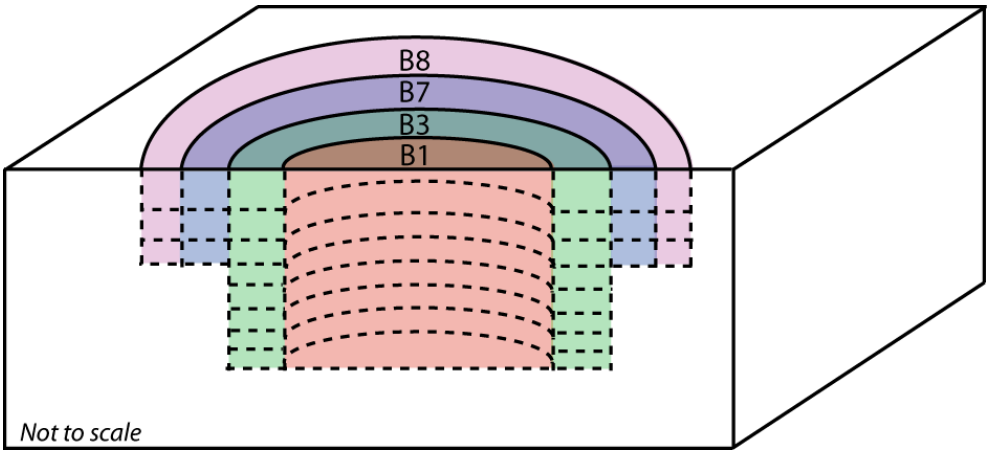

Figure 54. Illustration of cylindrical area used to calculate the amount of U in the soil. Eight soil "cylinders" (e.g., B1-1) for B1 (red) and B3 (green), and three "cylinders" from B7 (blue) were used to calculate the amount of U in each "cylinder." The B7 group layers 4-8 were integrated by using the radionuclide curves for B1 and B3. Then, all of the layers from B1+B3+B7 were added up to determine the uranium in the total area. B8 (purple) was below background, so it was not used in the calculation, but was used as the extent of uranium contamination.

4.2.2 Transport of Radionuclides from the Boulder and Within the Soil

In this section, activities of U, Th, and Ra are used to fit advection-dispersion curves to estimate radionuclides transport in soil from Peña Blanca. Some methods (e.g., leach testing and plain light microscopy) were used to test the boundary conditions of particulate versus dissolution transport of radionuclides.

Gamma spectroscopy

Twelve of the 31 total soil samples were analyzed by French et al. (2006). The remaining 19 soil samples were analyzed for this study using a Canberra High Purity Germanium (HPGe) detector and the gamma spectra were generated and analyzed with GENIE2000 software. The detailed analysis method and corrections were described by French et al. (2006).

Leach testing

A leach test of the highest U content soil samples, B1-1 and B3-2, and one of the lower concentration soil samples, B3-4, were used to estimate the retardation factors of radionuclides of interest to this study (i.e., U, Th, Ra). In order to determine the amount of U present as water

soluble and adsorbed/exchangeable species, a semi-selective extraction technique was used (modified from Tessier et al., 1979; Serne et al., 2002).

The extraction procedure used 25 g of each soil placed into 500 mL bottles. Soluble U was leached by shaking at room temperature with 200 mL of 18MΩ pure water for one hour. The samples were centrifuged (5 min at 6000 g), and the supernatant decanted, filtered (0.45 μm pre-rinsed nylon syringe filters). The process was repeated with 200 mL of 0.1 M $Mg(NO_3)_2$. The supernatant fractions were analyzed with a Perkin Elmer 5300 DV ICP-OES using USGS and internal standards. Only U values were reported, because Th and Ra were below the detection limit.

Plain light microscopy

The soil samples used in the leach test were separated into fresh and leached groups to determine if visible changes in characteristics could be observed. The leached samples were dried before observing any changes. Almost no change was observed between the two groups, with the exception that leached samples clumped together.

Advection-Dispersion calculations

In order to determine if diffusion or particulate transport of radionuclides occured from the boulder and within the soil, a chain decay and advection-dispersion (A-D) transport of U, Th, and Ra in the soil samples was evaluated using the explicit finite difference method with Mathematica software (Appendix H). The A-D equation simulates a random walk, which can approximate both diffusion and particle filtering. The activities of each radionuclide were plotted versus sample depth for the gamma spectroscopy measured data and the curve was fit to those data points based on estimated transport parameters. The starting one-dimensional A-D transport equation is as follows:

$$\frac{\partial C}{\partial t} = \frac{D}{R_d}\frac{\partial^2 C}{\partial x^2} - \frac{\nu}{R_d}\frac{\partial C}{\partial x} \pm R$$

where C is the concentration of radionuclide (dps/cm3), t is time (s), x is depth (cm), D is the dispersion coefficient (cm^2/s), R_d is the retardation factor, ν is the Darcy velocity or specific discharge (cm/s), and R is radioactive decay and/or ingrowth. The following is modified from Pekar et al. (2008).

The 22 year period that the boulder was weathering and contributing radionuclides into the soil was not monitored. As a result, some assumptions were made to the A-D transport equation in order to solve for transport parameters. Precipitation data specific to the site, the amount of water available to weather the boulder, the periods of saturated or unsaturated soil, and flow/no flow periods are unknown. The mechanisms of transport are known (Figure 55), but the contribution each makes to the system in relative terms can be calculated using the A-D equation.

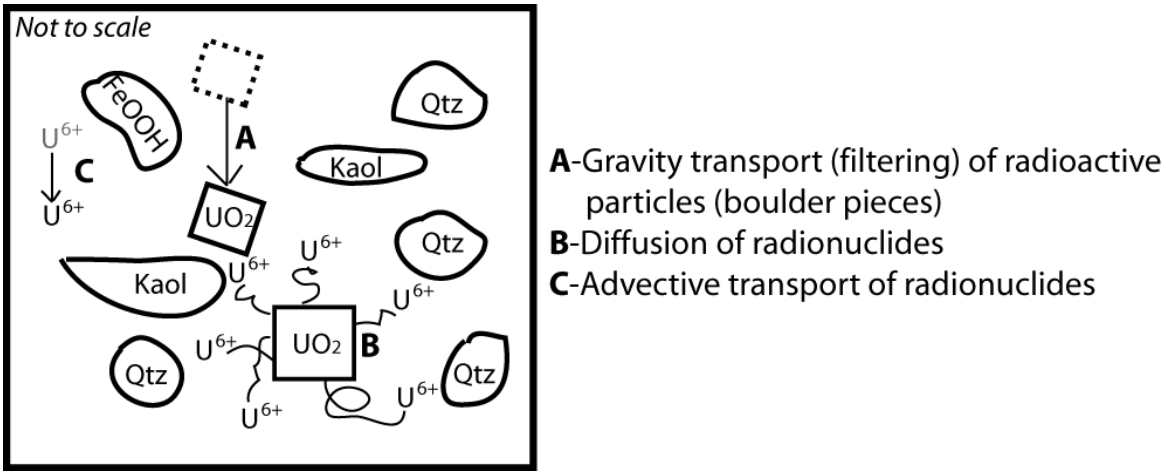

Figure 55. Different modes of transport, which account for radionuclide movement in the soil. **A** is the physical, gravity-driven movement of a particle with radionuclides in it, such as boulder pieces moving downward through the soil. **B** is diffusion, or leaching, of a radionuclide out of a particle in the soil or directly from the boulder during weathering. **C** is an example of advective transport, which involves the movement of a radionuclide with the flow of water, or when adsorbed, such as colloidal transport.

Assumptions used in the calculations are presented as follows. First, to keep the time steps at a reasonable period, radionuclides with half-lives shorter than several days were omitted. Radionuclides below ^{222}Rn in the decay series were omitted, because the samples were so close

to the surface that radon gas could escape or excess radon could be deposited into the system; therefore, the measured amounts of these nuclides would not be meaningful for this study.

The starting activity for ^{238}U was assumed to be the activity of ^{234}Th, because ^{234}Th has such a short half-life (24.1 days) that it would have ingrown to secular equilibrium with the ^{238}U activity in the time between sample collection and analysis. This also assumes that the $^{234}Th/^{238}U$ ratio of the boulder is in secular equilibrium. Using $^{231}Pa/^{235}U$ activity ratios in fractures, Murrell et al. (1999) reported that significant ^{238}U and ^{235}U redistribution has not occurred within the last 300 ka, which supports the $^{234}Th/^{238}U=1$ ratio assumption. The measured activity of ^{234}Th in the shallowest samples was divided by 22 years, to account for the residence time of the boulder and the deposition, decay, and A-D transport in the soil over that time period. This also assumed steady-state weathering of the boulder over the 22 year period, so long-term weathering may be overestimated. UO_2 pellets and Nopal I uraninite studies indicated that secondary uranium oxyhydroxides form protective crusts over the UO_2, which stabilized the weathering rate over time from a more rapid initial rate (Wronkiewicz et al., 1992, 1996; Pearcy et al., 1994; Stout and Leider, 1998).

Thorough an iterative process, the advection term was set to zero (v=0), because any v>0 produced convex curves, whereas the data sets defined concave curves. This assumption is supported by piston-like advective motion during wet/dry cycles (Figure 56).

Finally, retardation was normalized into the dispersion term (R_f=1) for all radionuclides to change only the numerator. Solving for both variables at the same time would have given several possible data pairs, but by setting R_f=1, it was possible to solve the equation for the effective dispersion coefficient (D_e). D/R_f is the effective dispersion coefficient (D_e). The transport equation then becomes:

$$\frac{\partial C}{\partial t} = D_e \frac{\partial^2 C}{\partial x^2} \pm R$$

where $D_e=(D/R_f)$, which is the effective dispersion (cm^2/s). The effective dispersion value for each radionuclide was calculated using this equation. This is a bulk parameter accounting for all modes of transport and retardation processes (e.g., adsorption), and provides the most robust results. The following calculations are used to determine the K_d for U, Th, and Ra, but increased complexity and number of assumptions yields increased uncertainty.

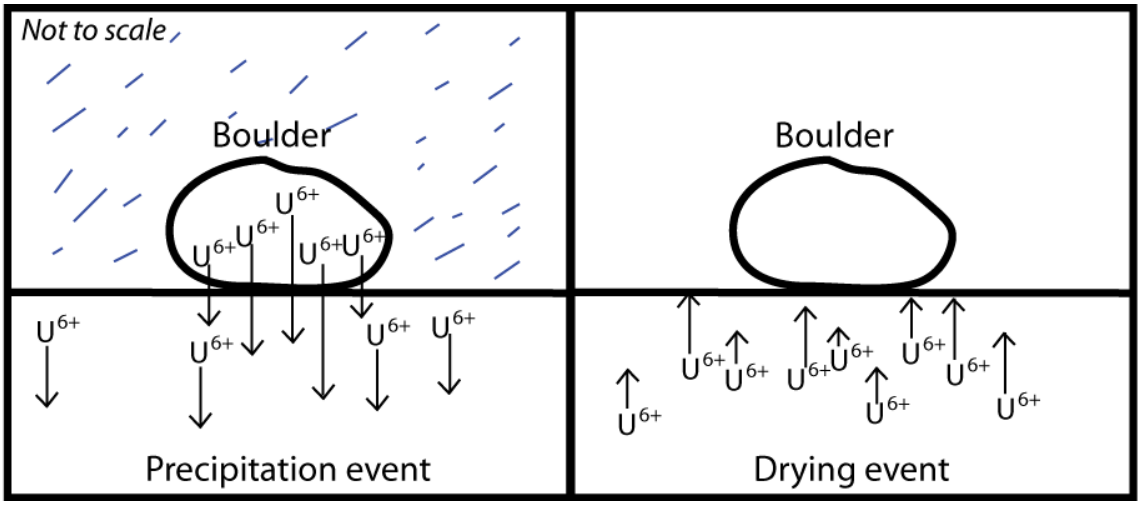

Figure 56. Illustration of the effect wet/dry cycles can have on advection. Precipitation drives species downward in the direction of flow; however, during drying cycles, the same species can be moved back up through the soil. This can effectively make net-zero advection.

Additional assumptions are needed for quantitatively obtaining the retardation factor, because the retardation factors from the ICP-OES were below the detection limit, except for U. The effective dispersion coefficient, when divided into the self-diffusion coefficient at infinite dilution, should be close to the retardation factor for each of the species:

$$\frac{D_w}{D_e} \approx R_f$$

where D_w is the self-diffusion coefficient at infinite dilution (Li and Gregory, 1974).

To obtain soil properties, mixed samples from all eight B1 and all eight B3 samples were sent to the Soil, Water, and Agricultural Testing Lab at New Mexico State University. The soil

samples were classified as sandy loam and loamy sand, and a pH between 6.1-6.6. The % saturation of soil, 31-36%, is equivalent to the soil water content (SWC) divided by 100, 0.3-0.4 g/g. The soil bulk density (ρ), 1.55 g/cm^3, was determined at UTEP by dividing the oven dry soil weight by the volume of soil (USDA, 2001). Volumetric water content (φ) is a variable property of soil that can range from zero, when completely dry, to the effective porosity of the soil when saturated. Peña Blanca is located in an arid region, so the water content is expected to be small; however, radionuclide migration most likely occurs during the few times that it does rain in the region. The volumetric water content is approximately equal to (USDA, 2001):

$$\varphi = \rho \times SWC$$

The volumetric water content is calculated to be 0.5-0.6. D_e is primarily a function of the moisture content of the soil and only secondarily dependent on the type of soil or soil (Conca and Wright, 1990). These soil parameters are used to calculate K_d for each species using the following equation:

$$R_f = 1 + \frac{\rho}{\varphi} K_d$$

where K_d is the partition coefficient (ml/g). K_d is calculated by rearranging the equation and using D_w/D_e as equivalent to the retardation factor and the soil properties above. The values used in D_w are: 4.3×10^{-10} m^2/s, UO_2^{+2} (at 25°C); 1.5×10^{-10} m^2/s, Th^{4+} (at 18°C); and 8.9×10^{-10} m^2/s, Ra^{+2} (at 25°C) (Li and Gregory, 1974). The D_w for Th is only given at 18ºC, so the retardation factor (R_f) is underestimated, because the temperature used is lower than for U or Ra, but no other values were given.

4.3 RESULTS AND DISCUSSION

One of the most important tasks for this study was determining the boundary conditions of radionuclide loss from the boulder. The time dimension of 22 years for the experiment is accurate, because of mine operation information (Reyes-Cortes, 1997). Determining the mode of transport (e.g., dissolution, particulate) was the more difficult question, because evidence of both chemical and physical weathering exists (Figure 57). It is nearly impossible to quantitatively determine the amount of input that each end member may have on radionuclide transport, but the observations from the following results will help to identify their relative influence.

Dissolution (chemical)	vs.	Particulate (mechanical)
Uranium oxyhydroxide minerals in boulder and soil Leaching from Nopal I uranium deposit into groundwater Adsorbers in soil (clay, iron oxyhydroxides, caliche) U-series ratios from the boulder are different from the soil (French et al., 2006)		Visible ore boulder pieces observed/removed during soil sampling Euhedral uranophane crystals in dust (Velarde, 2011)

Figure 57. Evidence for chemical vs. mechanical weathering of the boulder or source term collected by this study and others. In reality, it is probably a combination of the two conditions.

Another observation can be made by looking at the distribution of gamma activity using Figure 52. If transport from precipitation was the only way to weather the boulder, then the area of higher radioactivity coming from the boulder should be cone-shaped down slope from the boulder. A more southwesterly distribution is observed. Maximum winds reported from a DOE weather station at Peña Blanca are west to northwest in spring, whereas north to east minimum winds occurred in the summer (Velarde, 2011). Radionuclide transport observed at the high-grade ore storage site was less than 100 m over 2.4 years and the eastward pattern of migration observed is different from the boulder location. This does not match well with the distribution of

radioactivity around the boulder, but because the measured area is so small, localized eddying around the boulder could account for the disparity in wind direction.

4.3.1 Rate of Weathering from the Boulder

The total amount of U in the soil over the gamma surveyed area (Figure 52) is shown in Table 10; it is approximately 22 g U. The total amount of U in the soil calculated from B1, B3, and B7 in the cylindrical area (Figure 54) is shown in Table 11; it is approximately 8 g U. This difference could be caused by: 1) soil collection missing the highest radioactive hotspot; and 2) assuming the gamma survey is equivalent to uranium concentration, when shorter-lived daughters contribute the most to radioactivity.

The boulder was weathered at the sample location for 22 years. Assuming a constant rate of release and dividing the amount of U in the two soil areas by 22 years, 0.4-1 g U/year was released from the boulder. Concentrations of other radionuclides were not analyzed during chemical analysis; therefore this estimate only considers total U concentration. Any U that would have decayed over the 22 year time period should be minimal considering the half-lives are several orders of magnitude longer than the experiment.

The bulk density of the mineralized Nopal tuff ranges from 2.0-2.2 g/cm^3 (Dobson et al., 2008). The boulder, which was taken from the Nopal tuff, has an average of ~31,000 ppm U over a volume of 3.7x10^6 cm^3. Using the following equation:

$$Amt\ of\ U\ in\ Boulder(g) = 3x10^4\ ppm\ U \times \frac{1g\ U}{1x10^6\ g} \times Boulder\ Density\left(\frac{g}{cm^3}\right) \times Volume\ of\ Boulder(cm^3)$$

the total amount of U in the boulder is about 2.5x10^5 g. Dividing the amount of uranium released from the boulder (0.4-1 g U/yr) by the total amount of U in the boulder yields 2x10^{-6}-4x10^{-6} g U/yr (0.0002-0.0004 %U/yr) weathered out of the boulder. A study of the Santana tuff in the Trans-Pecos region of Texas found that surficial permeability of the tuff decreased an order of magnitude from ~55 mD on a fresh surface to 3-5 mD on varnished and weathered

surfaces (Fuller, 1990). Given the comparable climate, a similar decrease in weathering over time would be expected on the boulder, so these values may overestimate the rate of weathering.

The NRC 10 CFR 60.113 maximum annual release rate for spent fuel is 10^{-5} of 1000 yr inventory per year. The U release rates using unfiltered solutions in unsaturated tests on UO_2 pellets in mg U/m^2/day (Wronkiewicz et al., 1992, 1996) were compiled in Stout and Leider (1998). These values are generally range from 0.1-0.3 mg U/m^2/day, and trending towards the smaller value the longer the experiment period. The pellet sizes had smaller surface areas (thousandths of m^2) compared to the boulder, but similar time scales to our study (several years). In order to make a direct comparison with the UO_2 pellets, the amount of UO_2 in the boulder, not just U was needed. The theoretical density of UO_2 is 10.96×10^6 g/m^3 (McEachern and Taylor, 1998). The volume of UO_2 (0.026 m^3) in the boulder was calculated using this equation:

$$UO_2 \ in \ boulder(m^3) = Amt \ of \ U \ in \ Boulder(2.5x10^5 \, g) \times \frac{1g \ UO_2}{0.881g \ U} \times \frac{1}{Density \ UO_2\left(10.96x10^6 \frac{g}{m^3}\right)}$$

However, surficial UO_2 weathers the most, so that amount needs to be taken calculated. By assuming a uniform distribution of UO_2 throughout the boulder, the SA:volume ratio of the boulder (3.3-3.6) can be used to estimate the exposed surface area of UO_2 (0.1 m^2). With that amount, it is possible to calculate a rate equivalent to the UO_2 pellet studies using this equation:

$$mgU / m^2 / day = mgU \ in \ soil \times \frac{1}{SA \ of \ UO_2(m^2)} \times \frac{1}{365.25days \cdot 22}$$

The weathering rate from this study (12-34 mg U/m^2/day) is ~150 times greater than the UO_2 pellet drip experiment.

The higher rate could be explained in several ways. First, this is a boulder that has been outside exposed to daily and seasonal temperature changes, intermittent precipitation, wind, etc., which are not easily simulated during drip experiments on UO_2 in a controlled, laboratory setting. Boulder particles present in the soil, which would not be easily dissolved as in the UO_2 drip experiments. Boulder pieces containing large concentrations of uranium would cause an

apparent increase in the weathering rate. This boulder flaking process may be important to spent nuclear fuel studies, because while UO_2 is commonly used as a proxy, it is pure compared to spent nuclear fuel. The presence of other species in nuclear waste could cause a different rate or mechanism of weathering other than dissolution. It is also possible that airborne particles from an external source, as seen in the Peña Blanca Uranium District (Velarde, 2011), have increased the amount of uranium in the soil, which would overestimate the weathering rate.

Alternatively, the ~150 greater weathering rate can be attributed to differences in surface area calculations. Geometric surface area measurements, such as used in this study, are orders of magnitude greater than the scale than can be measured using more precise techniques (e.g., BET methods) (White and Brantley, 2003). Using silicate mineral roughness and weathering time, White and Brantley (2003) determined that the relationship between surface roughness and time, assuming that surface roughness increases consistently with time, is equal to:

$$\lambda = 13.6t^{-2}$$

where λ is surface roughness and t is time in years. Using this equation, the 22 year time period for the boulder to weather yields an increased surface area of 25 times the geometric area. This would decrease the apparent weathering rate to 0.4-1.4 mg U/m^2/day, which is much closer to the UO_2 weathering rate of 0.1-0.3 mg U/m^2/day (Wronkiewicz et al., 1992, 1996). This assumes that UO_2 surface area is affected at the same rates as silicate weathering. The higher weathering rates for the field studies are still best explained by boulder flaking, given data from the transport portion of this work. Flaking would give an apparent weathering rate for UO_2 that is much higher than it would be if weathering was due solely to dissolution.

Using information gleaned from the boulder, two important scientific questions about geologic storage of nuclear waste can be discussed (Bruno and Ewing, 2006): 1) the need to understand the potential release mechanisms for spent fuel as geochemical and hydrologic conditions change; and 2) the near- and far-field mobility of radionuclides. The most important data for testing source term behavior is dissolution, or leach, testing of spent fuel and UO_2 (Stout and Leider, 1998). Many lab- and theoretically-based studies of the oxidation of spent fuel, in

particular UO_2, have been completed, but few have relied on field experiments (e.g., Johnson and Shoesmith, 1988; Wronkiewicz et al., 1992, 1996; Leslie et al., 1993; Oversby, 1994, 1999; Pearcy et al., 1994; Stout and Leider, 1998; Janeczek, 1999; Shoesmith, 2000; Buck et al., 2004; Johnson et al., 2005; Poinssot et al., 2005a, b).

The weathering/oxidation sequence of Nopal I uraninite (UO_2) suggested by Leslie et al. (1993) is the same paragenesis observed in lab experiments that dissolved UO_2 (Wronkiewicz et al., 1992, 1996). The boulder is from the same source rock, so this paragenetic sequence is a valid assumption. The uranium oxyhydroxide minerals (e.g. schoepite, ianthinite) and even uranium silicates (e.g., uranophane, soddyite, boltwoodite) could form quickly, on the order of a few years, according to the UO_2 lab studies (Wronkiewicz et al., 1992, 1996). However, the U may also be mobilized by carbonate complexes (Grenthe et al., 1984; de Pablo et al., 1996; Torrero et al., 1997; Shoesmith et al., 2000; Zheng et al., 2003), and the presence of caliche in the soil and studies of caliche with up to 320 ppm U at Nopal I support this alternative mechanism (Pickett et al., 2000).

Uranium was the simplest radionuclide to measure using the various methods described by this study, but that does not necessarily limit its usefulness to U mobilization and stability. UO_2 makes up the majority of spent fuel, thus its dissolution is considered the first step necessary for the release of ~98% of fission products within the matrix; it sets the upper boundary for aqueous release for actinides (Stout and Leider, 1998). Transuranic elements, such as Np, Pu, and Am, are not present in significant quantities to allow natural studies of their mineralogy (Burns et al., 2006). Studies suggest that actinide incorporation into uranyl minerals present in natural analogs and expected in nuclear waste repositories is likely to occur (Loida et al., 1995; Quiñones et al., 1996; Burns et al., 1997a, b, 2004; Shoesmith, 2000; Burns and Klingensmith, 2006); however, more research on the behavior of the elements is needed.

Table 10. Total amount of uranium in the gamma surveyed area

Soil sample	U ppm	g U in 1 kg soil	CPS	Weight of survey area (g)	% of total area	kg soil in survey area	g U per kg soil
B3-2	**600**	0.6	**3000**	0.003	0.1	0.1	0.1
	595	0.6	2750	0.002	0.1	0.1	0.0
	546	0.5	2500	0.003	0.1	0.1	0.1
	497	0.5	2250	0.004	0.1	0.2	0.1
	449	0.4	2000	0.006	0.2	0.2	0.1
	400	0.4	1750	0.011	0.3	0.4	0.2
	351	0.4	1500	0.019	0.6	0.8	0.3
	303	0.3	1250	0.025	0.7	1.0	0.3
	254	0.3	1000	0.054	1.6	2.2	0.5
B1-1	**280**	0.3	**750**	0.336	10.1	13.4	3.8
B7-1	**184**	0.2	**500**	1.275	38.3	51.0	9.4
	108	0.1	250	1.560	46.8	62.4	6.7
	0	0.0	**0**	0.035	1.1	1.4	0.0
							22

Table 11. Total amount of uranium from the B1, B3, and B7 cylindrical soil area

Soil sample	Avg. depth (cm)	U ppm	g U in 1 kg soil	area	% total area	kg soil in cylindrical volume	g U per kg soil
B1-1	1	280	0.3	10050	2.8	1.2	0.3
B1-2	3	323	0.3	10050	2.8	1.2	0.4
B1-3	5	241	0.2	10050	2.8	1.2	0.3
B1-4	7	111	0.1	10050	2.8	1.2	0.1
B1-5	9	68	0.1	10050	2.8	1.2	0.1
B1-6	11	42	0.0	10050	2.8	1.2	0.1
B3-1	1	498	0.5	20735	5.9	2.6	1.3
B3-2	3	593	0.6	20735	5.9	2.6	1.5
B3-3	5	363	0.4	20735	5.9	2.6	0.9
B3-4	7	194	0.2	20735	5.9	2.6	0.5
B3-5	9	142	0.1	20735	5.9	2.6	0.4
B3-6	11	65	0.1	20735	5.9	2.6	0.2
B7-1	1	184	0.2	42097	11.9	5.2	1.0
B7-2	3	131	0.1	42097	11.9	5.2	0.7
B7-3	5	95	0.1	42097	11.9	5.2	0.5
B7-4*	7	31	0.0	42097	11.9	5.2	0.2
							8

4.3.2 Transport of Radionuclides from the Boulder and Within the Soil

The field (curve-fitting) effective dispersion (D_e) and partition coefficients (K_d) and the lab retardation factor and K_d are presented in Table 12. Three examples from the curve fitting results are shown in Figure 58.

Table 12. Retardation factors and partition coefficients for radionuclides in the Peña Blanca soil

	A-D Field		A-D Lab	
Radionuclide	D_e (m^2/s)	K_d (ml/g)	R_f	K_d (ml/g)
U	$2x10^{-12}$	50-150	1,500-9,200	400-3,300
Th	$3x10^{-12}$	15-60	N/A	
Ra	$2x10^{-12}$	200-400		

Free-water diffusion coefficients, partition coefficients, and solubility data for equivalent radionuclides from Yucca Mountain TSPA (DOE, 2004) is used (Table 13). Using diffusion data, the order of free-water diffusion coefficients are Ra>Th>U, but Th appears more soluble than it should be, especially when compared to the values from Li and Gregory (1974) used above; however, the overall difference in diffusion is minor. More importantly, the relative solubilities reflect the likelihood of release. The relative solubilities of each species controlling mineral phase is U>Ra>Th, which are probably a better comparison for the boulder, because the radionuclides would start as minerals.

The data indicate that diffusion occurs, because dissolved U was measured in the leachate experiment. However, the calculated K_d values suggest that Th is moving more rapidly than U or Ra. The Li and Gregory (1974) and Yucca Mountain data (DOE, 2004) indicate dissolved transport should result in Ra and U moving much faster than Th, which should be the least soluble and diffuse the slowest. Thorium is found in nature in the +4 oxidation state and is generally considered immobile as a dissolved species, but can be mobile as an adsorbed or colloidal species (Langmuir, 1978; Langmuir and Herman, 1980; Neck et al., 2003). U and Ra can be strongly sorbed, but Th is less likely to be available to movement given its lower solubility. In addition to relative diffusivities, the U field K_d is much less (1-2 orders of

magnitude) than the lab measured U K_d, so diffusion alone cannot account for how fast transport occurs within the soil.

Table 13. Yucca Mountain TSPA diffusion, partition coefficients, and solubilities

	Radionuclide	D (m^2/s)	K_d (ml/g)	Solubility (mol/l)	
Yucca Mountain	U	$4.9x10^{-10}$ *	0.2	$2.0x10^{-4}$	Schoepite controlled using J-13 water pH=8.5
	Th	$5.0x10^{-10}$ *	5000	$3.2x10^{-9}$	ThO_2 controlled in UZ water pH>6
	Ra	$8.9x10^{-10}$	300	$3.2x10^{-7}$	$Ra(SO_4)$ controlled using J-13 water

*-Mass corrected to UO^{2+} analog

Based on the evidence above, the data also support particle transport, by dispersion and filtration of boulder particles within the soil. The effective dispersion coefficients calculated above are of the same order of magnitude, and because they have a Gaussian distribution, D_e models particulate transport well. The spread of the source material for dissolution should be at a rate of about 10^{-12} m^2/s. Dispersion is supported by the net zero change in the advection component of the A-D equation due to wet/dry cycles. The gamma ray survey map (Figure 52) supports both wind and water transport, which serves as additional evidence for dispersion. The A-D curves (Figure 58) for each radionuclide show similar changes with depth, i.e., the isotope ratios maintain a near constant ratio with depth. Diffusion would show as chromatographic changes in isotope ranges occurring with depth. For example, the $^{226}Ra/^{230}Th$ ratio would become enriched in ^{226}with depth, because Ra is more mobile than Th. Without further research, any observed chromatographic changes are too small to be determined given the limited number of samples. Filtration of boulder particles within the soil, which would have an inherent isotope ratio, would maintain the isotope ratio of the surface sample over each successive depth.

Identifying the dominant mode(s) of transport from the boulder and within the soil is important for source term evaluation. Flaking of the boulder was observed during soil sampling and it is supported by data from the A-D equation. Diffusion is also supported by laboratory and A-D calculations. At present, the relative amounts of each could not be determined. The

greatest strength of the data, but also its greatest weakness, in this study is including all applicable transport parameters. Using this information, it is possible to make definitive statements concerning rates of transport in the environment; however, it is impossible to precisely define the processes influencing that transport.

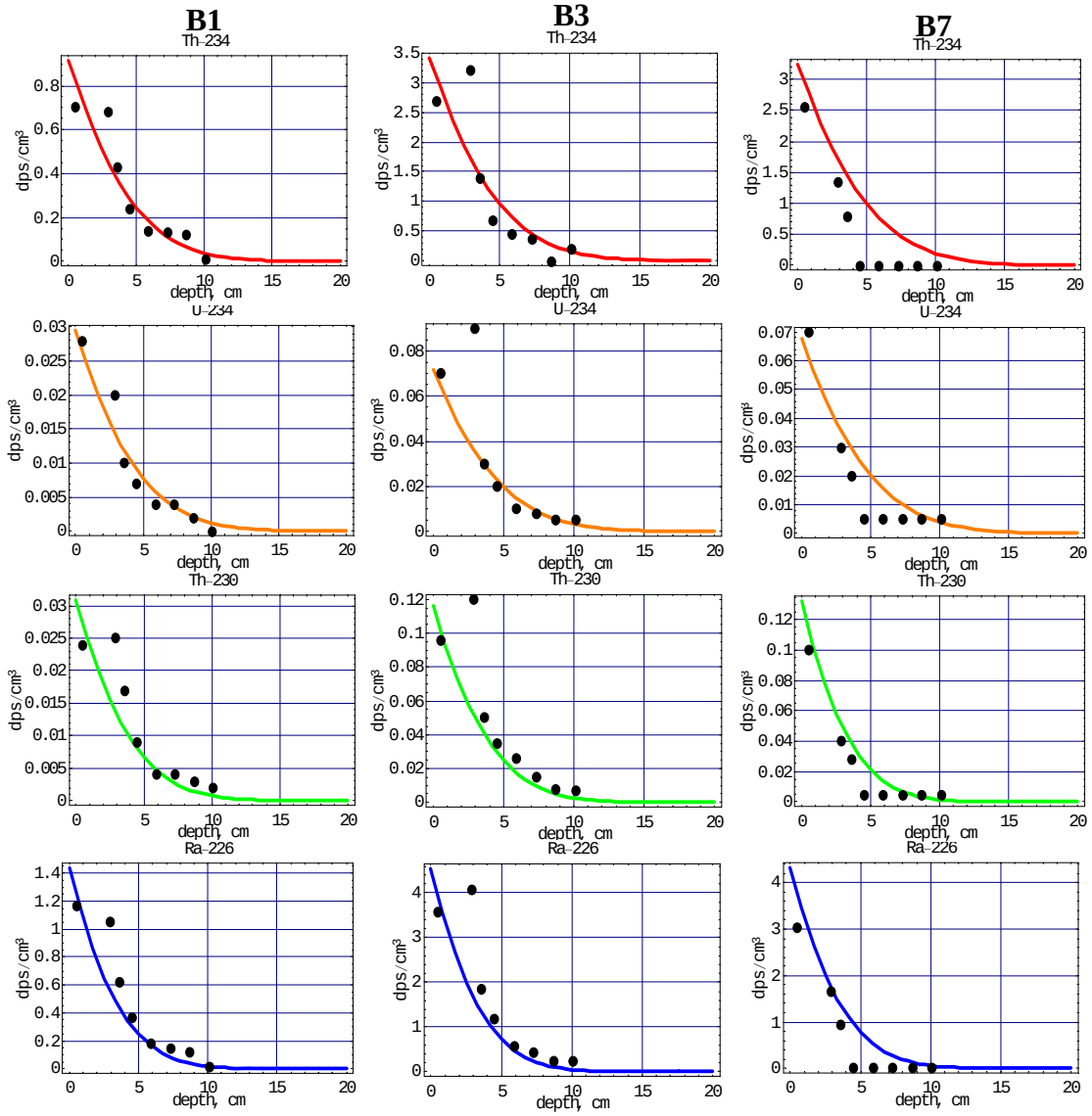

Figure 58. Mathematica curve fitting results. The black dots are the measured gamma activities and the colored lines are the solutions to the A-D equation. The red lines are ^{234}Th, which is assumed to in secular equilibrium with ^{238}U. The orange, green, and blue lines are ^{234}U, ^{230}Th, and ^{226}Ra, respectively.

4.4 CONCLUSIONS

The boundary conditions for radionuclide release from the boulder at Nopal I could not be determined quantitatively. The evidence provided from the leach testing, release rate, U-series ratios, and A-D curves support both diffusion and particle filtration, but their relative amounts could not be determined with the methods presented.

The U release rates from the boulder (12-34 mg U/m^2/day) are ~150 times higher than unsaturated drip tests using UO_2 pellets (0.1-0.3 mg U/m^2/day). The values from laboratory studies are often used in performance assessments of Yucca Mountain, and the results of this study can help model verification. The higher rates from this study represent the uncontrolled, outdoor environment, which could cause increased weathering due to changes in temperature, precipitation, and wind that are not adequately represented in laboratory studies. Future studies of nuclear waste storage could potentially use U ores from similar climates and geology to estimate site specific effects; in a similar way as the Nopal I boulder study is used as a comparison for the Yucca Mountain studies. Even if those values are higher, they would serve as a conservative estimate of release.

Radionuclide transport models for Yucca Mountain generally modeled far-field processes that are likely to be dominated by diffusion. Source term uncertainty dominates performance assessment uncertainty, because of the abundance of far-field research that may not accurately reflect near-field transport. This study suggests both diffusion and particle filtration from boulder flakes occur in the near-field, but their magnitudes are unknown. The mathematical approach to determining the mobilization of radionuclides is limited by its assumptions; this is not the first study to note the difficulty in modeling and calculating the weathering rates by using radionuclides (e.g., Chabaux et al., 2011). Site specific information on the mineralogy and adsorption/desorption in the soil could reduce the uncertainty inherent in the boulder study, in addition to greater sampling. The greatest value of the results of this study is for verification of lab and modeling results where the controls are known.

5. Summary

The Nopal I mine in the Peña Blanca Uranium District, Chihuahua, Mexico is a natural analog for the geologic storage of nuclear waste. This dissertation presents data from two sites within Nopal I: 1) the PB-1 core, which was drilled along the extent of uranium mineralization in the Nopal I mine; and 2) a mineralized boulder from the mineralized Nopal tuff, which rolled away from the high-grade ore stockpile.

The PB-1 core allowed an investigation into the mineralogical and geochemical changes that are important to research on a nuclear waste repository. Five zones were determined to control these changes: 1) Zone 1, the primary uranium mineralization (quartz-uraninite-pyrite-kaolinite-ilmenite); 2) Zone 2, the oxidized equivalent to zone 1; 3) Zones 3a and 3b, which are redox-transition zones; 4) Zone 4, or the Pozos Uranium Anomaly, which was a reducing zone for uranium and other redox sensitive elements; and 5) Zone 5, the Cretaceous limestone, which serves as a barrier to a majority of radionuclide transport. Investigation of uranium minerals showed that the Pozos Uranium Anomaly formed 375 ka-1 Ma, and unlike the primary uranium assemblage, the younger uranium minerals were associated with anatase and kaolinite, indicating their adsorptive capabilities in a potential repository setting. Uranium minerals were only associated with iron oxyhydroxide minerals in one sample, which indicates their ability to adsorb radionuclides may be less than that of kaolinite and anatase. A reducing environment must also be maintained over the long-term life of a repository, because later re-oxidation of the Pozos Uranium Anomaly is indicated by the U-series geochemistry.

The mineralized boulder was analyzed using qualitative and quantitative methods to determine the mode of radionuclide release from the boulder to the soil, the weathering rate, and the transport of radionuclides within the soil from the boulder. The weathering rate of uranium from the boulder (12-34 mg U/m^2/day) is ~150 times higher than in laboratory experiments using UO_2 fuel pellets, which can be explained by differences in field and laboratory controls. The boulder was exposed to daily and seasonal changes in temperature, precipitation, and wind that

are not easily simulated in a laboratory experiment. Models generally use conservative estimates of weathering, so using a higher weathering rate from a non-pure uranium source may be preferable.

Radionuclide transport from the boulder and within the soil is occurs by both diffusion and filtration of boulder flakes through the soil. Their relative magnitudes could not be determined using the methodology presented, but is important for near-field studies that characterize the source term.

References

Al, T.A., C.J. Martin, and D.W. Blowes, 2000, Carbonate-mineral/water interactions in sulfide-rich mine tailings, Geochimica et Cosmochimica Acta, v. 64, p. 3933-3948.

Alba, L.A. and R. Chavez, 1974, K-Ar Ages of Volcanic Rocks From the Sierra Peña Blanca, Chihuahua, Mexico, Isochron West v. 10, p. 21-22.

Altamirano, J.R., 1992, Recent Explorations for Uranium and Molybdenum in the Cuerva Amarilla, Sierra de Peña Blanca, Chihuahua, Mexico, *in*: Energy Resources of the Chihuahua Desert Region, The El Paso Geological Society, p. 192-220.

Aniel, B., and J. Leroy, 1985, The reduced uraniferous mineralizations associated with the volcanic rocks of the Sierra Pena Blanca (Chihuahua, Mexico), American Mineralogist, v. 70, p. 1290-1297.

Arnold, T., N. Baumann, E. Krawczyk-Baersch, S. Brockmann, U. Zimmermann, U. Jenk, and S. Weiss, 2011, Identification of the uranium speciation in an underground acid mine drainage environment, Geochimica et Cosmochimica Acta, v. 75, p. 2200-2212.

Australian Nuclear Science and Technology Organization (ANSTO), 1992, Alligator Rivers Analogue Project Final Report, DOE/HMIP/RR/92/072, SKI TR, v. 92, p. 20-22.

Bachmof, S., and B.J. Merkel, 2001, Sorption of uranium(VI) at the clay mineral-water interface, Environmental Earth Science, v. 63, p. 925-934.

Bass Becking, L.G.M., I.R. Kaplan, and D. Moore, 1960, Limits of the natural environment in terms of pH and oxidation-reduction potentials, Journal of Geology, v. 68, p. 243-284.

Bergey, E.A., 2006, Measuring the surface roughness of stream stones, Hydrobiologia, v. 563, p. 247-252.

Blowes, D.W., E.J. Reardon, J.L. Jambor, and J.A. Cherry, 1991, The formation and potential importance of cemented layers in inactive sulfide mine tailings, Geochimica et Cosmochimica Acta, v. 55, p. 965-978.

Blowes, D.W., C.J. Ptacek, and J. Jurjovec, 2003, Mill tailings: hydrogeology and geochemistry, *in*: D.W. Blowes, J.L. Jambor, and A.I.M. Ritchie, eds., The Environmental Geochemistry of Sulfide Mine-Wastes, Short Course Handbook, v. 31, p. 95-116.

Brookins, D.G., 1988, Eh-pH diagrams for geochemistry, New York: Springer-Verlag, 176 p.

Bruggeman, C., and N. Maes, 2010, Uptake of Uranium(VI) by Pyrite under Boom Clay Conditions: Influence of Dissolved Organic Carbon, v. 44, p. 4210-4216.

Bruno, J., L. Duro, and M. Grivé, 2002, The applicability and limitations of thermodynamic geochemical models to simulate trace element behaviour in natural waters. Lessons learned from natural analogue studies. Chemical Geology v. 190, p. 371-393.

Bruno, J., and R.C. Ewing, 2006, Spent nuclear fuel, Elements, v. 2, p. 343-349.

Bryan, C.R., M. Spilde, H. Xu, C. Schloesslin, and K.M. Davis, 2004, Results of uranium adsorption/desorption experiments and microanalytical studies characterizing sediment samples from the Great Miami Aquifer, Fernald DOE Site, Ohio, SAND2004-4085, 76 p.

Buck, E.C., Hanson, B.D., McNamara, B.K., 2004, The geochemical behaviour of Tc, Np and Pu in spent nuclear fuel in an oxidizing environment, *in*: Gieré, R., Stille, P., eds., Energy, Waste, and the Environment: a Geochemical Perspective, The Geological Society of London Special Publication, v. 236, p. 65-88.

Burns, P.C., R.C. Ewing, and F.C. Hawthorne, 1997a, The crystal chemistry of hexavalent uranium: polyhedral geometries, bond-valence parameters, and polymerization of polyhedra, Canadian Mineralogist v. 35, p. 1551-1570.

Burns, P.C., R.C. Ewing, and M.L. Miller, 1997b, Incorporation mechanisms of actinide elements into the structures of U^{6+} phases formed during the oxidation of spent nuclear fuel, Journal of Nuclear Materials v. 245, p. 1-9.

Burns, P.C., K.M. Deely, and S. Skanthakumar, 2004, Neptunium incorporation into uranyl compounds that form as alteration products of spent nuclear fuel: Implications for geologic repository performance, Radiochimica Acta, v. 92, p. 151-160.

Burns, P.C., 2005, U^{6+} minerals and inorganic compounds: insights into an expanded structural hierarchy of crystal structures, Canadian Mineralogist, v. 43, p. 1839-1894.

Burns, P.C., and A.L. Klingensmith, 2006, Uranium Mineralogy and Neptunium Mobility, Elements, v. 2, p. 351-356.

Calas, G., 1977, Les phenomenes d'alteration hydrothermale et leur relation avec les mineralizations uraniferes en milieu volcanique: le cas de ignibrites tertiaires de la Sierra Peña Blanca, Chihuahua (Mexique), Sciences Geologique Bulletin, v. 30, p. 3-18.

Calas, G., P. Agrinier, T. Allard, and P. Ildefonse, 2008, Alteration geochemistry of the Nopal I uranium deposit (Sierra Peña Blanca, Mexico), a natural analogue for a radioactive waste repository in volcanic tuffs, Terra Nova, v. 20, no. 3, p. 206-212.

Calas, G., S. Angiboust, M. Fayek, A. Camacho, T. Allard, and P. Agrinier, 2009, Epithermal uranium deposits in a volcanogenic context: the example of Nopal 1 deposit, Sierra de Pena Blanca, Mexico, EOS Transactions, AGU, v. 90, Abstract V54C-02.

Canfield, D.E., 2004, The evolution of the Earth surface sulfur reservoir, American Journal of Science, v. 304, p. 839-861.

Cardenas-Flores, D., 1985, Volcanic stratigraphy and U-Mo mineralization of the Sierra de Peña Blanca District, Chihuahua, Mexico, *in*: P.C. Goodell and A.C. Waters, eds., Uranium Deposits in Volcanic and Volcaniclastic Rocks, American Association of Petroleum Geologists Studies in Geology, v. 13, p. 125-136.

Caruso, L., T. Swinden, and G. Simmons, 1982, Uranium migration through microcracks, Geevor Tin Mine, Cornwall, England, EOS Transactions, AGU, v. 63, Abstract 1128.

Catalano J.G., and G.E. Brown, Jr, 2005, Uranyl adsorption onto montmorillonite: Evaluation of binding sites and carbonate complexation, Geochimica et Cosmochimica Acta, v. 69, p. 2995-3005.

Conca, J.L., and J. Wright, 1990, Diffusion Coefficients in Gravel Under Unsaturated Conditions, Water Resources Research, v. 26, no. 5, p. 1055-1066.

Cramer, J.J., 1986, Sandstone-hosted uranium deposits in northern Saskatchewan as natural analogs to nuclear fuel waste disposal vaults, Chemical Geology, v. 55, p. 269-279.

Curtis, D.B., T.M. Benjamin, and A.J. Gancarza, 1981, The Oklo reactors: natural analogs to nuclear waste repositories, *in*: Hofman, P.L., ed., The Technology of High-level Nuclear Waste Disposal, DOE/TIC-4621, p. 255-283.

Davis, J.A., and G.P. Curtis, 2007, Consideration of Geochemical Issues in Groundwater Restoration at Uranium In-Situ Leach Mining Facilities, U.S. Nuclear Regulatory Commission and U.S. Geological Survey, NUREG/CR-6780, 150 p.

Day, W.C., R.P. Dickerson, C.J. Potter, D.S. Sweetkind, C.A. San Juan, R.M. Drake, and C.J. Fridich, 1999, Bedrock Geologic Map of the Yucca Mountain Area, Nye County, Nevada, U.S. Geological Survey Miscellaneous Investigations Series Map I-2627, U.S. Geological Survey, Denver, Colorado.

Descostes, M., M.L. Schlegel, N. Eglizaud, F. Descamps, F. Miserque, and E. Simoni, 2010, Uptake of uranium and trace elements in pyrite (FeS_2) suspensions, Geochimica et Cosmochimica Acta, v. 74, p. 1551-1562.

Dobson, P.F., M. Fayek, P.C. Goodell, T.A Ghezzehei, F. Melchor, M.T. Murrell, R. Oliver, I.A. Reyes-Cortes, R. de la Garza, and A. Simmons, 2008, Stratigraphy of the PB-1 Well, Nopal I Uranium Deposit, Sierra Peña Blanca, Chihuahua, Mexico, International Geology Review, v. 50, p. 959-974.

Dolcater, D.L., J.K. Syers, and M.L. Jackson, 1970, Titanium as free oxide and substituted forms in kaolinites and other soil minerals, Clay and Clay Minerals, v. 18, p. 71-79.

Donald, R., and G. Southam, 1999, Low temperature anaerobic bacterial diagenesis of ferrous monosulfide to pyrite, Geochimica et Cosmochimica Acta, v. 63, p. 2019-2023.

Douglas, G.B., Butt, C.R.M., and Gray, D.J., 2011, Geology, geochemistry and mineralogy of the lignite-hosted Ambassador palaeochannel uranium and multi-element deposit, Gunbarrel Basin, Western Australia, Mineralium Deposita, published online April 27, DOI 10.1007/s00126-011-0349-4, p. 1-27.

Drake, H., E.-L. Tullborg, A.B. MacKenzie, 2009, Detecting the near-surface redox front in crystalline bedrock using fracture mineral distribution, geochemistry and U-series disequilibrium, Applied Geochemistry, v. 24, p. 1023-1039.

Fabryka-Martin, J.T., S.J. Wightman, W.J. Murphy, M.P. Wickham, M.W. Caffee, 1993, Distribution of chlorine-36 in the unsaturated zone at Yucca Mountain: an indicator of fast transport paths, *in*: FOCUS ’93, Site Characterization and Model Validation, Las Vegas, NV, Las Grange Park, IL: American Nuclear Society, p. 58-68.

Fayek, M., T.K. Kyser, and L.R. Riciputi, 2002, U an Pb isotope analysis of uranium minerals by ion microprobe and the geochronology of the McArthur River and Sue Zone uranium deposits, Saskatchewan, Canada, The Canadian Mineralogist, v. 40, p. 1553-1569.

Fayek, M., M. Ren, P. Goodell, P. Dobson, A. Saucedo, A, Kelts, S. Utsunomiya, R.C. Ewing., L.R. Riciputi, and I. Reyes, 2006, Paragenesis and geochronology of the Nopal I uranium deposit, Mexico, Proceedings of the 11th International High-Level Radioactive Waste Management Conference, Las Vegas, NV, April 30-May 2, p. 55-62.

Finch, R.J., and R.C. Ewing, 1991, Alteration of natural UO_2 under oxidizing conditions from Shinkolobwe, Katanga, Zaire: a natural analogue for the corrosion of spent fuel, Radiochimica Acta, v. 52/53, p. 395-401.

Finch, R.J., and R.C. Ewing, 1992, The corrosion of uraninite under oxidizing conditions, Journal of Nuclear Materials, v. 190, p. 133-156.

French, D.C., 2006, Gamma-ray Characterization of the U-series Intermediate Daughters from Soil Samples at the Peña Blanca Natural Analog, Chihuahua, Mexico, University of Texas at El Paso, M.S. Thesis, 64 p.

French, D.C., E.Y. Anthony, and P.C. Goodell, 2006, U-Series Disequilibrium in Soils, Peña Blanca Natural Analog, Chihuahua, Mexico, Proceedings of the 11th International High-Level Radioactive Waste Management Conference, Las Vegas, NV, April 30-May 2, p. 63-69.

Fuller, C.M., 1990, Fracture and permeability Analysis of the Santana Tuff, Trans-Pecos Texas, University of Texas at Austin, M.A. Thesis, 116 p.

Gabriela, U., J.-P. Gaudet, L. Spadini, and L. Charlet, 1998, Reactive transport of uranyl in a goethite column: an experimental and modelling study, Chemical Geology, v. 151, no. 1-4, p. 107-128.

Gascoyne, M., N.H. Miller, L.A., Neymark, 2002, Uranium-series disequilibrium in tuffs from Yucca Mountain, Nevada, as evidence of pore-fluid flow over the last million years, Applied Geochemistry, v. 17, p. 781–792.

George-Aniel, B., I. Leroy, and B. Poty, 1991, Volcanogenic uranium mineralization in the Sierra de Peña Blanca District, Chihuahua, Mexico: Three genetic models, Economic Geology, v. 86, p. 233-248.

Giammar, D.E., and J.G. Hering, 2001, Time Scales for Sorption-Desorption and surface Precipitation of Uranyl on Goethite, Environmental Science and Technology, v. 35, p. 3332-3337.

Gilbert, J.M., and C.F. Park, Jr., 2007, The Geology of Ore Deposits, Long Grove, IL: Waveland Press, 985 p.

Goodell, P. C., 1981, Geology of the Peña Blanca uranium deposit, Chihuahua, Mexico, *in*: P.C. Goodell and A.C. Waters, eds., Uranium Deposits in Volcanic and Volcaniclastic Rocks, American Association of Petroleum Geologists Studies in Geology, v. 13, p. 275-291.

Goodell, P.C., 1985, Chihuahua city uranium province, *in*: Uranium Deposits in Volcanic Rocks, IAEA, ed., International Atomic Energy Agency, IAEA-TC-490/19, p. 97-124.

Goodell, P., M. Fayek, M. Murrell, P. Dobson, and R. Oliver, 2003, Descriptions of core samples from PB-1 well (based on transcribed notes), *in*: P.F. Dobson, ed., Core Description for PB-1, Data Tracking Number LB0402PBCORELG.001. (http://www.lsnnet.gov/, Licensing Support Network access number DN2001644400)

Goldstein, S.J., A. Abdel-Fattah, M.T. Murrell, P.F. Dobson, D.E. Norman, R.S. Amato, and A.J. Nunn, 2010, Uranium-Series Constraints on Radionuclide Transport and Groundwater

Flow at the Nopal I Uranium Deposit, Sierra Peña Blanca, Mexico, Environmental Science and Technology, v. 44, p. 1579-1586.

Gordon, S.J., and Dorn, R.I., 2005, Localized Weathering: Implications for Theoretical and Applied Studies, The professional Geographer, v. 57, p. 28-43.

Graham, A.A., D.J. McCaughan, and F.S. McKee, 1988, Measurement of surface area of stones, Hydrobiologia, v. 157, p. 85-87.

Granger, H.C., and C.G. Warren, 1974, Zoning in the altered tongue associated with roll-type uranium deposits, *in*: Formation of Uranium Roll Fronts, International Atomic Energy Agency: Vienna, p. 185-200.

Gunsinger, M.R., C.J. Ptacek, D.W. Blowes, J.L. Jambor, and M.C. Moncur, 2006, Mechanisms controlling acid neutralization and metal mobility within a Ni-rich tailings impoundment, Applied Geochemistry, v. 21, p. 1301-1321.

Hammarstrom, J.M., P.L. Sibrell, and H.E. Belkin, 2003, Characterization of limestone reacted with acid-mine drainage in a pulsed limestone bed treatment system at the Friendship Hill National Historical Site, Pennsylvania, USA, Applied Geochemistry, v. 18, p. 1705-1721.

Harrod, J.J., and R.E. Hall, 1962, A method for determining the surface areas of various aquatic plants, Hydrobiologia, v. 20, p. 173-178.

Harshman, E.N., 1972, Geology and uranium deposits, Shirley Basin area, Wyoming: U.S. Geological Survey Professional Paper 745, 82 p.

Hayes, J.M., I.B. Lambert, H. Strauss, 1992, The sulfur-isotopic record, *in*: Schopf, J.W., and C. Klein, eds., The Proterozoic Biosphere, Cambridge University Press, p. 129-132.

Holloway, J .R., D.M. Jenkins, and J.D. Clemens, 1982, Experimental evidence for the effects of basalt on radionuclide levels in hot waste, *in*: R. Roy, ed., Waste Management '82, Univ. of Arizona, Tucson, AZ, v. 2, p. 369-379.

Hsi, C.-K.D., 1981, Sorption of Uranium (VI) by iron oxides, Ph.D. Dissertation, Colorado School of Mines, 154 p.

Hsi, C.-K.D., and D. Langmuir, 1985, Adsorption of uranyl onto ferric oxyhydroxides: applications of a surface complexation site binding model, Geochimica et Cosmochimica Acta, v. 49, p. 2423-2432.

Ildefonse, P., P. Agrineier, and J.P. Muller, 1990a, Crystal chemistry and isotope geochemistry of alteration associated with the Nopal I uranium deposit, Chihuahua, Mexico, Chemical Geology, v. 84, p. 371-372.

Ildefonse, P., J.P. Muller, B. Clozel, and G. Calas, 1990b, Study of two alteration systems as natural analogues for radionuclide release and migration, Engineering Geology, v. 29, p. 413-439.

International Atomic Energy Agency (IAEA), 1999, Use of natural analogues to support radionuclide transport models for deep geological repositories for long lived radioactive wastes, IAEA-TECDOC-1109, 39 p.

Ivanovich, M., 1991, Aspects of Uranium/Thorium Series Disequilibrium Applications to Radionuclide Migration Studies, Radiochimica Acta, v. 52/53, p. 257-268.

Janeczek, J., and R.C. Ewing, 1992, Structural formula of uraninite, Journal of Nuclear Materials, v. 190, p. 128-132.

Janeczek, J., R.C. Ewing, V.M. Oversby, and L.O. Werme, 1996, Uraninite and UO_2 in spent nuclear fuel: a comparison, Journal of Nuclear Materials, v. 238, p. 121-130.

Janeczek J., 1999, Mineralogy and geochemistry of natural fission reactors in Gabon, *in*: Burns, P.C., Finch, R., eds., Uranium: Mineralogy, Geochemistry and the Environment, Reviews in Mineralogy and Geochemistry, v. 38, p. 321-392.

Jefferson C.W., D. Thomas, S.S. Gandhi, P. Ramaekers, G. Delauney, D. Brisbin, C. Cutts, P. Portella, and R.A. Olson, 2007, Unconformity associated uranium deposits of the Athabasca Basin, Saskatchewan and Alberta, *in*: C.W. Jefferson, and G. Delaney, eds., EXTECH IV: Geology and Uranium EXploration TECHnology of the Proterozoic Athabasca Basin, Saskatchewan and Alberta, Geological Survey of Canada Bulletin, v. 588, p. 23-67.

Johnson, L.H., and D.W. Shoesmith, 1988, Spent fuel, *in*: W. Lutze, and R.C. Ewing, eds., Radioactive Waste Forms for the Future, Elsevier: Amsterdam, p. 635-698.

Johnson, L., Ferry, C., Poinssot, C., Lovera, P., 2005, Spent fuel radionuclide sourceterm model for assessing spent fuel performance in geological disposal, Part I: Assessment of the instant release fraction, Journal of Nuclear Materials, v. 346, p. 56-65.

Jørgensen, B.B., M.F. Isaksen, H.W. Jannasch, 1992, Bacterial sulfate reduction above 100°C in deep-sea hydrothermal vent sediments, Science v. 258, p. 1756-1757.

Kotzer, T.G., and T.K. Kyser, 1995, Petrogenesis of the Proterozoic Athabasca Basin, northern Saskatchewan, Canada, and its relation to diagenesis, hydrothermal uranium mineralization and paleohydrogeology, Chemical Geology, v. 120, p. 45-89.

Kuroda, P.K., 1956, On the nuclear physical stability of the uranium minerals, Journal of Chemical Physics, v. 25, p.781-782.

Kyser, K., and M. Cuney, 2008, Unconformity-related uranium deposits, *in*: M. Cuney, and K. Kyser, eds., Recent and not-so-recent developments in uranium deposits and implications for exploration, Mineralogical Association of Canada Short Course Series, v. 39, p. 161-219.

Langmuir, D., 1978, Uranium solution-minerals equilibria at low temperatures with application to sedimentary ore deposits, Geochimica et Cosmochimica Acta, v. 42, p. 547-569.

Langmuir, D., and J.S. Herman, 1980, The mobility of thorium in natural waters at low temperatures, Geochimica et Cosmochimica Acta, v. 44, p. 1753-1766.

Larsen, E.S., and D. Gottfried, 1960, Uranium and Thorium in selected suites of igneous rocks, American Journal of Science, Bradley Volume, v. 258-A, p. 151-169.

Laul, J.C., 1992, Natural Radionuclides in Groundwaters, Journal of Radioanalytical and Nuclear Chemistry, v. 156, p. 235-242.

Leroy, J.L., B. Aniel, and B. Poty, 1987, The Sierra Peña Blanca (Mexico) and the Meseta Los Frailes (Bolivia): The Uranium Concentration Mechanisms in Volcanic Environment during Hydrothermal Processes, Uranium, v. 3, p. 211-234.

Leslie, B.W., E.C. Pearcy, and J.D. Prikryl, 1993, Oxidative alteration of uraninite under hydrologically unsaturated conditions at Peña Blanca, Chihuahua, Mexico: contaminant transport and source term constraints for the proposed repository at Yucca Mountain, Nevada, *in*: Interrante, C.G., and R.T. Pabalan, eds., Scientific Basis for Nuclear Waste Management XVI, Materials Research Society Symposium Proceedings, v. 294, p. 505-512.

Levy, S., S. Goldstein, P.F. Dobson, P. Goodell, T-L. Ku, A. Abdel-Fattah, G. Saulnier, M. Fayek, and R. de la Garza, 2011, Peña Blanca Natural Analogue Project: Summary of Activities, Proceedings of the 13th International High-Level Radioactive Waste Management Conference, Albuquerque, NM, April 10-14, p. 330-341.

Li, Y.-H., and S. Gregory, 1974, Diffusion of ions in seawater and deep-sea sediments, Geochimica et Cosmochimica Acta, v. 38, p. 703-714.

Lindroos, H., and J. Smellie, 1979, A stratabound Uranium occurrence within Middle Precambrian Ignimbrites at Duoblon, North Sweden, Economic Geology, v. 74, p. 1118-1130.

Loida A., B. Grambow, H. Geckeis, and P. Dressier, 1995, Processes controlling radionuclide release from spent fuel, Materials Research Society Symposium Proceedings, v. 353, p. 577-584.

Lueth, V.W., R.O. Rye, and L. Peters, 2005, "Sour gas" hydrothermal jarosite: ancient to modern acid-sulfate mineralization in the southern Rio Grande Rift, Chemical Geology, v. 215, p. 339-360.

Machel, H.G., H.R. Krouse, R. Sassen, 1995, Products and distinguishing criteria of bacterial and thermochemical sulfate reduction, Applied Geochemistry, v. 10, p. 373–389.

Magonthier, M.C., 1984, Les ignimbrites de la Sierra Madre occidentale et de la province uranifere de la Sierra Pen a Blanca, Mexique. Mèm. Sci. Terre, University of Paris et M. Curie, v. 84-17, 351 p.

McEachern, R.J., and P. Taylor, 1998, A review of oxidation of uranium dioxide at temperatures below 400°C, Journal of Nuclear Materials, v. 254, p. 87-121.

Mercadier, J., M. Cuney, M. Cathelineau, and M. Lacorde, 2011, U redox fronts and kaolinisation in basement-hosted unconformity-related U ores of the Athabasca Basin (Canada): late U remobilisation by meteoric fluids, Mineralium Deposita, v. 46, p. 105-135.

Meshik, A.P., 2005, "The Workings of an Ancient Nuclear Reactor," Scientific American, October 2005, p. 82-91.

Min, M., H. Xu, J. Chen, and M. Fayek, 2005, Evidence of uranium biomineralization in sandstone-hosted roll-front uranium deposits, northwestern China, Ore Geology Reviews, v. 26, p. 198-206.

Moncur, M.C., C.J. Ptacek, D.W. Blowes, and J.L. Jambor, 2005, Release, transport and attenuation of metals from an old tailings impoundment, Applied Geochemistry, v. 20, p. 639-659.

Munfrom, D.J., D.G. Shaw, and T.L. Ke, 2005, Minimum sample sizes for conducting factor analyses, International Journal of Testing, v. 5, no. 2, p. 159-168.

Murphy, W.M., and R.B. Codell, 1999, Alternate Source Term Models for Yucca Mountain Performance Assessment based on Natural Analog Data and Secondary Mineral Solubility, Material Research Society Symposium Proceedings, v. 556, p. 551.

Murphy, W.M, and D.A. Pickett, 2002, Radioisotope Fractionation and Secular Disequilibrium in Performance Assessment for Geological Disposal of Nuclear Waste, Material Research Society Symposium Proceedings, v. 713, p. 867-874.

Murrell, M.T., p. Paviet-Hartmann, S.J. Goldstein, A.J. Nunn, R.C. Roback, P.A. Dixon, and A. Simmons, U-Series Natural Analog Studies at Pena Blanca, Mexico: How Mobile is Uranium?, EOS Transactions, AGU, v. 80, Abstract V52D-08.

Murrell, M.T., S.J. Goldstein, and P.A. Dixon, 2002, Uranium Decay Series Mobility at Peña Blanca, Mexico: Implications for Nuclear Repository Stability, *in*: von Maravic, H. and W.R. Alexander, eds., 8th European Commission Natural Analogue Working Group Meeting, European Commission Nuclear Science and Technology, EUR 19118 EN, p. 339-343.

National Academy of Sciences (NAS), 1995, Technical Bases for Yucca Mountain Standards, National Research Council, Committee on Technical Bases for Yucca Mountain Standards, National Academies Press: Washington, D.C., 222 p.

Navarre-Sitchler, A., and Brantley, S., 2007, Basalt weathering across scales, Earth and Planetary Science Letters, v. 261, p. 321-334.

Neck, V., M. Altmaier, R. Müller, A. Bauer, T. Fanghänel, and J.-I. Kim, 2003, Solubility of crystalline thorium dioxide, Radiochimica Acta, v. 91, no. 5, p. 253-262.

Nicholl, M.J., R.J. Glass, S.W. Wheatcraft, 1994, Gravity-driven infiltration instability in initially dry nonhorizontal fractures, Water Resources Research, v. 30, no. 9, p. 2533-2546.

Nordstrom, D.K., C.N. Alpers, C.J. Ptacek, and D.W. Blowes, 2000, Negative pH and extremely acidic mine waters from Iron Mountain, California, Environmental Science and Technology, v. 34, p. 254-258.

Ohmoto H., and M.B. Goldhaber, 1997, Sulfur and carbon isotopes, *in*: Barnes, H.L., ed., Geochemistry of Hydrothermal Ore Deposits, J. Wiley and Sons, p. 517-611.

Oliver, R.D., J.C. Dinsmoor, I. Reyes-Cortes, R. de la Garza Aguilar, 2005, Initial Test Well Conditioning at Nopal I, Uranium Deposit, Sierra Peña Blanca, Chihuahua, Mexico (presentation), GSA Annual Meeting, October 16-19, Salt Lake City, Utah. (http://www.osti.gov/bridge/product.biblio.jsp?query_id=0&page=0&osti_id=860240&Row=0).

Osmond, J. K., and M. Ivanovich, 1992, U-series mobilization and surface hydrology, *in*: N. Ivanovich and R.S. Harmon, eds., Uranium-Series Disequilibrium: Application to Earth, Marine, and Environmental Sciences, Clarendon: Oxford, UK, p. 259-289.

Oversby, V.M., 1994, Nuclear Waste Materials, *in*: Cahn R.W., Haasen, P., Kramer E.J., eds., Materials Science and Technology, Chapter 12, v. 10B, VCH Verlagsgessellschaft mbH, p. 391-442.

Oversby, V.M., 1999, Uranium Dioxide, SIMFUEL, and Spent Fuel Dissolution Rates – A Review of Published Data, SKB Technical Report 99-22, Swedish Nuclear Fuel and Waste Management Co., 35 p.

Paces, J.B., L.A. Neymark, G.J. Nunz, M. Gascoyne, B.C. Marshall, J.F. Whelan, , Z.E. Peterman, 1996, Ages and Origins of Subsurface Secondary Minerals in the Exploratory Studies Facility (ESF), USGS Milestone Report 3GQH450M, Washington, DC: USGS Yucca Mountain Project Branch, 55 pp.

Payne, T.E., J.A. Davis, G.R. Lumpkin, R. Chisari, T.D. Waite, 2004, Surface complexation model of uranyl sorption on Georgia kaolinite, Applied Clay Science, v. 26, p. 151-162.

Pearcy, E.C., J.D. Prikryl, W.M. Murphy, and B.W. Leslie, 1994, Alteration of Uraninite From the Nopal 1 Deposit, Pena Blanca District, Chihuahua, Mexico, Compared to Degradation of Spent Nuclear Fuel in the Proposed U.S. High-Level Nuclear Waste Repository at Yucca Mountain, Nevada, Applied Geochemistry v. 9, p. 713-732.

Pearcy, E.C., J. D. Prikryl, and B.W. Leslie, 1995, Uranium Transport Through Fractured Silicic Tuff and Relative Retention in Areas With Distinct Fracture Characteristics, Applied Geochemistry, v. 10, p. 685-704.

Pekar, K., J. Walton, and P. Goodell, 2008, Modeling of Transport Rates Through Unsaturated Soil at Peña Blanca, Proceedings of the 8th International High-Level Radioactive Waste Management Conference, Las Vegas, NV, September 7-11, p. 196-203.

Peterman, Z.E., and P.L. Cloke, 2002, Geochemistry of rock units at the potential repository level, Yucca Mountain, Nevada, Applied Geochemistry, v. 17, p. 683-698.

Pickett, D.A. and W.M. Murphy, 1997, Isotopic Constraints on Radionuclide Transport at Peña Blanca, *in*: von Maravic, H. and Smellie, J., eds.,7th European Commission Natural Analogue Working Group Meeting, European Commission Nuclear Science and Technology, EUR 17851 EN, p. 113-122.

Pickett, D., B. Leslie, W. Murphy, and M. Nugent, 2000, Estimating Radionuclide Release from a Uranium Deposit Through Uranium-Series Systematics in Carbonates and Opal, Goldschmidt Conference Sept. 3-8, Journal of conference Abstracts, v. 5, no. 2., p. 797.

Pickett, D.A. and W.M. Murphy, 2002, Uranium chemistry and isotopy in waters and rocks at Peña Blanca, *in*: von Maravic, H. and W.R. Alexander, eds., 8th European Commission Natural Analogue Working Group Meeting, European Commission Nuclear Science and Technology, EUR 19118 EN, p. 333-337.

Pigford, T.H., and P.L. Chambre, 1988, Near-field Mass Transfer in Geologic Disposal Systems: A Review, Materials Research Society Symposium Proceedings, v.112, p. 125.

Poinssot, C., Ferry, C., Lovera, P., Jégou, C., Gras, J.-M., 2005a, Spent fuel radionuclide source term model for assessing spent fuel performance in geological disposal, Part II: Matrix alteration model and global performance, Journal of Nuclear Materials, v. 346, p. 66-77.

Poinssot, C. et al., 2005b, Final Report of the European Project "Spent Fuel Stability under Repository Conditions" FIKW-CT-2001-00192 SFS, Poinssot C. (CEA), and Ferry, C. (CEA), Report CEA-R-6090, Commissariat à l'Énergie Atomique, Saclay, 104 p.

Pointer, C.M., Ashworth, J.R., and Simpson, P.R., 1989, Genesis of coffinite and the U-Ti association in Lower Old Red Sandstone sediments, Ousdale, Caithness, Scotland, Mineralium Deposita, v., 24, p. 112-123.

Preacher, K.J, and R.C. MacCallum, 2002, Exploratory factor analysis in behavior genetics research: factor recovery with small sample sizes, Behavior Genetics, v. 32, no. 2, p. 153-161.

Prikryl, J.D., D.A. Pickett, W.M. Murphy, and B.W. Leslie, 1997, Migration behavior of naturally occurring radionuclides at the Nopal I uranium deposit, Chihuahua, Mexico, Journal of Contaminant Hydrology, v. 26, p. 61-69.

Quafoku, N.P., R.K. Kukkadapu, J.P. Mckinley, B.W. Arey, S.D. Kelly, C. Wang, C.T. Resch, and P.E. Long, 2009, Uranium in Framboidal Pyrite from a Naturally Bioreduced Alluvial Sediment, Environmental Science and Technology, v. 43, p. 8528-8534.

Quiñones, J., B. Grambow, A. Loida, and H. Geckeis, 1996, Coprecipitation phenomena during spent fuel dissolution. Part 1: Experimental procedure and initial results on trivalent ion behaviour, Journal of Nuclear Materials, v. 238, p. 38-43.

Rackley, R.I., 1976, Origin of western-states-type uranium mineralization, *in*: Wolf, K.H., ed., Handbook of Stratabound and Stratiform Ore Deposits, v. 7, New York: Elsevier, p. 89-156.

Rearick, M., P. Dobson, S. Goldstein, J.A. Rodriguez, and S. Levy, unpublished, Groundwater analyses for Nopal I and the Peña Blanca Region, Chihuahua, Mexico.

Reed, S.J.B., 1989, Ion-microprobe analysis–a review of geological applications, Mineralogical Magazine, v. 53, p. 3-24.

Reyes-Cortes, I.A., 1997, Geologic Studies in the Sierra de Peña Blanca Chihuahua, Mexico, University of Texas at El Paso, Ph.D. Dissertation, 342 p.

Reyes-Cortes, I.A., 2002, Geologic setting and mineralization: Sierra Peña Blanca, Chihuahua, Mexico, *in*: von Maravic, H. and W.R. Alexander, eds., 8th European Commission Natural Analogue Working Group Meeting, European Commission Nuclear Science and Technology, EUR 19118 EN, p. 321-331.

Reynolds, R.L., Goldhaber, M.B., and Grauch, R.I., 1977, Uranium associated with iron-titanium oxide minerals and their alteration products in a South Texas roll-type deposit, *in*: Campbell, J. A., ed., Short papers of the U.S. Geological Survey Uranium-Thorium Symposium, 1977, U.S. Geological Survey Circular 753, p. 37-39.

Reynolds, R.L., M.B. Goldhaber, and D.J. Carpenter, 1982, Biogenic and Nonbiogenic Ore-Forming Processes in the South Texas Uranium District: Evidence from the Panna Maria Deposit, Economic Geology, v. 77, p. 541-556.

Robertson, F.N., 1975, Hexavalent chromium in the ground water in Paradise Valley, Arizona, Ground Water, v. 13, p. 516-527.

Rutgers van der Loeff, M.M., and D.A. Waijers, 1986, Application of Distribution Coefficients to Radiological Distribution Models, T.H. Sibley and C. Myttenaere (eds.), Application of distribution coefficients to radiological distribution models, Elsevier: London, UK, p. 181-190.

Rye, R.O., and C.N. Alpers, 1997, The stable isotope geochemistry of jarosite, U.S. Geological Survey Open-File Report, p. 88-97.

Salve, R., C.M. Oldenburg, J.S.Y. Wang, 2003, Fault-matrix interactions in non-welded tuff of the Painbrush Group at Yucca Mountain, Journal of Contaminant Hydrology, v. 62-63, p. 269-286.

Schaffer, M.B., 2011, Toward a viable nuclear waste disposal program, Energy policy, v. 39, p. 1382-1388.

Schoonen, M.A.A., and H.L. Barnes, 1991a, Reactions forming pyrite: I. Nucleation of FeS2 below 100°C, Geochimica et Cosmochimica Acta, v. 55, p. 1495-1504.

Schoonen, M.A.A., and H.L. Barnes, 1991b, Reactions forming pyrite and marcasite from solution: II. Via FeS_2 precursors below 100°C, Geochimica et Cosmochimica Acta, v. 55, p. 1505-1514.

Scism, C.D., 2006, The Sorption/Desorption Behavior of Uranium in Transport Studies Using Yucca Mountain Alluvium, M.S. Thesis, University of New Mexico, LA-14271-T, 116 p.

Scott, T.B., O. Riba Tort, and G.C. Allen, 2007, Aqueous uptake of uranium onto pyrite surfaces: reactivity of fresh versus weathered material, Geochimica et Cosmochimica Acta, v. 71, p. 5044-5053.

Seal, R.R. II, 2006, Sulfur Isotope Geochemistry of Sulfide Minerals, *in*: Vaughan, D.J., ed., Reviews in Mineralogy and Geochemistry, v. 61, p. 633-677.

Serne, R.J., C.F. Brown, H.T. Schaef, E.M. Pierce, J. Lindberg, Z. Wang, P. Gassman, J. Catalano, 2002, 300 Area Uranium Leach and Adsorption Project, PNNL 14022, 80 p.

Sharpe, S.E., 2007, Using modern through mid-Pleistocene climate proxy data to bound future variations in infiltration at Yucca Mountain, Nevada, *in*: Stuckless, J.S., and R.A. Levich, eds., The Geology and Climatology of Yucca Mountain and Vicinity, Southern Nevada and California, Geological Society of America Memoir, 119 p.

Shoesmith, D.W., 2000, Fuel corrosion processes under waste disposal conditions, Journal of Nuclear Materials, v. 282, p. 1-31.

Sidenko, N.V., and B.L. Sherriff, 2005, The attenuation of Ni, Zn and Cu, by secondary Fe phases of different crystallinity from surface and ground water of two sulfide mine tailings in Manitoba, Canada, Applied Geochemistry, v. 20, p. 1180-1194.

Simmons, A.M., and J.S. Stuckless, 2010, Analogues to features and processes of a high-level radioactive waste repository proposed for Yucca Mountain, Nevada: U.S. Geological Survey Professional Paper 1779, 195 p.

Smellie, J.A.T., 1982, The mineralogy and genesis of uranium in rhyolitic ignimbrites of Precambrian age from Duobblon, Sweden, v. 46, p. 187-199.

Spirikis, C.S., 1996, The roles of organic matter in the formation of uranium deposits in sedimentary rocks, Ore Geology Review, v. 11, p. 53-69.

Stammose, D., J. Ly, H. Pitsch, and J.-M. Dolo, 1992, Sorption mechanism of three actinides on a clayey mineral, Applied Clay Science, v. 7, p. 225-238.

Stege, B., N.E. Pingitore, P.C. Goodell, and D.V. LeMone, 1981, Limestone bedrock geology, Sierra de Pefia Blanca, Chihuahua, Mexico., in: Studies in Geology # 13, AAPG., p. 265-274.

Steiger, R.H., and E. Jager, 1977, Subcommission on Geochronology: Convention on the use of decay constants in geo- and cosmochronology, Earth and Planetary Science Letters, v. 36, p. 359-362.

Stewart, C. L., L. J. Reimann, 2000, Mineralogic considerations for uranium in-situ leach mining: A Preliminary study of uranium and associated mineralogy of roll-front uranium deposits in Wyoming and Nebraska, 30th Annual Hydrometallurgical Conference; September 9-15; Saskatoon, Canada, Saskatoon, Canada, Canadian Inst Mining, Metallurgy And Petroleum.

Stoffregen, R.E., 1993, Stability relations of jarosite to natrojarosite at 150–250°C, Geochimica et Cosmochimica Acta, v. 57, p. 2417-2429.

Stout, R.B., and Leider, H.R., 1998, Waste Form Characteristics Report, Revision 1, UCRL-ID-108314, v. 1.3, 376 p.

Strauss, H., 1997, The isotopic composition of sedimentary sulfur through time, Palaeogeography, Palaeoclimatology, Palaeoecology, v. 132, p. 97-118.

Stuckless, J.S., and W.W. Dudley, 2002, The geohydrologic setting of Yucca Mountain, Nevada: Applied Geochemistry, v. 17, p. 659-682.

Stuckless, J.S., and D.W. O'Leary, 2007, Geology of the Yucca Mountain region, *in*: Stuckless, J.S., and R.A. Levich, eds., The Geology and Climatology of Yucca Mountain and Vicinity, Southern Nevada and California, Geological Society of America Memoir, v. 119, p. 9-52.

Su, G.W., J.T. Geller, K. Pruess, F. Wen, 1999, Experimental studies of water seepage and intermittent flow in unsaturated, roughwalled fractures, Water Resources Research, v. 35, no. 4, p. 1019-1037.

Suksi, J., and K. Rasilainen, 2000, Isotope fractionation of U in rocks reflecting redox conditions around a groundwater flow route, Materials Research Society Symposium Proceedings, v. 663, p. 961-969.

Suksi, J., 2001, Natural uranium as a tracer in radionuclide geosphere transport studies, Ph.D. Dissertation, University of Helsinki, 54 p.

Summers, W.K., 1976, Catalog of thermal waters in New Mexico, NM Bureau of Mines and Mineral Resources, Hydrologic Report 4, 80 p.

Syed, H.S., 1999, Comparison studies of adsorption of thorium and uranium on pure clay minerals and local Malaysian soil sediments, Journal of Radioanalogy and Nuclear Chemistry, v. 241, p. 11-14.

Tessier, A., P.G.C Campbell, and M. Bisson, 1979, Sequential extraction procedure for the speciation of particulate trace metals, Analytical Chemistry, v. 51, p. 844-851.

Thomas, D.J., R.B. Matthews, and V.J. Sopuck, 1998, Athabasca Basin unconformity-type uranium deposits: a synopsis of the empirical model and review of exploration and production trends, *in*: Proceedings, Canadian Institute of Mining, Metallurgy and Petroleum meeting, Montreal, May 3-7.

Torrero, M.E., E. Baraj, J. de Pablo, J. Giménez, and I. Casas, 1997, Kinetics of corrosion and dissolution of uranium dioxide as a function of pH, International Journal of Chemical Kinetics, v. 29, p. 261-267.

Triay, I.R., A.J. Mitchell, and M.A. Ott, 1991, Radionuclide migration as a function of mineralogy, LA-UR-91-113, 9 p.

Tullborg, E.-L., J. Smellie, A.B. Mackenzie, 2003, The use of natural uranium decay series studies in support of understanding redox conditions at potential radioactive waste disposal sites, Materials Research Society Symposium Proceedings, v. 807, p. 571-576.

United States Department of Agriculture (USDA), 2001, Soil Quality Test Kit Guide, 82 p.

United States Department of Energy (DOE), 2004, Radionuclide Transport Models Under Ambient Conditions, MDL-NBS-HS-000008 Rev. 2, 550 p.

United States Geology Survey (USGS), 2010, A Deposit Model for Mississippi Valley-Type Lead-Zinc Ores, Chapter A of Mineral Deposit Models for Resource Assessment, USGS Scientific Investigations Report 2010–5070–A, 64 p.

Valley, J.W., and N.T. Kita, 2009, Chapter 2: In situ oxygen isotope geochemistry by ion microprobe, *in*: Fayek, M., ed., Secondary Ion Mass Spectrometry in the Earth Sciences: Gleaning the Big Picture from a Small Spot, Mineralogical Association of Canada Short Course v. 41, p. 19-63.

Velarde, R., 2011, Evaluating suspended dust particulate matter from anthropogenically-altered lands, Ph.D. Dissertation, University of Texas at El Paso, 356 p.

Vinokurov, S.F., and M.V. Nesterove, 2010, New mechanism of the formation of the uranium-titanium association in ores of paleo valley deposits, Doklady Earth Sciences, v. 431, p. 380-385.

Wazne, M., G.P. Korfiatis, X.G. Meng, 2003, Carbonate Effects on Hexavalent Uranium Adsorption by Iron Oxyhydroxide, Environmental Science and Technology, v. 37, p. 3619-3624.

Wersin, P., M.F. Hochella Jr., P. Persson, G. Redden, J.O. Leckie, and D.W. Harris, 1994 , Interaction between aqueous uranium (VI) and sulfide minerals: Spectroscopic evidence for sorption and reduction, Geochimica et Cosmochimica Acta, v. 58, no. 13, p. 2829-2843.

White, A.F., M.L. Peterson, and R.D. Solbau, 1990, Measurement and Interpretation of Low Levels of Dissolved Oxygen in Ground Water, Ground Water, v. 28, p. 584-590.

White, A.F., and Brantley, S.L., 2003, The effect of time on the weathering of silicate minerals: why do weathering rates differ in the laboratory and field?, Chemical Geology v. 202, p. 479-506.

Wong, V., 1994, Nopal I Uranium Deposit, Peña Blanca District, Chihuahua, Mexico: A Study of Radionuclide Migration in a Natural Analogue to Yucca Mountain, Nevada, University of Texas at El Paso, M.S. Thesis, 62 p.

Wong, V., E. Anthony, and P. Goodell, 1996, Nopal I Uranium Deposit: A Study of Radionuclide Migration, Proceedings of the 7th International High-Level Radioactive Waste Management Conference, Las Vegas, NV, April 29-May 3, p. 43-45.

Wong, V., P.C. Goodell, and E.Y. Anthony, 1999, Characterization of U-Series Disequilibria at the Peña Blanca Natural Analogue Site, Chihuahua, Mexico, Material Research Society Symposium Proceedings, v. 556, p. 801-809.

Wronkiewicz, D.J., J.K. Bates. T.J. Gerding, E. Veleckis, and B.S. Tani, 1992, Uranium release and secondary phase formation during unsaturated testing of UO_2 at 90°C. Journal of Nuclear Materials, v. 190, p. 107-127.

Wronkiewicz, D.J., J.K. Bates, S.F. Wolf, and E.C. Buck, 1996, Ten-year results from unsaturated drip tests with UO2 at 90C: Implications for the corrosion of spent nuclear fuel, Journal of Nuclear Materials, v. 238, p. 78-95.

Wronkiewicz, D.J., and E.C. Buck, 1999, Uranium mineralogy and the disposal of spent nuclear fuel, *in*: Burns, P.C., R. Finch, eds., Uranium: Mineralogy, Geochemistry and the Environment, Mineralogical Society of America Reviews in Mineralogy, v. 38, p. 475-497.

Xu, D., J. Cui, R. Bansal, X. Hao, J. Liu, W. Chen, and B.S. Peterson, 2009, The ellipsoidal area ratio: an alternative anisotropy index for diffusion tensor imaging, Magnetic Resonance imaging, v. 27, p. 311-323.

Zheng, T.K. Tokunaga and J. Wan, 2003, Influence of calcium carbonate on U(VI) sorption to soils, Environmental Science and Technology, v. 37, p. 5603–5608.

Appendix A. Core Descriptions

A.1 Core Sample Descriptions

The following section describes the core samples used in this study. The core box pictures and descriptions are taken directly from Goodell et al. (2003). These descriptions contain the radioactivity of the section, overall lithology and appearance, and the DOE sample numbers (Table 1, column 3) and the Peña Blanca project sample numbers (Table 1, column 2), which are the basis for the sample numbers used in this study (Table 1, column 1). Following each core box are the individual samples analyzed in this study with pictures and descriptions from within that core box. Sample numbers used in this study and equivalent sample numbers are presented in Table 1. The table also has the formation, depth, and sample analyses performed on each sample.

Table 1 Sample numbers and analyses for each sample in this study and equivalents to DOE and Peña Blanca project (previous work)

Equivalent sample names			Location		Analysis			
Sample number	Peña Blanca subsample number	DOE sample number	Formation	Depth	XRD	EMPA	SIMS	Bulk chemistry
PB772	PB1023772 MTM2 UTEP	SPC 1023772	Nopal	-7.5				x
PB 774	PB1023774 MTM3 UTEP	SPC 1023774	"	-8.6	x			
	PB1023774 MTM2 UTenn	"	"	"		x		x
PB 775	PB1023775 MTM3 UTEP	SPC 1023775	"	-9.1	x			x
	PB1023775 MTM4 UTenn	"	"	"		x		
PB 782	PB1023782 MTM2 UTEP	SPC 1023782	"	-17.8	x			x
PB 798	PB1023798 MTM5 UTEP	SPC 1023798	Coloradas	-29.8	x			x
	PB1023798 MTM3 UTenn	"	"	"		x		
PB 812	PB1023812 MTM3 UTEP	SPC 1023812	"	-37.8	x			x
	PB1023812 MTM2 UTenn	"	"	"		x		
PB 814	PB1023814 MTM3 UTEP	SPC 1023814	"	-40.0	x			x
	PB1023814 MTM2 UTenn	"	"	"		x		
PB 849	PB1023849 MTM4 UTEP	SPC 1023849	"	-66.5	x			x
	PB1023849 MTM3 UTenn	"	"	"		x		
PB 860	PB1023860 MTM3 UTEP	SPC 1023860	"	-76.6				x
PB 862	PB1023862 MTM3 UTEP	SPC 1023862	"	-78.2	x			x
	PB1023862 MTM2 UTenn	"	"	"		x		
PB 891	PB1023891 MTM1 UTEP	SPC 1023891	"	-103.7	x			x
PB 912	PB1023912 MTM3 UTEP	SPC 1023912	"	-119.0	x			x
	PB1023912 MTM4 UTenn	"	"	"		x		
PB 917	PB1023917 MTM4 UTEP	SPC 1023917	"	-123.2	x			x
PB 922	PB1023922 MTM1 UTEP	SPC 1023922	"	-127.0				x
PB 935	PB1023935 MTM4 UTEP	SPC 1023935	"	-136.0	x			x
	PB1023935 MTM2 UTenn	"	"	"		x		
PB 938	PB1023938 MTM5 UTEP	SPC 1023938	Pozos conglomerate	-138.4	x			x
	PB1023938 MTM2 UTenn	"	"	"		x		
PB 4009	PB1024009 MTM5 UTEP	SPC 1024009	"	-190.8	x			x
	PB1024009 MTM3 UTenn	"	"	"		x	x	
PB 4035	PB1024035 MTM2 UTEP	SPC 1024035	"	-210.3				x
PB 4049	PB10240549 MTM4 UTEP	SPC 1024049	"	-219.5	x			x
PB 4052	PB1024052 MTM3&8 UTEP	SPC 1024052	"	-220.8	x			x
	PB1024052 MTM2&7 UTenn	"	"	"		x	x	
PB 4085	PB1024085 MTM2 UTEP	SPC 1024085	Cretaceous Limestone	-245.6				x

A.1.1 Core Box 2

Sample(s): PB772, PB 774

Depth: 5.10-8.95 m

Radiation measurements: Background 30 counts per second (cps). Hot spot: 8.59 m, 100 cps

Homogenous, altered, bleached tuff. Light pink matrix, strong kaolinization, minor tight fractures. Depth 8.59 m strong limonite and goethite fracture 4-5 mm, 45°. 8.35-8.95 m fracture, dark pink around fracture.

SPC 1023772 (7.54 m)	PB1023772 MTM2 UTEP
SPC 1023774 (8.59 m)	PB1023774 MTM2 UTenn
	PB1023774 MTM3 UTEP

Figure 1. Photo from Goodell et al. (2003). Core box showing location of samples PB772 (top red rectangle; Figure 2) and PB774 (bottom red rectangle; Figure 3).

Figure 2. Image of sample PB772. Bleached Nopal ash-flow tuff with strong kaolinitization throughout the sample.

Figure 3. Image of sample PB774. Bleached Nopal ash-flow tuff with strong kaolinitization and iron oxyhydroxide alteration on the left edge.

A.1.2 Core Box 3

Sample(s): PB775

Depth: 8.95-16.60 m

Radiation measurements: Background 60 cps. Hot spots: 9.18-9.87 m, 120 cps

Highly altered, brecciated, orange red tuff, bleaching around the veins, goes to zone with fewer fractures, back into highly fractured zone. Fractures 1-4 mm, high angle 75-90°. Sample group has two main fractures at 75-90° and then multitude in other directions. Much goethite (hematite) cavity and fracture fillings with kaolinite. Minor visible hexavalent green and yellow.

SPC 1023775 (8.95-9.7 m) PB1023775 MTM3 UTEP

PB1023775 MTM4 UTenn

Figure 4. Photo from Goodell et al. (2003). Core box showing location of sample PB775 (see red rectangle; Figure 5).

Figure 5. Image of sample PB775. Bleached Nopal ash-flow tuff with strong kaolinitization and iron oxyhydroxide alteration along fractures, especially to left side.

A.1.3 Core Box 4

Sample(s): PB782

Depth: 16.60-23.60 m

Radiation measurements: No hot spots; Background 50 cps

16.6-18.1 sand sized material; altered vitrophyre, unconsolidated. 18.1-20.5 highly altered, oxidized tuff; consolidated altered vitrophyre. Past 20.5 minor light fractures, 1 mm, 45°, altered welded tuff with phenocrysts (1 mm) altered to kaolinite, occasional anomalous large pumice to 1 cm, Mn oxide on fractures.

SPC 1023782 (17.45-18.10 m) PB1023782 MTM2 UTEP

Figure 6. Photo from Goodell et al. (2003). Core box showing location of sample PB782 (see red rectangle; Figure 7).

Figure 7. Image of sample PB782. Unconsolidated (sand-sized) vitrophyre, altered to kaolinite and iron oxyhydroxides.

A.1.4 Core Box 6

Sample(s): PB798

Depth: 27.30-31.60 m

Radiation measurements: Background 50 cps. Hot spots: 27.30-27.60 m, 175-200 cps; 27.96-28.14 m, 250-200 cps; 28.14-29.00 m, 250-200 cps; 29.00-29.65 m, 150+ cps; 29.78 m, 250 cps (very hot); 30.25-30.70 m, 150 cps; 30.93-31.60 m (fracture zones), 150 cps

Welded ash-flow tuff, highly fractured, oxidized, much limonite, some hematite, much kaolinite. Semicontinuous to continuous anomalous zone, with some hotter spots. This is followed from 30.70 to 31.60 by bleached, kaolinized zone with three hematite bearing fractures with minor counts.

SPC 1023798 (29.78 m) PB1023798 MTM3 UTenn

PB1023798 MTM5 UTEP

Figure 8. Photo from Goodell et al. (2003). Core box showing location of sample PB798 (see red rectangle; Figure 9).

Figure 9. Image of sample PB798. Highly altered ash flow tuff. Iron oxyhydroxides and kaolinite along fracture lengthwise through core sample.

A.1.5 Core Box 8

Sample(s): PB812, PB 814

Depth: 36.22-40.46 m

Radiation measurements: Background 50 cps. Hot spots: 37.55 m, 120 cps; 38.94-39.30 m, 100 cps

Starts with altered tuff, welded tuff, phenocrysts 2-3 mm, moderately oxidized. At about 36.72 m grades into more oxidized, more altered fractured tuff, 45° fractures ~ 1mm in size, oxidation increases to 37.55 m to intense zone of alteration, fractures, brecciated, MnO_2 coatings, limonite. This zone continues up to 38.60 m, then back to altered tuff, then at 38.81 m another zone of intense fracturing and alteration. Two sets of fractures in zone, one set is near-vertical and the other at 45°, this fracture zone is ~50 cm long, then back in altered tuff. At 39.80 another zone of intense alteration, fracturing, oxidation, brecciation.

SPC 1023812 (37.75 m)	PB1023812 MTM2 UTenn
	PB1023812 MTM3 UTEP
SPC 1023814 (40.00 m)	PB1023814 MTM2 UTenn
	PB1023814 MTM3 UTEP

Figure 10. Photo from Goodell et al. (2003). Core box showing location of samples PB812 (top red rectangle; Figure 11) and PB814 (bottom red rectangle; Figure 12).

Figure 11. Image of sample PB812. Fractured piece of ash-flow tuff with iron oxyhydroxides and kaolinite alteration.

Figure 12. Image of sample PB814. Highly fractured ash-flow tuff with kaolinite fracture filling. Brecciated and oxidized (iron oxyhydroxides) zone on right side.

A.1.6 Core Box 15

Sample(s): PB849

Depth: 65.97-71.66 m

Radiation measurements: Background 50 cps. Hot spots: 66.35 m, 150 cps

Welded ash-flow tuff, intense alteration and kaolinization. Mobilization and reprecipitation of kaolinite. Some large masses of hematite. Entire box has a light yellow cast.

SPC 1023849 (66.50 m) PB1023849 MTM3 UTenn

PB1023849 MTM4 UTEP

Figure 13. Photo from Goodell et al. (2003). Core box showing location of sample PB849 (see red rectangle; Figure 14).

Figure 14. Image of sample PB849. Highly altered ash-flow tuff with kaolinitization and strong oxidation (see purplish areas).

A.1.7 Core Box 17

Sample(s): PB860, PB862

Depth: 75.97-79.70 m

Radiation measurements: Background: 40-50 cps, higher. Many hot spots up to 120 cps, 5 hot spots of 100 cps.

Strongly welded ash-flow tuff, pumice (30%) up to 3 cm, inclined 60° with hole direction, sample completely kaolinitized, small 3 mm lithic fragments, no phenocrysts. At 77.7 to 79.70 m (90-100 cps) rock is limonitic with high gamma, highly fractured, rock not competent.

SPC 1023860 (76.57 m) PB1023860 MTM3 UTEP

SPC 1023862 (78.2 m) PB1023862 MTM2 UTenn

PB1023862 MTM3 UTEP

Figure 15. Photo from Goodell et al. (2003). Core box showing location of samples PB860 (top red rectangle; Figure 16) and PB862 (bottom red rectangle; Figure 17).

Figure 16. Image of sample PB860. Ash-flow tuff with almost complete kaolinitization, some minor iron oxyhydroxides.

Figure 17. Image of sample PB862. Ash-flow tuff with alteration to iron oxyhydroxides. Larger fracture runs through core in vertical direction (see hole to left side).

A.1.8 Core Box 22

Sample(s): PB891

Depth: 102.85-106.31 m

Radiation measurements: Background: 25 cps. Hot spots: SPC 1023890 + 80 cm, 75 cps; SPC 1023891 + 35 cm, 125 cps

Moderately to strongly welded ash flow tuff, pumice to 2 cm is kaolinized (30%), small lithic fragments to 0.5 cm, altered, 10%+. Two inclined fractures (25-45 degrees), parallel to welding direction, minor limonite staining; no phenocrysts; lithics are volcanic. Samples from this box are quite homogeneous, varying in color from white to tan.

SPC 1023891 + 35 cm (75 cps) PB1023891 MTM1 UTEP

Figure 18. Photo from Goodell et al. (2003). Core box showing location of sample PB891 (see red rectangle; Figure 19).

Figure 19. Image of sample PB891. Ash-flow tuff with a vertical fracture passing vertically down its center. Kaolinitization throughout, but iron oxyhydroxides are present especially to the left side of the fracture.

A.1.9 Core Box 26

Sample(s): PB912

Depth: 116.93-120.63 m

Radiation measurements: Background: 50 cps. Hot spots: ?

Welded ash-flow tuff, Coloradas Formation. Phenocrysts leached, abundant small 3-5 mm pumice, mainly leached, all providing significant porosity. Down to 118.63 m, core has yellowish cast, then alternating white and reddish, some mineralized (hematite) fractures with bleaching. Sampling directed towards unique bleached veinlets, whereas bleaching is often represented by changes over large distances.

SPC 1023912 (118.91-119.15 m) PB1023912 MTM2 UTEP

PB1023912 MTM3 UTEP

PB1023912 MTM4 UTenn

Figure 20. Photo from Goodell et al. (2003). Core box showing location of sample PB912 (see red rectangle; Figure 21).

Figure 21. Image of sample PB912. Ash-flow tuff with lithic and pumice fragments. Zone of intense bleaching (~1 cm) along diagonal fracture.

A.1.10 Core Box 27

Sample(s): PB917

Depth: 120.73-124.31 m

Radiation measurements: None recorded.

Welded tuff with small lithic and pumice clasts, phenocrysts are kaolinized, 20% lithic and 15% pumice, lithics ≤ 2 cm (average ~1 cm), pumice ≤ 1 cm. Fractures throughout, some are mineralized with hematite, goethite ± limonite, 80° fractures, some near-horizontal fractures. Whole unit white-yellow bleaching, but 0.5 m zone at top is still pink.

SPC 1023917 (123.16-123.28 m) PB1023917 MTM2 UTenn

PB1023917 MTM4 UTEP

Figure 22. Photo from Goodell et al. (2003). Core box showing location of sample PB917 (see red rectangle; Figure 23)

Figure 23. Image of sample PB917. Ash-flow tuff bleached to yellowish-white color. Fracture filled with iron oxyhydroxides along the middle of sample.

A.1.11 Core Box 28

Sample(s): PB922

Depth: 124.31-128.32 m

Radiation measurements: Background: 30 cps. No hot spots.

Welded ash-flow tuff, Coloradas Formation. 10-15% 1-2 mm lithics, minor to no phenocrysts, 15-20% pumice, hematite or limonite replacing pumice (pinkish cast), flow foliation varies ± 25°, several high angle fractures, some tight, one 4 mm wide with limonite and breccia, also extensive bleached white zone with more remobilized and reprecipitated kaolinite. Bottom is mottled pink/white.

SPC 1023922 (127.00 m) PB1023922 MTM1 UTEP

Figure 24. Photo from Goodell et al. (2003). Core box showing location of sample PB922 (see red rectangle; Figure 25).

Figure 25. Image of sample PB922. Pink ash-flow tuff with white spots of kaolinite alteration. Large coatings of yellow iron oxyhydroxides in fractured areas.

A.1.12 Core Box 31

Sample(s): PB935, 938

Depth: 135.83-139.43 m

Radiation measurements: Background: 50 cps. No hot spots.

At 136.38 m, contact with ash-flow tuff above and conglomerate below. Base of ash-flow tuff is highly fractured with fracture of 75°, near vertical, 1-3 mm with limonite and hematite, pervasive kaolinite, minor remnants of lithics up to 2 cm (rounded?), texture not prominent, mottled. Top 10 cm begins to look like ash-flow tuff above. Pozos Conglomerate Formation: Fragments of limestone and volcanic rocks, many at 2 cm and up to 5 cm, one large limestone fragment up to 10 cm. Bottom 0.5 m is finer grained, but has a series of high angle (60-70°) fractures, with limonite. Limestone fragments have significant reaction rims. Some kaolinite present. Some void space lined with hematite (+ calcite). Volcanic rock fragments altered to kaolinite. Dissolution of chert fragments (?) and reprecipitation of drusy quartz in leached vuggy space.

SPC 1023935 (135.90-136.17 m)	PB1023935 MTM2 UTenn
	PB1023935 MTM4 UTEP
SPC 1023938 (138.44 m)	PB1023938 MTM1 UACH
	PB1023938 MTM2 UTenn

Figure 26. Photo from Goodell et al. (2003). Core box showing location of samples PB935 (top red rectangle; Figure 27) and PB938 (bottom red rectangle; Figure 28).

Figure 27. Image of sample PB935. Bleached ash-flow tuff with several fractures filled with iron oxyhydroxides and kaolinite.

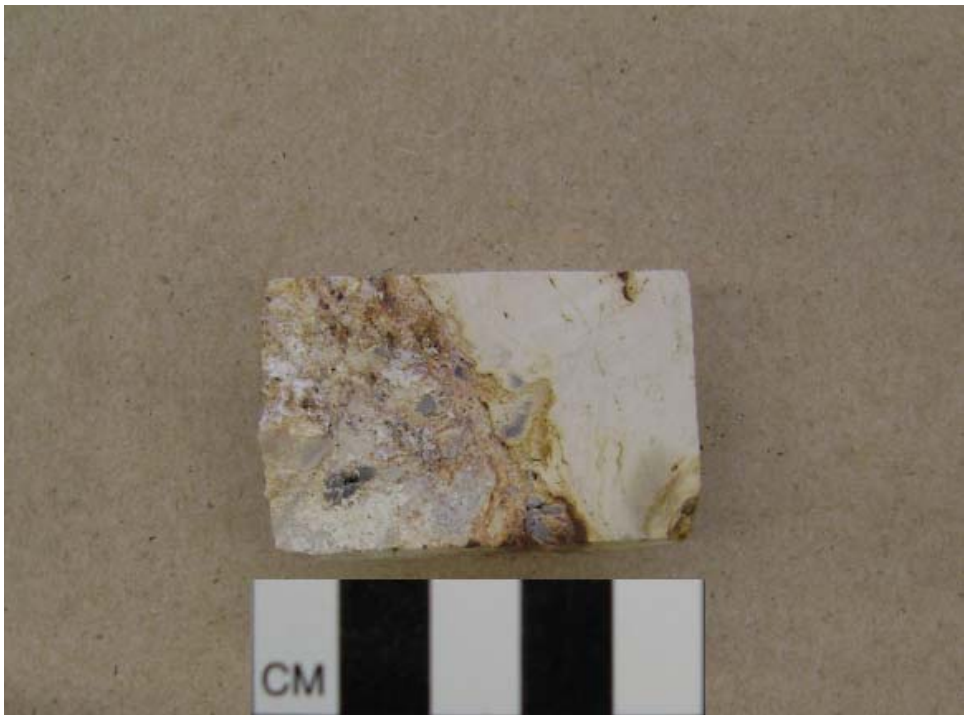

Figure 28. Image of sample PB938. Conglomerate with lithic and volcanic fragments. Matrix of kaolinite, iron oxyhydroxides, and calcite.

A.1.13 Core Box 44

Sample(s): PB4009

Depth: 188.0-191.63 m

Radiation measurements: Background: 50 cpm. Hot zone: 190.7-190.8 m, 100 cpm; 190.8-191.3 m, 400 at top, then 150 cpm, then background.

Highly altered conglomerate, all gray to end, from 190.8 to 191.11, clay-rich, cannot see fragments, large fracture filled with clay? Poorly sorted conglomerate, clasts ≤ 5 cm, chert ~10%, other altered fragments ~ 40%, fragments are angular to rounded.

SPC 1024009 (190.8 m) PB1024009 MTM3 UTenn

PB1024009 MTM5 UTEP

Figure 29. Photo from Goodell et al. (2003). Core box showing location of sample PB4009 (see red rectangle; Figure 30).

Figure 30. Image of sample PB4009. This sample measured ~1000 cpm. It is rich in clay and calcite with some staining by iron oxyhydroxides visible to the left side.

A.1.14 Core Box 49

Sample(s): PB4035

Depth: 206.60-210.39 m

Conglomerate to 207.82 m and then red brown sandstone to 208.90 m. Below is limestone and limestone breccia. Large masses of limestone breccia with fractures and breccia. Oxidized with limonite color, but at 210.29 m is oxidation zone up front, with distinctive gray cast. Sample taken at oxidation/reduction contact.

SPC 1024035 (210.29 m) PB1024035 MTM2 UTEP

Figure 31. Photo from Goodell et al. (2003). Core box showing location of sample PB4035 (see red rectangle; Figure 32).

Figure 32. Image of sample PB4035. Sample was broken in two during sampling. Micritic limestone with some iron oxyhydroxide staining visible as yellowed area to upper right. This appears to be an oxidation/reduction contact.

A.1.15 Core Box 52

Sample(s): PB4049, PB4052a, PB4052b

Depth: 218.96-222.52 m; water table reached at ~222 m

Radiation measurements: Background 50 cps. Hot spots: 219.11 m, 100 cps; 219.57-219.77 m, 120 cps (stops at lithic fragment); 220.17-220.55 m, 120-250 cps; 220.99-221.57 m, 175-250 cps.

Conglomerate the entire box. Highly altered conglomerate, limonite in the matrix, 1-2 cm angular to subangular clasts. At 220.55 m, fresher. Chert fragments with strange central voids, leaching (?). Some andesite fragments are chloritized.

SPC 1024049 (219.4-219.55 m)	PB10240549 MTM2 UTenn
	PB10240549 MTM4 UTEP
SPC 1024052 (40 cm down from top)	PB1024052 MTM2 UTenn
	PB1024052 MTM3 UTEP
SPC 1024052 (25 cm up from base)	PB1024052 MTM7 UTenn
	PB1024052 MTM8 UTEP

Figure 33. Photo from Goodell et al. (2003). Core box showing location of samples PB4049 (top red rectangle), PB4052a (bottom left rectangle; Figure 34), and PB4052b (bottom right rectangle; Figure 35).

Figure 34. Image of PB4049. Limestone conglomerate with minor clasts and iron oxyhydroxide staining (yellow color).

Figure 35. Images of PB4052A&B. PB4052A&B are similar in composition: limestone conglomerate with chert and volcanic fragments. The volcanic fragments are being chloritized (greenish color). Some localized staining by iron oxyhydroxides. The samples are separated, because PB4052B has a higher radioactivity than PB4052A.

A.1.16 Core Box 58

Sample(s): PB4085

Depth: 241.56-245.59 m

Radiation measurements: Background: 30 cps. No hot spots.

Conglomerate down to 244.40 m, highly altered conglomerate, clasts angular, range to 6 cm, one very large clast (16 cm), limestone at 242.66 m. Altered conglomerate, smaller clasts, 1-2 cm, volcanic and limestone, all bleached. Contact – clay only, sheared contact?, slicks in the clay. Then limestone, breccia near top.

SPC 1024085 (245.59 m) PB1024085 MTM2 UTEP

Figure 36. Photo from Goodell et al. (2003). Core box showing location of sample PB4085 (see red rectangle).

Figure 37. Image of PB4085. Cretaceous micritic limestone bedrock.

Appendix B. XRD Patterns

B.1 XRD PATTERNS

These x-ray diffraction patterns are the results of analyses at the University of Manitoba, Department of Geological Sciences. The following section lists samples from Nopal I in order of descending depth. Each XRD pattern has the identified mineral diffraction patterns from JADE peak analysis software in colored peaks on the sample patterns and below it. A summary table of the dominant minerals in each sample and the depth of the sample is shown below (Table 1). Ore samples were collected from within the Nopal I mine adit on the +00 level, and the PB# samples are from the PB-1 core described in Appendix A. If a sample is follow by a dash and description, e.g., PB798-Yellow; it means the sample was micro-drilled to remove the color described (see Appendix A for pictures of samples).

Raw files are provided in a folder labeled Appendix B-XRD Patterns. A sub folder, named Not PB-1 core, contains samples of Nopal I uranium ore and uranophane crystals. Each sample is in its own Word document and labeled with its sample name. A spreadsheet is also provided, which contains the raw counts over each 2θ distance; samples are separated into worksheets and labeled with their sample name.

Table 1 Sample numbers and dominant minerals identified in XRD analysis

SampleID	Depth	Quartz	Kaolinite	Calcite	Dolomite	Pyrite	Goethite	Hematite	Uraninite	Uranophane	Vandendriesscheite	(Meta-)Schoepite
Ore	0	x	x						x	**x**	x	x
PB774	-8.59	**x**	**x**									
PB775	-9.145	**x**	**x**									
PB812	-37.75	**x**	**x**									
PB814	-40	**x**	**x**									
PB849	-66.5	**x**	x				x	x				
PB862	-78.2	**x**	**x**									
PB891	-103.7	**x**	x				x	x				
PB912	-119.03	**x**	x									
PB917	-123.22	**x**	x				x	x				
PB935	-136.04	**x**	x				x	x				
PB938	-138.44	**x**	x									
PB4009	-190.8	**x**	x	x	x	x						
PB4049	-219.48	**x**	x									
PB4052	-220.82	**x**	x		x							

B.1.1 Nopal I Mine Adit Ore samples

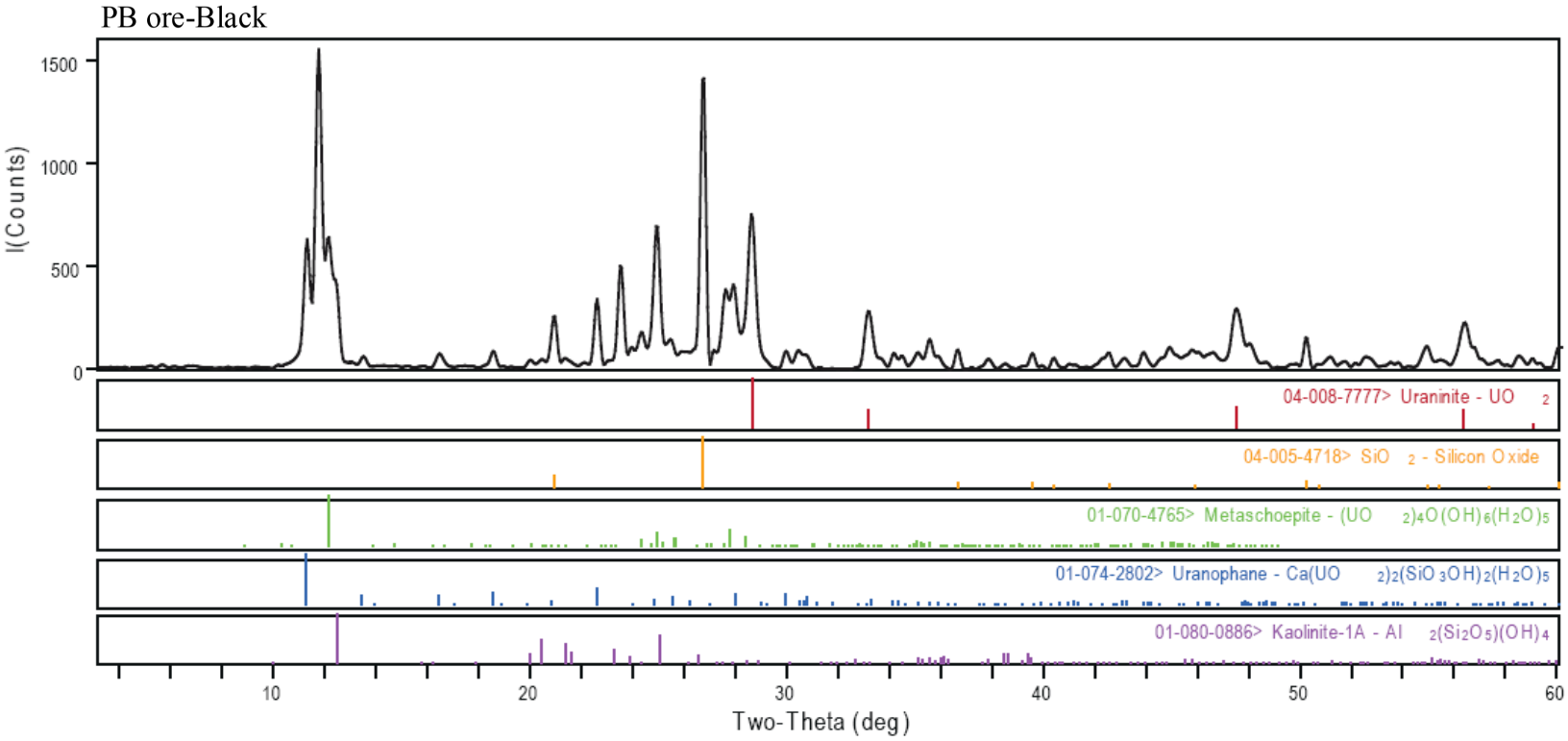

Figure 1. XRD diffraction pattern of PB ore-Black (black colored ore) from the Nopal I mine adit.

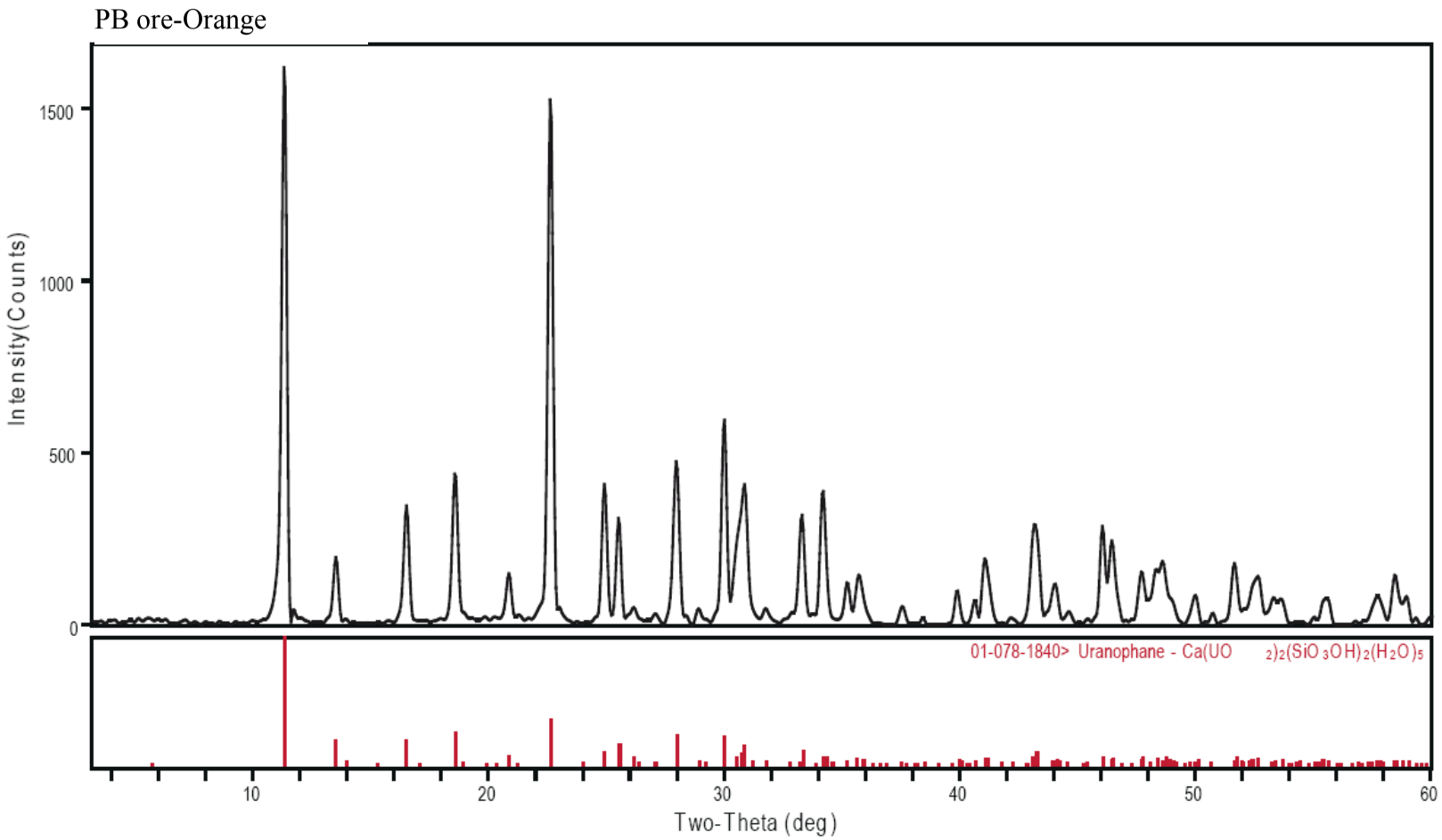

Figure 2. XRD diffraction pattern of PB ore-Orange (orange-yellow colored ore) from the Nopal I mine adit.

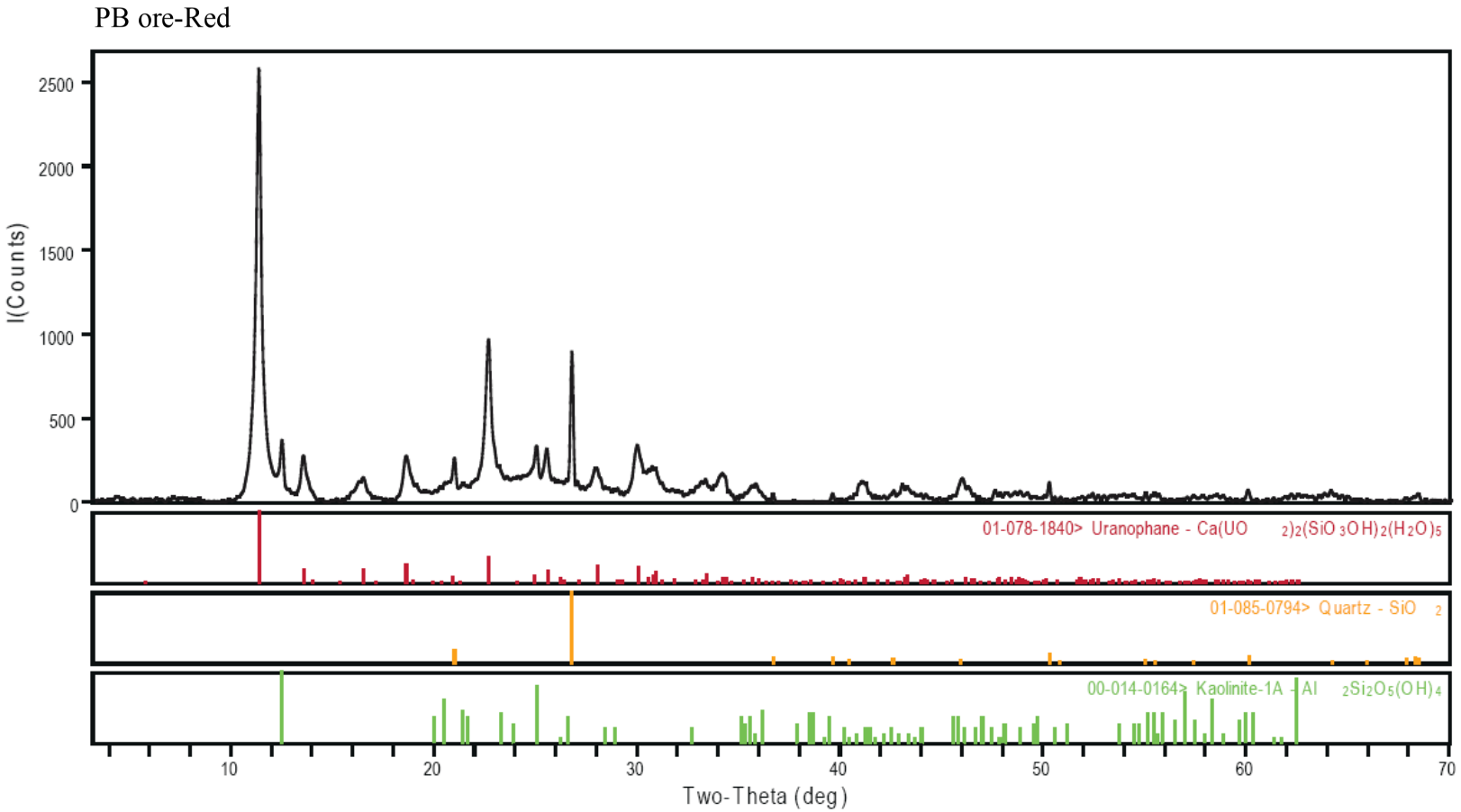

Figure 3. XRD diffraction pattern of PB ore-Red (red colored ore) from the Nopal I mine adit.

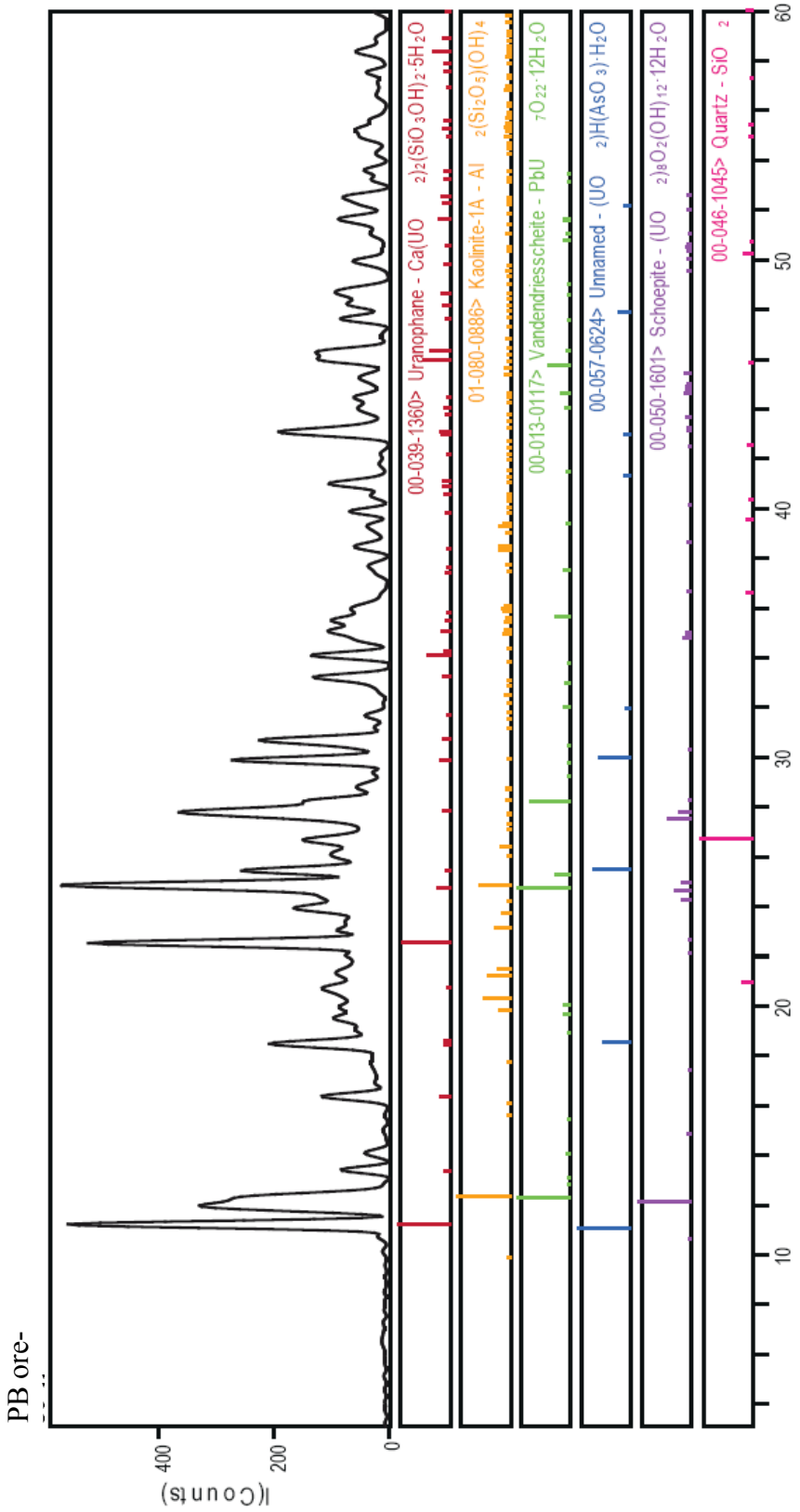

Figure 4. XRD diffraction pattern of PB ore-Yellow (yellow colored ore) from the Nopal I mine adit.

B.1.2 PB-1 Core samples

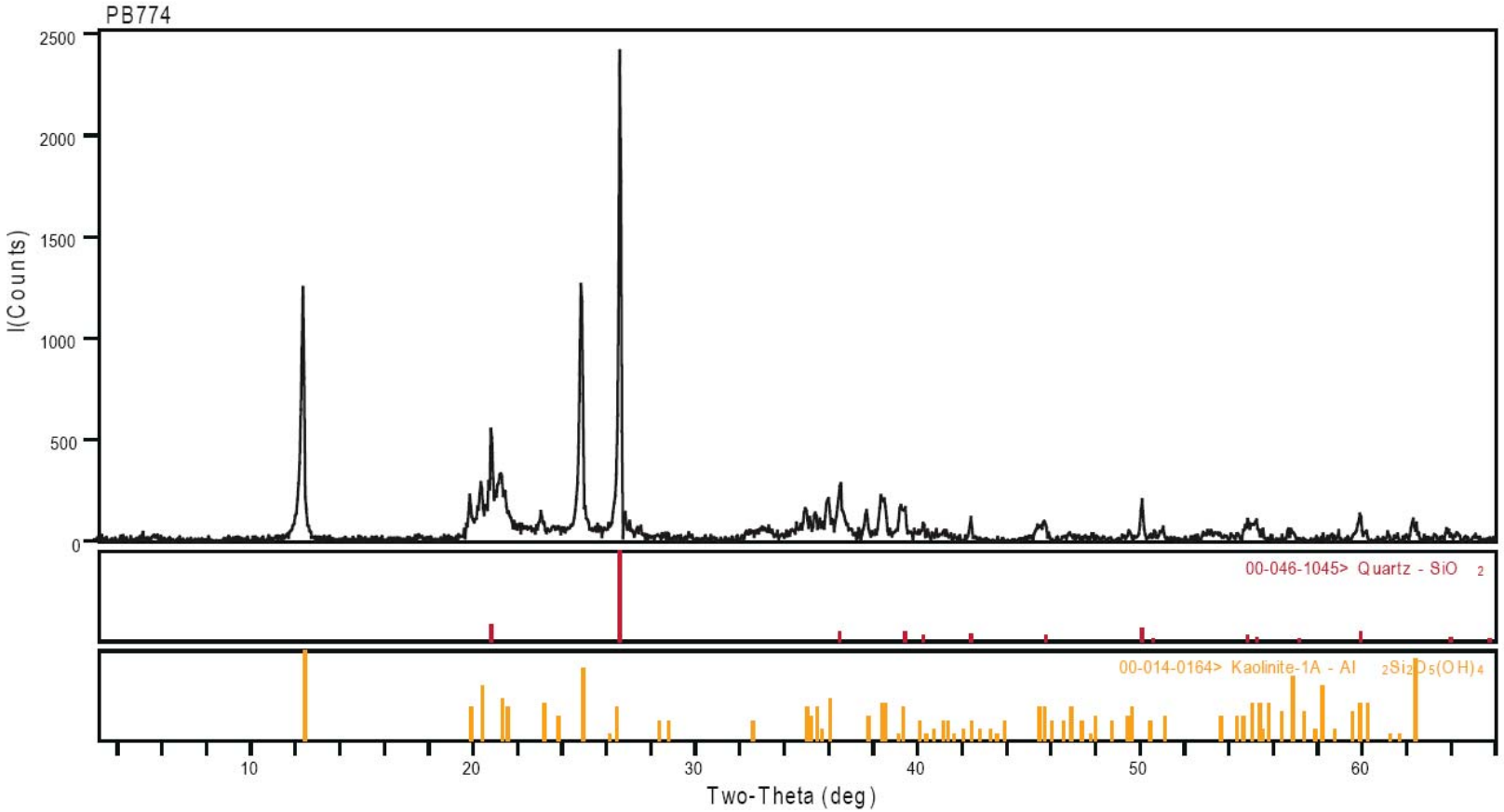

Figure 5. XRD diffraction pattern of PB774 fracture/alteration minerals.

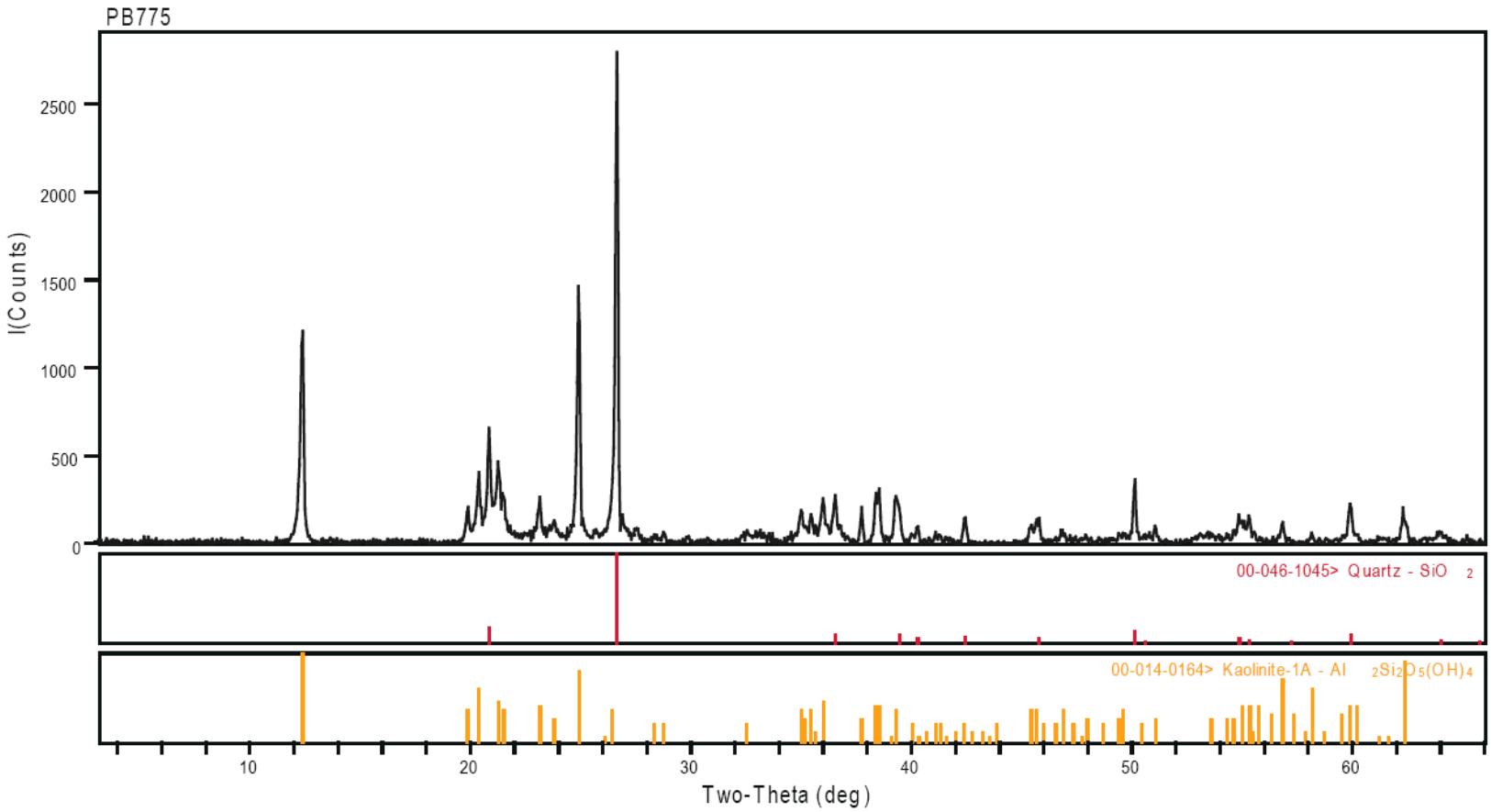

Figure 6. XRD diffraction pattern of PB775 fracture/alteration minerals.

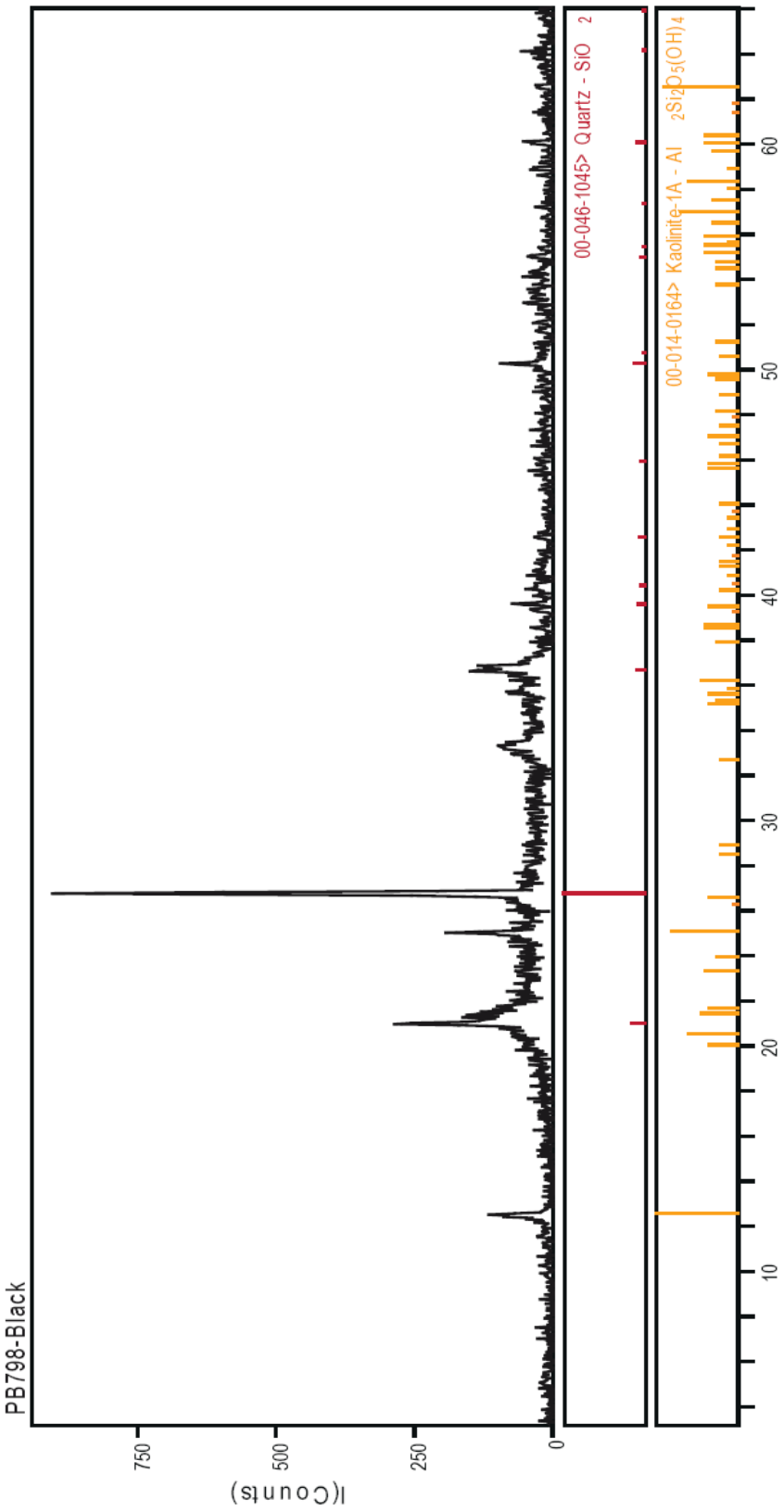

Figure 7. XRD diffraction pattern of PB798 black colored fracture/alteration minerals.

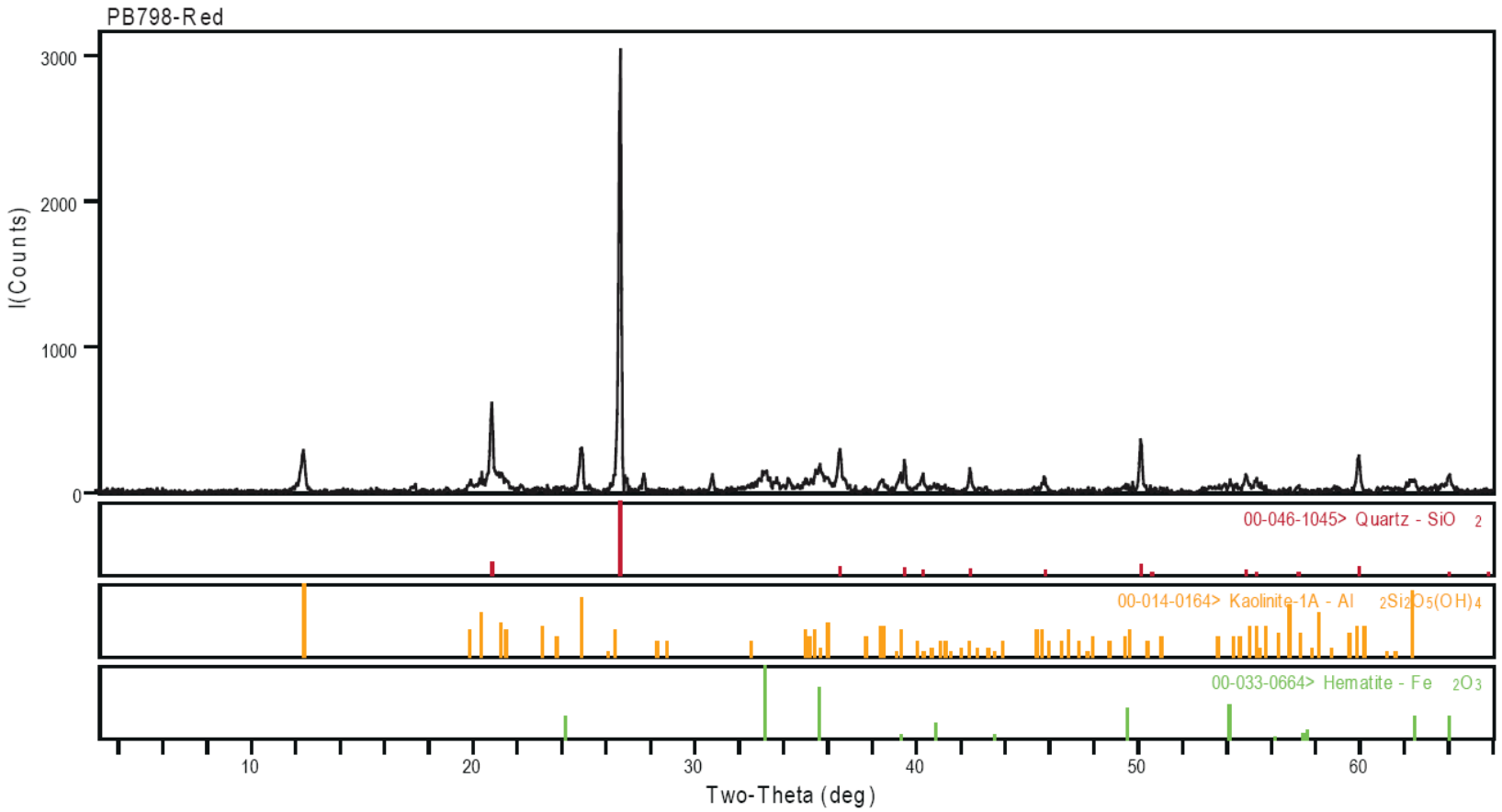

Figure 8. XRD diffraction pattern of PB798 red colored fracture/alteration minerals.

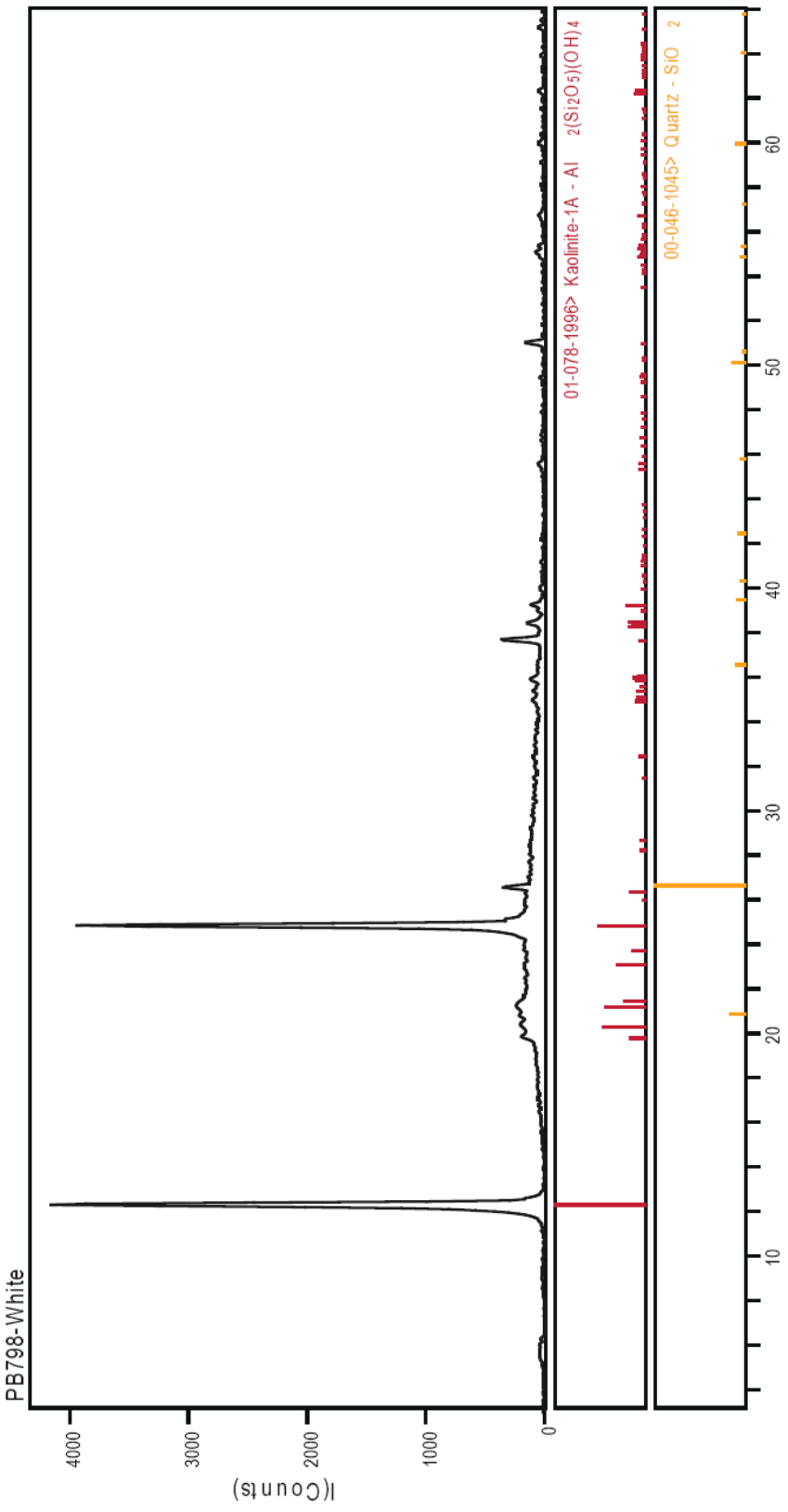

Figure 9. XRD diffraction pattern of PB798 white colored fracture/alteration minerals.

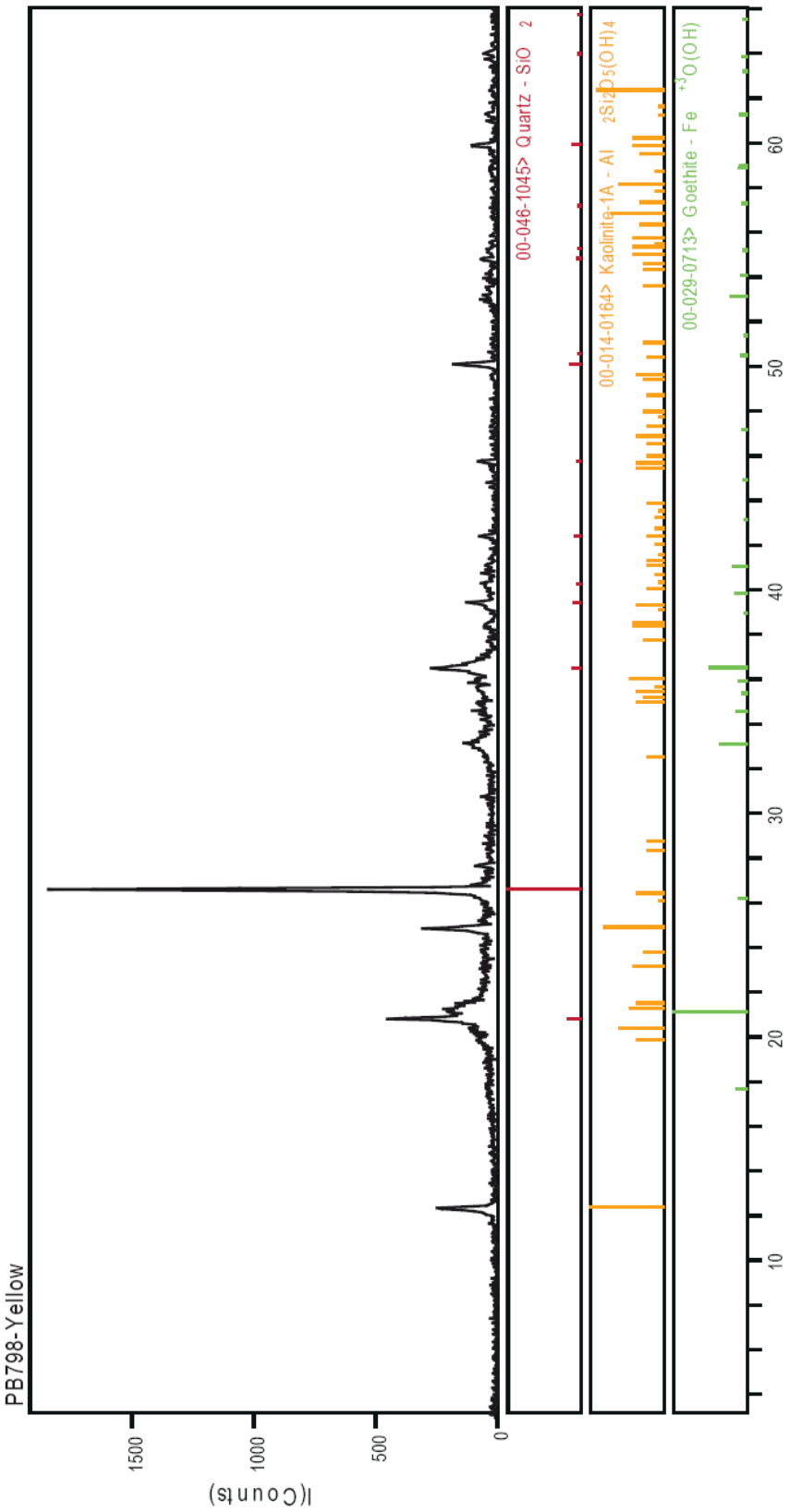

Figure 10. XRD diffraction pattern of PB798 yellow colored fracture/alteration minerals.

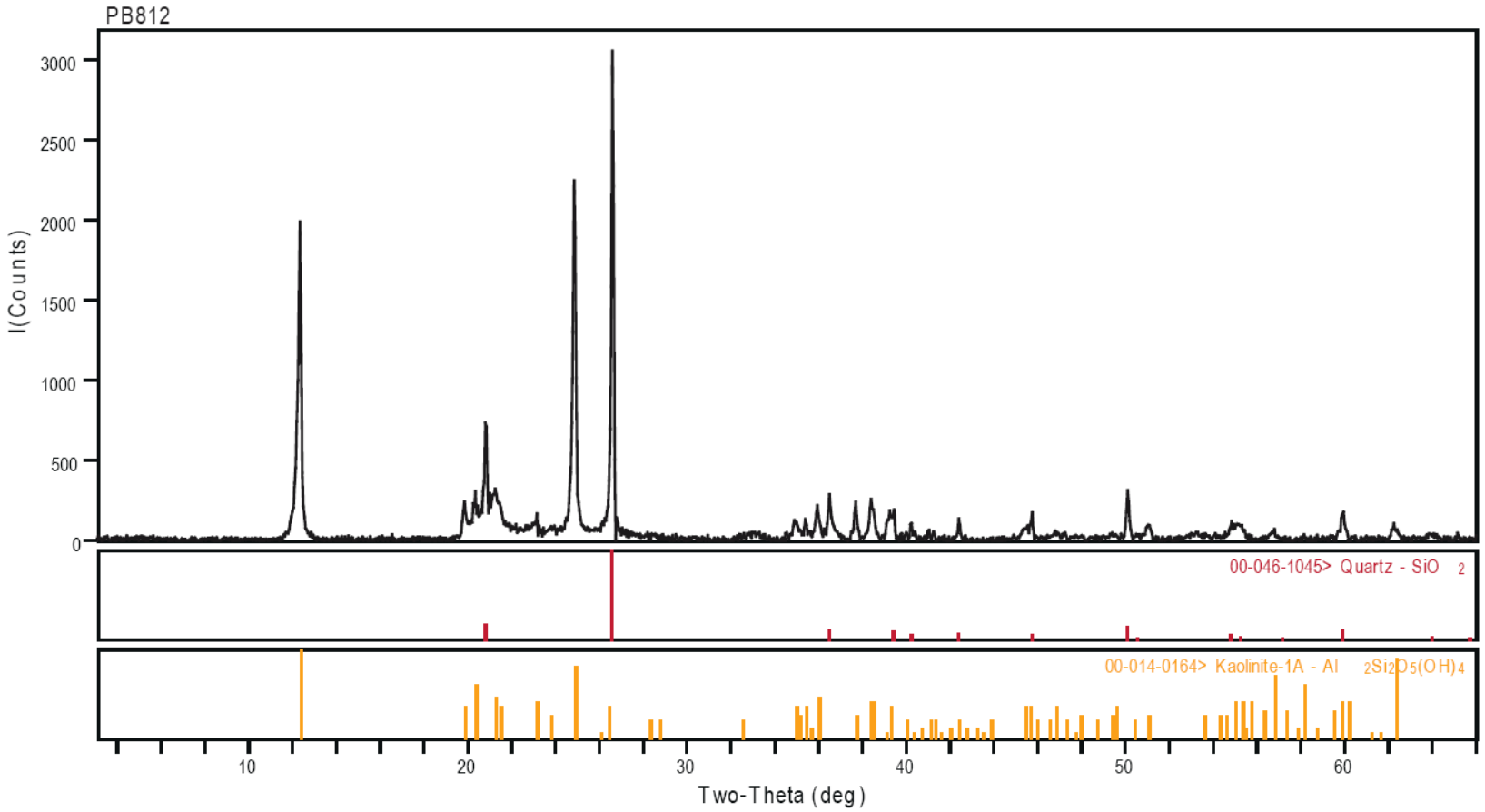

Figure 11. XRD diffraction pattern of PB812 fracture/alteration minerals.

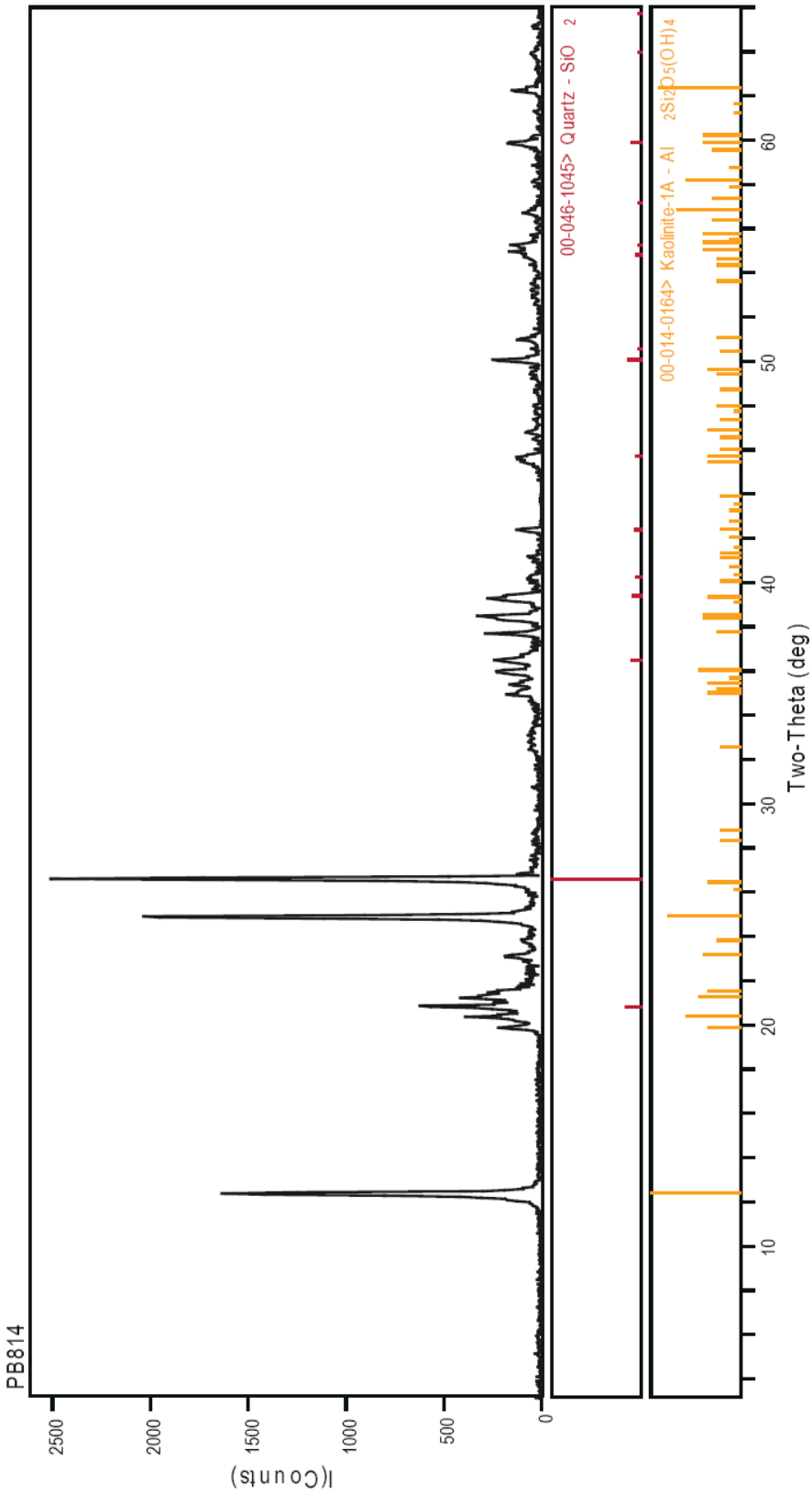

Figure 12. XRD diffraction pattern of PB814 fracture/alteration minerals.

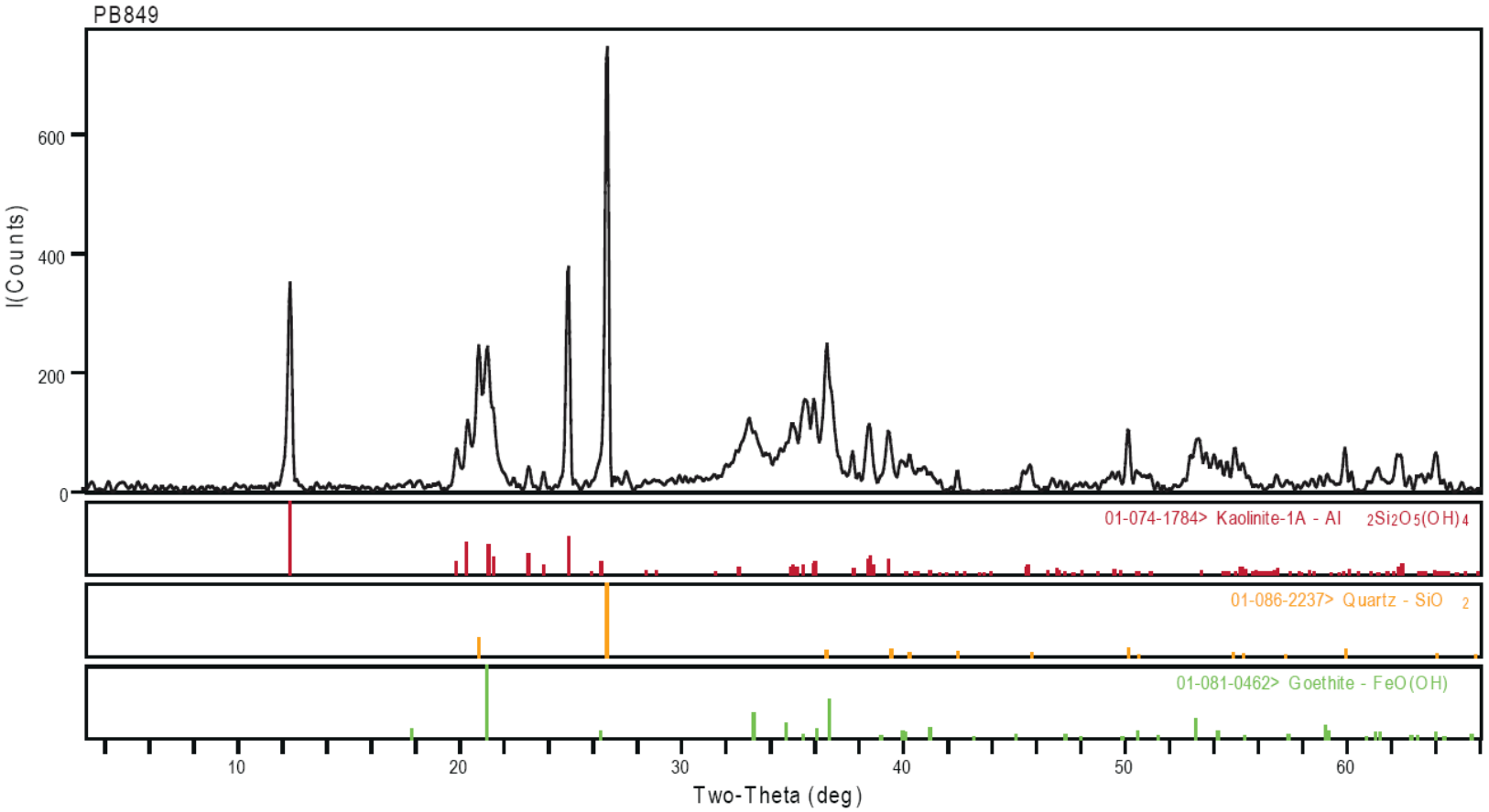

Figure 13. XRD diffraction pattern of PB849 fracture/alteration minerals.

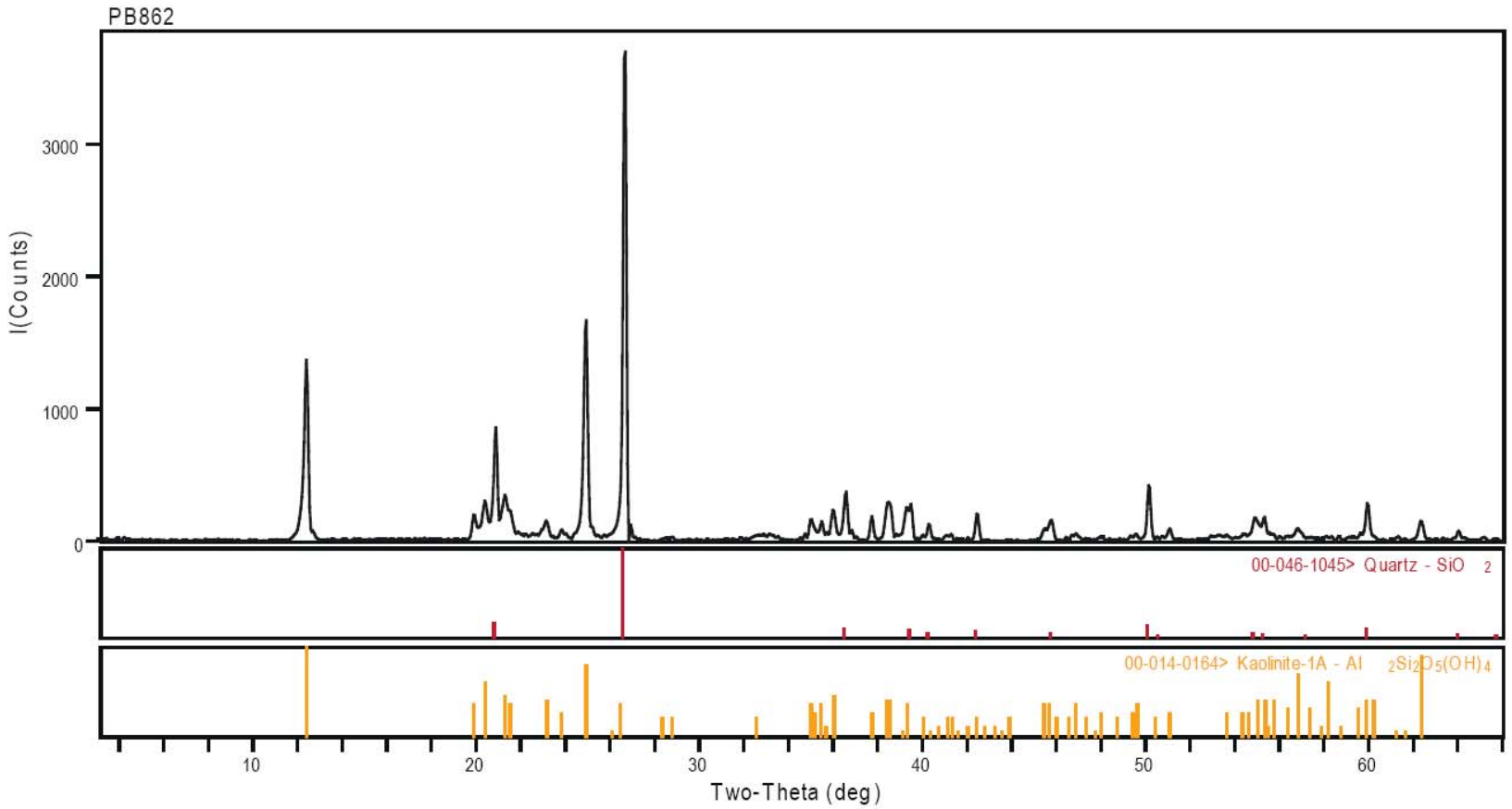

Figure 14. XRD diffraction pattern of PB862 fracture/alteration minerals.

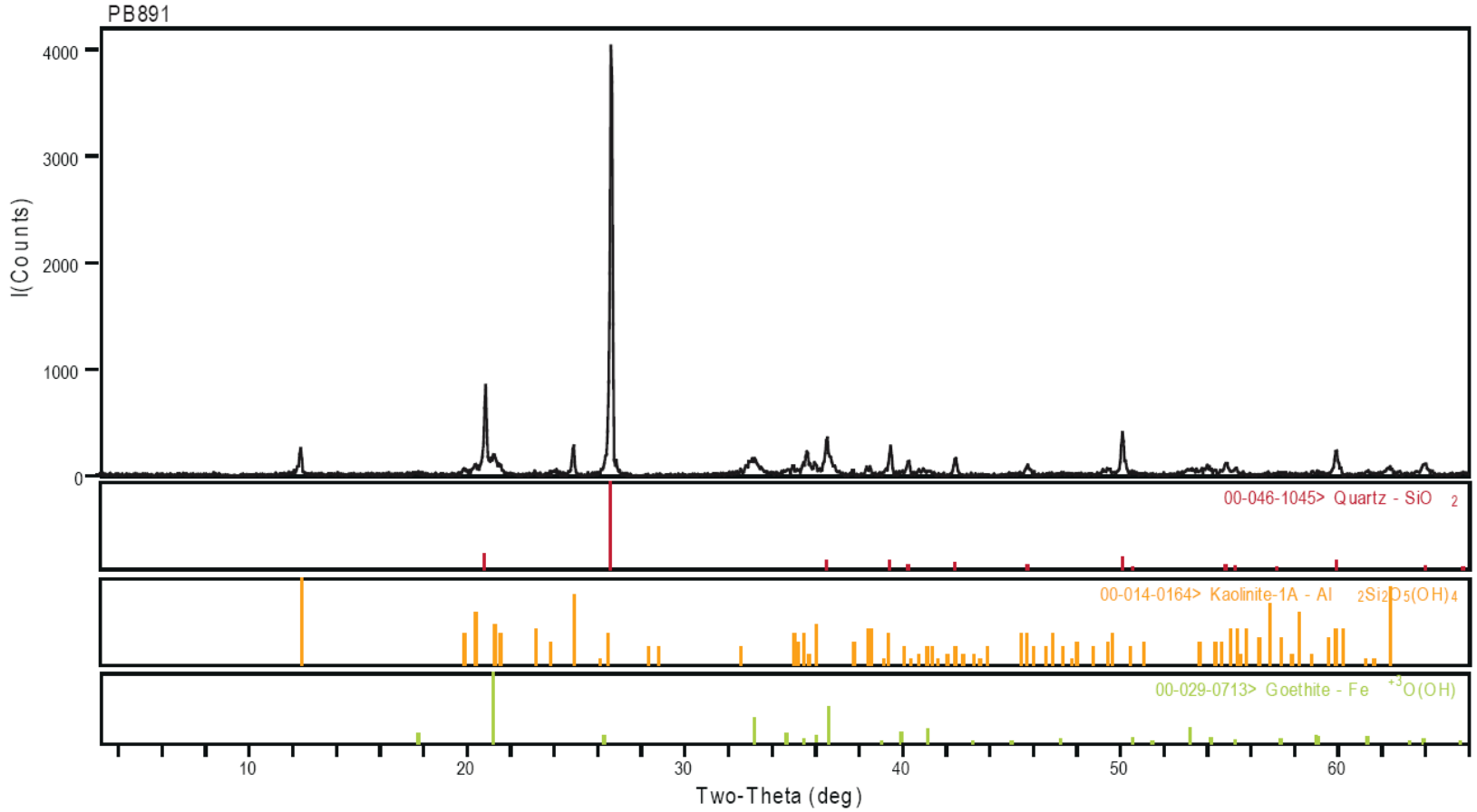

Figure 15. XRD diffraction pattern of PB891 fracture/alteration minerals.

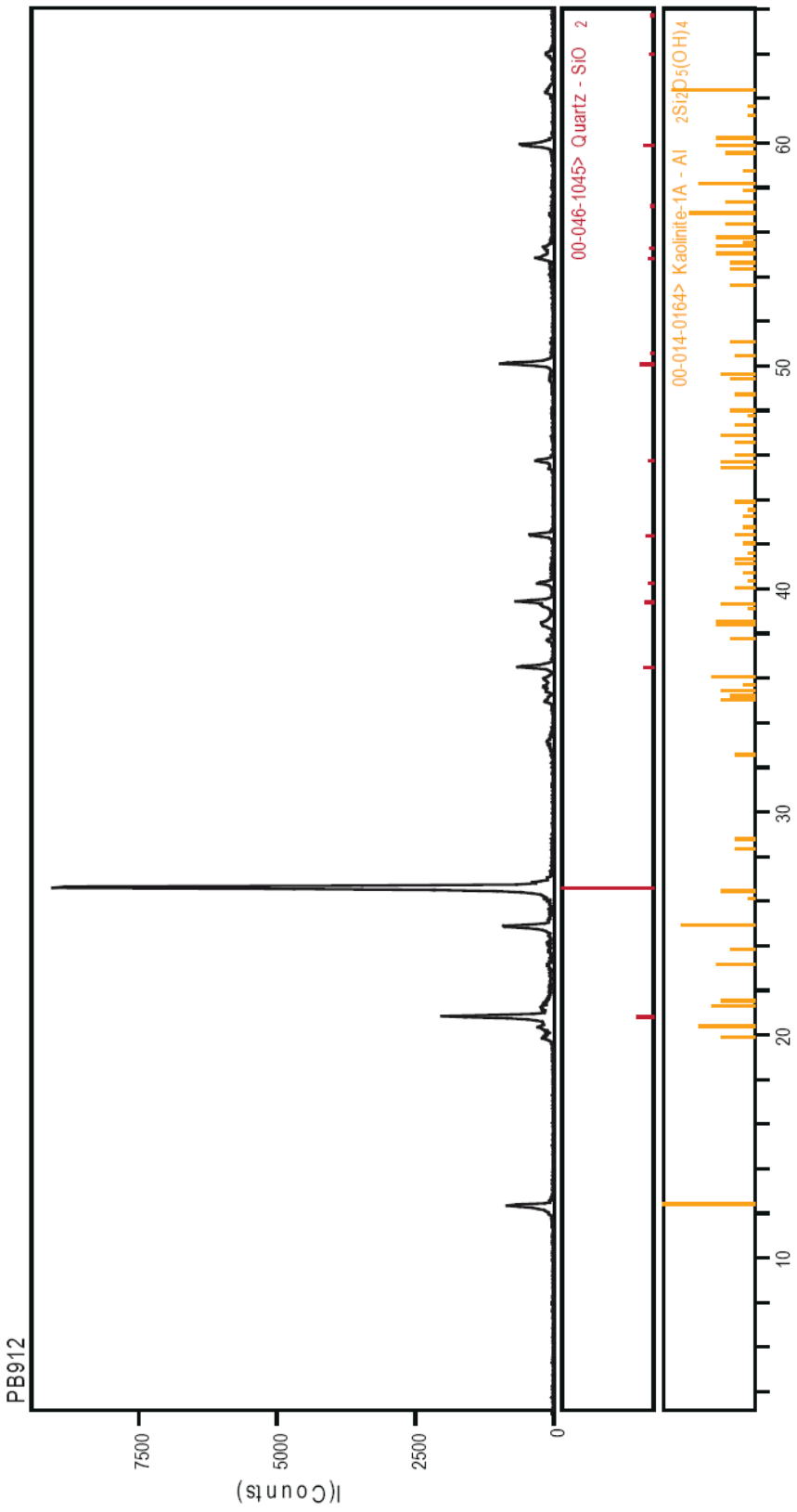

Figure 16. XRD diffraction pattern of PB912 portion fracture/alteration minerals.

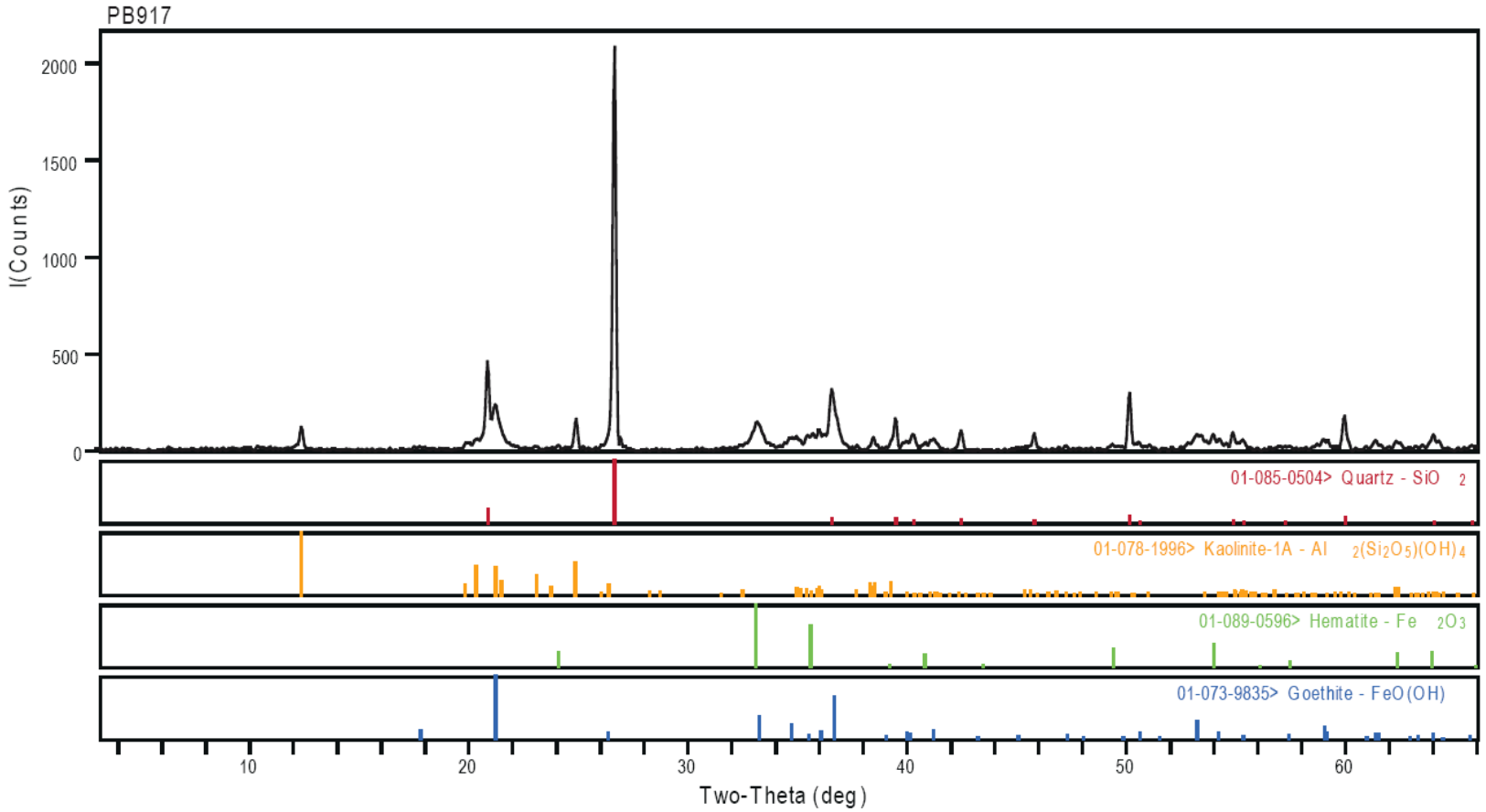

Figure 17. XRD diffraction pattern of PB917 fracture/alteration minerals.

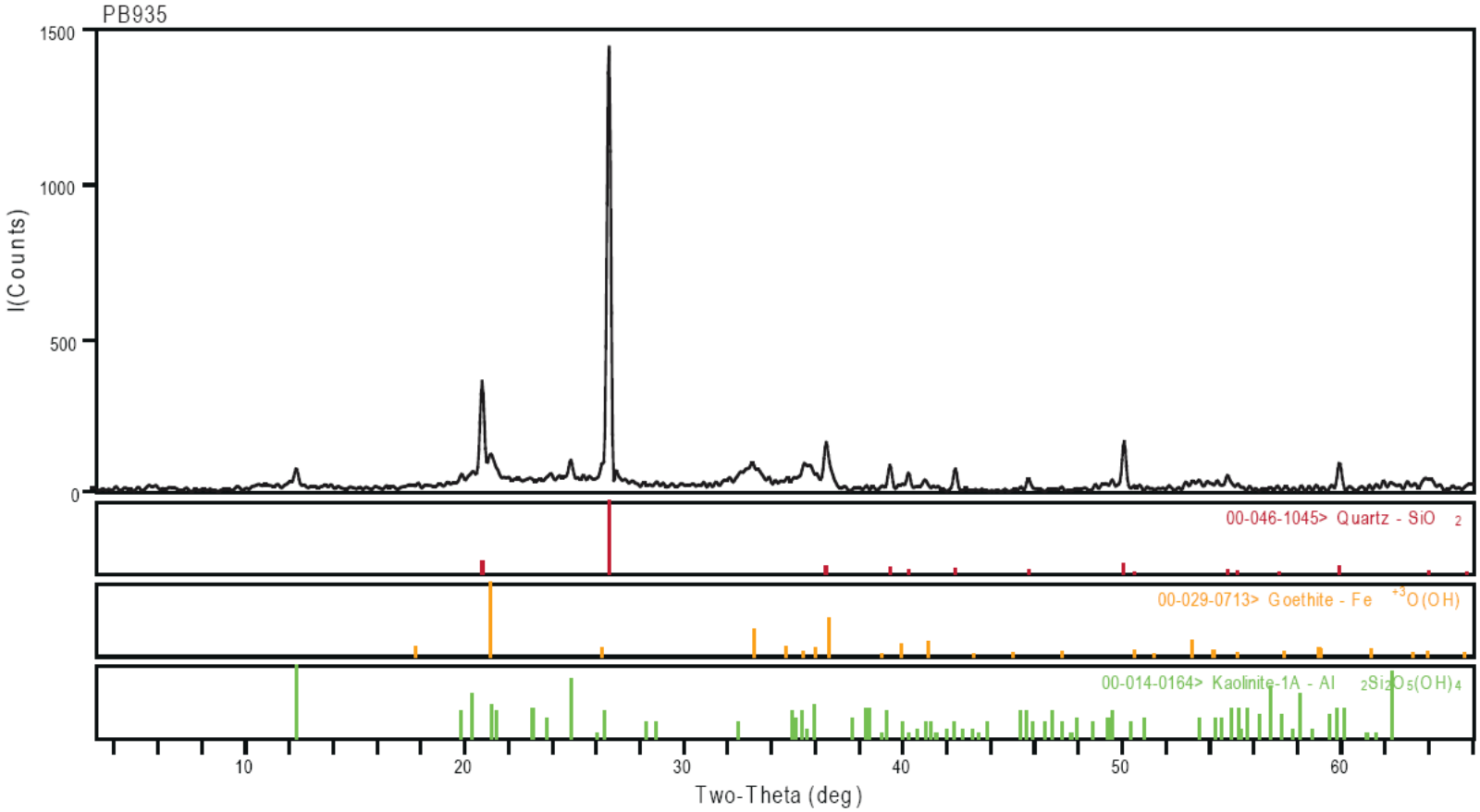

Figure 18. XRD diffraction pattern of PB935 fracture/alteration minerals.

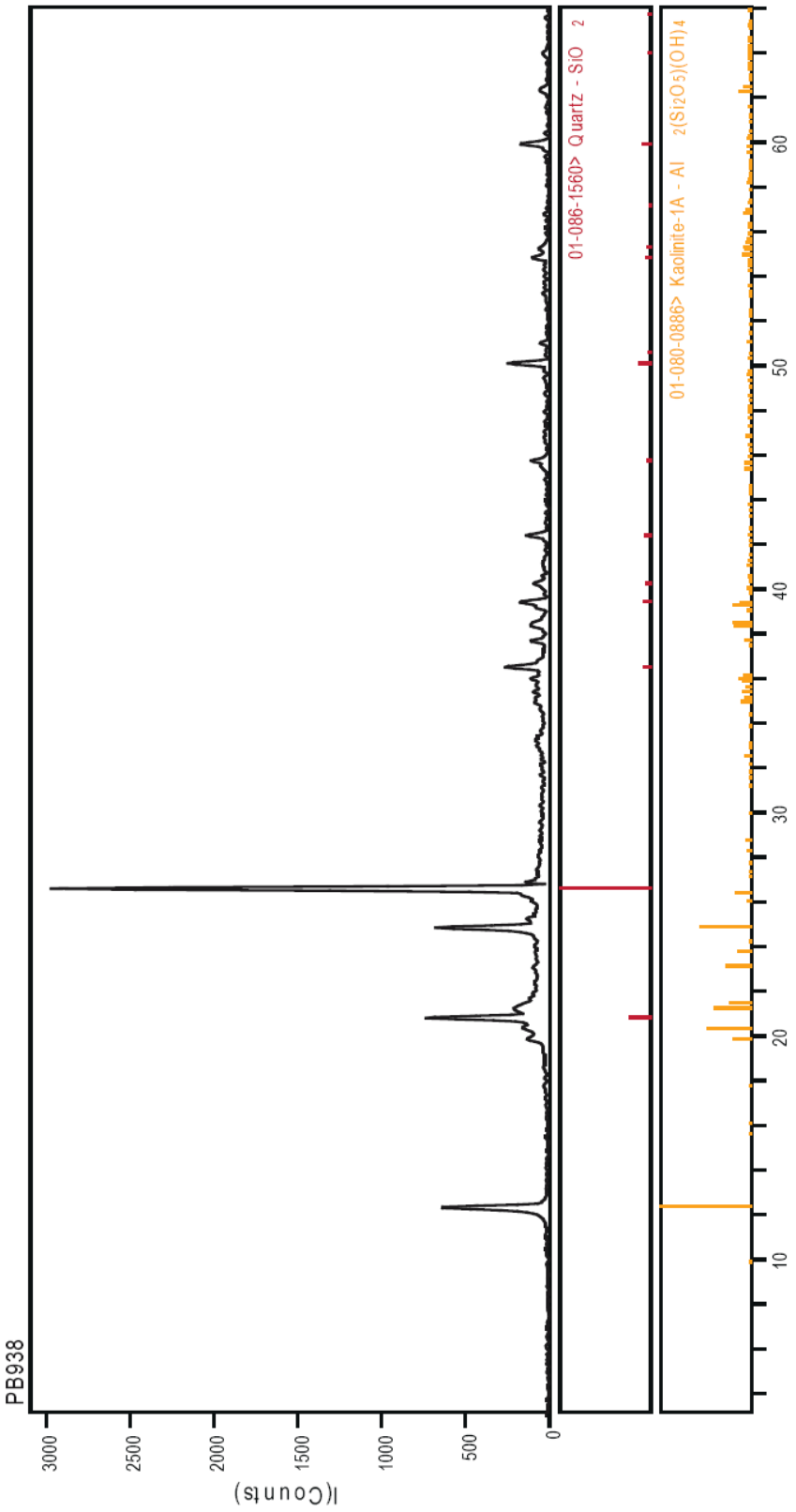

Figure 19. XRD diffraction pattern of PB938 fracture/alteration minerals.

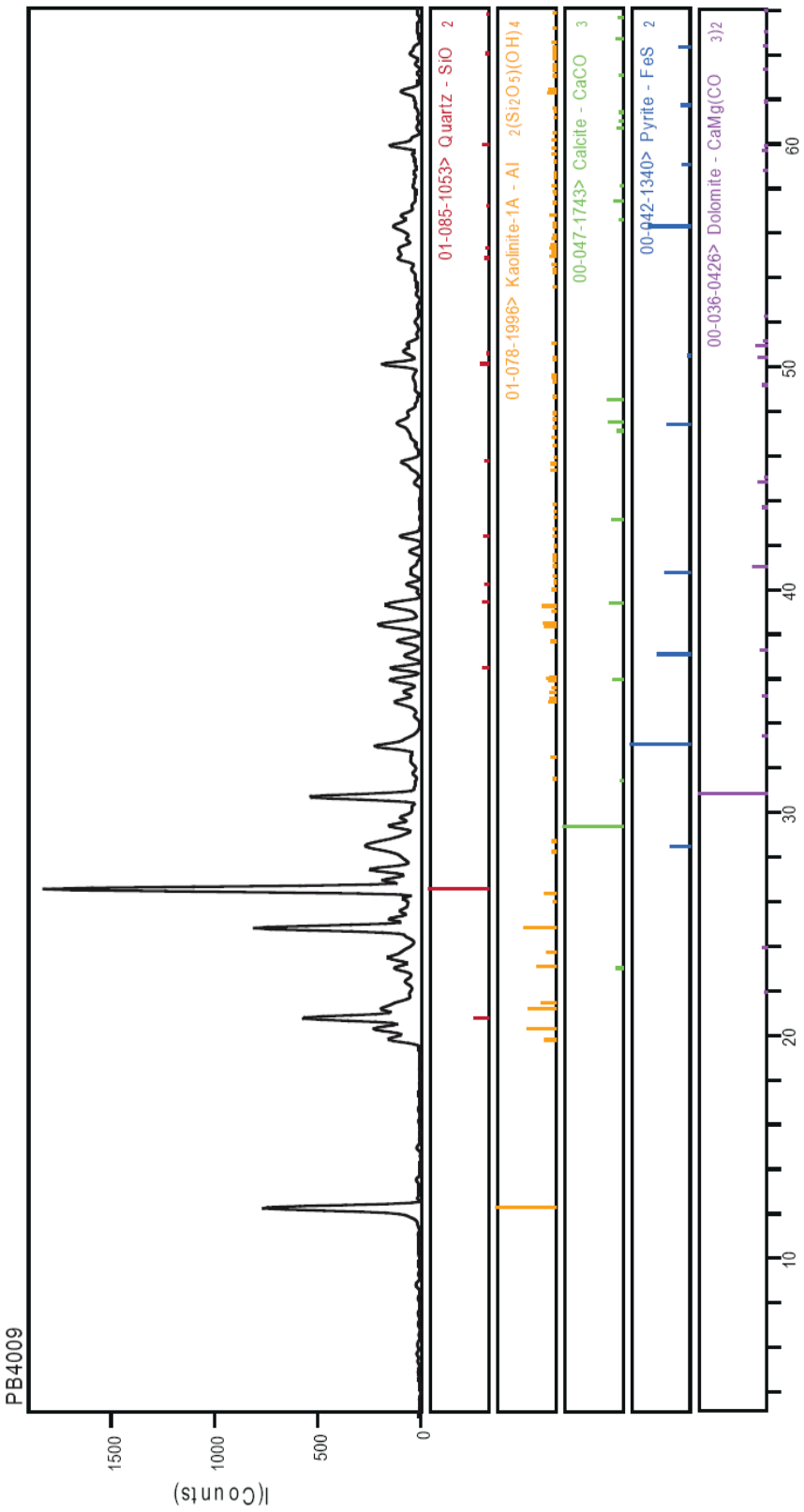

Figure 20. XRD diffraction pattern of PB4009 fracture/alteration minerals.

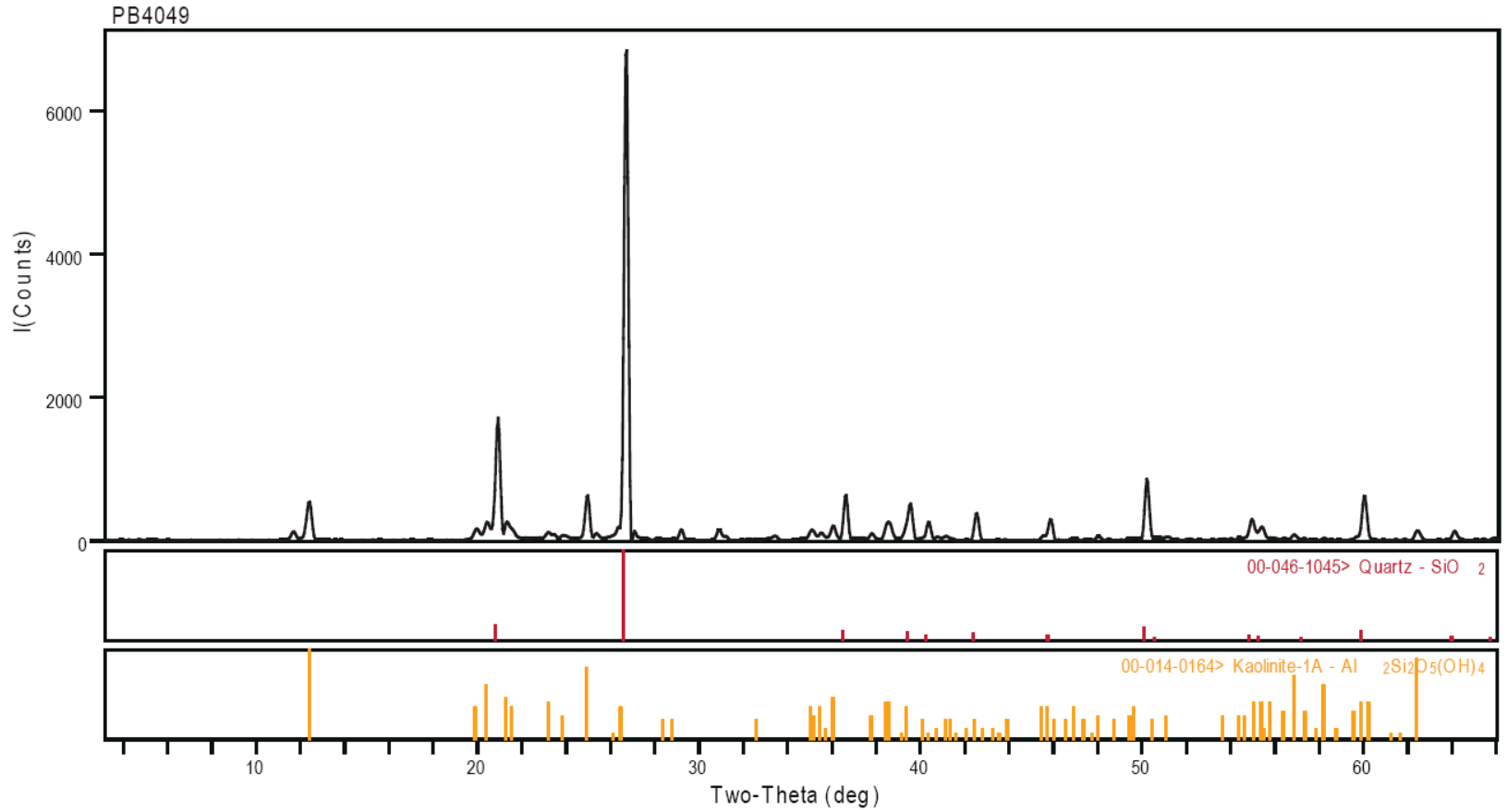

Figure 21. XRD diffraction pattern of PB4049 fracture/alteration minerals.

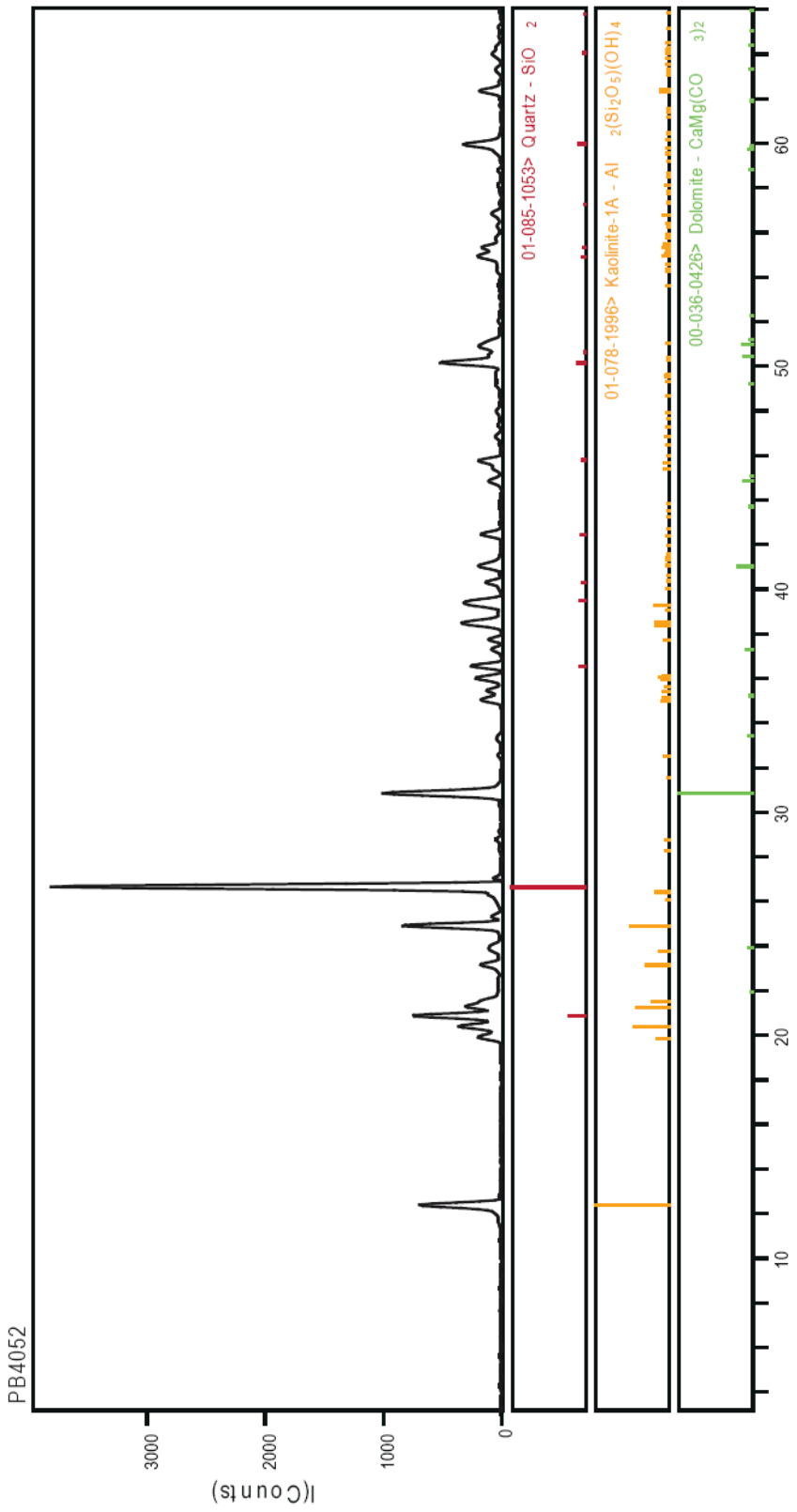

Figure 22. XRD diffraction pattern of PB4052 fracture/alteration minerals.

Appendix C. EMPA

C.1 EMPA Results

The results of the electron microprobe analyses are presented in this section. Each analysis group: 1) uranium minerals (Table 1); 2) kaolinite (Table 2); and 3) iron oxyhydroxides (Table 3) are presented. All analyses are included regardless of reliability. Samples with intermixing or that were destroyed during analysis are noted in each subsection.

Images for the analyses above are provided in a subfolder labeled BSE Images. These are the backscattered electron images from the EMPA analyses at the University of Manitoba, Department of Geological Sciences. Images are labeled with the sample number and type of analysis, e.g. 774-1 Kaol is sample PB774 spot 1 kaolinite analysis. Minerals can generally be identified by using previously described samples in the PB-1 Core section.

C.1.1 Uranium mineral analyses

Uranium mineral analyses are listed in Table 1 with decreasing depth. The uranium minerals are not named, because intermixing prevents a reliable normative mineral calculation to be completed. Sample numbers are followed by a dash, which precedes the spot number, e.g., 774-1 is PB774 spot 1. Samples with an asterisk, *, before the sample number were intermixed or the sample was destroyed by the beam during analysis, which prevented a reliable analysis.

Table 1. Uranium mineral analyses

Uranium minerals										
Sample	SiO2	UO2	TiO2	Fe2O3	PbO	CaO	Al2O3	ThO2	SO2	Total
774-1	24.75	35.88	6.93	9.26	0.55	1.45	3.06	0.34	0.04	82.26
*774-2	0.00	0.00	0.00	0.00	0.00	0.00	0.00	0.00	0.00	0.00
*774-3	0.00	0.00	0.00	0.00	0.00	0.00	0.00	0.00	0.00	0.00
774-4	8.01	7.57	0.11	46.54	0.33	0.96	1.37	0.11	0.01	65.00
775-1	0.02	61.47	0.00	0.64	0.16	0.50	0.12	0.00	0.00	62.90
*775-2	4.60	0.00	0.00	1.47	0.00	0.00	2.13	0.00	0.21	8.40
775-3	0.00	62.02	0.00	0.17	0.16	0.53	0.02	0.00	0.00	62.91
775-4	29.65	59.95	0.07	0.62	0.44	0.71	0.48	0.04	0.03	91.97
775-5	26.73	29.13	4.82	7.41	0.24	1.42	0.58	0.24	0.16	70.75
*798-1	0.00	0.00	0.00	0.00	0.00	0.00	0.00	0.00	0.00	0.00
*798-2	1.10	0.00	0.00	1.33	50.71	0.08	0.64	0.00	0.00	53.85
798-3	42.87	44.05	10.72	1.26	0.49	0.82	0.30	0.07	1.86	102.44
798-4	83.99	12.82	2.04	1.05	0.24	0.45	1.00	0.03	0.49	102.09
798-5	40.49	12.13	0.65	0.66	0.07	0.23	32.34	0.00	0.50	87.07
798-6	81.02	6.81	0.15	3.00	0.40	0.25	0.54	0.02	4.72	96.91
798-7	20.62	56.02	13.86	0.82	0.90	1.71	0.23	0.08	1.56	95.82
812-1	2.26	71.49	8.01	1.24	0.27	2.32	0.28	0.14	0.08	86.11
812-2	11.09	64.98	3.13	1.32	4.58	0.37	0.12	0.77	2.69	89.05
812-3	2.49	40.42	10.69	15.00	0.72	1.11	0.11	0.71	27.53	98.78
812-4	18.88	61.07	0.08	0.55	0.03	5.44	0.14	0.03	0.03	86.25
812-5	48.07	35.98	0.00	0.89	0.05	2.58	5.24	0.04	0.02	92.87
812-6	9.07	74.88	2.18	0.87	0.34	1.22	0.17	0.40	1.14	90.26
812-7	36.77	38.43	4.05	1.04	0.10	1.26	0.60	1.16	0.21	83.61
*814-1	91.92	0.50	0.05	0.78	1.47	0.32	0.55	0.00	0.32	95.91
814-2	49.79	33.13	15.77	1.01	0.18	0.96	0.37	0.02	0.53	101.75
814-3	17.97	33.94	0.84	1.47	1.30	0.98	1.74	0.01	0.23	58.48
814-4	33.29	52.35	1.05	0.91	2.35	1.45	0.37	0.03	0.26	92.05
814-5	30.94	57.64	1.04	0.84	3.81	1.72	0.38	0.00	0.01	96.37
*814-6	94.89	2.96	0.06	0.74	0.00	0.16	1.30	0.00	0.15	100.27
814-7	87.13	10.41	0.33	1.57	0.13	0.44	1.53	0.01	0.12	101.68
*849-1	7.14	1.40	0.10	74.50	0.92	0.57	0.13	0.08	0.15	84.99
*849-2	3.92	0.64	0.23	74.55	0.22	0.76	0.15	0.09	0.08	80.63
*849-3	5.70	0.11	0.47	75.49	0.54	0.69	0.38	0.00	0.02	83.40

Table 1. Uranium mineral analyses (continued)

Uranium minerals										
Sample	SiO2	UO2	TiO2	Fe2O3	PbO	CaO	Al2O3	ThO2	SO2	Total
*862-1	96.72	0.29	1.26	0.25	0.01	0.07	0.80	0.01	0.02	99.43
862-2	28.64	56.41	2.85	1.14	0.21	1.15	0.25	0.04	3.36	94.03
862-3	59.98	21.32	8.64	0.85	1.09	0.79	0.46	0.01	0.04	93.19
862-4	76.10	24.94	1.01	0.40	0.14	0.69	0.63	0.03	0.06	103.99
862-5	23.12	53.50	3.81	1.04	0.56	2.24	0.19	0.15	0.00	84.61
862-6	77.18	15.11	1.62	0.47	0.89	0.55	0.79	0.00	0.34	96.94
912-1	14.60	64.62	0.00	2.32	0.35	6.66	0.00	0.02	0.00	88.56
912-2	13.01	54.57	0.00	0.44	0.04	5.91	0.04	0.01	0.01	74.02
912-3	15.89	62.35	0.00	2.22	0.09	4.79	0.13	0.00	0.03	85.49
912-4	18.69	55.77	0.00	2.07	0.11	5.85	0.91	0.00	0.03	83.43
912-5	15.01	63.94	0.02	1.52	0.05	5.48	0.08	0.01	0.01	86.13
938-1	13.71	51.91	0.23	1.78	0.07	4.77	0.53	0.00	0.08	73.07
938-2	23.31	43.91	0.10	1.23	0.00	0.20	1.25	0.04	0.05	70.09
938-3	17.09	62.21	0.10	4.94	0.39	0.64	0.32	0.00	0.03	85.71
4009-1a	0.86	72.05	10.44	0.23	0.06	4.32	0.05	0.00	0.03	88.04
4009-1b	2.86	41.08	46.45	0.61	0.18	2.08	0.63	0.00	0.09	93.98
4009-1c	9.85	63.10	9.60	0.26	0.05	3.28	3.21	0.01	0.03	89.39
4009-2	10.01	53.18	16.93	1.02	0.00	2.76	4.09	0.00	0.05	88.05
4009-3	1.19	61.83	27.60	0.17	0.04	3.28	0.18	0.00	0.02	94.31
4009-4	1.10	59.39	25.05	0.16	0.11	3.03	0.10	0.00	0.02	88.94
4009-5	3.52	48.00	30.04	1.79	0.12	4.23	2.22	0.04	0.19	90.14
4052b-1a	9.88	44.18	24.18	0.78	0.21	2.28	5.79	0.24	0.04	87.57
4052b-1b	1.48	27.59	66.49	1.78	0.11	2.15	0.75	0.07	0.04	100.45
4052b-2	0.76	46.58	42.11	0.90	0.25	2.55	0.22	0.13	0.02	93.51
4052b-3	2.44	51.98	29.83	1.01	0.32	2.86	0.88	0.08	0.06	89.47
4052b-4	2.90	27.62	56.18	1.17	0.16	1.54	1.22	0.05	0.10	90.94
4052b-5	0.85	29.43	59.95	0.91	0.24	1.46	0.90	0.07	0.03	93.84
4052b-6	2.15	51.60	32.64	0.88	0.28	2.42	0.86	0.00	0.05	90.88
4052b-7	1.57	42.84	43.55	0.95	0.34	1.90	0.59	0.00	0.12	91.86

C.1.2 Kaolinite analyses

Kaolinite analyses are listed in Table 1 with decreasing depth. Sample numbers are followed by a dash, which precedes the spot number, e.g., 774-1 is PB774 spot 1. Samples with an asterisk, *, before the sample number were intermixed or the sample was destroyed by the beam during analysis, which prevented a reliable analysis.

Table 2. Kaolinite analyses

Clay minerals											
Sample	SiO2	Al2O3	Na2O	MgO	K2O	CaO	TiO2	FeO	UO2	H2O	Total
*774-1	52.88	13.36	0.05	0.02	0.40	0.22	0.04	21.26	0.22	11.56	100.00
*774-2	58.21	4.73	0.07	0.05	0.17	0.22	0.02	24.93	0.15	11.47	100.00
774-3	43.92	36.85	0.08	0.81	0.07	0.16	0.01	1.66	0.00	16.39	99.96
774-4	41.35	21.19	0.21	1.57	5.53	0.20	0.07	8.01	0.00	21.79	99.92
775-1	43.44	36.28	0.16	0.12	0.05	0.10	0.00	0.68	0.00	19.12	99.95
775-2	38.27	32.89	0.11	0.07	0.04	0.13	0.04	3.42	0.00	24.81	99.79
775-3	34.42	29.92	0.08	0.07	0.06	0.05	0.01	0.20	0.00	35.02	99.84
775-4	54.17	32.30	0.17	0.07	0.06	0.08	0.01	0.85	0.06	12.24	100.00
*775-5	71.20	1.03	0.05	0.02	0.04	0.16	0.11	19.61	0.28	7.49	100.00
798-1	45.69	39.87	0.11	0.09	0.03	0.11	0.01	0.05	0.00	13.82	99.78
798-2	39.94	34.02	0.11	0.25	0.04	0.17	0.01	0.34	0.00	24.87	99.75
798-3	43.88	38.12	0.10	0.14	0.04	0.17	0.02	0.22	0.00	17.32	100.00
798-4	43.09	35.09	0.07	0.23	0.03	0.12	0.01	0.58	0.00	20.74	99.96
812-1	43.50	36.61	0.05	0.57	0.03	0.17	0.02	0.38	0.01	18.66	100.00
812-2	45.06	38.70	0.06	0.48	0.09	0.24	0.00	0.46	0.12	14.79	100.00
812-3	45.61	38.97	0.07	0.33	0.40	0.15	0.00	0.23	0.00	14.13	99.89
812-4	44.90	33.09	0.14	0.81	0.35	0.18	0.03	4.95	0.12	15.43	100.00
812-5	42.06	27.58	0.17	3.25	0.24	0.13	0.01	1.06	0.04	25.45	100.00
814-1	55.05	32.09	0.09	0.09	0.03	0.07	0.00	0.35	0.00	12.17	99.94
814-2	36.05	29.84	0.15	0.06	0.42	0.18	0.32	11.72	0.00	21.03	99.77
814-3	26.39	21.17	0.21	0.05	0.02	0.21	0.21	33.05	0.14	18.54	100.00
849-1	41.62	38.69	0.05	0.04	0.06	0.13	0.01	4.41	0.00	14.77	99.77
849-2	46.49	40.85	0.03	0.04	0.02	0.08	0.01	0.55	0.00	11.70	99.77
849-3	43.53	37.04	0.04	0.10	0.02	0.12	0.01	5.23	0.00	13.84	99.91

Table 2. Kaolinite analyses (continued)

Clay minerals											
Sample	SiO2	Al2O3	Na2O	MgO	K2O	CaO	TiO2	FeO	UO2	H2O	Total
862-1	53.19	26.08	0.13	0.03	0.07	0.07	0.04	2.09	0.00	18.24	99.95
862-2	44.72	38.56	0.13	0.08	0.06	0.09	0.00	0.14	0.00	16.06	99.83
862-3	46.29	38.00	0.12	0.14	0.03	0.06	0.01	0.26	0.00	15.06	100.00
862-4	43.36	37.55	0.24	0.04	0.04	0.05	0.00	2.21	0.00	16.43	99.94
862-5	42.17	36.13	0.19	0.05	0.06	0.08	0.06	5.32	0.00	15.73	99.80
*912-1	24.38	5.32	0.37	0.49	0.34	0.49	0.07	21.11	0.07	47.35	100.00
912-2	67.98	24.64	0.12	0.09	0.13	0.17	0.09	5.98	0.00	0.67	99.89
*912-3	42.15	6.25	0.29	0.36	0.47	0.44	0.08	18.11	0.00	31.83	99.99
*912-4	53.16	5.72	0.31	0.38	0.31	0.26	0.10	11.86	0.00	27.81	99.91
*935-1	97.81	1.71	0.04	0.02	0.05	0.04	0.01	0.63	0.00	0.00	100.30
935-2	57.34	28.85	0.02	0.08	0.02	0.09	0.00	0.53	0.00	12.78	99.71
935-3	47.49	33.18	0.01	0.08	0.03	0.09	0.01	0.57	0.00	18.49	99.94
935-4	66.40	21.81	0.04	0.06	0.05	0.15	0.00	1.33	0.00	10.00	99.84
935-5	43.76	29.62	0.02	0.15	0.04	0.33	0.00	10.39	0.00	15.41	99.73
935-6	38.48	34.06	0.05	0.09	0.04	0.17	0.02	1.05	0.00	25.96	99.93
938-1	57.51	18.93	0.17	5.31	0.20	0.79	0.18	2.10	0.00	14.70	99.90
938-2	66.43	24.75	0.09	0.17	0.07	0.06	0.00	0.72	0.00	7.57	99.88
938-3	61.55	26.23	0.11	0.18	0.09	0.07	0.02	0.90	0.00	10.61	99.75
*938-4	78.14	0.68	0.36	0.58	0.12	0.16	0.03	1.78	0.09	18.05	100.00
4009-1	46.30	38.45	0.09	0.53	0.06	0.15	0.01	0.32	0.14	13.94	100.00
4009-2	43.05	33.67	0.08	0.90	0.51	0.27	0.06	1.10	0.23	20.12	100.00
*4009-3	90.27	0.95	0.10	0.00	0.09	0.18	5.46	0.11	1.40	1.45	100.00
4009-4	44.98	36.91	0.08	0.77	0.61	0.42	0.04	0.34	0.09	15.76	100.00
4009-5	36.19	31.73	0.06	0.26	0.10	0.31	13.74	0.86	6.10	10.65	100.00
4052b-1	41.93	36.04	0.07	0.15	0.22	0.07	0.02	0.27	0.03	21.20	100.00
*4052b-2	96.31	1.23	0.13	0.17	0.22	0.37	0.20	0.32	0.00	0.97	99.92
4052b-3	42.40	21.72	0.34	2.36	4.13	0.65	3.14	3.60	6.02	15.63	100.00
4052b-4	44.11	38.11	0.13	0.09	0.09	0.06	0.02	0.23	0.00	17.12	99.97
4052b-5	43.30	36.93	0.13	0.31	0.35	0.10	0.02	0.39	0.00	18.38	99.90
4052b-6	39.48	34.70	0.08	0.23	0.30	0.13	0.02	0.40	0.00	24.54	99.89
4052b-7	43.88	38.26	0.11	0.10	0.08	0.05	0.05	0.19	0.00	17.13	99.86

C.1.3 Iron oxyhydroxide analyses

Iron oxyhydroxide mineral analyses are listed in Table 3 with decreasing depth. The iron oxyhydroxide minerals are not named, because intermixing prevents a reliable normative mineral calculation to be completed, but are likely to be hematite or goethite based on XRD analyses (see Appendix B). Sample numbers are followed by a dash, which precedes the spot number, e.g., 774-1 is PB774 spot 1. Samples with an asterisk, *, before the sample number were intermixed or the sample was destroyed by the beam during analysis, which prevented a reliable analysis. Fewer iron oxyhydroxide samples are represented, because some data was corrupted.

Table 3. Iron oxyhydroxide mineral analyses

Iron oxyhydroxide minerals						
Sample	MnO	FeO	SiO2	H2O	Al2O3	Total
774-1	-0.03	71.52	4.66	23.31	0.48	99.97
774-2	0.00	71.41	5.57	22.63	0.38	100.00
774-3	0.02	72.84	3.68	22.86	0.60	100.00
774-4	0.05	73.83	3.66	21.89	0.57	100.00
775	N/A					
798	N/A					
812-1	0.01	49.78	30.17	17.26	2.78	100.00
812-2	-0.02	64.05	8.72	26.32	0.89	99.98
812-3	-0.02	57.21	14.00	23.87	4.90	99.98
812-4	0.01	61.75	12.70	21.93	3.61	100.00
812-5	0.00	67.98	6.90	24.68	0.44	100.00
814	N/A					
849-1	0.01	69.65	3.91	25.55	0.88	100.00
849-2	-0.02	75.30	3.99	20.70	0.00	99.98
849-3	-0.03	72.95	5.78	20.85	0.40	99.97
862	N/A					
912-1	0.69	52.12	10.94	33.81	2.44	100.00
*912-2	0.19	13.16	84.06	1.03	1.56	100.00
935-1a	0.18	86.15	3.37	9.90	0.39	100.00
935-1b	0.06	79.02	4.85	13.96	2.10	100.00
*935-2	-0.03	0.65	52.64	13.59	33.10	99.97
935-3	0.03	86.80	8.58	3.64	0.94	100.00
935-4	0.12	81.02	4.42	12.29	2.16	100.00
935-5	0.06	68.81	16.60	11.81	2.72	100.00
935-6	0.06	85.30	3.17	11.29	0.18	100.00
*938-1	0.07	4.12	0.00	95.81	0.00	100.00
*938-2	0.04	0.20	47.94	51.82	0.00	100.00
938-3a	0.15	73.85	6.28	19.72	0.00	100.00
938-3b	0.06	76.16	6.20	17.58	0.00	100.00
938-3c	0.14	70.48	5.11	22.03	2.23	100.00
938-4	0.12	71.65	3.64	23.47	1.12	100.00
938-5	0.11	75.77	3.57	20.54	0.00	100.00
*938-6	0.03	17.46	23.98	42.51	16.02	100.00
938-7	0.06	78.76	3.45	17.73	0.00	100.00
4009	N/A					
4052b	N/A					

Appendix D. EMPA Statistics

D.1 EMPA STATISTICS

A stepwise analysis of the zone 4 uranium mineral analyses, which consists of PB4009 and PB4052 (see Appendix C for raw data), was done using SPSS to determine the association between uranium and titanium in the Pozos uranium anomaly. The raw results are within the Appendix D folder in the spreadsheet called Zone 4-Stepwise linear regression_raw data.

UO_2 was used as the dependent variable and the stepwise inclusion of "predictors:" SiO_2, TiO_2, Fe_2O_3, PbO, CaO, Al_2O_3, ThO_2, and SO_2 was used to determine the best linear regression. TiO_2 (R=.92; adjusted R^2=83%) was the highest fit alone, but TiO_2+Al_2O_3 (R=.99; adjusted R^2=98%) was the best fit overall. R is the correlation between the observed and predicted values of dependent variable. R Square (R^2) is the proportion of variance in the dependent variable that can be explained by the independent variables. Adjusted R^2 adjusts the true R^2 by penalizing the addition of extraneous predictors to the model. Adjusted R^2=1 - ((1 – R^2)((N- 1) /(N - k - 1)), where k is the number of predictors.

Appendix E. Multi-Element chemistry

E.1 Multi-Element Chemistry

The multi-element chemistry results from Actlabs are located in Table 1. All samples, including outliers, are provided. Major elements are in wt% and trace elements are in ppm, unless otherwise noted. The organic carbon results are in wt%.

Table 1. Multi-element chemistry results

		Wt%										ppm, unless otherwise noted																																						wt%
Analyte Symbol	Depth (m)	SiO2	Al2O3	Fe2O3	MnO	MgO	CaO	Na2O	K2O	TiO2	P2O5	Au (ppb)	Ag	As	Ba	Be	Cd	Co	Cr	Cs	Cu	Hf	Mo	Ni	Pb	Rb	Sb	S (wt%)	Sc	Se	Sr	Ta	Th	U	V	W	Y	Zn	Zr	La	Ce	Nd	Sm	Eu	Tb	Yb	Lu	C-Organ
1		67.46	11.38	1.50		0.246	1.4	1.89	5.74	0.25	0.04			10	105	5		5.0	21.0	16.3	4		2.03	5	12		1.03			1			3.87	12	2.63		36	325										0.02
2		74.28	12.38	1.50	0.03	0.11	0.28	1.58	7.66	0.24	0.14																					37.17	4.32																
3		71.3	13.09	1.92	0.01	0.61	0.86	2.71	6.17	0.28	0.09																					18.6	3.9																
4		74.48	13.57	1.38		0.42	0.52	2.43	6.12	0.22	0.07				142					10.6						318					55	2.74	34.4	9.7														
5		68.11	14.96	2.35		0.54	0.57	4.69	6.88	0.5	0.07				185					4.4						167					35	1.68	14.4	6.2														
6		13	0.59	0.20	0	0.28	45.09	0.02	0.13	0.02	0.02			3	30			19.1	8.6	46.4	5		1	22	29		0.5	0.049						3.46	6.36	0.5		12	7										
PB 772	-8	73.73	14.4	0.88	0.006	0.05	0.1	0.34	6.07	0.282	0.02	<1	<0.5	41	74	3	0.8	2.5	8.6	8.7	3	8.3	<2	3	36	250	1.3	0.003	3.46	<0.5	41	2.9	39	49	50	9	36	156	242	69.7	102	51	9.77	<.005	1.1	3.78	0.57	
PB 774	-9	77.18	10.97	3.07	0.017	0.02	0.09	0.21	3.56	0.218	0.03	<1	1.4	382	180	4	5.7	4.4	21.7	6.5	11	8.5	11	3	178	140	7	0.011	4.48	<0.5	48	2.2	29.7	276	145	20	34	972	243	31.3	75	35	8.14	<.005	0.8	3.04	<0.01	
PB 775	-9	75.61	10.38	4.64	0.014	0.03	0.09	0.2	3.25	0.236	0.03	<1	1.7	589	183	3	6	7.9	16.7	5.7	14	8.5	20	6	207	130	10.1	0.018	6.17	<0.5	76	2	29.3	433	234	25	29	1650	258	44.9	111	51	11.4	<.005	<0.1	2.61	<0.01	
PB 775 Replicate	-9	73.6	11.08	6.25	0.014	0.03	0.09	0.17	2.96	0.244	0.04	<1	1.7	681	172	3	6.7	11.0	22.5	5.7	14	9	23	7	270	110	16.3	0.017	6.64	<0.5	109	3.4	32.1	523	279	35	32	2110	293	68.5	119	46	12	<.005	<0.1	2.9	<0.01	
PB 782	-18	77.56	6.9	10.1	0.23	0.03	0.12	0.09	0.11	0.166	0.04	<1	7.9	394	572	3	10.3	158.0	51.2	3.3	77	6.8	93	35	716	<10	36.3	0.151	5.19	<0.5	117	1.6	22.8	506	125	173	104	1550	227	69.2	404	100	23.4	2.15	4.3	12.9	1.41	
PB 798	-30	68.46	6.97	14.67	0.039	0.03	0.17	0.06	0.08	0.158	0.03	<1	2.1	2130	257	5	70.7	119.0	59.3	2.6	14	5.9	488	21	2300	<10	92.6	0.238	11	<0.5	134	1.9	29.5	1670	475	70	85	7600	517	112	143	171	33.6	1.81	3	5.53	<0.01	
*PB 798-YELLOW	-30	39.83	9.01	33.11	0.23	0.32	0.36	0.04	0.05	0.288	0.13	<1	<0.5	5730	1125	11		783.0	<0.5	<0.2		<0.2				<10	<0.1		28.1	<0.5	74	<0.3	110.1	1480	2059	163	172	26000	1425	182	866	503	91.8	<.005	12.4	22	<0.01	
*PB 798-WHITE	-30	60.35	10.6	3.61	0.067	0.83	6.19	1.2	3.28	0.766	0.09				388	2															142				55		30		669										
PB 812	-38	82.96	9.64	1.74	0.014	0.03	0.09	0.11	1.05	0.22	0.03	<1	0.9	160	266	2	8.8	5.2	15.7	4.1	4	8.6	84	4	240	40	6.5	0.099	2.72	<0.5	154	2.3	26	446	76	13	24	771	283	60.8	73	46	10.5	<.005	0.8	2.94	<0.01	
PB 814	-40	73.51	9.91	8.15	0.013	0.03	0.12	0.1	1.11	0.197	0.03	<1	1.3	1120	344	3	35.8	15.6	29.7	4.0	9	10.5	306	12	1190	30	30.7	0.083	6.82	5.1	176	1.7	28.4	806	236	32	45	4100	516	81	108	112	22.7	1.34	1.8	3.61	<0.01	
*PB 849	-67	28.62	12.09	35.56	0.005	0.03	0.5	0.04	0.29	0.224	0.1	<1	1.6	13600	71	2	173	145.0	44.0	<0.2	12	10.6	125	31	1120	<10	22.4	0.024	5.59	15.2	129	<0.3	19.1	1000	831	95	29	13000	681	77.1	<1	<1	<0.01	1.13	<0.1	2.28	<0.01	
PB 860	-77	66.7	21.75	0.76	0.005	0.02	0.11	0.11	0.09	0.359	0.09	<1	<0.5	42	14	2	0.6	2.1	10.0	2.0	3	13.4	5	5	15	<10	1.2	0.004	8.31	<0.5	299	2.1	21.4	24.2	44	8	49	330	462	100	143	50	7.03	0.81	1.2	6.14	0.94	
PB 862	-78	77.12	12.31	2.97	0.005	0.02	0.11	0.06	0.08	0.312	0.08	<1	1.5	492	86	2	7.5	5.2	32.1	2.5	6	15.1	92	6	338	<10	32.3	0.014	10.4	<0.5	166	1.7	18.7	819	365	24	52	1530	759	80.8	140	100	24.9	1.75	2.3	4.79	<0.01	
PB 862 Replicate	-78	75.15	13.05	3.93	0.005	0.02	0.11	0.07	0.09	0.303	0.05	<1	1.3	636	102	2	7.7	5.9	33.6	2.9	7	14.2	82	6	336	<10	39.5	0.015	11.6	<0.5	192	2	19.5	840	441	28	47	1910	767	86.1	143	94	23.5	<.005	2.1	4.08	<0.01	
PB 891	-104	77.4	9.5	3.82	0.007	0.02	0.1	0.08	0.09	0.237	0.1	7	<0.5	435	27	2	1.5	4.2	18.2	2.7	15	7.5	44	9	139	<10	7.1	0.006	7.34	<0.5	274	1.7	13.1	146	187	12	36	1330	283	56.5	105	41	9.52	<.005	1.3	3.9	0.5	
PB 912	-119	69.43	10.36	10.33	0.204	0.12	0.17	0.2	0.24	0.176	0.02	<1	1.2	356	38	2	3.5	30.5	18.4	5.1	2	22.7	15	14	57	20	16.5	0.005	11.4	3.6	53	1.1	27.6	118	286	13	158	558	570	44.1	114	49	15.4	1.59	4	17.8	2.59	
PB 912-N	-119	76.1	13.22	4.47	0.345	0.16	0.16	0.04	0.18	0.244	0.04	<1	<0.5	34	422	2		7.8	0.3	5.9		<0.2				<10	<0.1		4.46	<0.5	94	<0.3	14.9	16.2	67	<1	20	<1	187	36.3	93	<1	4.91	<.005	<0.1	2.95	0.56	
PB 917	-123	79.55	11.05	3.6	0.032	0.09	0.1	0.07	0.25	0.221	0.05	<1	<0.5	167	39	2	<0.5	10.0	13.1	6.4	82	7.3	10	11	46	10	1.9	0.003	6.52	<0.5	142	1.9	16.7	40.4	132	10	50	300	168	39.4	77	33	8.3	0.87	1.5	5.38	0.78	
PB 922	-127	68.13	11.12	3.22	0.303	0.13	6.77	0.08	0.24	0.226	0.03	<1	<0.5	50	159	2	<0.5	5.7	12.2	6.1	2	8.8	7	9	<5	20	1	0.007	6.58	<0.5	151	1.4	17.5	26.9	78	7	44	269	218	31.8	67	27	7.02	0.68	1.3	5.25	0.78	
PB 935	-136	78.13	11.1	5.4	0.009	0.1	0.11	0.07	0.2	0.221	0.05	<1	<0.5	271	30	1	0.9	7.9	11.3	5.2	7	5.6	9	12	18	10	0.8	0.004	2.93	12.4	165	1.7	14.8	27	98	5	36	44	161	26	60	43	12.4	2.26	1.4	2.97	0.46	
PB 938	-138	78.39	11.25	4.29	0.013	0.12	0.23	0.1	0.33	0.406	0.08	6	<0.5	358	89	1	0.7	14.8	11.6	4.4	16	7	13	23	22	10	1.8	0.009	3.83	4.2	127	<0.3	7.6	30.2	149	8	21	107	187	20.1	41	17	3.31	0.95	0.3	2.62	0.63	
PB 4009	-191	55.98	12.46	2.66	0.049	0.55	8.98	0.13	1.37	0.731	0.23	<1	1	122	2835	2	<0.5	7.9	15.5	5.0	16	7.6	7	14	15	40	0.5	0.731	8.81	<0.5	573	<0.3	16.3	1610	71	<1	21	45	206	102	<1	<1	65.6	2.55	<0.1	1.86	<0.01	
PB 4035	-210	64.33	7.59	2.76	0.166	2.97	7.55	0.06	0.26	0.338	0.04	<1	<0.5	28	28	2	<0.5	13.9	13.2	6.6	10	4.4	3	16	6	20	0.6	0.449	4.98	<0.5	150	<0.3	5.5	362	77	<1	8	59	96	21.3	<1	<1	20.4	0.67	<0.1	0.78	<0.01	0.19
PB 4049	-219	68.68	12.2	4	0.075	1.2	2.67	0.3	0.41	0.547	0.12				113	<1															154				81		17		148									
PB 4049 CLAY RICH	-219	69.37	12.37	4.03	0.075	1.24	2.54	0.31	0.42	0.538	0.12	<1	1	38	222	1	<0.5	18.7	<0.5	9.9	25	11.6	3	22	21	<10	2.4	0.964	8.6	217	157	<0.3	19.2	1510	83	19	17	38	148	75.2	<1	154	<0.01	1.84	<0.1	2.72	<0.01	
PB 4052-MTM3P	-221	65.18	20.59	3.43	0.158	3.25	6.67	0.06	0.35	0.756	0.17	<1	<0.5	36	2894	1		22.6	10.4	8.3		20.7				<10	1.2		19.2	<0.5	435	7.1	34.5	3090	177	<1	97	<1	783	128	397	344	<0.01	3.04	<0.1	10.4	<0.01	
PB 4052-MTM3	-221	63.43	15.35	3.55	0.071	1.31	2.82	0.14	0.38	0.747	0.16	<1	1.2	36	2622	<1	<0.5	11.2	11.9	7.4	23	5.4	<2	25	12	20	0.6	1.53	5.87	<0.5	192	1.1	9.2	1040	100	12	18	37	175	48.5	191	<1	49.1	1.15	<0.1	1.53	<0.01	
PB 4052-MTM8	-221	67.26	13.66	2.13	0.084	1.59	3.6	0.07	0.22	0.644	0.16	<1	1.1	19	174	1	<0.5	10.4	11.2	4.5	22	7.2	<2	18	11	10	0.4	0.545	9.75	<0.5	205	1.4	10	1060	97	13	25	36	238	50.8	<1	<1	50.3	1.23	<0.1	2.09	<0.01	
PB 4085	-246	7.78	0.53	0.21	0.05	0.33	50.91	0.03	0.08	0.016	0.04	<1	<0.5	5	5	<1	<0.5	0.6	4.4	0.4	<1	<0.2	<2	2	<5	<10	0.2	0.092	2.09	<0.5	514	<0.3	0.3	6.7	17	<1	2	6	7	1.3	3	<1	0.62	0.15	<0.1	0.16	<0.01	< 0.05

*outliers removed during analysis

1 Nopal/Coloradas n=33 (Goodell 1985)

2 Nopal n=5 (Calas et al., 2008)

3 Coloradas n=5 (Calas et al., 2008)

4 Nopal rhyolite (Magonthier, 1984)

5 Nopal tuff (Magonthier, 1984)

6 Limestone n=11 (Goodell, 1985)

Appendix F. Multi-Element Chemistry Statistics

F.1 Multi-Element Chemistry Statistics

The statistical analyses used for multi-element chemical analysis are included in this section. Table 1 is the correlation matrix for all samples (excluding outliers, see Appendix E) and selected elements as listed in the matrix. The raw correlation matrix and associated bivariate correlation graphs are in the spreadsheet, Appendix F- Correlation matrix and bivariate plots.

The factor loadings of the eight factor analyses are in Table 2. The factor analyses used a R-mode, varimax rotation of the correlation matrix (Table 1). The factors were described in the PB-1 Core section, so they will not be re-described here. The raw factor loadings and factor graphs are in the spreadsheet, Appendix F-Factor analyses.

Table 1. Correlation matrix of all samples and selected species

Row	SiO2	Al2O3	Fe2O3	MnO	MgO	CaO	Na2O	K2O	TiO2	P2O5	Ag	As	Ba	Cd	Co	Cr	Cs	Cu	Hf	Mo	Ni	Pb	Rb	Sb	S	Sc
SiO2	1.000	0.122	-0.536	-0.074	-0.069	-0.619	0.110	0.052	0.172	-0.316	-0.017	-0.462	-0.065	-0.440	-0.301	0.009	0.397	-0.145	-0.123	-0.113	-0.173	-0.389	0.017	0.084	-0.015	-0.441
Al2O3	0.122	1.000	-0.329	-0.074	0.184	-0.299	-0.026	-0.073	0.310	0.120	-0.393	-0.088	0.213	-0.104	-0.110	0.093	0.111	-0.203	-0.100	-0.232	0.052	-0.411	-0.092	-0.261	0.179	0.020
Fe2O3	-0.536	-0.329	1.000	0.107	-0.185	-0.185	0.098	0.113	-0.282	0.260	0.469	0.616	-0.081	0.610	0.450	0.166	-0.232	0.520	0.552	0.393	0.332	0.882	0.164	0.260	-0.163	0.749
MnO	-0.074	-0.074	0.107	1.000	0.267	0.053	-0.131	-0.236	0.051	0.044	0.008	-0.054	0.181	-0.048	0.331	-0.238	0.153	0.309	-0.077	0.039	0.357	0.035	-0.194	-0.148	0.112	0.108
MgO	-0.069	0.184	-0.185	0.267	1.000	0.182	-0.094	-0.186	0.649	0.435	-0.250	-0.154	0.493	-0.166	-0.038	-0.250	0.427	-0.075	0.002	-0.209	0.377	-0.241	-0.192	-0.294	0.746	0.009
CaO	-0.619	-0.299	-0.185	0.053	0.182	1.000	-0.219	-0.145	-0.084	0.042	-0.197	-0.114	0.065	-0.120	-0.084	-0.217	-0.218	-0.168	-0.240	-0.165	-0.153	-0.182	-0.142	-0.205	0.098	-0.166
Na2O	0.110	-0.026	0.098	-0.131	-0.094	-0.219	1.000	0.763	0.061	0.028	0.153	-0.216	-0.081	-0.211	-0.218	-0.227	0.635	0.198	0.418	-0.285	-0.122	0.104	0.763	-0.108	0.028	0.163
K2O	0.052	-0.073	0.113	-0.236	-0.186	-0.145	0.763	1.000	-0.104	-0.112	0.111	-0.093	-0.086	-0.092	-0.165	-0.111	0.443	0.133	0.245	-0.182	-0.334	0.147	0.991	-0.085	-0.188	0.105
TiO2	0.172	0.310	-0.282	0.051	0.649	-0.084	0.061	-0.104	1.000	0.750	-0.291	-0.142	0.751	-0.179	-0.045	-0.285	0.422	-0.167	-0.037	-0.219	0.374	-0.352	-0.153	-0.313	0.813	-0.142
P2O5	-0.316	0.120	0.260	0.044	0.435	0.042	0.028	-0.112	0.750	1.000	-0.079	0.128	0.668	0.085	0.176	-0.196	0.112	0.169	0.245	-0.070	0.451	0.126	-0.128	-0.246	0.599	0.335
Ag	-0.017	-0.393	0.469	0.008	-0.250	-0.197	0.153	0.111	-0.291	-0.079	1.000	0.050	-0.070	0.048	-0.020	0.277	-0.067	0.564	0.442	0.091	0.144	0.593	0.138	0.407	-0.052	0.428
As	-0.462	-0.088	0.616	-0.054	-0.154	-0.114	-0.216	-0.093	-0.142	0.128	0.050	1.000	-0.058	0.960	0.490	0.295	-0.491	-0.032	0.000	0.420	0.412	0.371	-0.105	0.199	-0.130	0.116
Ba	-0.065	0.213	-0.081	0.181	0.493	0.065	-0.081	-0.086	0.751	0.668	-0.070	-0.058	1.000	-0.068	0.149	-0.145	0.238	-0.027	-0.034	0.010	0.372	-0.097	-0.130	-0.177	0.809	0.061
Cd	-0.440	-0.104	0.610	-0.048	-0.166	-0.120	-0.211	-0.092	-0.179	0.085	0.048	0.960	-0.068	1.000	0.481	0.425	-0.496	-0.017	-0.007	0.566	0.456	0.445	-0.103	0.393	-0.142	0.114
Co	-0.301	-0.110	0.450	0.331	-0.038	-0.084	-0.218	-0.165	-0.045	0.176	-0.020	0.490	0.149	0.481	1.000	-0.017	-0.421	-0.023	-0.238	0.697	0.366	0.388	-0.156	0.047	-0.008	0.278
Cr	0.009	0.093	0.166	-0.238	-0.250	-0.217	-0.227	-0.111	-0.285	-0.196	0.277	0.295	-0.145	0.425	-0.017	1.000	-0.358	-0.112	0.074	0.359	0.275	0.183	-0.113	0.734	-0.243	0.006
Cs	0.397	0.111	-0.232	0.153	0.427	-0.218	0.635	0.443	0.422	0.112	-0.067	-0.491	0.238	-0.496	-0.421	-0.358	1.000	0.196	0.236	-0.489	0.017	-0.233	0.432	-0.307	0.427	-0.040
Cu	-0.145	-0.203	0.520	0.309	-0.075	-0.168	0.198	0.133	-0.167	0.169	0.564	-0.032	-0.027	-0.017	-0.023	-0.112	0.196	1.000	0.436	-0.090	0.229	0.568	0.180	0.074	-0.057	0.576
Hf	-0.123	-0.100	0.552	-0.077	0.002	-0.240	0.418	0.245	-0.037	0.245	0.442	0.000	-0.034	-0.007	-0.238	0.074	0.236	0.436	1.000	-0.160	0.006	0.516	0.291	0.178	-0.004	0.675
Mo	-0.113	-0.232	0.393	0.039	-0.209	-0.165	-0.285	-0.182	-0.219	-0.070	0.091	0.420	0.010	0.566	0.697	0.359	-0.489	-0.090	-0.160	1.000	0.226	0.569	-0.190	0.622	-0.092	0.202
Ni	-0.173	0.052	0.332	0.357	0.377	-0.153	-0.122	-0.334	0.374	0.451	0.144	0.412	0.372	0.456	0.366	0.275	0.017	0.229	0.006	0.226	1.000	0.167	-0.338	0.167	0.426	0.094
Pb	-0.389	-0.411	0.882	0.035	-0.241	-0.182	0.104	0.147	-0.352	0.126	0.593	0.371	-0.097	0.445	0.388	0.183	-0.233	0.568	0.516	0.569	0.167	1.000	0.196	0.488	-0.155	0.777
Rb	0.017	-0.092	0.164	-0.194	-0.192	-0.142	0.763	0.991	-0.153	-0.128	0.138	-0.105	-0.130	-0.103	-0.156	-0.113	0.432	0.180	0.291	-0.190	-0.338	0.196	1.000	-0.079	-0.222	0.169
Sb	0.084	-0.261	0.260	-0.148	-0.294	-0.205	-0.108	-0.085	-0.313	-0.246	0.407	0.199	-0.177	0.393	0.047	0.734	-0.307	0.074	0.178	0.622	0.167	0.488	-0.079	1.000	-0.179	0.114
S	-0.015	0.179	-0.163	0.112	0.746	0.098	0.028	-0.188	0.813	0.599	-0.052	-0.130	0.809	-0.142	-0.008	-0.243	0.427	-0.057	-0.004	-0.092	0.426	-0.155	-0.222	-0.179	1.000	0.010
Sc	-0.441	0.020	0.749	0.108	0.009	-0.166	0.163	0.105	-0.142	0.335	0.428	0.116	0.061	0.114	0.278	0.006	-0.040	0.576	0.675	0.202	0.094	0.777	0.169	0.114	0.010	1.000
Sr	-0.236	-0.053	-0.333	-0.108	0.329	0.614	-0.331	-0.308	0.453	0.475	-0.215	-0.156	0.535	-0.175	-0.172	-0.207	-0.144	-0.242	-0.142	-0.158	-0.035	-0.295	-0.358	-0.177	0.445	-0.222
Ta	0.399	0.205	-0.274	-0.124	0.273	-0.164	0.056	0.223	0.236	-0.049	0.005	-0.229	0.293	-0.205	-0.196	-0.010	0.298	-0.106	0.203	-0.077	-0.122	-0.150	0.188	0.086	0.297	-0.064
Th	-0.096	-0.047	0.417	0.213	-0.097	-0.266	0.088	0.195	-0.041	0.097	-0.015	0.324	0.162	0.325	0.858	-0.076	-0.159	-0.049	0.005	0.642	0.100	0.412	0.191	0.054	-0.035	0.354
U	-0.237	0.222	0.270	0.053	0.534	-0.059	-0.032	-0.110	0.538	0.633	0.054	0.199	0.655	0.267	0.272	0.169	0.114	0.067	0.265	0.327	0.496	0.295	-0.144	0.231	0.672	0.433
V	-0.429	-0.135	0.724	0.153	-0.135	-0.173	-0.143	-0.060	-0.152	0.230	0.064	0.624	0.036	0.607	0.881	0.104	-0.443	0.086	0.108	0.679	0.273	0.622	-0.034	0.171	-0.126	0.548
W	-0.375	-0.326	0.836	0.190	-0.237	-0.201	0.050	0.070	-0.311	0.156	0.639	0.461	-0.063	0.484	0.590	0.360	-0.303	0.496	0.355	0.490	0.441	0.794	0.112	0.375	-0.176	0.621
Y	-0.382	-0.272	0.800	0.144	-0.107	-0.130	0.337	0.266	-0.242	0.260	0.523	0.077	-0.079	0.101	0.107	-0.005	0.075	0.724	0.794	0.074	0.106	0.810	0.342	0.164	-0.141	0.869
Zn	-0.433	-0.156	0.659	0.181	-0.146	-0.131	-0.165	-0.063	-0.158	0.178	0.021	0.717	0.035	0.737	0.905	0.094	-0.495	0.073	-0.063	0.754	0.347	0.589	-0.052	0.213	-0.124	0.386
Zr	-0.393	-0.215	0.862	0.087	-0.094	-0.215	0.155	0.156	-0.154	0.331	0.408	0.317	0.010	0.324	0.366	0.050	-0.134	0.509	0.744	0.334	0.123	0.848	0.212	0.246	-0.098	0.876
La	-0.137	0.182	0.368	0.090	0.101	-0.278	-0.016	-0.023	0.293	0.469	-0.019	0.339	0.421	0.405	0.651	0.157	-0.195	-0.007	0.161	0.623	0.332	0.399	-0.048	0.282	0.240	0.396
Ce	-0.111	-0.017	0.346	0.404	0.085	-0.152	-0.138	-0.084	0.078	0.222	0.092	0.194	0.349	0.199	0.842	-0.030	-0.206	0.113	-0.016	0.551	0.357	0.351	-0.070	0.064	0.155	0.357
Nd	-0.166	0.103	0.338	0.260	0.222	-0.124	-0.065	-0.101	0.114	0.257	-0.046	0.192	0.308	0.239	0.755	-0.012	-0.104	0.023	0.093	0.608	0.317	0.382	-0.104	0.134	0.236	0.466
Sm	-0.235	-0.049	0.330	0.184	0.075	-0.101	-0.086	-0.056	0.300	0.529	0.061	0.110	0.424	0.149	0.625	0.010	-0.212	0.099	-0.063	0.486	0.267	0.384	-0.036	0.082	0.215	0.392
Eu	-0.241	-0.087	0.484	0.138	0.235	-0.068	0.214	-0.005	0.218	0.535	0.366	0.007	0.282	0.080	-0.086	0.110	0.238	0.549	0.672	-0.030	0.477	0.473	0.023	0.203	0.267	0.548
Tb	-0.374	-0.298	0.802	0.272	-0.206	-0.164	0.174	0.123	-0.298	0.203	0.407	0.200	-0.077	0.231	0.564	0.003	-0.176	0.558	0.509	0.425	0.175	0.825	0.197	0.200	-0.222	0.807
Yb	-0.372	-0.260	0.804	0.241	-0.099	-0.149	0.321	0.224	-0.231	0.264	0.506	0.095	-0.048	0.112	0.230	-0.039	0.046	0.709	0.764	0.123	0.158	0.796	0.301	0.132	-0.135	0.870
Lu	-0.311	-0.252	0.687	0.169	-0.168	-0.116	0.398	0.270	-0.290	0.163	0.520	-0.021	-0.179	-0.009	-0.073	-0.057	0.136	0.763	0.785	-0.119	0.061	0.679	0.353	0.087	-0.222	0.754

Table 2. Factor loadings

Factor 1		Factor 2		Factor 3		Factor 4		Factor 5		Factor 6		Factor 7		Factor 8	
Cs	-0.647	Al2O3	-0.519	Sb	-0.444	Ni	-0.570	Cr	-0.645	As	-0.558	SiO2	-0.560	Ag	-0.334
SiO2	-0.414	SiO2	-0.482	Cr	-0.387	Cr	-0.471	Sb	-0.571	Cd	-0.512	Al2O3	-0.313	Sb	-0.297
Na2O	-0.379	TiO2	-0.434	Ag	-0.350	Sb	-0.383	Cd	-0.358	Ni	-0.439	Cr	-0.296	Mo	-0.167
Ta	-0.266	Sr	-0.392	Rb	-0.331	MnO	-0.320	As	-0.305	Fe2O3(T)	-0.316	Ni	-0.260	Sm	-0.145
MgO	-0.240	Ta	-0.360	W	-0.295	Mo	-0.299	Mo	-0.221	Zn	-0.290	Cs	-0.259	W	-0.145
Sr	-0.238	Ba	-0.339	K2O	-0.295	Cd	-0.295	U	-0.200	W	-0.241	Sb	-0.231	Pb	-0.131
K2O	-0.224	S	-0.335	Pb	-0.295	U	-0.279	La	-0.155	V	-0.236	Na2O	-0.219	Ni	-0.118
CaO	-0.207	MgO	-0.311	Tb	-0.245	As	-0.254	Ag	-0.152	Co	-0.195	Ta	-0.215	Cu	-0.108
Rb	-0.205	CaO	-0.183	Mo	-0.235	Sr	-0.250	Pb	-0.151	Sm	-0.169	Ag	-0.147	SiO2	-0.100
TiO2	-0.195	Cs	-0.037	Fe2O3(T)	-0.231	CaO	-0.179	Ta	-0.150	Cr	-0.163	K2O	-0.117	Cr	-0.094
Hf	-0.187	Co	0.019	Lu	-0.218	Co	-0.175	Hf	-0.143	P2O5	-0.160	Rb	-0.106	MnO	-0.089
S	-0.180	Mo	0.030	Cd	-0.215	Nd	-0.148	Fe2O3(T)	-0.106	Pb	-0.149	La	-0.104	CaO	-0.082
Eu	-0.179	U	0.045	As	-0.185	Ce	-0.146	K2O	-0.080	Tb	-0.099	Cu	-0.095	Tb	-0.047
Al2O3	-0.149	La	0.046	Y	-0.175	Zn	-0.145	W	-0.075	Mo	-0.096	Hf	-0.091	Eu	-0.044
Cu	-0.101	Th	0.063	Yb	-0.172	La	-0.142	Zr	-0.074	Cu	-0.083	Th	-0.088	Co	-0.041
Lu	-0.059	Cr	0.075	Zn	-0.164	MgO	-0.131	Zn	-0.052	CaO	-0.076	W	-0.076	Ce	-0.033
Ag	-0.044	Ni	0.080	V	-0.151	W	-0.111	Rb	-0.047	Zr	-0.075	Ce	-0.065	Fe2O3(T)	-0.032
Ba	0.046	Nd	0.092	Cu	-0.146	Ba	-0.109	Sr	-0.042	Lu	-0.072	Nd	-0.057	S	-0.031
P2O5	0.134	Ce	0.098	Zr	-0.140	S	-0.108	Eu	-0.038	Y	-0.067	Mo	-0.055	Sr	-0.024
Y	0.143	As	0.111	Th	-0.125	V	-0.105	V	-0.035	Yb	-0.060	MnO	-0.053	Ba	-0.023
Cr	0.171	Cd	0.116	Na2O	-0.082	Sm	-0.094	Al2O3	0.004	MnO	-0.058	TiO2	-0.049	K2O	-0.014
Yb	0.243	P2O5	0.164	Co	-0.064	Eu	-0.090	Sc	0.009	Eu	-0.049	Eu	-0.042	Na2O	-0.014
Sb	0.287	MnO	0.176	Sc	-0.049	P2O5	-0.063	Y	0.023	Sc	-0.026	U	-0.040	Zn	-0.012
MnO	0.297	Sm	0.183	SiO2	-0.036	Ag	-0.048	Na2O	0.054	Ag	-0.009	Cd	-0.024	Y	-0.011
Ni	0.336	Zn	0.184	Hf	-0.034	Fe2O3(T)	-0.021	SiO2	0.054	Sb	0.011	Lu	-0.001	Rb	-0.009
Sc	0.376	K2O	0.215	Ce	0.062	Al2O3	-0.017	Ni	0.065	Th	0.013	Pb	-0.001	Yb	-0.007
U	0.412	Sb	0.282	MnO	0.130	Pb	-0.015	Lu	0.070	La	0.042	Yb	0.000	Lu	-0.006
Pb	0.481	V	0.302	Nd	0.179	TiO2	0.006	Th	0.072	Rb	0.067	Fe2O3(T)	0.006	Cd	0.003
Zr	0.484	Rb	0.309	CaO	0.211	Tb	0.054	Yb	0.077	Na2O	0.069	Tb	0.006	Cs	0.009
Fe2O3(T)	0.495	Na2O	0.344	La	0.273	Zr	0.068	P2O5	0.082	Ce	0.077	Zr	0.010	Th	0.011
Tb	0.564	W	0.666	Sm	0.287	Cu	0.068	Nd	0.083	K2O	0.081	As	0.011	V	0.027
W	0.596	Fe2O3(T)	0.763	Ta	0.294	Sc	0.070	Tb	0.083	U	0.083	Y	0.011	Zr	0.038
Cd	0.655	Tb	0.771	Cs	0.350	Th	0.117	Co	0.113	TiO2	0.093	V	0.018	As	0.051
As	0.658	Pb	0.782	Eu	0.368	Yb	0.140	Sm	0.114	Hf	0.102	Sc	0.020	TiO2	0.052
Sm	0.825	Ag	0.814	Al2O3	0.443	SiO2	0.152	CaO	0.121	MgO	0.129	Co	0.021	La	0.073
Mo	0.867	Zr	0.850	Ni	0.492	Y	0.161	Ba	0.123	S	0.138	S	0.021	U	0.076
V	0.902	Eu	0.891	Sr	0.656	Ta	0.173	TiO2	0.131	Ba	0.139	Zn	0.025	Nd	0.082
Zn	0.909	Sc	0.908	MgO	0.815	Lu	0.192	S	0.131	Nd	0.141	MgO	0.060	P2O5	0.084
La	0.921	Hf	0.919	U	0.818	Hf	0.226	Ce	0.204	Sr	0.148	Sm	0.067	Hf	0.095
Nd	0.938	Cu	0.928	TiO2	0.856	Cs	0.478	Cu	0.206	Al2O3	0.152	Ba	0.077	MgO	0.096
Ce	0.947	Yb	0.939	S	0.887	Na2O	0.804	MgO	0.261	Cs	0.253	P2O5	0.177	Sc	0.108
Co	0.954	Lu	0.949	Ba	0.896	Rb	0.844	Cs	0.277	SiO2	0.468	Sr	0.504	Ta	0.118
Th	0.975	Y	0.958	P2O5	0.919	K2O	0.876	MnO	0.832	Ta	0.715	CaO	0.878	Al2O3	0.584

Appendix G. PB Water Analyses

G.1 Adit Seepage Water and Groundwater Analyses

The water chemical analyses in the following pages were collected as part of the Peña Blanca Natural Analogue project. This data was provided by M. Rearick, P. Dobson, S. Goldstein, J. A. Rodriguez, and S. Levy. Well locations and seepage samples were described previously (Goldstein et al., 2010; Goodell et al., 2010). This study is most interested in unsaturated (adit seepage) vs. saturated (groundwater), i.e. changes between them.

Table 1. Water Chemistry of Samples from Nopal 1 Wells.

	PB1, filtered	PB1, unfiltered	PB2, filtered	PB2, unfiltered	PB3, filtered	PB3, unfiltered	PB4, filtered	PB4, unfiltered
Sample ID	SPC01041433 SPC01041431	SPC01041434	SPC01041437 SPC01041435	SPC01041438	SPC01041441 SPC01041439	SPC01041442	SPC01041430 SPC01041425	SPC01041429
Collection date	12/14/06	12/14/06	12/14/06	12/14/06	12/14/06	12/14/06	12/13/06	12/13/06
Analysis date	02/01/07 03/13/07	02/01/07	02/01/07 03/13/07	02/01/07	02/01/07 03/13/07	02/01/07	02/01/07 03/13/07	02/01/07
Ag, ppm	<0.001	<0.001	<0.001	<0.001	<0.001	<0.001	<0.001	<0.001
Al, ppm	0.008±0.000	0.014±0.000	0.004±0.000	0.011±0.000	0.003±0.000	0.013±0.000	0.002±0.000	0.005±0.000
Total alkalinity, ppm $CaCO_3$	331	—	277	—	207	—	73.4	—
As, ppm	0.0464±0.0006	0.0590±0.0020	0.0105±0.0000	0.0127±0.0009	0.0478±0.0001	0.0603±0.0014	0.0003±0.0000	0.0003±0.0000
B, ppm	0.181±0.000	0.167±0.001	0.153±0.002	0.154±0.001	0.134±0.001	0.185±0.004	0.048±0.001	0.077±0.002
Ba, ppm	0.078±0.001	0.073±0.001	0.051±0.001	0.059±0.000	0.063±0.001	0.051±0.000	0.029±0.000	0.010±0.000
Be, ppm	<0.001	<0.001	<0.001	<0.001	<0.001	<0.001	<0.001	<0.001
Br, ppm	0.25	—	0.19	—	0.23	—	0.11	—
Ca, ppm	35.5±0.2	37.2±0.2	50.8±0.4	54.1±1.4	78.4±1.2	78.6±1.2	22.8±0.3	22.8±0.5
Cd, ppm	<0.001	<0.001	<0.001	<0.001	<0.001	<0.001	<0.001	<0.001
Cl, ppm	14.8	—	12.6	—	12.8	—	8.39	—
Co, ppm	<0.001	<0.001	<0.001	<0.001	<0.001	<0.001	<0.001	<0.001
CO_3, ppm	16.5	—	9.17	—	0.0	—	0.0	—
Cr, ppm	0.002±0.000	0.013±0.000	0.0.001±0.000	0.012±0.000	0.001±0.000	0.010±0.001	<0.001	0.003±0.000
Cs, ppm	0.006±0.000	0.007±0.000	0.012±0.000	0.013±0.001	0.007±0.000	0.008±0.000	0.002±0.000	0.002±0.000
Cu, ppm	0.013±0.000	0.014±0.001	0.004±0.000	0.010±0.001	0.005±0.000	0.005±0.000	0.004±0.000	0.002±0.001
F, ppm	3.69	—	2.37	—	2.66	—	1.85	—
Fe, ppm	0.04±0.00	0.06±0.00	0.03±0.00	0.02±0.00	0.04±0.00	0.03±0.00	0.02±0.00	0.02±0.00
HCO_3, ppm	370	—	320	—	252	—	89.6	—
Hg, ppm	0.00007±0.00001	0.000014±0.00000	<0.00005	0.00002±0.00000	<0.00005	<0.00005	<0.00005	<0.00005
K, ppm	4.69±0.02	4.64±0.04	10.9±0.1	11.0±0.0	3.21±0.02	3.14±0.08	2.04±0.02	2.08±0.03
Li, ppm	0.206±0.001	0.203±0.002	0.224±0.002	0.214±0.019	0.112±0.001	0.108±0.002	0.033±0.000	0.034±0.000
Mg, ppm	11.8±0.0	11.7±0.1	27.0±0.2	27.4±0.0	11.6±0.0	11.3±0.0	8.12±0.10	8.17±0.05
Mn, ppm	0.086±0.001	0.095±0.001	0.049±0.000	0.002±0.000	0.243±0.002	0.095±0.001	0.017±0.000	<0.001

Mo, ppm	0.032±0.001	0.047±0.000	0.020±0.000	0.033±0.000	0.124±0.004	0.172±0.000	0.001±0.000	0.002±0.000
Na, ppm	110±0	109±1	101±2	102±0	62.3±1.7	60.9±0.6	25.3±0.1	25.3±0.2
Ni, ppm	0.003±0.000	0.003±0.000	0.003±0.000	0.003±0.000	0.004±0.000	0.006±0.000	0.002±0.000	0.002±0.000
NO_2, ppm	<0.01	—	<0.01	—	<0.01	—	<0.01	—
NO_3, ppm	<0.01	—	0.03	—	0.03	—	2.06	—
C_2O_4, ppm	<0.01	—	<0.01	—	<0.01	—	<0.01	—
Pb, ppm	0.0128±0.0001	0.0375±0.0010	0.0030±0.0000	0.0019±0.0001	0.0008±0.0000	0.0009±0.0000	<0.0002	<0.0002
PO_4, ppm	<0.01	—	<0.01	—	0.04	—	<0.01	—
Rb, ppm	0.017±0.000	0.018±0.000	0.033±0.000	0.035±0.002	0.013±0.000	0.014±0.000	0.007±0.000	0.007±0.000
Sb, ppm	<0.001	<0.001	<0.001	<0.001	<0.001	<0.001	<0.001	<0.001
Se, ppm	<0.001	<0.001	<0.001	<0.001	<0.001	<0.001	<0.001	<0.001
Si, ppm	9.9±0.0	10.0±0.1	12.5±0.1	12.9±0.0	10.7±0.0	10.5±0.1	5.80±0.04	5.80±0.04
SiO_2, calculated ppm	21.1	21.4	26.8	27.7	22.9	22.4	12.4	12.4
SO_4, ppm	81.4	—	195	—	156	—	79.5	—
Sn, ppm	<0.001	<0.001	<0.001	<0.001	<0.001	<0.001	<0.001	<0.001
Sr, ppm	0.81±0.00	0.83±0.01	1.09±0.01	1.15±0.01	1.01±0.01	1.00±0.01	0.47±0.00	0.48±0.00
Th, ppm	<0.001	<0.001	<0.001	<0.001	<0.001	<0.001	<0.001	<0.001
Ti, ppm	<0.002	<0.002	<0.002	<0.002	<0.002	<0.002	<0.002	<0.002
Tl, ppm	<0.001	<0.001	<0.001	<0.001	<0.001	<0.001	<0.001	<0.001
U, ppm	0.0205±0.0002	0.0247±0.0004	0.0338±0.0002	0.0393±0.0016	0.3274±0.0099	0.3650±0.0026	0.0012±0.0000	0.0014±0.0000
V, ppm	<0.001	0.004±0.000	<0.001	0.003±0.000	<0.001	0.003±0.000	<0.001	0.001±0.000
Zn, ppm	0.017±0.000	0.028±0.000	0.008±0.000	0.012±0.000	0.024±0.000	0.014±0.000	0.013±0.000	0.001±0.001
pH, field	7.1	7.1	7.4	7.4	7.1	7.1	7.1	7.1
pH, laboratory	8.24	—	8.03	—	7.76	—	8.00	—
Total dissolved solids, ppm	671	—	757	—	605	—	253	—
Cation sum, meq/l	7.688	—	9.469	—	7.703	—	2.977	—
Anion sum, meq/l	8.933	—	10.080	—	7.892	—	3.493	—
Cation/anion balance, %	−7.49	—	−3.12	—	−1.21	—	−7.97	—

Table 2. Water Chemistry of Samples from Peña Blanca Regional Wells

	Peña Blanca, filtered	Peña Blanca, unfiltered	Pozos Ranch tank, filtered	Pozos Ranch tank, unfiltered
Sample ID	SPC01041428 SPC01041423	SPC01041427	SPC01041450 SPC01041448	SPC01041451
Collection date	12/13/06	12/13/06	12/14/06	12/14/06
Analysis date	02/01/07, 03/13/07	02/01/07	02/01/07, 03/13/07	02/01/07
Ag, ppm	<0.001	<0.001	<0.001	<0.001
Al, ppm	0.002±0.000	0.007±0.000	0.010±0.001	0.011±0.000
Total alkalinity, ppm $CaCO_3$	233	—	164	—
As, ppm	0.0407±0.0008	0.0463±0.0006	0.0226±0.0061	0.0179±0.0003
B, ppm	0.153±0.001	0.170±0.002	0.050±0.003	0.069±0.002
Ba, ppm	0.009±0.000	0.008±0.000	0.032±0.001	0.028±0.000
Be, ppm	<0.001	<0.001	<0.001	<0.001
Br, ppm	0.15	—	0.09	—
Ca, ppm	39.5±0.8	38.9±1.5	66.4±2.8	63.8±1.6
Cd, ppm	<0.001	<0.001	<0.001	<0.001
Cl, ppm	12.7	—	8.96	—
Co, ppm	<0.001	<0.001	<0.001	<0.001
CO_3, ppm	13.9	—	0.0	—
Cr, ppm	<0.001	0.008±0.000	0.002±0.001	<0.001
Cs, ppm	0.010±0.000	0.011±0.000	0.006±0.001	0.005±0.000
Cu, ppm	0.004±0.000	0.004±0.000	0.002±0.000	0.001±0.000
F, ppm	2.45	—	1.94	—
Fe, ppm	<0.01	<0.01	<0.01	<0.01
HCO_3, ppm	256	—	200	—
Hg, ppm	<0.0005	<0.0005	<0.0005	<0.0005
K, ppm	4.42±0.02	4.24±0.15	2.04±0.07	1.96±0.02
Li, ppm	0.042±0.000	0.041±0.001	0.033±0.002	0.033±0.001
Mg, ppm	4.89±0.05	4.82±0.04	8.59±0.30	8.39±0.03
Mn, ppm	<0.001	<0.001	<0.001	<0.001
Mo, ppm	0.004±0.000	0.005±0.000	0.004±0.000	0.005±0.000
Na, ppm	49.8±0.4	47.9±0.4	25.8±0.9	24.9±0.1
Ni, ppm	0.002±0.000	0.002±0.000	0.004±0.001	0.003±0.000
NO_2, ppm	<0.01	—	<0.01	—
NO_3, ppm	8.81	—	7.84	—
C_2O_4, ppm	<0.01	—	<0.01	—
Pb, ppm	0.0003±0.0000	0.0003±0.0000	0.0004±0.0001	0.0005±0.0000
PO_4, ppm	<0.01	—	<0.01	—
Rb, ppm	0.017±0.000	0.018±0.000	0.011±0.003	0.008±0.000
Sb, ppm	<0.001	<0.001	<0.001	<0.001
Se, ppm	<0.001	0.001±0.000	0.001±0.001	<0.001
Si, ppm	26.1±0.4	25.3±0.4	11.0±0.3	10.6±0.1
SiO_2, calculated ppm	55.9	54.2	23.6	22.7
SO_4, ppm	20.8	—	78.8	—

Sn, ppm	<0.001	<0.001	<0.001	<0.001
Sr, ppm	0.35±0.01	0.35±0.00	0.66±0.02	0.65±0.00
Th, ppm	<0.001	<0.001	<0.001	<0.001
Ti, ppm	<0.002	<0.002	<0.002	<0.002
Tl, ppm	<0.0001	<0.0001	<0.0001	<0.0001
U, ppm	0.0098±0.0003	0.0105±0.0001	0.0067±0.0013	0.0051±0.0000
V, ppm	0.020±0.000	0.022±0.000	0.007±0.002	0.005±0.000
Zn, ppm	0.016±0.000	0.017±0.000	0.007±0.001	0.006±0.001
pH, field	6.8	6.8	7.1	7.1
pH, laboratory	8.41	—	7.99	—
Total dissolved solids, ppm	470	—	425	—
Cation sum, meq/l	4.667	—	5.213	—
Anion sum, meq/l	5.724	—	5.410	—
Cation/anion balance, %	–10.17	—	–1.86	—

Table 3. Water Chemistry of Seepage from Nopal I.

	8B	18A	Left adit	18A column	Condensate	34E column	39B-III	47E-II
Sample ID	SPC01037918	SPC01037979	SPC01038241	SPC02041957	SPC01040904	SPC01040953	SPC01040975	SPC01041416
Collection date	11/08/05	11/08/05	11/10/05	08/26/06	12/12/06	12/12/06	12/13/06	12/13/06
Analysis date	06/05/07	06/05/07	06/05/07	06/05/07	06/05/07	06/05/07	06/05/07	06/05/07
Ag, ppm	<0.001	<0.001	<0.001	<0.001	<0.001	0.0017±0.0000	<0.001	<0.001
Al, ppm	0.015±0.001	<0.002	0.004±0.000	0.016±0.000	0.072±0.002	0.006±0.000	0.040±0.001	0.078±0.002
Total alkalinity, ppm $CaCO_3$	70.9	22.2	0.0	6.35	17.3	24.4	17.6	—
As, ppm	0.0215±0.0015	0.0567±0.0088	0.0716±0.0006	0.0540±0.0015	0.0091±0.0002	0.0103±0.0003	0.3553±0.0079	0.4150±0.0111
B, ppm	0.012±0.001	<0.002	0.082±0.001	<0.002	0.006±0.001	<0.002	<0.002	<0.002
Ba, ppm	<0.001	<0.001	0.042±0.001	0.005±0.000	0.066±0.004	0.020±0.000	0.074±0.015	0.055±0.002
Be, ppm	<0.001	<0.001	<0.001	<0.001	<0.001	<0.001	<0.001	<0.001
Br, ppm	<0.01	<0.01	<0.01	0.05	0.44	0.59	<0.01	<0.01
Ca, ppm	22.4±0.2	8.09±0.04	84.0±0.9	10.1±0.1	9.53±0.07	13.0±0.0	248±1	442±8
Cd, ppm	<0.001	<0.001	0.012±0.000	<0.001	<0.001	<0.001	0.035±0.001	0.013±0.000
Cl, ppm	0.94	1.07	18.7	4.37	10.4	13.1	225	31.4
Co, ppm	<0.001	<0.001	0.005±0.000	<0.001	0.001±0.000	<0.001	0.019±0.001	0.018±0.001
CO_3, ppm	0.0	0.0	0.0	0.0	0.0	0.0	0.0	0.0
Cr, ppm	<0.001	<0.001	<0.001	<0.001	0.005±0.000	0.003±0.000	<0.001	0.004±0.000
Cs, ppm	0.003±0.000	0.003±0.000	0.004±0.000	0.002±0.000	<0.001	0.001±0.000	0.007±0.000	0.009±0.000
Cu, ppm	0.001±0.000	0.002±0.000	0.003±0.000	0.003±0.000	0.005±0.000	0.004±0.000	0.012±0.000	0.045±0.003
F, ppm	0.50	1.07	0.57	1.02	0.15	0.19	5.22	7.16
Fe, ppm	<0.01	<0.01	<0.01	<0.01	0.01±0.00	0.02±0.00	<0.01	<0.01
HCO_3, ppm	86.5	27.0	<0.8	7.75	21.1	29.8	21.5	—
Hg, ppm	<0.00005	<0.00005	<0.00005	<0.00005	<0.00005	<0.00005	0.00011±0.00001	0.00014±0.00000
K, ppm	1.02±0.01	1.15±0.01	6.93±0.10	3.6±0.0	11.4±0.0	9.00±0.07	16.1±0.1	24.5±0.1
Li, ppm	0.004±0.000	0.002±0.000	0.080±0.001	0.001±0.000	0.007±0.000	0.001±0.000	0.52±0.00	0.14±0.00
Mg, ppm	0.54±0.01	0.36±0.00	6.39±0.08	0.39±0.00	1.06±0.00	0.52±0.00	29.3±0.2	20.8±0.1
Mn, ppm	<0.001	<0.001	0.25±0.00	0.021±0.000	0.029±0.000	0.16±0.00	0.31±0.00	0.17±0.00
Mo, ppm	0.059±0.000	0.066±0.002	0.049±0.000	0.068±0.001	0.012±0.000	0.007±0.000	0.118±0.000	0.319±0.003
Na, ppm	4.32±0.05	3.26±0.02	66.7±0.9	3.07±0.02	3.99±0.01	3.55±0.01	485±1	1150±2
Ni, ppm	<0.001	<0.001	0.004±0.000	0.001±0.000	0.007±0.000	0.005±0.000	0.025±0.001	0.040±0.002
NO_2, ppm	<0.01	<0.01	<0.01	<0.01	<0.01	<0.01	<0.01	<0.01
NO_3, ppm	2.21	0.12	117	19.0	6.77	2.06	891	254
C_2O_4, ppm	<0.01	<0.01	<0.01	<0.01	<0.01	<0.01	<0.01	<0.01
Pb, ppm	<0.0002	<0.0002	0.0003±0.0000	0.0002±0.0000	0.0020±0.0000	0.0003±0.0000	0.0012±0.0000	0.0014±0.0001

PO_4, ppm	<0.01	<0.01	1.22	2.31	1.09	0.05	1.01	<0.01
Rb, ppm	0.007±0.000	0.009±0.001	0.032±0.001	0.012±0.000	0.016±0.001	0.013±0.000	0.041±0.002	0.082±0.002
Sb, ppm	<0.001	<0.001	<0.001	<0.001	0.25±0.00	<0.001	<0.001	0.004±0.000
Se, ppm	<0.001	<0.001	0.007±0.000	<0.001	<0.001	<0.001	0.067±0.004	0.196±0.003
Si, ppm	7.31±0.07	6.63±0.05	23.0±0.2	5.53±0.03	0.69±0.00	1.76±0.02	22.85±0.10	11.44±0.03
SiO_2, calculated ppm	15.6±0.2	14.2±0.1	49.2±0.5	11.8±0.1	1.5±0.0	3.8±0.0	48.9±0.2	24.5±0.1
SO_4, ppm	4.47	10.4	295	10.5	18.1	13.9	515	3285
Sn, ppm	<0.001	<0.001	<0.001	<0.001	<0.001	<0.001	<0.001	<0.001
Sr, ppm	0.05±0.00	0.04±0.01	0.39±0.01	0.03±0.00	0.03±0.00	0.05±0.00	1.36±0.00	2.39±0.01
Th, ppm	<0.001	<0.001	<0.001	<0.001	<0.001	<0.001	<0.001	<0.001
Ti, ppm	<0.002	<0.002	<0.002	<0.002	<0.002	<0.002	<0.002	<0.002
Tl, ppm	<0.001	<0.001	<0.001	<0.001	<0.001	<0.001	<0.001	0.001±0.000
U, ppm	0.0141±0.0011	0.0002±0.0000	<0.0002±	0.0006±0.0000	0.0014±0.0000	0.0013±0.0001	0.0008±0.0001	0.0147±0.0004
V, ppm	0.014±0.001	0.013±0.002	0.002±0.000	0.008±0.000	0.002±0.000	0.002±0.000	0.007±0.000	0.006±0.000
Zn, ppm	0.002±0.000	0.010±0.001	1.46±0.01	0.098±0.000	0.076±0.001	0.033±0.000	9.98±0.08	1.60±0.02
pH, laboratory	7.93	7.01	5.71	6.40	6.81	7.29	5.16	6.99
Total dissolved solids, ppm	139	67.0	648	74.4	85.8	90.0	2498	5242
Cation sum, meq/l	1.379	0.606	7.869	0.770	1.034	1.086	36.595	74.188
Anion sum, meq/l	1.600	0.751	8.595	0.859	1.154	1.201	31.996	73.262
Cation/anion balance, %	–7.42	–10.72	–4.41	–5.46	–5.47	–5.04	6.70	0.63

Appendix H. Mathematica

H.1 Advection-Dispersion Chain Decay Equation in Mathematica

The following Advection-Dispersion Chain Decay Equation was written by J. Walton to calculate curves to fit the measured gamma ray activities of U-series radionuclides. U, Th, Ra, Rn, and Pb are solved using the equation, but only the results of the U, Th, and Ra isotopes were used, because Rn is a gas and the amount of input or escape from the system is unknown. The example in the following pages uses the B1 series of soil samples.

Radionuclide Chain Decay for Pena Blanca

John Walton, May 2007

Large coroplast sample area squares were 30x30 cm in size

SetDirectory[...]

Definitions:
Units: cm, year, disintegrations per second
a[[i,n]] = atoms/cc by radionuclide (i) and by grid node (n); note this is total concentration, dps = N*lambda
disper[[i]] = diffusion/ dispersion coefficient cm^2/yr
darcy = Darcy velocity, specific discharge = , cm/yr
lamba[[i]] = decay constant (1/yr)
source[[i]] = deposition on ground in dps/cm^2/yr = rate it drops from boulder onto ground
xmax = maximum simulation depth
ngrid = number of points in grid
dx = grid steps, cm
nchain = number of radionuclides in decay chain
dt = time step, yr
Rd[[i]] = retardation factors
background[[i]] = background concentration in dps/cm^3
a[[inuclide,nnode]] = activity of each radionuclide at each node in units of dps/cm^3 TOTAL concentration
simulationtime = length of simulation, yr

Radionuclide list =

Notes:
Zeroed out radon as a source of lead by artificially giving it a low decay rate. This is because the gaseous transport of radon is so fast out of soil that its contribution to lead is insignificant.
Multiplied U-238 source by 22, because it has been accumulating for 22 years, other nuclides divided by 22, which is the deposition rate on a per year basis.

```
radionuclides = {"U238", "Th234",
   "U234", "Th230", "Ra226", "Rn222",
   "Pb210", "Bi210", "Po210"};
radionuclides // TableForm
ngrid = 41; xmax = 20.;
nchain = 9;
lambda =
 {1.55 10^-10, 10.51, 2.83 10^-6, 9.19 10^-6,
  4.34 10^-4, 1. 10^-15, 0.031, 50.53, 1.83}
source = {22 * 0.703 / 8.7, 0., 0.028 * 2.,
   0.024 * 2.2, 1.17 * 1.9, 0., 0.12, 0., 0.} /
  (22 lambda / (3.14 * 10^7))
(* source from boulder is entered
  in activity per cm^2 and
  converted to atoms per cm^2 *)
Rd = {1., 1., 1., 1., 1., 1., 1., 1., 1.};
dt = 0.002;
darcy = 0.;
disper = {.75, .6, .75,
  .6, .48, 2.50, 1.18, 2.50, 2.50}
simulationtime = 22.;
```

```
U238
Th234
U234
Th230
Ra226
Rn222
Pb210
Bi210
Po210
```

```
{1.55×10^-10, 10.51, 2.83×10^-6, 9.19×10^-6, 0.000434, 1.×10^-15, 0.031, 50.53, 1.83}
{1.63694×10^16, 0., 2.82429×10^10,
 8.20022×10^9, 7.31066×10^9, 0., 5.52493×10^6, 0., 0.}
```

```
{0.75, 0.6, 0.75, 0.6, 0.48, 2.5, 1.18, 2.5, 2.5}
```

```
{source, lambda, Rd, disper} // TableForm
```

1.63694×10^16	0.	2.82429×10^10	8.20022×10^9	7.31066×10^9	
1.55×10^-10	10.51	2.83×10^-6	9.19×10^-6	0.000434	
1.	1.	1.	1.	1.	
0.75	0.6	0.75	0.6	0.48	

Set up grid, set initial activities to zero for all radionuclides at all nodes.

```
dx = xmax / (ngrid - 1)
a = {};
x = Table[dx * i, {i, 0, ngrid - 1}]
a = Table[0.,
  {i, 1, nchain}, {n, 1, ngrid}]
```

```
0.5

{0, 0.5, 1., 1.5, 2., 2.5, 3., 3.5, 4., 4.5, 5., 5.5, 6., 6.5, 7.,
 7.5, 8., 8.5, 9., 9.5, 10., 10.5, 11., 11.5, 12., 12.5, 13., 13.5,
 14., 14.5, 15., 15.5, 16., 16.5, 17., 17.5, 18., 18.5, 19., 19.5, 20.}

{{0., 0., 0., 0., 0., 0., 0., 0., 0., 0., 0., 0., 0., 0., 0., 0., 0., 0., 0., 0., 0.,
  0., 0., 0., 0., 0., 0., 0., 0., 0., 0., 0., 0., 0., 0., 0., 0., 0., 0., 0., 0.},
 {0., 0., 0., 0., 0., 0., 0., 0., 0., 0., 0., 0., 0., 0., 0., 0., 0., 0., 0., 0.,
  0., 0., 0., 0., 0., 0., 0., 0., 0., 0., 0., 0., 0., 0., 0., 0., 0., 0., 0., 0., 0.},
 {0., 0., 0., 0., 0., 0., 0., 0., 0., 0., 0., 0., 0., 0., 0., 0., 0., 0., 0., 0.,
  0., 0., 0., 0., 0., 0., 0., 0., 0., 0., 0., 0., 0., 0., 0., 0., 0., 0., 0., 0., 0.},
 {0., 0., 0., 0., 0., 0., 0., 0., 0., 0., 0., 0., 0., 0., 0., 0., 0., 0., 0., 0.,
  0., 0., 0., 0., 0., 0., 0., 0., 0., 0., 0., 0., 0., 0., 0., 0., 0., 0., 0., 0., 0.},
 {0., 0., 0., 0., 0., 0., 0., 0., 0., 0., 0., 0., 0., 0., 0., 0., 0., 0., 0., 0.,
  0., 0., 0., 0., 0., 0., 0., 0., 0., 0., 0., 0., 0., 0., 0., 0., 0., 0., 0., 0., 0.},
 {0., 0., 0., 0., 0., 0., 0., 0., 0., 0., 0., 0., 0., 0., 0., 0., 0., 0., 0., 0.,
  0., 0., 0., 0., 0., 0., 0., 0., 0., 0., 0., 0., 0., 0., 0., 0., 0., 0., 0., 0., 0.},
 {0., 0., 0., 0., 0., 0., 0., 0., 0., 0., 0., 0., 0., 0., 0., 0., 0., 0., 0., 0.,
  0., 0., 0., 0., 0., 0., 0., 0., 0., 0., 0., 0., 0., 0., 0., 0., 0., 0., 0., 0., 0.},
 {0., 0., 0., 0., 0., 0., 0., 0., 0., 0., 0., 0., 0., 0., 0., 0., 0., 0., 0., 0.,
  0., 0., 0., 0., 0., 0., 0., 0., 0., 0., 0., 0., 0., 0., 0., 0., 0., 0., 0., 0., 0.},
 {0., 0., 0., 0., 0., 0., 0., 0., 0., 0., 0., 0., 0., 0., 0., 0., 0., 0., 0., 0.,
  0., 0., 0., 0., 0., 0., 0., 0., 0., 0., 0., 0., 0., 0., 0., 0., 0., 0., 0., 0., 0.}}
```

Add Time Steps

set initial concentrations to zero and calculate number of steps.

```
background =
  {0., 0., 0., 0., 0., 0., 0., 0., 0.};
a = Table[background[[i]],
  {i, 1, nchain}, {n, 1, ngrid}]
nsteps = simulationtime / dt
```

```
General::spell1 : Possible spelling error: new symbol
   name "background" is similar to existing symbol "Background". More…
```

```
{{0., 0., 0., 0., 0., 0., 0., 0., 0., 0., 0., 0., 0., 0., 0., 0., 0., 0., 0., 0., 0.,
  0., 0., 0., 0., 0., 0., 0., 0., 0., 0., 0., 0., 0., 0., 0., 0., 0., 0., 0., 0.},
 {0., 0., 0., 0., 0., 0., 0., 0., 0., 0., 0., 0., 0., 0., 0., 0., 0., 0., 0., 0.,
  0., 0., 0., 0., 0., 0., 0., 0., 0., 0., 0., 0., 0., 0., 0., 0., 0., 0., 0., 0., 0.},
 {0., 0., 0., 0., 0., 0., 0., 0., 0., 0., 0., 0., 0., 0., 0., 0., 0., 0., 0., 0.,
  0., 0., 0., 0., 0., 0., 0., 0., 0., 0., 0., 0., 0., 0., 0., 0., 0., 0., 0., 0., 0.},
 {0., 0., 0., 0., 0., 0., 0., 0., 0., 0., 0., 0., 0., 0., 0., 0., 0., 0., 0., 0.,
  0., 0., 0., 0., 0., 0., 0., 0., 0., 0., 0., 0., 0., 0., 0., 0., 0., 0., 0., 0., 0.},
 {0., 0., 0., 0., 0., 0., 0., 0., 0., 0., 0., 0., 0., 0., 0., 0., 0., 0., 0., 0.,
  0., 0., 0., 0., 0., 0., 0., 0., 0., 0., 0., 0., 0., 0., 0., 0., 0., 0., 0., 0., 0.},
 {0., 0., 0., 0., 0., 0., 0., 0., 0., 0., 0., 0., 0., 0., 0., 0., 0., 0., 0., 0.,
  0., 0., 0., 0., 0., 0., 0., 0., 0., 0., 0., 0., 0., 0., 0., 0., 0., 0., 0., 0., 0.},
 {0., 0., 0., 0., 0., 0., 0., 0., 0., 0., 0., 0., 0., 0., 0., 0., 0., 0., 0., 0.,
  0., 0., 0., 0., 0., 0., 0., 0., 0., 0., 0., 0., 0., 0., 0., 0., 0., 0., 0., 0., 0.},
 {0., 0., 0., 0., 0., 0., 0., 0., 0., 0., 0., 0., 0., 0., 0., 0., 0., 0., 0., 0.,
  0., 0., 0., 0., 0., 0., 0., 0., 0., 0., 0., 0., 0., 0., 0., 0., 0., 0., 0., 0., 0.},
 {0., 0., 0., 0., 0., 0., 0., 0., 0., 0., 0., 0., 0., 0., 0., 0., 0., 0., 0., 0.,
  0., 0., 0., 0., 0., 0., 0., 0., 0., 0., 0., 0., 0., 0., 0., 0., 0., 0., 0., 0., 0.}}
```

```
11000.
```

```
Do[
 Do[If[i == 1,
   a[[1, 1]] = a[[1, 1]] + (source[[1]] * 2 / dx -
        a[[1, 1]] * lambda[[1]] +
        (+disper[[1]] / Rd[[1]] * (a[[1, 2]] -
              a[[1, 1]]) / dx) / dx) * dt,
   a[[i, 1]] = a[[i, 1]] + (source[[i]] * 2 / dx -
        a[[i, 1]] * lambda[[i]] +
        a[[i - 1, 1]] * lambda[[i - 1]]
        + (+disper[[i]] / Rd[[i]] *
           (a[[i, 2]] - a[[i, 1]]) / dx) / dx) *
      dt], {i, 1, nchain}];
 a[[6, 1]] = 0. (* set surface radon to zero,
  escapes to atmosphere *);
```

```
Do[If[i == 1, a[[i, n]] = a[[i, n]] + (
       -a[[i, n]] * lambda[[i]]
        + (-disper[[i]] / Rd[[i]] *
             (a[[i, n]] - a[[i, n - 1]]) / dx
           + disper[[i]] / Rd[[i]] *
             (a[[i, n + 1]] - a[[i, n]]) /
              dx) / dx) * dt,
  a[[i, n]] = a[[i, n]] + (
       -a[[i, n]] * lambda[[i]] +
        a[[i - 1, n]] * lambda[[i - 1]]
        + (-disper[[i]] / Rd[[i]] *
             (a[[i, n]] - a[[i, n - 1]]) / dx
           + disper[[i]] / Rd[[i]] *
             (a[[i, n + 1]] - a[[i, n]]) /
              dx) / dx) * dt],
 {i, 1, nchain}, {n, 2, ngrid - 1}];
If[Mod[istep, 1000] == 1,
 Print["time = ", istep * dt]],
{istep, 1, nsteps}]
```

```
time = 0.002

time = 2.002

time = 4.002

time = 6.002

time = 8.002

time = 10.002

time = 12.002

time = 14.002

time = 16.002

time = 18.002

time = 20.002
```

```
nsteps * dt
a // TableForm
```

```
22.
```

1.89896×10^{17}	1.69589×10^{17}	1.5078×10^{17}	1.33447×10^{17}	1.17556×1
2.73773×10^{6}	2.49002×10^{6}	2.22097×10^{6}	1.9667×10^{6}	1.73259×1
3.27854×10^{11}	2.92813×10^{11}	2.60353×10^{11}	2.30437×10^{11}	2.03008×1
1.05597×10^{11}	9.29927×10^{10}	8.14354×10^{10}	7.09057×10^{10}	6.13748×1
1.04086×10^{11}	9.01889×10^{10}	7.76015×10^{10}	6.62908×10^{10}	5.62104×1
0.	1.56548×10^{7}	2.7474×10^{7}	3.60703×10^{7}	4.19908×1
4.1574×10^{7}	3.72957×10^{7}	3.33914×10^{7}	2.9834×10^{7}	2.65985×1
25061.1	22849.2	20511.	18334.3	16347.8
577498.	557592.	525287.	486478.	445047.

```
radionuclides // TableForm
```

```
U238
Th234
U234
Th230
Ra226
Rn222
Pb210
Bi210
Po210
```

Put results into single vectors by radionuclide

```
U238 = a[[1]];
Th234 = a[[2]];
U234 = a[[3]];
Th230 = a[[4]];
Ra226 = a[[5]];
Rn222 = a[[6]];
Pb210 = a[[7]];
tmp = Table[{x[[n]],
    U238[[n]] * lambda[[1]] / (3.14 * 10^7)},
   {n, 1, ngrid}];
U238sim = Interpolation[tmp,
   InterpolationOrder → 1];
tmp = Table[{x[[n]], Th234[[n]] * lambda[[2]] /
      (3.14 * 10^7)}, {n, 1, ngrid}];
Th234sim = Interpolation[tmp,
   InterpolationOrder → 1];
tmp = Table[{x[[n]], U234[[n]] * lambda[[3]] /
      (3.14 * 10^7)}, {n, 1, ngrid}];
```

```
U234sim = Interpolation[tmp,
   InterpolationOrder→1];
tmp = Table[{x[[n]], Th230[[n]]*lambda[[4]]/
      (3.14*10^7)}, {n, 1, ngrid}];
Th230sim = Interpolation[tmp,
   InterpolationOrder→1];
tmp = Table[{x[[n]], Ra226[[n]]*lambda[[5]]/
      (3.14*10^7)}, {n, 1, ngrid}];
Ra226sim = Interpolation[tmp,
   InterpolationOrder→1];
tmp = Table[{x[[n]], Rn222[[n]]*lambda[[6]]/
      (3.14*10^7)}, {n, 1, ngrid}];
Rn222sim = Interpolation[tmp,
  InterpolationOrder→1];
tmp = Table[{x[[n]], Pb210[[n]]*lambda[[7]]/
     (3.14*10^7)}, {n, 1, ngrid}];
Pb210sim = Interpolation[tmp,
   InterpolationOrder→1];
```

```
Needs["Graphics`Colors`"]
Needs["Graphics`MultipleListPlot`"]
Needs["Graphics`Graphics`"]
p1 = Plot[Th234sim[depth],
    {depth, 0, xmax}, PlotRange → All,
    PlotStyle → {Red, Thickness[0.014]},
    Frame → True,
    FrameLabel → {"depth, cm", "dps/cm^3"},
    PlotLabel -> "Th-234",
    GridLines → Automatic,
    DisplayFunction → Identity];
```

```
General::spell1 :
 Possible spelling error: new symbol name "depth" is similar to existing symbol "Depth". More…
```

```
Th234data = {{0.5, .703}, {2.9, .68},
    {3.6, .43}, {4.5, .24}, {5.9, .14},
    {7.3, .13}, {8.7, 0.12}, {10.1, 0.01}};
p2 = ListPlot[Th234data,
    PlotStyle → PointSize[0.03],
    Frame → True, DisplayFunction → Identity];
Show[p1, p2,
  DisplayFunction → $DisplayFunction];
```

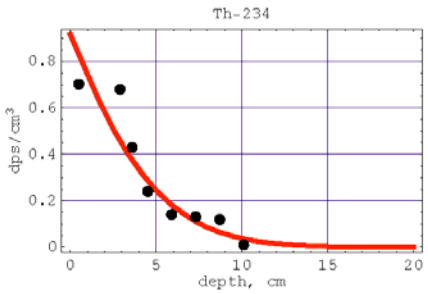

```
Needs["Graphics`Colors`"]
Needs["Graphics`MultipleListPlot`"]
Needs["Graphics`Graphics`"]
p3 = Plot[U234sim[depth],
    {depth, 0, xmax}, PlotRange → All,
    PlotStyle → {Orange, Thickness[0.014]},
    Frame → True,
    FrameLabel → {"depth, cm", "dps/cm^3"},
    PlotLabel -> "U-234",
    GridLines → Automatic,
    DisplayFunction → Identity];
U234data = {{0.5, .028}, {2.9, .02},
    {3.6, .01}, {4.5, .007}, {5.9, .004},
    {7.3, .004}, {8.7, 0.002}, {10.1, 0.000}};
p4 = ListPlot[U234data,
    PlotStyle → PointSize[0.03],
    Frame → True, DisplayFunction → Identity];
Show[p3, p4,
  DisplayFunction → $DisplayFunction];
```

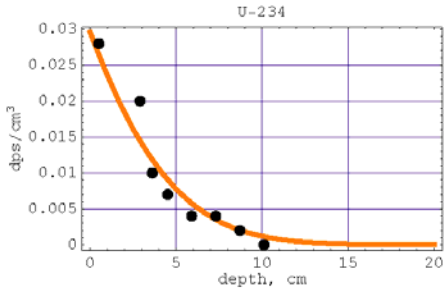

```
Needs["Graphics`Colors`"]
Needs["Graphics`MultipleListPlot`"]
Needs["Graphics`Graphics`"]
p5 = Plot[Th230sim[depth],
   {depth, 0, xmax}, PlotRange → All,
   PlotStyle → {Green, Thickness[0.014]},
   Frame → True,
   FrameLabel → {"depth, cm", "dps/cm^3"},
   PlotLabel -> "Th-230",
   GridLines → Automatic,
   DisplayFunction → Identity];

Th230data = {{0.5, .024}, {2.9, .025},
   {3.6, .017}, {4.5, .009}, {5.9, .004},
   {7.3, .004}, {8.7, 0.003}, {10.1, 0.002}};
p6 = ListPlot[Th230data,
   PlotStyle → PointSize[0.03],
   Frame → True, DisplayFunction → Identity];
Show[p5, p6,
  DisplayFunction → $DisplayFunction];
```

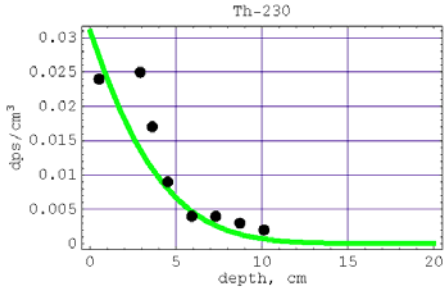

```
Needs["Graphics`Colors`"]
Needs["Graphics`MultipleListPlot`"]
Needs["Graphics`Graphics`"]
p7 = Plot[Ra226sim[depth],
   {depth, 0, xmax}, PlotRange → All,
   PlotStyle → {Blue, Thickness[0.014]},
   Frame → True,
   FrameLabel → {"depth, cm", "dps/cm^3"},
   PlotLabel -> "Ra-226",
   GridLines → Automatic,
   DisplayFunction → Identity];
Ra226data = {{0.5, 1.17}, {2.9, 1.05},
   {3.6, .62}, {4.5, .37}, {5.9, .18},
   {7.3, .15}, {8.7, 0.12}, {10.1, 0.01}};
p8 = ListPlot[Ra226data,
   PlotStyle → PointSize[0.03],
   Frame → True, DisplayFunction → Identity];
Show[p7, p8,
  DisplayFunction → $DisplayFunction];
```

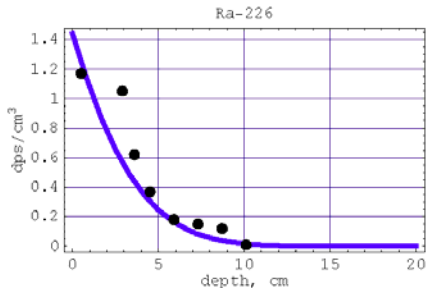

```
Needs["Graphics`Colors`"]
Needs["Graphics`MultipleListPlot`"]
Needs["Graphics`Graphics`"]
p9 = Plot[Rn222sim[depth],
   {depth, 0, xmax}, PlotRange → All,
   PlotStyle → {Blue, Thickness[0.014]},
   Frame → True,
   FrameLabel → {"depth, cm", "dps/cm^3"},
   PlotLabel -> "Rn-222",
   GridLines → Automatic,
   DisplayFunction → Identity];
Rn222data = {{0.5, 1.169}, {2.9, 1.046},
   {3.6, .615}, {8.7, 0.116}, {10.1, 0.081}};
p10 = ListPlot[Rn222data,
   PlotStyle → PointSize[0.03],
   Frame → True, DisplayFunction → Identity];
Show[p9, p10,
  DisplayFunction → $DisplayFunction];
```

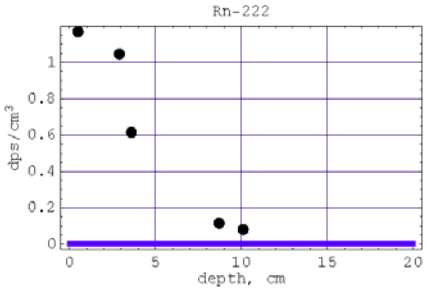

```
Needs["Graphics`Colors`"]
Needs["Graphics`MultipleListPlot`"]
Needs["Graphics`Graphics`"]
p11 = Plot[Pb210sim[depth],
  {depth, 0, xmax}, PlotRange → All,
  PlotStyle → {Purple, Thickness[0.014]},
  Frame → True
  FrameLabel → {"depth, cm", "dps/cm^3"},
  PlotLabel -> "Pb-210",
  GridLines → Automatic
  DisplayFunction → Identity];

Pb210data = {{0.5, .033}, {2.9, .027},
   {3.6, .018}, {8.7, 0.004}, {10.1, 0.004}};
p12 = ListPlot[Pb210data,
   PlotStyle → PointSize[0.03],
   Frame → True, DisplayFunction → Identity];
Show[p11, p12,
  DisplayFunction → $DisplayFunction];
```

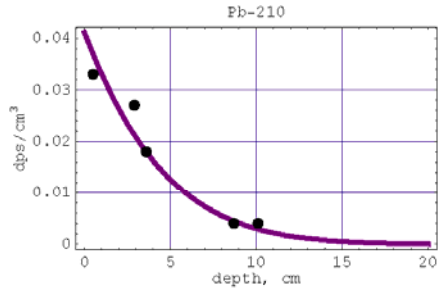

Vita

Katrina Pekar-Carpenter began her academic career at the University of Dayton. She earned her Bachelor of Science in Geology in 2004. She was the recipient of a University of Dayton Learn, Lead, and Serve award and a GSA North-Central Section Undergraduate Student research grant, which supported her research and senior thesis. She served as an undergraduate lab teaching assistant. She was also the co-recipient of the Springer Scholarship for the Outstanding Senior in Geology.

Katrina continued her studies at Kansas State University and earned a Master of Science degree in Geology in 2006. She was a part-time teaching assistant for introductory geology, mineralogy, and petrology labs. She was the recipient of numerous scholarships and became a member of the professional chemistry fraternity, Alpha Chi Sigma, and an associate member of Sigma Xi.

In 2006, Katrina began work on her doctorate in Geology at the University of Texas at El Paso. After serving as a research assistant on the Peña Blanca Natural Analogue project for a year, Katrina was awarded a fellowship with the Department of Energy, Office of Civilian Radioactive Waste Management. As part of this fellowship, she spent a three months at Oak Ridge National Laboratory in Tennessee helping with research on a radioactive waste plume on the Y-12 site. Katrina was selected for a summer internship in 2009 with the U.S. Government Accountability Office, Office of Science, Technology, and Engineering, continued working with GAO through the Student Career Experience Program until graduation. She has accepted a permanent position as a Physical Scientist at GAO.